

Fall 12-13-2013

Mechanistic Studies of Bimolecular Electron Transfer Self-Exchange Rates of Ruthenium Ammine Pyridyl Complexes Measured by NMR Line Broadening Techniques

Yishun Qin
yqin2@usfca.edu

Follow this and additional works at: <https://repository.usfca.edu/thes>

 Part of the [Inorganic Chemistry Commons](#)

Recommended Citation

Qin, Yishun, "Mechanistic Studies of Bimolecular Electron Transfer Self-Exchange Rates of Ruthenium Ammine Pyridyl Complexes Measured by NMR Line Broadening Techniques" (2013). *Master's Theses*. 74.
<https://repository.usfca.edu/thes/74>

This Thesis is brought to you for free and open access by the Theses, Dissertations, Capstones and Projects at USF Scholarship: a digital repository @ Gleeson Library | Geschke Center. It has been accepted for inclusion in Master's Theses by an authorized administrator of USF Scholarship: a digital repository @ Gleeson Library | Geschke Center. For more information, please contact repository@usfca.edu.

**Mechanistic Studies of Bimolecular Electron Transfer Self-Exchange Rates of
Ruthenium Ammine Pyridyl Complexes Measured by NMR Line Broadening
Techniques**

A Thesis Presented to the Faculty
Of the Department of Chemistry
At the University of San Francisco
in partial fulfillment of the requirement for the Degree of
Master of Science in Chemistry

Written by
Yishun Qin
Bachelor of Science in Chemical Engineering and Technology
Shanghai University, Shanghai

11/27/2013

Mechanistic Studies of Bimolecular Electron Transfer Self-Exchange Rates of Ruthenium Ammine Pyridyl Complexes Measured by NMR Line Broadening Techniques

Thesis written by Yishun Qin

This thesis is written under the guidance of the Faculty Advisory Committee, and approved by all its members, has been accepted in partial fulfillment of the requirements for the degree of

**Master of Science
in Chemistry
at
The University of San Francisco**

Thesis Committee

Jeff Curtis, Ph.D.
Research Advisor

Kim Summerhays, Ph.D.
Professor

Larry Margerum, Ph.D.
Professor

Marcelo Camperi, Ph.D.
Dean, Collage of Arts and Sciences

Acknowledgement

I would like to thank my research advisor Dr. Jeff Curtis for his guidance, patience and providing me with a wonderful atmosphere of doing research. I would also like to thank Dr. Kim Summerhays Dr. Larry and Margerum for taking their time to put valuable comments on my thesis.

I would like to thank all my lab mates, Gina Pengra, Po-Kai Chen, Prakash Sista, Hassan Imran for showing me the basic synthesis and instruments in our lab and Zhiji Han for providing valuable suggestions for my experiments. Many thanks to Jeff Oda, Andy Huang, Dorothy Stuebner and Deidre Shymanski and others in the Department of Chemistry for their help whenever I needed throughout my years at USF.

Finally, I would like to thank my parents and my husband for always standing by me through the good times and bad times. I would never be able to finish this thesis without their support.

Table of Contents

| | |
|-----------------|------|
| List of Figures | v |
| List of Tables | xvii |
| Abstract | xxi |

Chapter One: Introduction to some basic concepts of electron-transfer reactions and NMR line broadening techniques for measurement of kinetic rate constants

| | |
|---|----|
| Electron transfer | 1 |
| Potential Energy Surfaces | 10 |
| Optical Electron Transfer vs. Thermal Electron Transfer | 12 |
| Adiabatic vs. Non-adiabatic ET | 16 |
| Application of the NMR line broadening technique to ET kinetic measurements | 20 |
| References | 33 |

Chapter Two: NMR line broadening measurements of electron transfer self-exchange rates of ruthenium ammine pyridyl complexes and evidence for pyridyl ligand substituent effects on rates

| | |
|---|----|
| Introduction | 36 |
| Experimental | |
| Materials | 41 |
| Preparation of the pentaamine Ruthenium Complexes | |
| $[(\text{NH}_3)_5\text{Ru}^{\text{III}}\text{Cl}]\text{Cl}_2$ | 41 |

| | |
|---|----|
| [L-(NH ₃) ₅ Ru ^{II}](PF ₆) ₂ | |
| Method 1 (L= py, 3-Clpy, 4-Clpy, 3-Brpy, 4-Brpy, 3-Fpy, 3-tfmpy) | 42 |
| Preparation of Zn/Hg amalgam | 43 |
| Method 2 (L= 3,5-Br ₂ py, 3,5-Cl ₂ py, 3-Etpy, 3,5-Me ₂ py, 3-pic, 4-pic) | 43 |
| Purification methods | 44 |
| [L-(NH ₃) ₅ Ru ^{II}]Cl ₂ | 45 |
| [L-(NH ₃) ₅ Ru ^{III}]Cl ₃ | 45 |
| Spectrophotometric Measurements | 46 |
| Electrochemical Measurements | 47 |
| NMR line broadening Measurements | 50 |
| Sample preparation | |
| NMR tubes | 51 |
| Preparation of samples for self-exchange reaction rate studies | 51 |
| Optimizing NMR signals | |
| Field/Frequency Locking | 52 |
| Spectrometer Shimming | 52 |
| Typical ¹ H and ¹⁹ F parameters used | 54 |
| Exporting NMR spectra | 56 |
| Spectral deconvolution using “PeakFit” | 60 |
| Calibration of the variable temperature controller used in the NMR experiments | 64 |

| | |
|--|-----|
| Results and Discussion | |
| Rates of Self-exchange Electron Transfer Reactions | 70 |
| Activation Parameters and Mechanistic Interpretation | 94 |
| References | 107 |

Chapter Three: Kinetic Studies of Salt Effects on Self-exchange Electron Transfer Reactions Monitored by ^{19}F NMR Spectroscopy

| | |
|--|-----|
| Introduction | 110 |
| The effect of ionic strength on ET rates | 114 |
| Superexchange | 116 |
| Rate constants for reactant association/dissociation | 121 |
| Experimental | |
| Materials | 124 |
| Preparation of $\text{K}_4\text{Ru}^{\text{II}}(\text{CN})_6$ (MW=413g/mol) | 124 |
| Preparation of $\text{K}_4\text{Os}^{\text{II}}(\text{CN})_6$ (MW= 502g/mol) | 125 |
| Preparation of sodium muconate, Na_2Muc | 125 |
| Preparation of sodium adipate, Na_2adip | 126 |
| Calculation of μ and GP in the reactant solutions | 126 |
| Methods of addition of salts used in the NMR line broadening experiments | 127 |
| Measurement of the ion-pair formation constant K_{ip} between the $[\text{NH}_3]_5\text{Ru}(\text{III})(3\text{-tfmpy})]^{3+}$ cation and the $[\text{M}^{\text{II}}(\text{CN})_6]^{4-}$ anions | 127 |

Results and Discussions

| | |
|---|-----|
| Kinetic salt effect data | 129 |
| Interpretation of the observed kinetic salt effects | 142 |
| Kinetic Modeling | 149 |
| Catalysis by $M(CN)_6^{4-}$ (M = Fe, Os, Ru) | 166 |
| Ion-pair formation constants between Ru^{III} ammine complexes and $M^{II}(CN)_6^{4-}$ based on outer-sphere charge-transfer absorption measurements | 175 |
| Activation Parameters and Mechanistic Interpretation | 193 |
| References | 204 |

List of Figures

Chapter One

- Figure 1-1. Schematic illustration of the inner-sphere and outer-sphere ET mechanisms. 2
- Figure 1-2. Potential energy surfaces for reactant ($R = D/A$) and product ($P = D^+/A^-$) redox states as a function of nuclear configuration q when ($G^0 = 0$). 11
- Figure 1-3. Potential energy surfaces representing a case $\Delta G^0 > 0$. 12
- Figure 1-4. Schematic illustration of optical and thermal ET processes as they relate to inner-sphere nuclear coordinates. The different-sized circles are intended to represent longer metal-ligand bond lengths at D (Ru^{II} in our specific systems) or A^- , and shorter distances at A or D^+ (Ru^{III} in our systems). 13
- Figure 1-5. Potential energy curves relevant to the adiabatic ($\kappa_{el} \sim 1$) electron-transfer limit 17
- Figure 1-6. Potential energy surfaces relevant to the non-adiabatic ($H_{ab}, \kappa_{el} \sim 0$) electron-transfer process. 17
- Figure 1-7. Potential energy curves for the quantum mechanical model of non-adiabatic electron transfer reactions. The vibrational wave functions are drawn so as to illustrate how overlap of the vibrational (nuclear) wave functions can facilitate the tunneling process. 20

- Figure 1-8. Schematic illustration of the ET self-exchange reaction between $L-(NH_3)_5Ru^{2+}$ and $L-(NH_3)_5Ru^{3+}$ (L represents a variety of different possible ligands, including the pyrdyl ligands used in this work, see Table 2-1) 21
- Figure 1-9. Dependence of magnetic resonance line shapes on kinetic exchange rates as would be expected for exchange of the ^{19}F signals due to the ET self-exchange reaction $3\text{-tfmpy}(NH_3)_5Ru^{II} + 3\text{tfmpy}(NH_3)_5Ru^{III} \rightleftharpoons 3\text{-tfmpy}(NH_3)_5Ru^{II} + 3\text{-tfmpy}(NH_3)_5Ru^{III}$ (3-tfmpy is 3-trifluoromethylpyridine, see Table 2-1) 24
- Figure 1-10. Example of an 1H NMR spectrum showing the effects of slow chemical exchange between $A_5Ru^{II}3,5\text{-Me}_2\text{py}$ and $A_5Ru^{III}3,5\text{-Me}_2\text{py}$ in D_2O (3,5-Me₂Py=3,5-dimethylpyridine, A= NH_3 , ring protons of the Ru^{II} complex shown here). Rate calculated using Equation 1-31. 29
- Figure 1-11. Example of an 1H NMR spectrum showing the effects of intermediate chemical exchange between $A_5Ru^{II}(4\text{-Phpy})^{2+}$ and $A_5Ru^{III}(4\text{-Phpy})^{3+}$ in D_2O (4-Phpy = 4-phenylpyridine, A= NH_3 , ring protons of the Ru^{II} complex shown here, see Chapter Two). Rate calculated using Ru^{III} peaks (see Chapter Two) and Equation 1-31. 30

Figure 1-12. Illustration of ^{19}F NMR spectrum for fast chemical exchange reaction between $\text{A}_5\text{Ru}^{\text{II}}(\text{3-tfmpy})^{2+}$ and $\text{A}_5\text{Ru}^{\text{III}}(\text{3-tfmpy})^{3+}$ at $5.0 \times 10^{-3} \text{ M}$ in each before and after addition of the ET catalyst $\text{Fe}(\text{CN})_6^{4-}$ at $7.8 \times 10^{-4} \text{ M}$ concentration (see Chapter Three) (3-tfmpy = trifluoromethylpyridine, $\text{A}=\text{NH}_3$). It is the ^{19}F resonance of the CF_3 group on the Ru^{II} and Ru^{III} complexes which is shown here). Rate calculated using Equation 1-35. 31

Chapter Two

Figure 2-1. Illustration of the line-broadening effect on the 3-Brpy- $(\text{NH}_3)_5\text{Ru}^{\text{II/III}}$ proton NMR spectrum due to electron-transfer self-exchange in the mixture 40

Figure 2-2. Illustration of how the magnetic field changes after loading the sample. 53

Figure 2-3. the “sma1” window 56

Figure 2-4. the “tojdx” window 57

Figure 2-5. Rough fitting performed by the Peakfit program after clicking the “Autofit peaks | Residuals” button. 61

Figure 2-6. Illustration of chemical shift difference between $-\text{OH}$ and $-\text{CH}_3$ in methanol 65

Figure 2-7. Graph of NMR read-out temperature vs actual temperature calculated from Equation 2-4 (The regression line is shown as reference only.) 67

| | |
|--|----|
| Figure 2-8. Graph of instrument temperature error, ($T_{\text{actual}} - T_{\text{read}}$) vs T_{read} | 68 |
| (these values can be directly added to T_{read} in order to arrived at T_{actual}) | |
| Figure 2-9(a). ^1H NMR spectrum of $\text{A}_5\text{Ru}^{\text{II}}$ (4-Clpy) $^{2+}$ complex in D_2O , [Ru^{II}] = 5.0 <u>mM</u> | 71 |
| Figure 2-9(b). ^1H NMR spectrum of $\text{A}_5\text{Ru}^{\text{III}}$ (4-Clpy) $^{3+}$ complex in D_2O , [Ru^{III}] = 5.0 <u>mM</u> | 71 |
| Figure 2-9(c). ^1H NMR spectrum of $\text{A}_5\text{Ru}^{\text{II/III}}$ (4-Clpy) $^{2+/3+}$ mixture in D_2O , [Ru^{II}] = [Ru^{III}] = 5.0 <u>mM</u> | 71 |
| Figure 2-10(a). ^1H NMR spectrum of $\text{A}_5\text{Ru}^{\text{II}}$ (4-Brpy) $^{2+}$ complex in D_2O , [Ru^{II}] = 5.0 <u>mM</u> | 72 |
| Figure 2-10(b). ^1H NMR spectrum of $\text{A}_5\text{Ru}^{\text{III}}$ (4-Brpy) $^{3+}$ complex in D_2O , [Ru^{III}] = 5.0 <u>mM</u> | 72 |
| Figure 2-10(c). ^1H NMR spectrum of $\text{A}_5\text{Ru}^{\text{II/III}}$ (4-Brpy) $^{2+/3+}$ mixture in D_2O , [Ru^{II}] = [Ru^{III}] = 5.0 <u>mM</u> | 72 |
| Figure 2-11(a). ^1H NMR spectrum of $\text{A}_5\text{Ru}^{\text{II}}$ (4-pic) $^{2+}$ complex in D_2O , [Ru^{II}] = 5.0 <u>mM</u> | 73 |
| Figure 2-11(b). ^1H NMR spectrum of $\text{A}_5\text{Ru}^{\text{III}}$ (4-pic) $^{3+}$ complex in D_2O , [Ru^{III}] = 5.0 <u>mM</u> | 73 |
| Figure 2-11(c). ^1H NMR spectrum of $\text{A}_5\text{Ru}^{\text{II/III}}$ (4-pic) $^{2+/3+}$ mixture in D_2O , [Ru^{II}] = [Ru^{III}] = 5.0 <u>mM</u> | 73 |
| Figure 2-12(a). ^{19}F NMR spectrum of $\text{A}_5\text{Ru}^{\text{II}}$ (3-tfmpy) $^{2+}$ complex in D_2O , [Ru^{II}] = 5.0 <u>mM</u> | 74 |
| Figure 2-12(b). ^{19}F NMR spectrum of $\text{A}_5\text{Ru}^{\text{III}}$ (3-tfmpy) $^{3+}$ complex in D_2O , [Ru^{III}] = 5.0 <u>mM</u> | 74 |

| | |
|--|----|
| Figure 2-12(c). ^{19}F NMR spectrum of $\text{A}_5\text{Ru}^{\text{II/III}}$ (3-tfmpy) $^{2+/3+}$ mixture in D_2O , | 74 |
| $[\text{Ru}^{\text{II}}] = [\text{Ru}^{\text{III}}] = 5.0 \text{ mM}$ | |
| Figure 2-13(a). ^1H NMR spectrum of $\text{A}_5\text{Ru}^{\text{II}}$ (4-Phpy) $^{2+}$ complex in D_2O , | 75 |
| $[\text{Ru}^{\text{II}}] = 5.0 \text{ mM}$ | |
| Figure 2-13(b). ^1H NMR spectrum of $\text{A}_5\text{Ru}^{\text{III}}$ (4-Phpy) $^{3+}$ complex in D_2O , | 75 |
| $[\text{Ru}^{\text{III}}] = 5.0 \text{ mM}$ | |
| Figure 2-13 (c). ^1H NMR spectrum of $\text{A}_5\text{Ru}^{\text{II/III}}$ (4-Phpy) $^{2+/3+}$ mixture in D_2O , | 75 |
| $[\text{Ru}^{\text{II}}] = [\text{Ru}^{\text{III}}] = 5.0 \text{ mM}$ | |
| Figure 2-14(a). ^1H NMR spectrum of $\text{A}_5\text{Ru}^{\text{II}}$ py $^{2+}$ complex in D_2O , $[\text{Ru}^{\text{II}}] = 5.0 \text{ mM}$ | 76 |
| Figure 2-14(b). ^1H NMR spectrum of $\text{A}_5\text{Ru}^{\text{II/III}}$ py $^{2+/3+}$ mixture in D_2O , | 76 |
| $[\text{Ru}^{\text{II}}] = [\text{Ru}^{\text{III}}] = 5.0 \text{ mM}$ | |
| Figure 2-15(a). ^1H NMR spectrum of $\text{A}_5\text{Ru}^{\text{II}}$ (3-Clpy) $^{2+}$ complex in D_2O , | 77 |
| $[\text{Ru}^{\text{II}}] = 5.0 \text{ mM}$ | |
| Figure 2-15(b). ^1H NMR spectrum of $\text{A}_5\text{Ru}^{\text{II/III}}$ (3-Clpy) $^{2+/3+}$ mixture in D_2O , | 77 |
| $[\text{Ru}^{\text{II}}] = [\text{Ru}^{\text{III}}] = 5.0 \text{ mM}$ | |
| Figure 2-16(a). ^1H NMR spectrum of $\text{A}_5\text{Ru}^{\text{II}}$ (3-Brpy) $^{2+}$ complex in D_2O , | 78 |
| $[\text{Ru}^{\text{II}}] = 5.0 \text{ mM}$ | |
| Figure 2-16(b). ^1H NMR spectrum of $\text{A}_5\text{Ru}^{\text{II/III}}$ (3-Brpy) $^{2+/3+}$ mixture in D_2O , | 78 |
| $[\text{Ru}^{\text{II}}] = [\text{Ru}^{\text{III}}] = 5.0 \text{ mM}$ | |
| Figure 2-17(a). ^1H NMR spectrum of $\text{A}_5\text{Ru}^{\text{II}}$ (3-Fpy) $^{2+}$ complex in D_2O , | 79 |
| $[\text{Ru}^{\text{II}}] = 5.0 \text{ mM}$ | |
| Figure 2-17(b). ^1H NMR spectrum of $\text{A}_5\text{Ru}^{\text{II/III}}$ (3-Fpy) $^{2+/3+}$ mixture in D_2O , | 79 |
| $[\text{Ru}^{\text{II}}] = [\text{Ru}^{\text{III}}] = 5.0 \text{ mM}$ | |

| | |
|---|----|
| Figure 2-18(a). ^1H NMR spectrum of $\text{A}_5\text{Ru}^{\text{II}}$ (3-pic) $^{2+}$ complex in D_2O , [Ru ^{II}] = 5.0 mM | 80 |
| Figure 2-18(b). ^1H NMR spectrum of $\text{A}_5\text{Ru}^{\text{II/III}}$ (3-pic) $^{2+/3+}$ mixture in D_2O , [Ru ^{II}] = [Ru ^{III}] = 5.0 mM | 80 |
| Figure 2-19(a). ^1H NMR spectrum of $\text{A}_5\text{Ru}^{\text{II}}$ (3-Etpy) $^{2+}$ complex in D_2O , [Ru ^{II}] = 5.0 mM | 81 |
| Figure 2-19(b). ^1H NMR spectrum of $\text{A}_5\text{Ru}^{\text{II/III}}$ (3-Etpy) $^{2+/3+}$ mixture in D_2O , [Ru ^{II}] = [Ru ^{III}] = 5.0 mM | 81 |
| Figure 2-20(a). ^1H NMR spectrum of $\text{A}_5\text{Ru}^{\text{II}}$ (3,5-Cl ₂ py) $^{2+}$ complex in D_2O , [Ru ^{II}] = 5.0 mM | 82 |
| Figure 2-20(b). ^1H NMR spectrum of $\text{A}_5\text{Ru}^{\text{II/III}}$ (3,5-Cl ₂ py) $^{2+/3+}$ mixture in D_2O , [Ru ^{II}] = [Ru ^{III}] = 5.0 mM | 82 |
| Figure 2-21(a). ^1H NMR spectrum of $\text{A}_5\text{Ru}^{\text{II}}$ (3,5-Br ₂ py) $^{2+}$ complex in D_2O , [Ru ^{II}] = 5.0 mM | 83 |
| Figure 2-21(b). ^1H NMR spectrum of $\text{A}_5\text{Ru}^{\text{II/III}}$ (3,5-Br ₂ py) $^{2+/3+}$ mixture in D_2O , [Ru ^{II}] = [Ru ^{III}] = 5.0 mM | 83 |
| Figure 2-22(a). ^1H NMR spectrum of $\text{A}_5\text{Ru}^{\text{II}}$ (3,5-Me ₂ py) $^{2+}$ complex in D_2O , [Ru ^{II}] = 5.0 mM | 84 |
| Figure 2-22(b). ^1H NMR spectrum of $\text{A}_5\text{Ru}^{\text{II/III}}$ (3,5-Me ₂ py) $^{2+/3+}$ mixture in D_2O , [Ru ^{II}] = [Ru ^{III}] = 5.0 mM | 84 |
| Figure 2-23(a). ^1H NMR spectrum of $\text{A}_5\text{Ru}^{\text{II}}$ (3-tfmpy) $^{2+}$ complex in D_2O , [Ru ^{II}] = 5.0 mM | 85 |
| Figure 2-23(b). ^1H NMR spectrum of $\text{A}_5\text{Ru}^{\text{II/III}}$ (3-tfmpy) $^{2+/3+}$ mixture in D_2O , [Ru ^{II}] = [Ru ^{III}] = 5.0 mM | 85 |

| | |
|---|-----|
| Figure 2-24(a). ^1H NMR spectrum of $\text{A}_5\text{Ru}^{\text{II}}$ (3-Phpy) $^{2+}$ complex in D_2O , [Ru^{II}] = 5.0 mM | 86 |
| Figure 2-24(b). ^1H NMR spectrum of $\text{A}_5\text{Ru}^{\text{II/III}}$ (3-Phpy) $^{2+/3+}$ mixture in D_2O , [Ru^{II}] = [Ru^{III}] = 5.0 mM | 86 |
| Figure 2-25. Rates for ET self-exchange in D_2O ([Ru^{II}] = [Ru^{III}] = 5.0 mM) vs the measured $E_{1/2}$ value of the $\text{Ru}^{\text{II/III}}$ couple | 92 |
| Figure 2-26. Illustration of possible π - π stacking interactions between the 4-Phpy and 3-Phpy ligands. | 93 |
| Figure 2-27. Illustration of π -backbonding. The electron density from the Ru^{II} d π orbital can be partially donated to the empty π^* orbital of the pyridyl ligand to an extent depending on the electron-withdrawing ability of the substituent group R. | 93 |
| Figure 2-28 (a). Eyring plots for complexes of selected ligands; full temperature Range | 100 |
| Figure 2-28 (b). Eyring plots for complexes of selected ligands; experimental temperature range | 101 |
| Figure 2-29. Eyring plots for the $(\text{NH}_3)_5\text{Ru}^{\text{II}}$ and Ru^{III} complex of the 4-pic ligand in D_2O ([Ru^{II}] = [Ru^{III}] = 5.0 mM, rates were calculated from both Ru^{II} and Ru^{III} peaks) | 102 |
| Figure 2-30. ΔH^\ddagger in KJ/mol vs. ΔS^\ddagger in J/mol·K | 104 |

Chapter Three

| | |
|--|-----|
| Figure 3-1. Illustration of double square-well potential function. | 117 |
|--|-----|

- Figure 3-2. A schematic illustration of how the region of overlap between the $\psi(D, A)$ and $\psi(D^+, A^-)$ wavefunctions depends on the distance between the D and A groups. 118
- Figure 3-3. Illustration of the virtual states which establish the two pathways of superexchange mediation 120
- Figure 3-4. ^{19}F NMR spectra of equimolar $[(\text{NH}_3)_5(3\text{-tfmpy})\text{Ru}^{\text{II/III}}]^{2+/3+}$ mixture ($[\text{Ru}^{\text{II}}] = [\text{Ru}^{\text{III}}] = 5.0 \text{ mM}$ in D_2O) as a function of added NaF concentration (all spectra exhibit slow-exchange limit here). 130
- Figure 3-5. ^{19}F NMR spectra of the equimolar $[(\text{NH}_3)_5(3\text{-tfmpy})\text{Ru}^{\text{II/III}}]^{2+/3+}$ mixture ($[\text{Ru}^{\text{II}}] = [\text{Ru}^{\text{III}}] = 5.0 \text{ mM}$ in D_2O) as a function of added NaCl concentration (slow exchange limit at $[\text{NaCl}] < \sim 0.66 \text{ M}$ but intermediate exchange seen at $[\text{NaCl}] > \sim 0.13 \text{ M}$). 131
- Figure 3-6. ^{19}F NMR spectra of the equimolar $[(\text{NH}_3)_5(3\text{-tfmpy})\text{Ru}^{\text{II/III}}]^{2+/3+}$ mixture ($[\text{Ru}^{\text{II}}] = [\text{Ru}^{\text{III}}] = 5 \text{ mM}$ in D_2O) as a function of NaBr (intermediate exchange rate region.) 132
- Figure 3-7. ^{19}F NMR spectra of the equimolar $[(\text{NH}_3)_5(3\text{-tfmpy})\text{Ru}^{\text{II/III}}]^{2+/3+}$ mixture ($[\text{Ru}^{\text{II}}] = [\text{Ru}^{\text{III}}] = 5.0 \text{ mM}$ in D_2O) as a function of $\text{K}_4\text{Fe}(\text{CN})_6$ (fast exchange rate region reached at $[\text{Fe}(\text{CN})_6]^{4-} > \sim 1.3 \times 10^{-5} \text{ M}$). 133
- Figure 3-8. Rates (log k_{ex} vs GP) for the $[(\text{NH}_3)_5(3\text{-tfmpy})\text{Ru}^{\text{II/III}}]^{2+/3+}$ self-exchange reaction in D_2O with addition of various simple sodium salts (Based on Ru^{II} peak, $[\text{Ru}^{\text{II}}] = [\text{Ru}^{\text{III}}] = 5.0 \text{ mM}$) 138
- Figure 3-9. Rates (log k_{ex} vs GP) for the $[(\text{NH}_3)_5(3\text{-tfmpy})\text{Ru}^{\text{II/III}}]^{2+/3+}$ self-exchange in D_2O with addition of $\text{K}_4\text{M}^{\text{II}}(\text{CN})_6$ effect ($\text{M}=\text{Fe}, \text{Os}, \text{Ru}$; $[\text{Ru}^{\text{II}}] = [\text{Ru}^{\text{III}}] = 5 \text{ mM}$) 139

- Figure 3-10. Rates ($\log k_{ex}$ vs μ) for the $[(NH_3)_5(3\text{-tfmpy})Ru^{II/III}]^{2+/3+}$ self-exchange reaction in D_2O with addition of various simple and dicarboxylic sodium salts (Based on Ru^{II} peak, $[Ru^{II}] = [Ru^{III}] = 5.0 \text{ mM}$) 144
- Figure 3-11. Rates ($\log k_{ex}$ vs $[\text{anion}]$) for the $[(NH_3)_5(3\text{-tfmpy})Ru^{II/III}]^{2+/3+}$ self-exchange reaction in D_2O with addition of various simple and dicarboxylic sodium salts (Based on Ru^{II} peak, $[Ru^{II}] = [Ru^{III}] = 5.0 \text{ mM}$) 145
- Figure 3-12. Rates ($\log k_{ex}$ vs μ_{total}) for the $[(NH_3)_5(3\text{-tfmpy})Ru^{II/III}]^{2+/3+}$ self-exchange reaction in D_2O with addition of $K_4M(CN)_6$ ($M=Ru, Os$ and Fe) (Based on Ru^{II} peak, $[Ru^{II}] = [Ru^{III}] = 5.0 \text{ mM}$) 146
- Figure 3-13. Rates ($\log k_{ex}$ vs $[K^+]$) for the $[(NH_3)_5(3\text{-tfmpy})Ru^{II/III}]^{2+/3+}$ self-exchange reaction in D_2O with addition of $K_4M(CN)_6$ ($M=Ru, Os$ and Fe) (Based on Ru^{II} peak, $[Ru^{II}] = [Ru^{III}] = 5.0 \text{ mM}$) 147
- Figure 3-14(a). $\log k_{ex}$ for the $(NH_3)_5Ru^{II/III}(3\text{-tfmpy})^{2+/3+}$ ($[Ru^{II}] = [Ru^{III}] = 5.0 \text{ mM}$) in D_2O with addition of NaF : experimental data and the best-fit simulation from the 2-channel fitting using Equation 3-23 with $k_{et} = 1.20 \times 10^5$, $k_{etx} = 1.85 \times 10^5$ 159
- Figure 3-14(b). $\log k_{ex}$ for the $(NH_3)_5Ru^{II/III}(3\text{-tfmpy})^{2+/3+}$ ($[Ru^{II}] = [Ru^{III}] = 5.0 \text{ mM}$) in D_2O with addition of NaF : experimental data and the best-fit simulation from 3-channel fitting using Equation 3-25 with $k_{et} = 1.20 \times 10^5$, $k_{etx} = 1.00 \times 10^4$ and $k_{etxx} = 2.89 \times 10^4$ 160
- Figure 3-15(a). $\log k_{ex}$ for the $(NH_3)_5Ru^{II/III}(3\text{-tfmpy})^{2+/3+}$ ($[Ru^{II}] = [Ru^{III}] = 5.0 \text{ mM}$) in D_2O with addition of $NaCl$: experimental data and the best-fit simulation from the 2-channel fitting using Equation 3-23 with $k_{et} = 1.20 \times 10^5$, $k_{etx} = 1.50 \times 10^5$ 161

- Figure 3-15(b). $\log k_{\text{ex}}$ for the $(\text{NH}_3)_5\text{Ru}^{\text{II/III}}(\text{3-tfmpy})^{2+/3+}$ ($[\text{Ru}^{\text{II}}] = [\text{Ru}^{\text{III}}] = 5.0 \text{ mM}$) 162
in D_2O with addition of NaCl : experimental data and the best-fit
simulation from the 2-channel model using Equation 3-25 with
 $k_{\text{et}} = 1.20 \times 10^5$, $k_{\text{etx}} = 2.40 \times 10^5$ and $k_{\text{etxx}} = 2.00 \times 10^5$
- Figure 3-16(a). $\log k_{\text{ex}}$ for the $(\text{NH}_3)_5\text{Ru}^{\text{II/III}}(\text{3-tfmpy})^{2+/3+}$ ($[\text{Ru}^{\text{II}}] = [\text{Ru}^{\text{III}}] = 5.0 \text{ mM}$) 163
in D_2O with addition of NaBr : experimental data and the best-fit
simulation from the 2-channel fitting using Equation 3-23 with
 $k_{\text{et}} = 1.20 \times 10^5$, $k_{\text{etx}} = 4.40 \times 10^5$
- Figure 3-16(b). $\log k_{\text{ex}}$ for the $(\text{NH}_3)_5\text{Ru}^{\text{II/III}}(\text{3-tfmpy})^{2+/3+}$ ($[\text{Ru}^{\text{II}}] = [\text{Ru}^{\text{III}}] = 5.0 \text{ mM}$) 164
in D_2O with addition of NaBr : experimental data and the best-fit
simulation from 3-channel model using Equation 3-25 with
 $k_{\text{et}} = 1.20 \times 10^5$, $k_{\text{etx}} = 3.90 \times 10^5$ and $k_{\text{etxx}} = 4.00 \times 10^5$
- Figure 3-17. $\log k_{\text{ex}}$ for the $(\text{NH}_3)_5\text{Ru}^{\text{II/III}}(\text{3-tfmpy})^{2+/3+}$ ($[\text{Ru}^{\text{II}}] = [\text{Ru}^{\text{III}}] = 5.0 \text{ mM}$) 172
in D_2O with addition of $\text{K}_4\text{Fe}(\text{CN})_6$: experimental data and the best-fit
simulation from the 2-channel model using Equation 3-23 with
 $k_{\text{et}} = 1.20 \times 10^5$ and $k_{\text{etx}} = 1.51 \times 10^7$
- Figure 3-18. $\log k_{\text{ex}}$ for the $(\text{NH}_3)_5\text{Ru}^{\text{II/III}}(\text{3-tfmpy})^{2+/3+}$ ($[\text{Ru}^{\text{II}}] = [\text{Ru}^{\text{III}}] = 5.0 \text{ mM}$) 173
in D_2O with addition of $\text{K}_4\text{Os}(\text{CN})_6$: experimental data and the best-fit
simulation from the 2-channel model using Equation 3-23 with
 $k_{\text{et}} = 1.20 \times 10^5$ and $k_{\text{etx}} = 1.80 \times 10^5$
- Figure 3-19. $\log k_{\text{ex}}$ for the $(\text{NH}_3)_5\text{Ru}^{\text{II/III}}(\text{3-tfmpy})^{2+/3+}$ ($[\text{Ru}^{\text{II}}] = [\text{Ru}^{\text{III}}] = 5.0 \text{ mM}$) 174
in D_2O with addition of $\text{K}_4\text{Ru}(\text{CN})_6$: experimental data and the best-fit
simulation from the 2-channel model using Equation 3-23 with
 $k_{\text{et}} = 1.20 \times 10^5$ and $k_{\text{etx}} = 5.50 \times 10^4$

- Figure 3-20. (a) Vis-NIR Spectrum of the ion pair $[(\text{NH}_3)_5\text{Ru}^{\text{III}}(3\text{-tfmpy}), \text{Fe}^{\text{II}}(\text{CN})_6]^-$ in 1cm cell ($[\text{Fe}(\text{II})] = [\text{Ru}(\text{III})]$, concentration from 0.1 mM to 9 mM) 177
- (b) a close look at λ_{max} area
- Figure 3-21. Vis-NIR Spectrum of the ion pair $[(\text{NH}_3)_5\text{Ru}^{\text{III}}(3\text{-tfmpy}), \text{Os}^{\text{II}}(\text{CN})_6]^-$ in 1cm cell ($[\text{Os}(\text{II})] = [\text{Ru}(\text{III})]$, concentrations range from 0.2 mM to 6mM) 178
- Figure 3-22. Vis-NIR Spectrum of the ion pair $[(\text{NH}_3)_5\text{Ru}^{\text{III}}(3\text{-tfmpy}), \text{Ru}^{\text{II}}(\text{CN})_6]^-$ in 1cm cell ($[\text{Ru}(\text{II})] = [\text{Ru}(\text{III})]$, concentrations range from 0.2 mM to 6 mM) 178
- Figure 3-23. Beer's law plot for the ion pair $[(\text{NH}_3)_5\text{Ru}^{\text{III}}(3\text{-tfmpy}), \text{Fe}^{\text{II}}(\text{CN})_6]^-$ at 25°C in water 180
- Figure 3-24. Beer's law plot for the ion pair $[(\text{NH}_3)_5\text{Ru}^{\text{III}}(3\text{-tfmpy}), \text{Os}^{\text{II}}(\text{CN})_6]^-$ at 25°C in water 181
- Figure 3-25. Beer's law plot for the ion pair $[(\text{NH}_3)_5\text{Ru}^{\text{III}}(3\text{-tfmpy}), \text{Ru}^{\text{II}}(\text{CN})_6]^-$ at 25°C in water 182
- Figure 3-26. $k_{\text{etx}}/k_{\text{et}}$ values for halide catalysis of reaction 3-1 obtained from Specfit simulations of stopped-flow data⁷ plotted against the ionization potentials of the halides 187
- Figure 3-27. $k_{\text{etx}}/k_{\text{et}}$ values from Table 3-13 plotted against ionization potential 188
- Figure 3-28. Average interionic distance (\AA) vs. molar concentration in a solution of 1:1 electrolyte 190

- Figure 3-29. $k_{\text{etx}}/k_{\text{et}}$ ratio from best-fit simulations of the $\text{M}(\text{CN})_6^{4-}$ kinetic data plotted here against redox potentials (vs. SCE) of the aqueous $\text{M}(\text{CN})_6^{4-}$ species 192
- Figure 3-30. Eyring plots for the $[(\text{NH}_3)_5\text{Ru}^{\text{II/III}}(\text{3-tfmpy})]^{2+/3+}$ self-exchange 197
- Figure 3-31. Activational entropy-enthalpy compensation effect between measured ΔS^\ddagger vs ΔH^\ddagger for the ET self-exchange reaction of $[(\text{NH}_3)_5\text{Ru}^{\text{II/III}}(\text{3-tfmpy})]^{2+/3+}$ both by itself and in the presence of added $\text{K}_4\text{M}^{\text{II}}(\text{CN})_6^{\text{a,b}}$ as $\text{M} = \text{Ru} \rightarrow \text{Os} \rightarrow \text{Fe}$ 201

List of Tables

Chapter Two

| | |
|--|-----|
| Table 2-1. Pyridyl ligands (names, structures and abbreviations) used in this study | 38 |
| Table 2-2. Extinction coefficients and $E_{1/2}$ values of $L-(NH_3)_5Ru^{II}(PF_6)_2$ | 48 |
| Table 2-3. Spectral data and $E_{1/2}$ values of the $L-(NH_3)_5Ru^{II}Cl_2$ complexes in water | 49 |
| Table 2-4. Elemental analyses of the ruthenium complexes | 50 |
| Table 2-5. Sample 1H NMR parameters | 54 |
| Table 2-6. Sample ^{19}F NMR parameters | 55 |
| Table 2-7. Sample Peakfit numerical result output | 63 |
| Table 2-8. NMR read-out temperature and actual temperature calibrated from Equation 2-4 | 69 |
| Table 2-9. Rates of self-exchange for $L-A_5Ru^{II/III}$ in D_2O monitored by 1H or ^{19}F NMR at room temperature (L= various pyridyl ligands, see Table 2-1 for structures) | 87 |
| Table 2-10. Illustration of rate variations in two cases where rates could be calculated from different pyridyl ring protons. | 88 |
| Table 2-11. Results of Eyring experiments for reaction 2-1 with selected ligands (in all cases $[Ru^{II}] = [Ru^{III}] = 5.0 \text{ mM}$) | 96 |
| Table 2-12. Eyring plots data for 4-pic ligand (rates were calculated from both Ru^{II} and Ru^{III} peaks). | 99 |
| Table 2-13. ET activation parameters calculated for selected complex as shown in Figures 2-28 and 2-29 | 103 |

Chapter Three

| | |
|---|-----|
| Table 3-1. Dicarboxylic dianions and $M(CN)_6^{4-}$ complexes used as added salts in this study. | 113 |
| Table 3-2. Elemental analysis data for $K_4M(CN)_6$ (M = Os, Ru) | 125 |
| Table 3-3. Measured variations in the rates of the $[(NH_3)_5(3\text{-tfmpy})Ru^{II/III}]^{2+/3+}$ self-exchange ET due to the addition of various simple and dicarboxylate salts (based on the width of the RuII peak and Equation 1-31) | 135 |
| Table 3-4. Rates of $[(NH_3)_5(3\text{-tfmpy})Ru^{II/III}]^{2+/3+}$ self-exchange ET due to the addition of $K_4M(CN)_6$, M= Ru, Os, Fe (based on RuII peak) | 136 |
| Table 3-5. Early and late slopes in the log k_{ex} vs GP plots shown in Figures 3-7 and 3-8 for reaction 3-2 in D_2O due to the addition of various salts at $25^\circ C$ ($[Ru^{II}] = [Ru^{III}] = 5.0 \text{ mM}$) | 140 |
| Table 3-6. Radii of the ions, complexes and ion pairs used in calculation of the association/dissociation constants | 153 |
| Table 3-7. Association and dissociation rate constants calculated for application of Equation 3-25 to reaction 3-2 in the presence of added NaF | 155 |
| Table 3-8. Association and dissociation rate constants calculated for application of Equation 3-25 to reaction 3-2 in the presence of added NaCl | 156 |
| Table 3-9. Association and dissociation rate constant values calculated for application of Equation 3-25 to reaction 3-2 in the presence of added NaBr | 157 |
| Table 3-10. Best-fit simulation data for reaction 3-2 at $[Ru^{II}] = [Ru^{III}] = 5.0 \text{ mM}$ in the presence of added NaF | 158 |
| Table 3-11. Best-fit simulation data for reaction 3-2 at $[Ru^{II}] = [Ru^{III}] = 5.0 \text{ mM}$ in the presence of added NaCl | 158 |

| | |
|--|-----|
| Table 3-12. Best-fit simulation data for reaction 3-2 at $[Ru^{II}] = [Ru^{III}] = 5.0 \text{ mM}$ in the presence of added NaBr | 158 |
| Table 3-13. Best-fit values of k_{et} , k_{etx} and k_{etxx} for added halide and values of k_{etx}/k_{et} | 165 |
| Table 3-14. Radii of the ions, complexes and ion pairs used in calculation of association/dissociation rate constants (for added $K_4M(CN)_6$ salts, M= Fe, Os and Ru) | 166 |
| Table 3-15. Association and dissociation rate constants calculated for application of Equation 3-23 to reaction 3-2 in the presence of $K_4[Fe(CN)_6]$ | 167 |
| Table 3-16. Association and dissociation rate constants calculated for application of Equation 3-23 to reaction 3-2 in the presence of added $K_4[Os(CN)_6]$ | 168 |
| Table 3-17. Association and dissociation rate constants calculated for application of Equation 3-23 to reaction 3-2 in the presence of added $K_4[Ru(CN)_6]$ | 169 |
| Table 3-18. Best-fit simulation data for reaction 3-2 at $[Ru^{II}] = [Ru^{III}] = 5.0 \text{ mM}$ in the presence of added $K_4Fe(CN)_6$ | 170 |
| Table 3-19. Best-fit simulation data for reaction 3-2 at $[Ru^{II}] = [Ru^{III}] = 5.0 \text{ mM}$ in the presence of added $K_4Os(CN)_6$ | 171 |
| Table 3-20. Best-fit simulation data for reaction 3-2 at $[Ru^{II}] = [Ru^{III}] = 5.0 \text{ mM}$ in the presence of added $K_4Ru(CN)_6$ | 171 |
| Table 3-21. k_{etx}/k_{et} ratios for $K_4M(CN)_6$ (M= Ru, Os and Fe) | 175 |
| Table 3-22. Ion-pair spectral and formation constant data for $[(NH_3)_5Ru^{III}(3\text{-tfmpy}), M^{II}(CN)_6]^-$ (M=Fe, Os, Ru) | 185 |

| | |
|--|-----|
| Table 3-23. Eyring plots data for the $[(\text{NH}_3)_5\text{Ru}^{\text{II/III}}(\text{3-tfmpy})]^{2+/3+}$ self-exchange | 194 |
| in the presence of added $\text{K}_4\text{Fe}(\text{CN})_6$ (all k_{ex} values calculated from fast exchange Equation 1-36) | |
| Table 3-24. Eyring plots data for the $[(\text{NH}_3)_5\text{Ru}^{\text{II/III}}(\text{3-tfmpy})]^{2+/3+}$ self-exchange | 195 |
| in the presence of added $\text{K}_4\text{Os}(\text{CN})_6$ (For $T = 310\text{K}$, k_{ex} was calculated from intermediate exchange rate Equation 1-35; For $T = 315, 326\text{K}$, k_{ex} was obtained from fast exchange rate Equation 1-36.) | |
| Table 3-25. Eyring plots data data for the $[(\text{NH}_3)_5\text{Ru}^{\text{II/III}}(\text{3-tfmpy})]^{2+/3+}$ self- | 196 |
| exchange in the presence of added $\text{K}_4\text{Ru}(\text{CN})_6$ | |
| Table 3-26. ET self-exchange activation parameters for reaction 3-2 derived | 198 |
| from Figure 3-30 | |

Abstract

The electron transfer (ET) self-exchange rates on a series of complexes of $(\text{NH}_3)_5\text{Ru}^{\text{II/III}}\text{L}^{2+/3+}$ in D_2O (where L is a substituted pyridyl ligand) were investigated by dynamic NMR measurements. Significant rate enhancement was observed for the cases of L = 3-phenylpyridine and 4-phenylpyridine due to possible π - π stacking between Phpy ligands. These observations match well with recent stopped-flow work by Mehmood on a similar set of related pseudo-self exchange reactions. Kinetics of the $(\text{NH}_3)_5\text{Ru}^{\text{II/III}}(\text{3-trifluoromethylpyridine})^{2+/3+}$ self-exchange reactions with addition of various simple/complex salts and hexacyano salts ($\text{K}_4\text{M}(\text{CN})_6$ with M = Fe, Os and Ru) were also studied. The halide ions showed qualitatively-similar behavior compared to the stopped-flow work by Sista and the same quantitative decrease in the magnitude of salt effect as reported by Inagaki. The hexacyano salts were found to have a striking effect on the ET rate with a clear trend of $\text{Fe} > \text{Os} > \text{Ru}$. This could be explained as a probable “superexchange” type mechanism dominated by the “hole-transfer” pathway based on the trend between the catalytic effect and the redox potential of the particular $\text{M}(\text{CN})_6^{4-}$ ion. Kinetic modeling data also show the strongest catalytic effect of Fe which gives a $k_{\text{etx}}/k_{\text{et}}$ of 126. Temperature-dependent experiments show that the rate enhancement of hexacyano series is due to an increased enthalpic barrier and less negative entropic barrier.

Chapter One

Introduction to some basic concepts of electron-transfer reactions and NMR line broadening techniques for measurement of kinetic rate constants

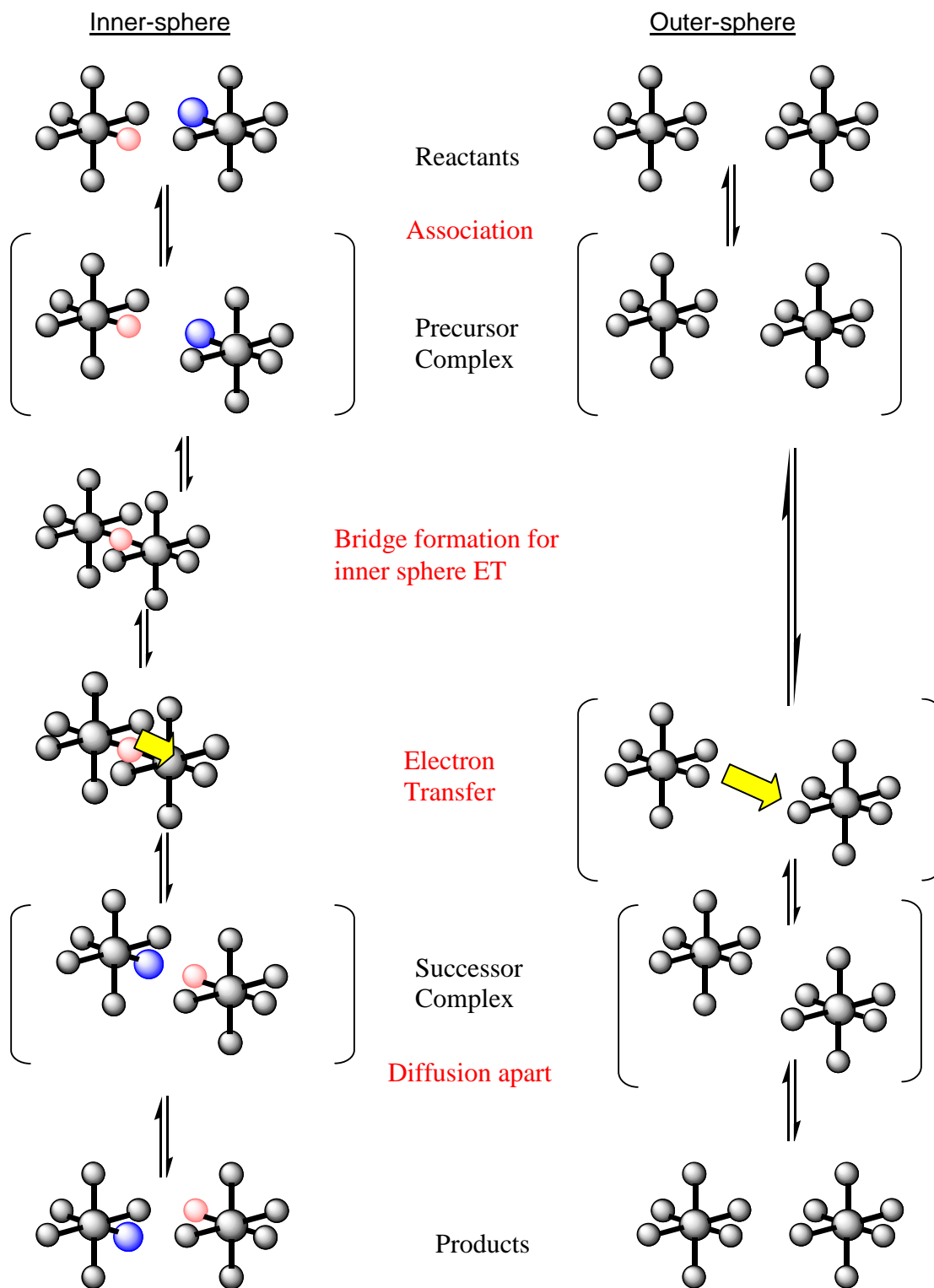
Electron Transfer

Electron transfer (ET) is one of the most important and fundamental reactions encountered in biological, physical, inorganic, and organic chemical systems.¹ For example, the biochemical process of respiration (the metabolic pathways by which an organism obtains energy by reacting oxygen with glucose to give water, carbon dioxide and energy) and photosynthesis (the metabolic pathway which converts carbon dioxide into sugars using the energy from sunlight) both rely extensively on electron transfer reactions between cofactors in proteins.² Corrosion in mechanical and electrochemical systems is caused by surface electron-transfer reactions typically between metal atoms and dissolved oxygen.³ Thus, understanding and manipulating the nature and rates of ET process has become a very active research area in inorganic and physical chemistry.

The intensity of research activity in this area has been building since the 1950s when Marcus introduced the basic electron-transfer theory, for which he won the Nobel Prize in 1991. Hush and others later made more contributions to this theory.⁴ In this chapter, the basic ideas and elements of the electron-transfer theory will be introduced.

There are two main mechanistic pathways which have been identified for electron-transfer reactions. These are the “inner-sphere” and “outer-sphere” ET mechanisms.⁵ The two mechanisms are illustrated in Figure 1-1.⁶

Figure 1-1. Schematic illustration of the inner-sphere and outer-sphere ET mechanisms.



Inner-sphere ET is possible when the ET step itself proceeds *via* a covalent linkage or “bridging ligand” between the two interacting redox partners, the oxidant and the reductant (or “acceptor” and “donor” as they are also called). This pathway can be inhibited by large ligands which prevent the formation of the crucial bridged intermediate.⁶

Outer-sphere ET refers to an electron-transfer event that occurs between two reactants which remain intact, separate species before, during, and after the ET event. Because the elementary ET step in outer-sphere electron transfer occurs between two non-bonded species, the electron is forced to tunnel at the van der Waals contact point from one redox center to the other. Outer sphere electron transfer can occur between different chemical species or between identical species that differ only in their oxidation states. The latter case is termed electron-transfer "self-exchange".

In the work to be discussed in this thesis, all the reactions investigated occurred *via* the outer-sphere ET mechanism. In the Marcus theory framework used for outer-sphere ET reactions between an electron donor D and an electron acceptor A, the second-order reaction mechanism can be further divided into three component steps as follows,



In the first step, D and A diffuse together and form a “precursor complex”, D|A (also referred to as the reactant’s “encounter complex”). k_a and k_d are the rate constants for association and dissociation of the freely-diffusing reactants to form this complex, respectively. In the second step, the D|A complex undergoes a geometrical reorganization toward a “transition state” where the electron-transfer event can happen iso-energetically at constant (“frozen”) nuclear coordinates so as to form the “successor complex”, $D^+|A^-$. The rate constants for the forward and reverse electron transfer in the precursor complex are k_{et} and k_{-et} . Finally, the successor complex relaxes to a new set of nuclear coordinates and then dissociates to form the product ions, D^+ and A^- according to rate constant k_s . In simple outer-sphere ET, it is often the case that the “pre-equilibrium” condition applies such that the first and third steps are diffusion controlled and the second step (the ET act itself) is the rate-determining step ($k_a, k_d \gg k_{et}$).⁷

By a steady-state approximation kinetic analysis of steps 1-1 through 1-3, we can derive an expression for k_{obs} , the “observed” bimolecular ET rate constant, which would be obtained from a kinetic measurement at some set of reactant

concentrations *via rate* $= -\frac{d(\text{rcts})}{dt} = k_{obs}[A][D]$.⁸ From step 1-1, the rate of

change in precursor complex concentration is,

$$\frac{d[D|A]}{dt} = k_a[D][A] - k_d[D|A] - k_{et}[D|A] \cong 0 \quad 1-4$$

and thus,

$$[D | A] = \frac{k_a}{k_d + k_{et}} [D][A] \quad 1-5$$

From step 1-2, the rate of change in successor complex concentration is,

$$\frac{d[D^+ | A^-]}{dt} = k_{et}[D | A] - (k_{-et} + k_s)[D^+ | A^-] \cong 0 \quad 1-6$$

After substituting for the [D|A] using Equation 1-5, we can solve for [D⁺|A⁻],

$$[D^+ | A^-] = \frac{k_{et} k_a}{(k_d + k_{et})(k_s + k_{-et})} [D][A] \quad 1-7$$

The rate of final products formation is then,

$$\frac{d[D^+ \text{ or } A^-]}{dt} = k_s [D^+ | A^-] \quad 1-8$$

and combining Equations 1-7 and 1-8, we have,

$$\frac{d[D^+ \text{ or } A^-]}{dt} = \frac{k_s k_{et} k_a}{(k_d + k_{et})(k_s + k_{-et})} [D][A] \quad 1-9$$

Now, we can express the second order ET rate constant k_{obs} as,

$$k_{obs} = \frac{k_s k_{et} k_a}{(k_d + k_{et})(k_s + k_{-et})} \quad 1-10^9$$

In the pre-equilibrium limit, it is also true that $k_s \gg k_{-et}$ and then Equation 1-10 can be simplified to,

$$\frac{1}{k_{obs}} = \frac{1}{k_a} + \frac{1}{K_a k_{et}} = \frac{1}{k_a} + \frac{1}{\frac{k_a}{k_d} \bullet k_{et}} = \frac{1}{k_a} \left(1 + \frac{k_d}{k_{et}} \right) \quad 1-11$$

where $K_a = k_a/k_d$ is the formation constant for the precursor complex. Since $k_d \gg k_{et}$,

Equation 1-11 can be further simplified to the surprisingly compact result,

$$k_{obs} \cong K_a k_{et} \quad 1-12^9$$

which characterizes this important sub-case. On the other hand, if the reaction is “diffusion controlled”, $k_d \ll k_{et}$, and then Equation 1-6 can be expressed as,

$$k_{obs} \cong k_a \quad 1-13$$

In this case the observed second-order ET rate constant k_{obs} will not provide any direct information about k_{et} except for an approximate lower bound. In the reactions to be described in this thesis, the rates of precursor complex formation and successor complex dissociation are known to be much faster than that of the elementary electron-transfer event itself.⁷ Therefore, the pre-equilibrium limit expressed in Equation 1-12 applies.

Marcus's theory of electron-transfer reactions builds on the traditional Arrhenius equation for the rates of chemical reactions in two important ways. First, it provides an expression for the pre-exponential factor in the Arrhenius equation based on the quantum mechanical “electronic coupling” between the reactant and product states of the electron transfer reaction (*i.e.*, the resonance energy arising from overlap of the electronic wave functions of the two electronic states, [D, A] and [D⁺, A⁻] which can be used to describe the and successor encounter complexes, *vide infra*). Second, it provides a formula for the activation energy based on a parameter called the reorganization energy as well as the Gibbs free-energy driving force (if any) attending the ET reaction. The reorganization energy is defined as the energy which would be required to “reorganize” the system’s nuclear coordinates from the reactant geometry + solvation sphere product nuclear coordinates *without* changing the

electronic state.

Svante Arrhenius was the first to discover that the rate constant depends strongly on temperature^[7]. The empirically-derived Arrhenius equation for the rate constant is,

$$k(T) = A \exp(-E_a / RT) \quad 1-14$$

where A is the pre-exponential or the “frequency factor” and E_a is the Arrhenius activation energy, which can be thought of as the amount of energy that must be supplied to the reactants in order to drive the reaction. In the context of electron transfer theory, E_a can be identified as the thermal activation barrier E_{th} (ΔG^* , if described in terms of free energy) over which the precursor complex has to pass in order for thermal electron transfer to happen.

$$E_a = E_{th} = \Delta G^* = \frac{(\lambda + \Delta G^0)^2}{4\lambda} \quad 1-15^{10}$$

where λ is the reorganization energy (which is related to optical electron transfer energy gap E_{op} , *vide infra*) and ΔG^0 is the thermodynamic driving force. λ can, in many cases, be effectively divided into two distinct parts, λ_{in} and λ_{out} ,

$$\lambda = \lambda_{in} + \lambda_{out} \cong E_{op} - \Delta G^0 \quad 1-16$$

The internal or “inner-sphere” reorganization energy λ_{in} is to a first approximation solvent-independent and arises from the structural (skeletal) differences between the

equilibrium nuclear configurations of the reactant and product states as distributed over both redox sites,

$$\lambda_{in} = \frac{1}{2} \sum_i^N \overline{f}_i (r_R^{eq} - r_p^{eq})^2 \quad 1-17^{11}$$

where \overline{f}_i is the reduced force constant for the i^{th} vibration, and the sum is taken over all significant inter- and intramolecular vibrations of the entire encounter complex (the former category being well-approximated by the normal modes of the individual reductant and oxidant ions of the precursor complex). r_R^{eq} and r_p^{eq} are the equilibrium bond lengths in the reactant and product states, respectively (a more comprehensive analysis would involve bond angles and dihedral angles as well). The “outer-sphere” reorganization energy λ_{out} is related to the difference between the orientation and polarization of solvent molecules around precursor complex and successor complex, therefore it is also called the solvent reorganization energy.

If the solvent exterior to the primary coordination spheres of the reactant ions in the precursor complex is modeled as a featureless, polarizable “dielectric continuum”, Marcus and Hush have both derived the following expression for the outer-sphere reorganization energy,

$$\lambda_{out} = \frac{(\Delta e)^2}{4\pi\epsilon_0} \left(\frac{1}{2a_D} + \frac{1}{2a_A} - \frac{1}{r_{DA}} \right) \left(\frac{1}{\epsilon_{op}} - \frac{1}{\epsilon_s} \right) \quad 1-18^{11}$$

In Equation 1-18, Δe corresponds to the amount of charge transferred in the reaction (approximately one electronic charge in most cases, ϵ_0 is the permittivity of

vacuum, a_D and a_A are the radii of the electron donor and electron acceptor complexes, respectively, r_{DA} is the center-to-center distance between the donor and acceptor redox sites, and ϵ_{op} and ϵ_s are the optical and static dielectric constants, respectively, of the surrounding solvent medium (“optical” meaning at high frequencies such as those of electronic motions and visible-wavelength photon frequencies used in refractive index measurements and “static” meaning at low frequency when all forms of solvent polarization have time to stay in equilibrium with the charge distribution).

In Equation 1-15, ΔG^0 is the difference in Gibbs free energy between the reactants and products, and it is often referred to as “the thermodynamic driving force” for the reaction (for a self-exchange reaction such as the ones we will be discussing in this thesis $\Delta G^0 = 0$). The free energy difference between D/A and D^+/A^- can, to a first approximation be obtained directly from the potentials of the individual D^+/D and A/A^- redox couples (as measured by differential pulse voltammetry or some other electroanalytical method). Finally, we note that in a more precise sense, ΔG^0 refers to the Gibbs free energy difference specifically between the associated reactants of the precursor complex D/A and successor complex D^+/A^- . A more thorough expression, which accounts explicitly for the thermodynamics within the associated precursor complex, may be written as,

$$\Delta G^0 = e \left(E_{D^+/D}^0 - E_{A/A^-}^0 \right) + \omega^P - \omega^R \quad 1-19^9$$

where e is the electronic charge; $E_{D^+/D}^0$ is the standard reduction potential for separated D^+ ; E_{A/A^-}^0 is the standard reduction potential for separated A , and ω^P and

ω^R correct for any difference in the electrostatic work required to associate the D^+ and A^- pair and the D and A pair, respectively. If D and A are the same species and differ only in their redox states (self-exchange), then $\omega^P = \omega^R$ exactly and ΔG^0 equals zero and the last terms in Equation 1-19 cancel out.

Potential Energy Surfaces

Both the precursor and successor complexes can be described as existing on nuclear configurational potential energy surfaces which reflect how the energy of the system varies with a large number of nuclear coordinates (e.g., inner-sphere bond lengths and angles as well as intermolecular and intramolecular orientations and the positions of nearby solvent dipoles). There will be one such surface for the D/A “reactants” precursor complex and one for the D^+/A^- “products” successor complex, and there will be a minimum-energy pathway (the reaction coordinate) leading from the bottom of one potential well to the other. It is helpful to project this highly multi-dimensional potential energy pathway (easily >200 dimensions) onto a two-dimensional plane so that we can see how the various energy quantities relevant to electron transfer are related to each other using the representative 2D-potential energy curves (which are the Marcus-Hush parabolas that result from applying the harmonic approximation to all the various normal modes involved).¹² Figures 1-2 and 1-3 show the Marcus potential energy curves for cases where $\Delta G^0 = 0$ and $\Delta G^0 \neq 0$, respectively. The left well represents the potential energy of the reactant state $D|A$ (precursor complex), and the right one is for the successor complex $D^+|A^-$. E_{op} is the energy required for the optical (vertical or ~instantaneous photon-driven) ET process. E_{th} is the activation energy for thermal ET (where nuclear oscillations

take reactants to products over the energy barrier and q refers to the nuclear configurations which pertain a given energy.

Potential Energy Surfaces ($\Delta G^0=0$)

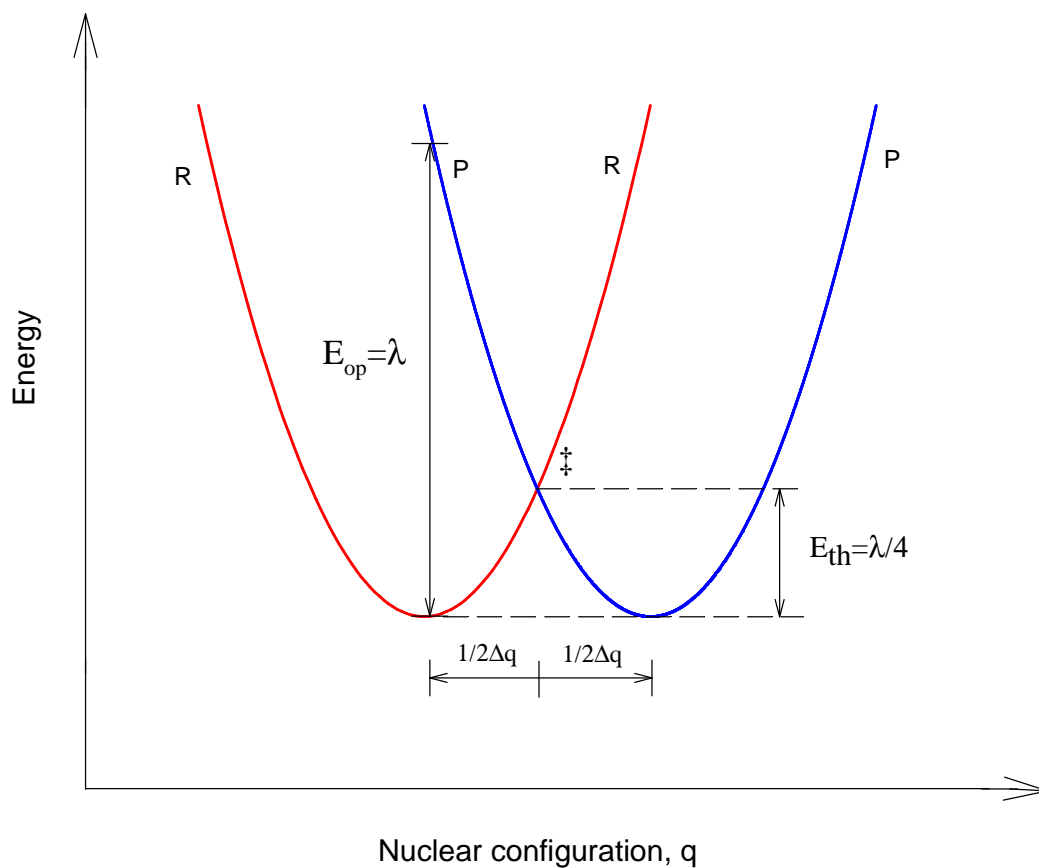


Figure 1-2. Potential energy surfaces for reactant ($R = D/A$) and product ($P = D^+/A^-$) redox states as a function of nuclear configuration q when ($G^0 = 0$).

motions, ET occurs between D and A in their equilibrium geometry without any metal-ligand bond length or solvent shell rearrangement. The product is thus formed in a vibrationally excited state (indicated by the "*" at energy E_{op} above the ground state, with D^+ having the D nuclear configuration and A^- having A nuclear configuration. The excited state can then relax back to ground state or fall into the product's well to form D^+/A^- in their equilibrium nuclear positions.

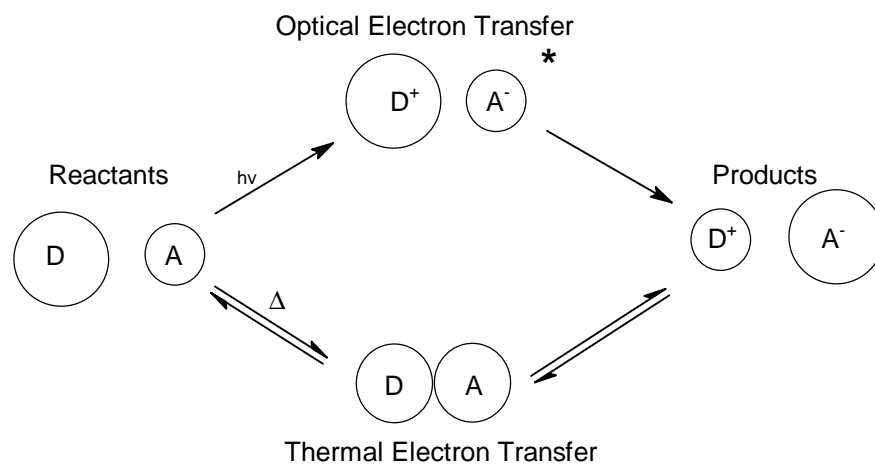


Figure 1-4. Schematic illustration of optical and thermal ET processes as they relate to inner-sphere nuclear coordinates. The different-sized circles are intended to represent longer metal-ligand bond lengths at D (Ru^{II} in our specific systems) or A^- , and shorter distances at A or D^+ (Ru^{III} in our systems).

The bottom route illustrates the thermal electron-transfer pathway. Since nuclear motions occur on a time scale ($\sim 10^{-13}$ sec) much longer than that of electronic motion ($< 10^{-15}$ sec), and because ET can only happen isoenergetically in the absence of photon-absorption, a thermal activation barrier must exist. The electron donor and acceptor must reorganize by thermal fluctuation/activation to a

compatible “intermediate” or “transition state” nuclear configuration before the thermal ET step can take place. The work required for the formation of this activated complex is the thermal barrier E_{th} . The electron is thus transferred without any nuclear reorganization in the precursor complex to form the successor complex at this intermediate state or “transition” state geometry (which corresponds to the surface intersection point in nuclear-configurational space marked by “‡” in Figure 1-2). Finally, the successor complex (D^+/A^-) further relaxes and then dissociates to form the separated products.

According to Hush theory,¹⁰ for a symmetrical one-electron transfer, the activation energy of the thermal process is related to the energy of the vertical optical transition from the reactant state to the product state (see the arrows labeled “ E_{op} ” in Figures 1-2) according to Equation 1-20,

$$E_{op} = h\nu_{max} = 4E_{th} = \lambda \quad 1-20$$

This is a necessary result if the surfaces are harmonic (parabolic) since all geometric displacements of coordinates upon going from reactants to products occur to exactly half of their eventual values in order to attain the intersection geometry at “‡”.

From the standard Arrhenius relationship between activation free energy and rate constant, we can rewrite Equation 1-14 and obtain the following expression for k_{et} ,

$$k_{et} = A \exp \left[\frac{-(\Delta G^0 + \lambda)^2}{4\lambda k_B T} \right] \quad 1-21^1$$

In this Equation, k_B is the Boltzmann constant, k_{et} is the electron transfer rate constant, and A is the pre-exponential factor which incorporates the frequency of crossing at the barrier top.

In the Hush theoretical framework, nuclear tunneling corrections are ignored since these are not important unless the temperature is very low or the activation process is dominated by changes in high frequency modes. In the absence of such a correction, for unimolecular reactions the rate constant can be expressed as,

$$k_{et} = \kappa_{el} \nu_n \kappa_n \quad 1-22^{11}$$

where κ_{el} is the electronic factor (also called electronic transmission coefficient or adiabaticity coefficient) and has a range from 0 to 1. ν_n is the nuclear frequency factor (an effective nuclear vibration frequency which characterizes the rate of forming/destroying the transition state nuclear configuration, and κ_n is a “nuclear factor”, typically taken as the simple Boltzmann activation expression

$\kappa_n = \exp(-\Delta G^* / RT)$ where $\Delta G^* \sim E_{th}$ of Equation 1-20. According to the Landau-Zener framework,¹³ κ_{el} is an important controlling element of the electron-transfer event and essentially describes the tunneling efficiency of the electron from one redox site to the other, which takes the system from the reactants’ surface to the products’ surface. It is given by,

$$\kappa_{el} = \frac{2 \left[1 - \exp\left(\frac{-\nu_{el}}{2\nu_n}\right) \right]}{2 - \exp\left(\frac{-\nu_{el}}{2\nu_n}\right)} \quad 1-23^{11}$$

where ν_{el} , the electronic frequency factor at the intersection region (see Figure 1-2), is given in the non-adiabatic limit by,

$$\nu_{el} = \frac{2H_{AB}^2}{h} \left(\frac{\pi}{\lambda RT} \right)^{1/2} \quad 1-24^{11}$$

where H_{AB} is the electronic coupling matrix element which arises due to delocalization of electron density on D or A⁻ onto either A or D⁺ (the units of H_{ab} are energy and it can be thought of as a “resonance energy”).

Adiabatic vs. Non-adiabatic ET

In Equation 1-23, if $\nu_{el} \gg 2\nu_n$, $\kappa_{el} = 1$ and the reaction is then said to be “adiabatic”, and if $\nu_{el} \ll 2\nu_n$, $\kappa_{el} = \frac{\nu_{el}}{\nu_n} < 1$ and the reaction is “non-adiabatic”.

Figures 1-5 and 1-6 show the relevant potential energy surfaces for adiabatic and non-adiabatic ET reactions, respectively. In the adiabatic case, the electronic coupling energy H_{AB} between the precursor complex and successor complex states is large enough that the surfaces are effectively “separated” by the resonance interaction in the intersection region, and the reacting system always remains on the lower surface as nuclear motions take it back and forth near/over the activation barrier (Figure 1-5). In the non-adiabatic case, however, H_{AB} is small enough to ensure that the D|A and D⁻|A⁺ surface splitting is $\ll k_bT$. The system will thus usually remain on the D|A surface as it oscillates through the intersection region and then relax back down to the ground vibrational level of the reactants well. In these non-adiabatic cases, ET happens only when the system vibrates into (or very near)

the intersection region and the quantum electron tunneling from D to A which allows the reactants to reach the product surface is a rare event compared to the frequency of barrier “attempts” (Figure 1-6).

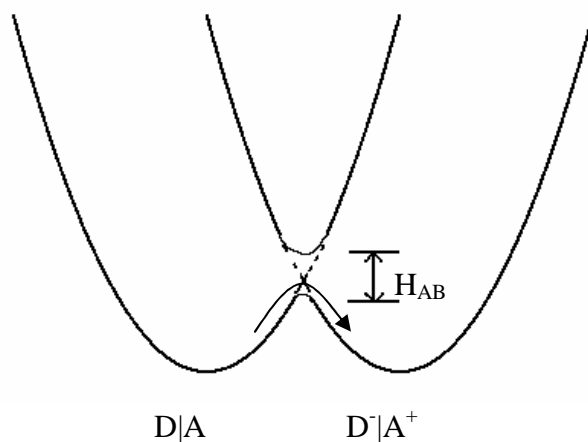


Figure 1-5. Potential energy curves relevant to the adiabatic ($\kappa_{el} \sim 1$) electron-transfer limit

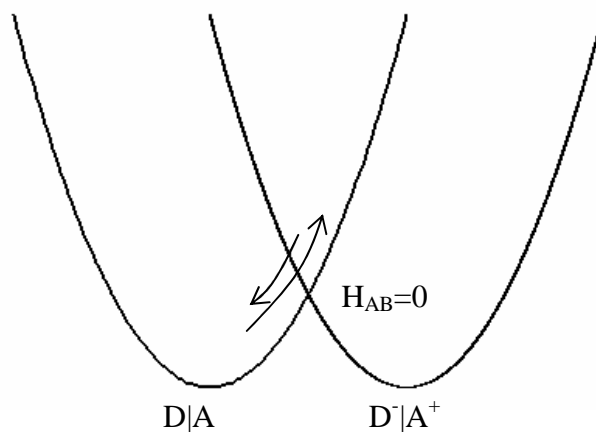


Figure 1-6. Potential energy surfaces relevant to the non-adiabatic ($H_{ab}, \kappa_{el} \sim 0$) electron-transfer process.

Marcus theory was originally derived for systems at or near the non-adiabatic limit, but experiments show that it also works quite well for most adiabatic ET reactions where $\kappa_{el} \cong 1$ (corresponding to a unit probability for ET whenever the system reaches transition state).¹⁴ However, a full quantum-mechanical approach is required in order to explain observed rates of non-adiabatic ET reactions over large temperature ranges. This approach explicitly introduces the concepts of both electron tunneling from D to A at the intersection (*vide supra*) and also nuclear tunneling from the reactant to the product surfaces “underneath” the potential barrier as a parallel process in addition to thermally-activated barrier crossing. The degree of overlap between the electronic wave functions describing the D, A and D⁺, A⁻ redox states (which is related to the electronic coupling energy H_{AB}) and the overlap between the vibrational (nuclear) wave functions of the D|A state and the D⁺|A⁻ state underneath (through) the classical potential barrier are key quantities necessary for quantitative understanding of non-adiabatic ET reaction rates in such cases. Electron transfer may occur nonadiabatically in three identifiable ways,⁹

1. Thermally-activated; Electron tunneling may occur from D to A at the transition state which is when the reactant and product states have the same nuclear configurations (at the intersection point in Figure. 1-7a where there is large vibrational wave function overlap). Even though H_{AB} may be very small such that $0 < \kappa_{el} \ll 1$, there is finite probability of electron tunneling from D to A once the intersection is reached, but nuclear tunneling through/under the barrier is still negligible. The overall reaction rate will thus be temperature-dependent due to the activation required to reach the intersection point

(experimentally, a small κ_{el} will show up as a negative contribution to the measured entropy of activation).

2. Activated nuclear tunneling; ET may also occur through activated nuclear tunneling. Although the system may not reach the intersection point, the reactant and product surfaces are close enough to each other in nuclear configurational space for nuclear tunneling to take the system from the reactant to product surfaces due to finite ψ_{vib} (Franck-Condon) overlap below the intersection (see Figure 1-7b). In this case, the reaction is also temperature dependent, but less-so than in case 1.
3. Temperature-independent nuclear tunneling-limited; Slow but finite ET may occur by temperature-independent nuclear tunneling from the lowest vibrational levels of the reactant and product states (see Figure 1-7c).

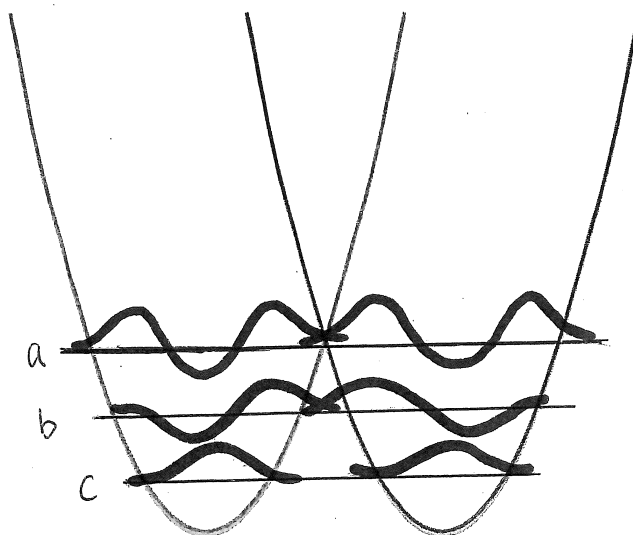


Figure 1-7. Potential energy curves for the quantum mechanical model of non-adiabatic electron transfer reactions. The vibrational wave functions are drawn so as to illustrate how overlap of the vibrational (nuclear) wave functions can facilitate the tunneling process.

Application of the NMR line broadening technique to ET kinetic measurements

In the work to be described in this thesis, the rates of the bimolecular ET self-exchange reactions such as the one shown in Figure 1-8 below were measured by the NMR line broadening technique.¹⁵ It is well-known that both the Ru^{II} and Ru^{III} oxidation states of ruthenium-pentaammine-L complexes such as the ones in Figure 1-8 below are substitution-inert over periods of hours in solution. Therefore, the ET reaction taking place in a mixture of the two redox states necessarily follows the outer-sphere mechanism mentioned previously.¹⁶

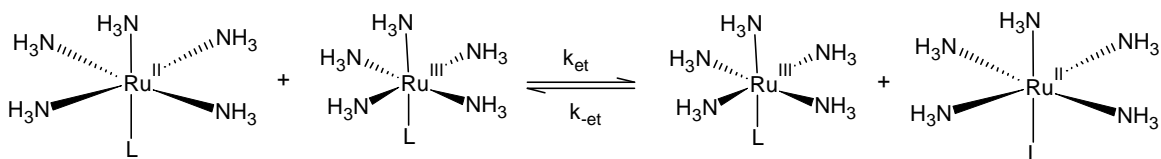


Figure 1-8. Schematic illustration of the ET self-exchange reaction between L-(NH₃)₅Ru²⁺ and L-(NH₃)₅Ru³⁺ (L represents a variety of different possible ligands, including the pyridyl ligands used in this work, see Table 2-1)

As is typical for 2nd and 3rd row transition metals, the high-spin/low-spin characteristic of the electronic spin states of Ru^{II}/Ru^{III} redox sites will not change during the course of the ET event (staying low-spin throughout), so the “extra” electron on the Ru^{II} center simply jumps back and forth between the filled “non-bonding” dπ (or t_{2g}) levels of the low-spin (t_{2g})⁶ Ru^{II} and “hole” in the low-spin (t_{2g})⁵ Ru^{III} electronic configuration. NMR can be a useful tool to monitor the rate of such a “chemical exchange” event if there is a resonance peak observable on one or both of the reactant ions which shifts position (resonance frequency) in response to a change in redox state. If the exchange dynamics match the NMR data collection timescale (~the length of the collection period of the time-domain “FID” signal), then the line widths of the NMR spectra will give us valuable information about the rates of any “chemical exchange” processes (such as the ET reaction shown in Figure 1-8) which are scrambling or “swapping” the chemical environments (and hence resonance frequencies of the exchanging species).¹⁷

According to second-order kinetics, the mean kinetic lifetimes of the distinct Ru^{II} and Ru^{III} species are related to the rate constant of the ET self-exchange reaction which swaps their identities (and thus their NMR resonance frequencies *via* Ru^{II} + Ru^{III} ⇌ Ru^{III} + Ru^{II}) as follows,

$$\tau_{Ru^{II}} = \frac{[Ru^{II}]}{k_{et}[Ru^{II}][Ru^{III}]} = \frac{1}{k_{et}[Ru^{III}]} \quad 1-25^{18}$$

and similarly, the mean kinetic lifetime for Ru^{III} can be expressed as,

$$\tau_{Ru^{III}} = \frac{1}{k_{et}[Ru^{II}]} \quad 1-26$$

If concentrations are adjusted such that $[Ru^{II}] = [Ru^{III}]$ in a given experiment, then these kinetic lifetimes will be equal.

The natural spectral line shapes of NMR resonance peaks are of the Lorentzian type and the line width can be calculated by the following equation,

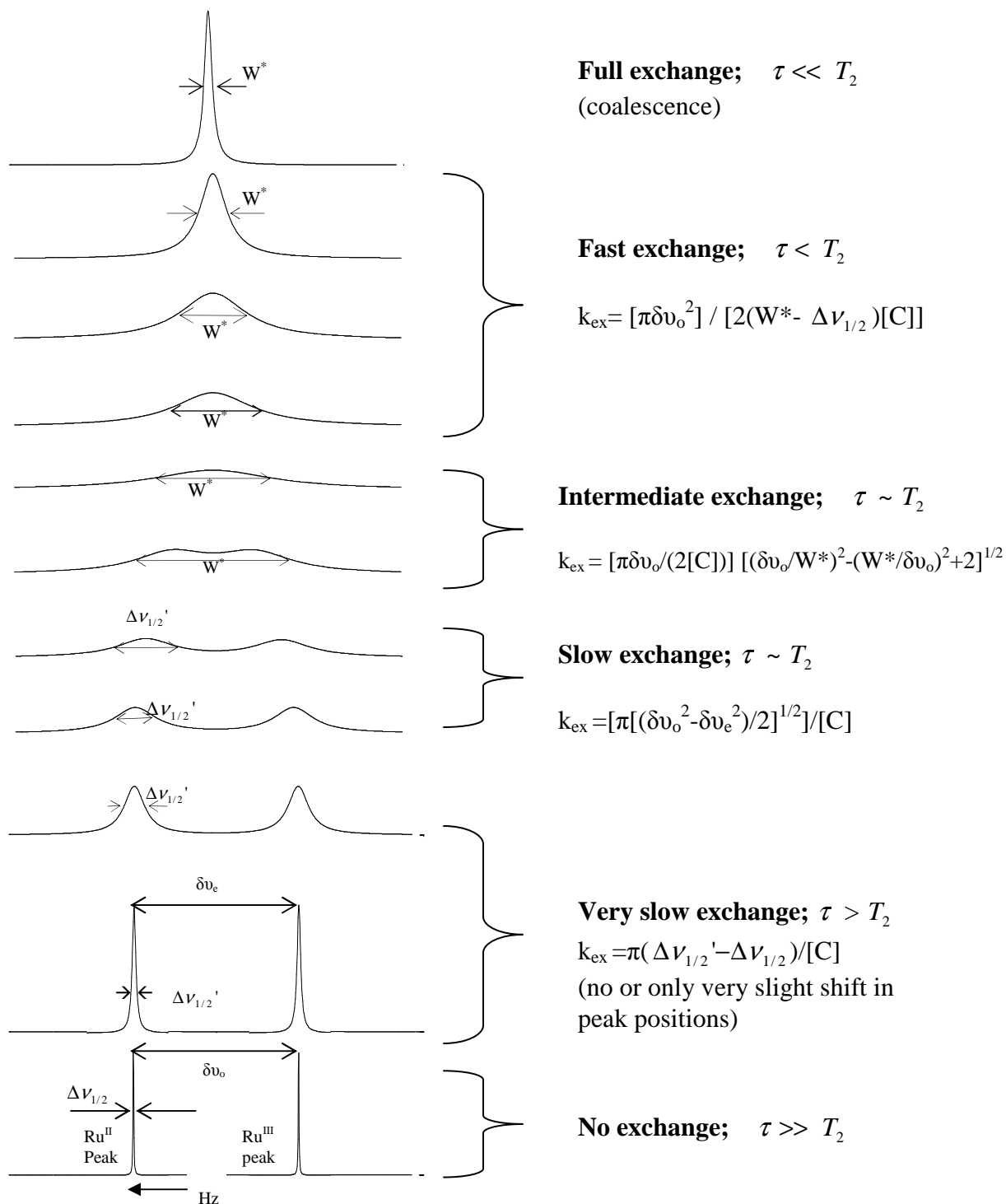
$$\Delta\nu_L = \frac{1}{\pi\tau_L} \quad 1-27^{18}$$

where $\Delta\nu_L$ is the width of the peak at half-maximum height and τ_L is the average NMR “excited state” lifetime (which is equal to the “transverse” or “spin-spin” relaxation time T_2 for decoherence of the net magnetization vector after rotation by a 90° RF pulse into the X-Y plane, *vide infra*). If the lifetime of a given NMR-active nucleus in its magnetic excited state is predominantly determined by the rate at which some conformational or redox-state change affects its environment, then measuring the line width in the presence of such exchange can be equivalent to measuring the rate of the kinetic process which sets the lifetime. In non-exchanging situations, the spin-spin and spin-lattice relaxation mechanisms determine the width of an NMR absorption peak by governing the rate at which transverse phase coherence persists in the X-Y plane after a 90° pulse.¹⁹ T_2 can also be thought of as

a measurement of the lifetime in a given nuclear-magnetic spin “excited” state²¹ since this is the rate at which spins become eigenstates of the “final” Hamiltonian operator (static field along Z, no pulse field). In our case, the spin-state coherence in the X-Y plane after pulse will be destroyed at a rate which corresponds to the natural spin-spin relaxation plus any added rate of environment scrambling between the different redox states, Ru^{II} and Ru^{III}, introduced by the stochastic chemical exchange process.

The specific line shape consequences of such chemical exchange processes greatly depend on how fast the kinetic chemical exchange rates are compared to the natural excited-state lifetime/linewidth and the absolute difference in resonance frequencies (line positions) of the exchanging NMR nuclei in the two different environments (δ_{ν_0} in Figure 1-9 and in Equations 1-31 to 1-35). There are several identifiable exchange rate “regions” spanning from very slow exchange (which barely enhances the natural transverse dephasing rate) to very fast exchange (the case when the kinetic lifetime τ is $\ll T_2$, T_2 is the natural line width here). Figure 1-9 illustrates the dependence of measured NMR line shapes on exchange rate as the relative magnitudes of τ and T_2 are varied at constant δ_{ν_0} .

Figure 1-9. Dependence of magnetic resonance line shapes on kinetic exchange rates as would be expected for exchange of the ^{19}F signals due to the ET self-exchange reaction $3\text{-tfmpy}(\text{NH}_3)_5\text{Ru}^{\text{II}} + 3\text{-tfmpy}(\text{NH}_3)_5\text{Ru}^{\text{III}} \rightleftharpoons 3\text{-tfmpy}(\text{NH}_3)_5\text{Ru}^{\text{II}} + 3\text{-tfmpy}(\text{NH}_3)_5\text{Ru}^{\text{III}}$ (3-tfmpy is 3-trifluoromethylpyridine, see Table 2-1)



In the figure, W_0 is the natural line width of a given resonance in the absence of chemical exchange, W^* is the line width of the broadened peak in the presence of chemical exchange, $\delta\nu_0$ is the frequency difference between pure the Ru^{II} (non-exchanging) and pure Ru^{III} resonances, and $\delta\nu_c$ is the frequency difference between the broadened Ru^{II} and Ru^{III} peaks when they are undergoing chemical exchange.

In the “very slow” exchange rate region (second panel from bottom), the peaks become slightly broadened but stay centered at the same frequencies as for the pure Ru^{II} or Ru^{III} parent species. As mentioned previously, the kinetic “exchange” line broadening is caused by the reduced duration of spin coherence in the X-Y plane for a given precessing spin system after a 90° pulse (the smaller effective T_2 leads to a broader peak according to Equation 1-27). With increasing rate of chemical exchange, which would mean more frequent bimolecular electron-transfer events between Ru^{II} and Ru^{III} in our case, the peaks begin to move toward each other and get even broader as shown in the sequence of panels moving up the figure. The reason why the two peaks move toward the center is because each Ru^{II} nucleus (or in our case, NMR-active nucleus connected to Ru^{II}) spends some of its time as a Ru^{III} site. The stochastic “chemical exchange” events happen randomly during the T_2 dephasing time and thus speed up the dephasing since precession rates in the X-Y plane vary according to which redox state (Ru^{II} or Ru^{III}) the NMR-active nucleus is ligated to. In the “fast-exchange” region, only one peak is showing at the averaged chemical shift position because the exchange is so rapid that each nucleus spends equal 50% portions of time as both Ru^{II} and Ru^{III} and this results in one sharp signal (the information about the two exchanging resonance lines is lost, but the width of the “averaged” resonance now shows up).

The effect of chemical exchange will be to shorten the spin-spin (transverse) relaxation (dephasing) time T_2 of a given species or “NMR isochromat”, and the relaxation frequency $1/T_2'$ in the presence of chemical exchange will be the sum of the transverse-relaxation frequency $1/T_2$ without chemical exchange and the chemical-exchange scrambling or “relaxation” frequency $1/\tau$. Thus,

$$\frac{1}{\tau} = \frac{1}{T_2'} - \frac{1}{T_2} \quad 1-28^{21}$$

where T_2' is the apparent transverse relaxation time and τ is kinetic lifetime mentioned previously in Equations 1-25 through 1-27 (in our case, T_2' refers to one of the lines in the mixture of Ru^{II} and Ru^{III} and T_2 refers to the transverse relaxation time of that resonance line without chemical exchange). Thus T_2' will be shortened relative to T_2 by the stochastic electron-transfer events which cause the kinetic lifetime τ to become shorter as k_{et} increases (see Figure 1-8 and Equation 1-25, 26).

Using the Lorentzian linewidth expression (Equation 1-27), we can rewrite Equation 1-28 and get,

$$\frac{1}{\tau} = \pi(\Delta\nu_{1/2}' - \Delta\nu_{1/2}) \quad 1-29$$

where $\Delta\nu_{1/2}'$ is the linewidth (Hz) at half maximum height for one of the peaks in the Ru^{II} and Ru^{III} mixture, and $\Delta\nu_{1/2}$ is the linewidth (Hz) at half maximum height for that line in the non-exchanging case. If we combine Equation 1-25 (or 1-26) and 1-29 together, the following expression for the second-order rate constant for ET self-exchange is obtained,

$$k_{\text{ex}} = \frac{\pi(\Delta\nu_{1/2}' - \Delta\nu_{1/2})}{[C]} \quad 1-30^{[22]}$$

in the simplifying case when Ru^{II} and Ru^{III} have the same concentration; [C] = [Ru^{II}] = [Ru^{III}].

Another expression which can be used in the less-slow-exchange limit is obtained from methods based on peak separation,

$$k_{ex} = \frac{\pi}{\sqrt{2}[C]} (\delta\nu_0^2 - \delta\nu_e^2)^{1/2} \quad 1-31^{23}$$

where $\delta\nu_0$ is the frequency difference between parent peak positions in the absence of exchange (in our case, the two non-exchanging Ru^{II} and Ru^{III} peaks) and $\delta\nu_e$ is the frequency difference between exchange-broadened signals in the presence of chemical exchange.

Takeda and Stejskal have derived a general bandwidth expression from the Bloch equations for an equally populated two-site case without any approximations.^{18,24} A slightly modified form of their result can be expressed as,

$$\frac{W^*}{\delta\nu} = \{[(A+B)^2[2(2A+B)^{-1} - 8A]^2 + (4B[2A+B]+1)^2]^{1/2} + (A+B)[2(2A+B)^{-1} - 8A]\}^{1/2}$$

where $A = k/2\pi\delta\nu_0$ and $B = W_0/2\delta\nu_0$ 1-32²³

Here, W_0 is the natural line width of the peak in the absence of chemical exchange, W^* is the line width of the broadened peak in the presence of chemical exchange and $\delta\nu_0$ is the frequency difference between A and B (in our case, A and B refer to pure Ru^{II} and pure Ru^{III}, respectively).

Equation 1-32 can be solved for k_{ex} by expanding $(2A+B)^{-1}$ in a series and neglecting all terms higher than second order in B,

$$k_{ex} = \frac{\pi\delta\nu_0(W^* + W_0) \left[1 + 2\left(\frac{W^*}{\delta\nu_0}\right)^2 - \left(\frac{W^*}{\delta\nu_0}\right)^4 \right]^{1/2}}{2(W^{*2} - W_0^2)[C]} \quad 1-33^{23}$$

If the natural linewidth can be neglected compared to the linewidth in the presence of chemical exchange ($W_0 \ll W^*$), the following equation can be obtained for the domain of “intermediate” exchange rates where strongest broadening is observed short of complete merging,

$$k_{ex} = \frac{\pi\delta\nu_0}{2[C]} \left[\left(\frac{\delta\nu_0}{W^*}\right)^2 - \left(\frac{W^*}{\delta\nu_0}\right)^2 + 2 \right]^{1/2} \quad 1-34^{23}$$

(W^* here is defined more generally as the width of the resonance at the intensity which is half the intensity at the center of the doublet; see Figure 1-9 for illustration)

In the “fast exchange” case when the peaks merge fully and progress to “coalescence” $\frac{W^*}{\delta\nu_0} \ll 1$, and Equation 1-34 can be further simplified into

$$k_{ex} = \frac{\pi\delta\nu_0^2}{2(W^* - W_0)[C]} \quad 1-35^{23}$$

and we note that now $W^* = \Delta\nu_{1/2}'$ and $W_0 = \Delta\nu_{1/2}$ in the notation of Equation 1-30.

Figures 1-10 through 1-12 show some examples of NMR spectra obtained in this work which fell in different chemical-exchange rate regions.

Figure 1-10. Example of an ^1H NMR spectrum showing the effects of slow chemical exchange between $\text{A}_5\text{Ru}^{\text{II}}3,5\text{-Me}_2\text{py}$ and $\text{A}_5\text{Ru}^{\text{III}}3,5\text{-Me}_2\text{py}$ in D_2O (3,5-Me₂Py=3,5-dimethylpyridine, A= NH_3 , ring protons of the Ru^{II} complex shown here). Rate calculated using Equation 1-31.

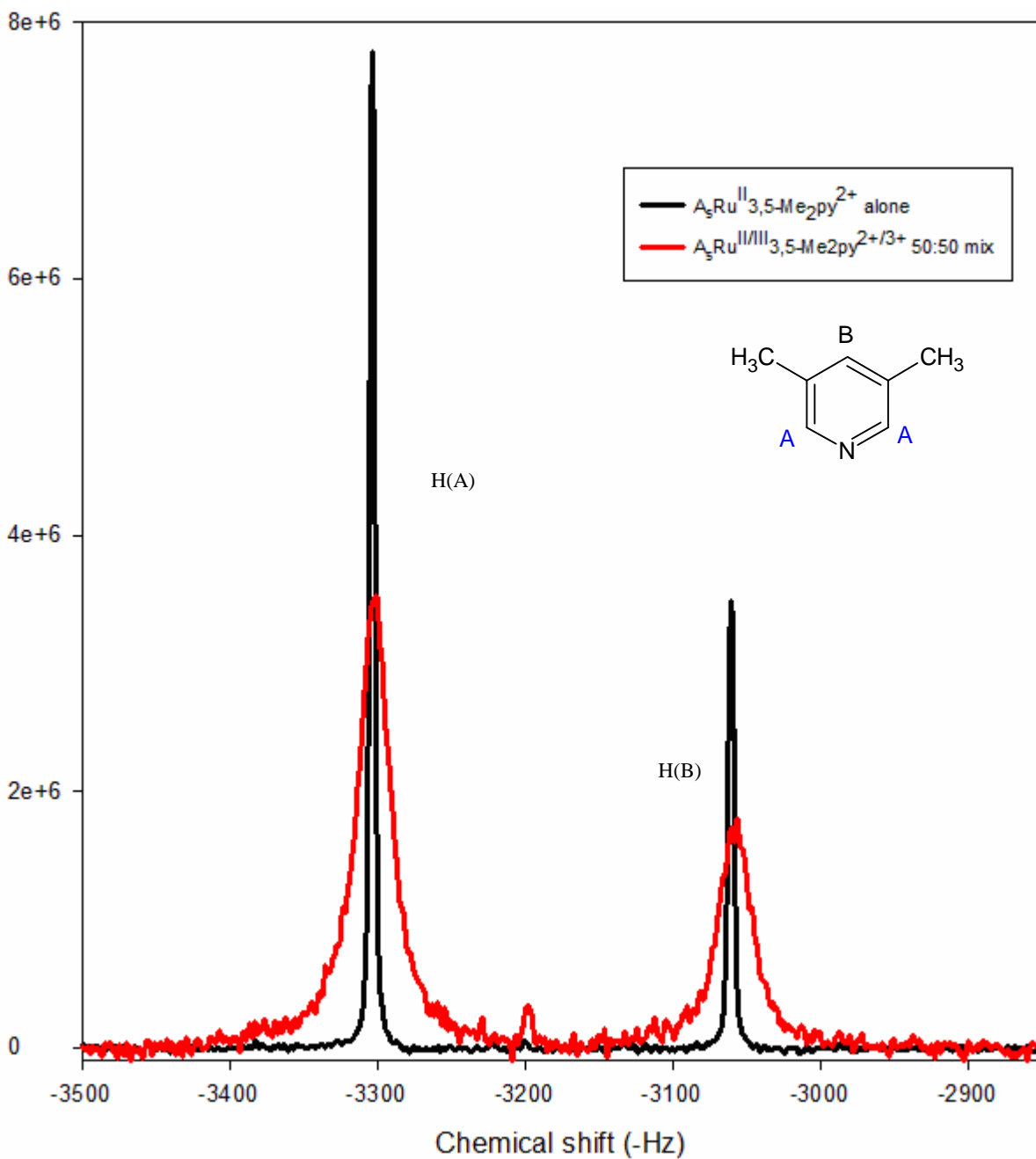


Figure 1-11. Example of an ^1H NMR spectrum showing the effects of intermediate chemical exchange between $\text{A}_5\text{Ru}^{\text{II}}(4\text{-Phpy})^{2+}$ and $\text{A}_5\text{Ru}^{\text{III}}(4\text{-Phpy})^{3+}$ in D_2O (4-Phpy = 4-phenylpyridine, $\text{A}=\text{NH}_3$, ring protons of the Ru^{II} complex shown here, see Chapter Two). Rate calculated using Ru^{III} peaks(see Chapter Two) and Equation 1-31.

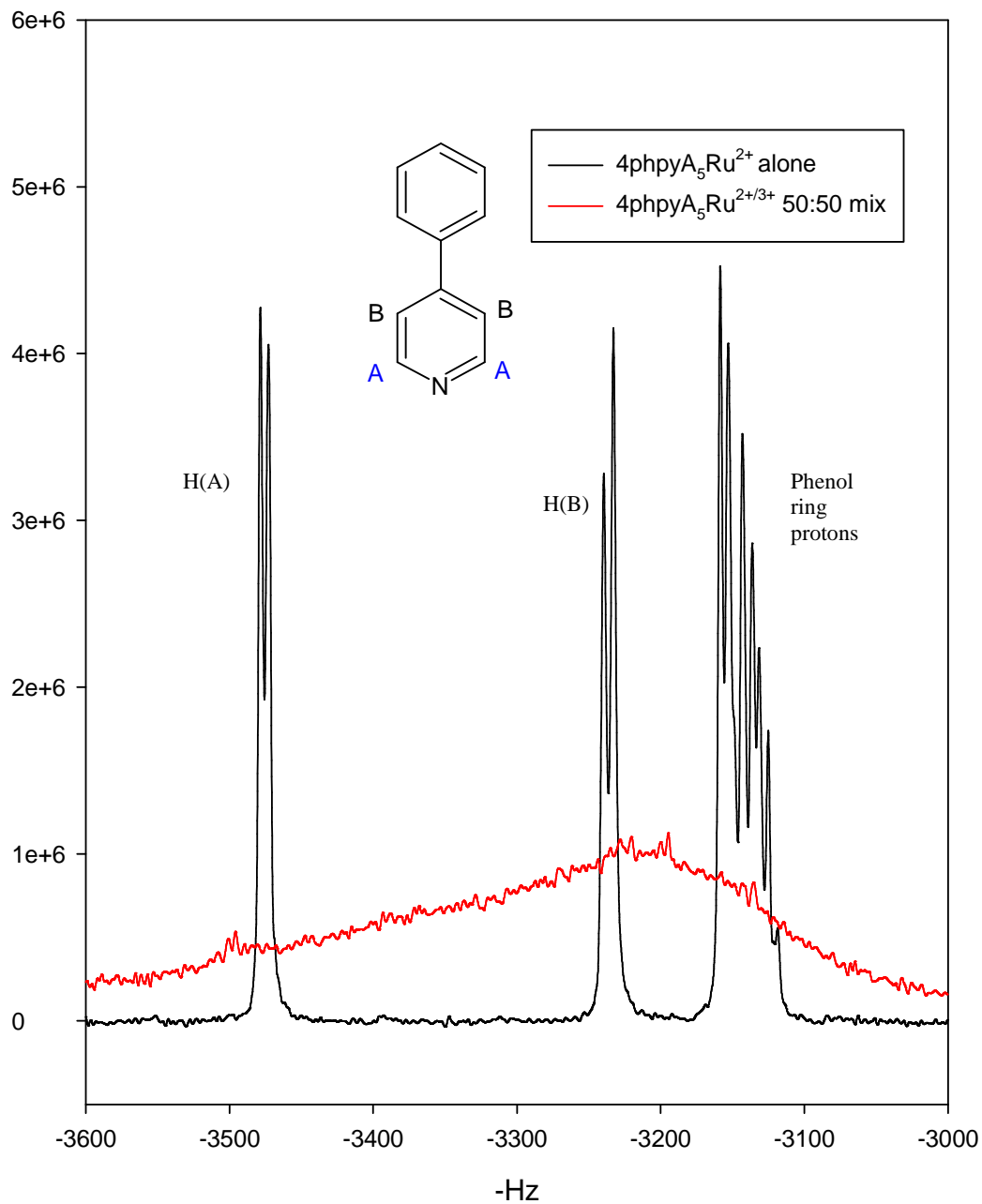
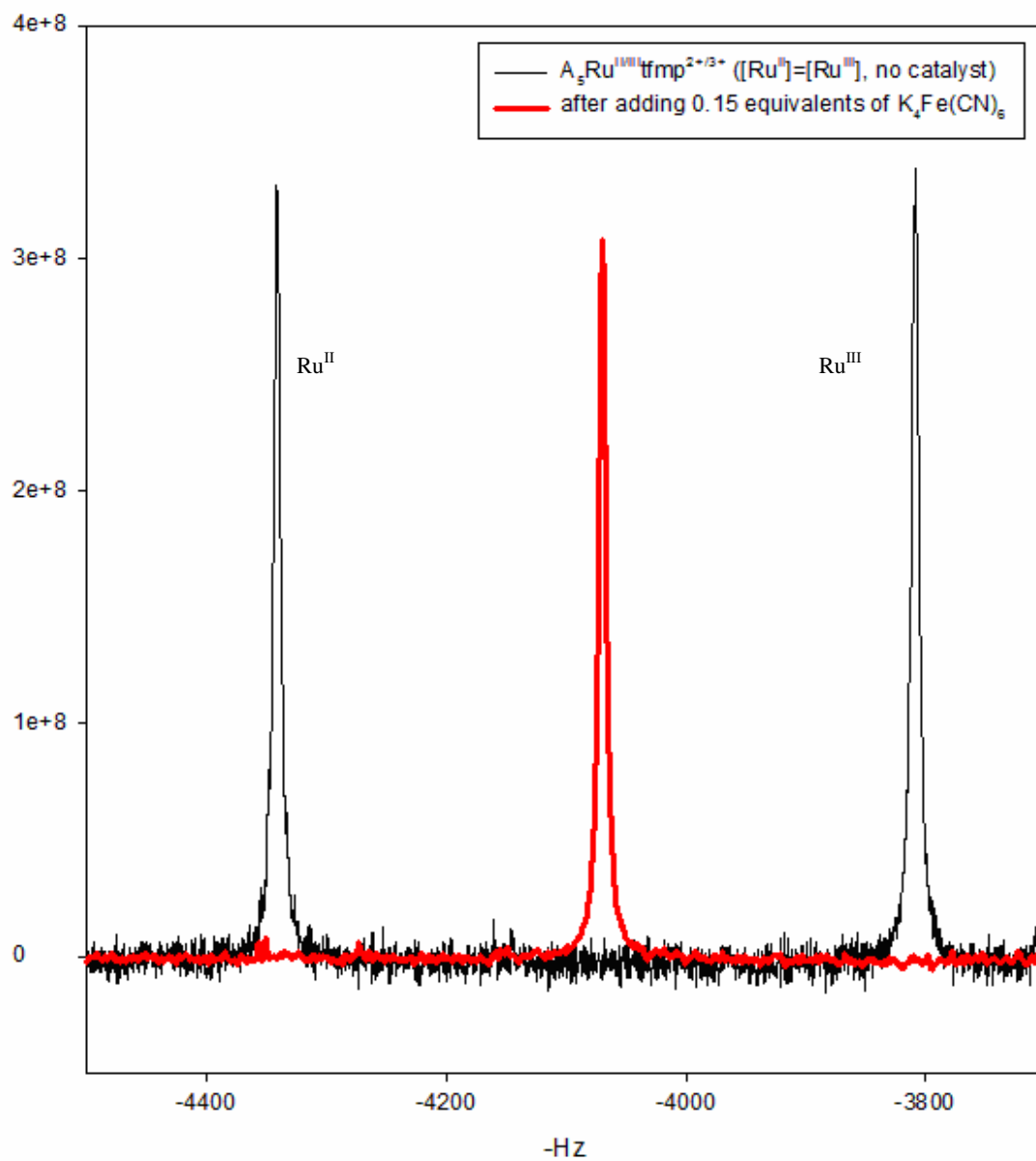


Figure 1-12. Illustration of ^{19}F NMR spectrum for fast chemical exchange reaction between $\text{A}_5\text{Ru}^{\text{II}}(\text{3-tfmpy})^{2+}$ and $\text{A}_5\text{Ru}^{\text{III}}(\text{3-tfmpy})^{3+}$ at $5.0 \times 10^{-3} \text{ M}$ in each before and after addition of the ET catalyst $\text{Fe}(\text{CN})_6^{4-}$ at $7.8 \times 10^{-4} \text{ M}$ concentration (see Chapter Three) (3-tfmpy = trifluoromethylpyridine, $\text{A}=\text{NH}_3$). It is the ^{19}F resonance of the CF_3 group on the Ru^{II} and Ru^{III} complexes which is shown here). Rate calculated using Equation 1-35.



In Chapter Two we will describe application of dynamic NMR measurements of ET self-exchange rates to a series of complexes of the general formulation $(\text{NH}_3)_5\text{Ru}^{\text{II/III}}\text{L}^{2+/3+}$ in D_2O (where L is a substituted pyridyl ligand, see Figures 1-8, 1-10, 1-11 and Table 2-1). A variety of ring protons were used in the kinetic measurements, and the goal was to search for and characterize any unexpected rate effects due to substituent placement and identity. Significant rate effects were indeed revealed for the cases of L = 3-phenylpyridine and 4-phenylpyridine. These observations matched well with recent stopped-flow work by Mehmood on a similar set of related pseudo-self exchange reactions.²⁵

In Chapter Three we used kinetic measurements of the $(\text{NH}_3)_5\text{Ru}^{\text{II/III}}(\text{3-trifluoromethylpyridine})^{2+/3+}$ self-exchange reaction to verify and extend the work started by Inagaki²⁶ in characterizing salt effects on rates. We found that the halide anions exhibited qualitatively-similar behavior to that which was seen by Sista²⁷ in stopped-flow work and we also found the same quantitative decrease in the magnitude of the salt effect as was reported by Inagaki. The hexacyano salts, $\text{M}^{\text{II}}(\text{CN})_6^{4-}$ with M = Fe, Ru, Os, were found to catalyze the ET rate in a very dramatic fashion, and magnitude of the effect followed a clear trend with Fe > Os > Ru. This was interpreted as evidence of a probable “superexchange” type mechanism dominated by the “hole-transfer” pathway based on the trend between the catalytic effect and the redox potential of the particular $\text{M}^{\text{II}}(\text{CN})_6^{4-}$ ion involved in a given reaction.

References

1. Barbara, P.F.; Meyer, T. J.; Ratner, M. A. *J. Phys. Chem.* **1996**, 100,13148.
2. Alberts, B.; Bray, D.; Roberts, K.; Lewis, J.; Raff, M. *Essential Cell Biology: An Introduction to the Molecular Biology of the Cell*, Taylor & Francis, Inc. **1997**, p 83.
3. Kaesche, H. *Corrosion of Metals*, Springer-Verlag New York, LLC, **2007**, p 1.
4. (a) Marcus, R.A. *J. Chem. Phys.* **1956**, 24, 966.
(b) Marcus, R.A. *J. Chem. Phys.* **1956**, 24, 979.
(c) Marcus, R.A. *J. Chem. Phys.* **1957**, 26, 867.
(d) Marcus, R.A. *J. Chem. Phys.* **1957**, 26, 872.
5. Taube, H.; Myers, H.; Rich, R.L. *J. Am. Chem. Soc.*,**1953**, 75, 4118.
6. Atkins, P.; Overto, T.; Rourke, J.; Weller, M.; Armstrong, F. *Inorganic Chemistry*, 4th Edition, Oxford University Press, **2000**, p 515.
7. Brown, G.M.; Sutin, N. *J.Am.Chem.Soc.*, **1979**, 101(4), 883.
8. Steinfeld, J.I.; Francisco, J.S.; Hase, W.L. *Chemical Kinetics and Dynamics*, Prentice-Hall, Inc, **1989**, p 38, p 14.
9. Mataga, N.; Mclendon, G.; Bolton, J.R. *Basic Electron Transfer Theory, ET in Inorganic, Organic, and Biological Systems*, Advances in Chemistry Series, American Chemical Society, **1991**, p 8.
10. (a) Allen, G.C.; Hush, N.S. *Prog. Inorg. Chem.* Vol. 8, Cotton, F.A., Ed.; Wiley-interscience: New York, **1967**, p 357.
(b) Hush, N.S. *Prog. Inorg. Chem.*, Vol. 8, Cotton, F.A., Ed.; Wiley-Interscience: New York, **1967**, p 391.
11. Sutin, N. *Acc. Chem. Res.* **1982**, 15, 275.

12. Marcus, R.A., Sutin, N. *Biochim Biophys. Acta*, **1985**, 881, 265.
13. (a) Landau, L., *Phys. Z. Sowjetunion*, **1932**, 2, 46.
(b) Zener, C., *Proc. R. Soc. London, Ser. A*, **1932**, 137, 696; **1933**, 140, 66.
14. Sutin, N. *J. Phys. Chem.* **1986**, 90, 3465.
15. Webb, G. A. *Nuclear Magnetic Resonance*, Chemical Society (Great Britain), Royal Society of Chemistry, **1991**, p 468.
16. Ige, J.; Ojo, J.F.; Olubuyide, O. *Inorg. Chem.* **1981**, 20, 1757.
17. Bertini, I. *NMR of paramagnetic molecules in biological systems*. The Benjamin/Cummings Publishing Company, Inc. **1986**, p 88.
18. Gardiner, W.C. *Rates and Mechanisms of Chemical Reactions*, W. A. Benjamin, INC. **1969**, p 234.
19. Pople, H.A., Schneider, W.G., and Bernstein, H.J., *High Resolution Nuclear Magnetic Resonance*, McGraw-Hill, New York, **1967**, pp 74-77.
20. McQuarrie, D.A. ; Simonred, J.D. *Physical Chemistry: A Molecular Approach*, University Science Books, **1997**, p 23.
21. (a) Nielson, R.M.; Wherland, S. *Inorg. Chem.* **1984**, 23, 1338-1344.
(b) McConnel, H.M. Berger, S.B. *J. Chem.. Phys.* **1957**, 27, 230-234.
(c) Allerhand, A., Gutowsky, H.S., Jonas, J. and Meinzer, R.A. *J. Am. Chem. Soc.* **1966**, 88, 3185.
22. Chun, S.J. Master's thesis, University of San Francisco, **2001**.
23. Sandstrom. J. *Dynamic NMR Spectroscopy*, Chemical Center University of Lund, Academic Press, **1982**, p79.
24. Takeda, M.; Stejskal, E. O. *J. Am. Chem. Soc.* **1960**, 82, 25.
25. Mehmood, F. Master's thesis, University of San Francisco, **2011**.

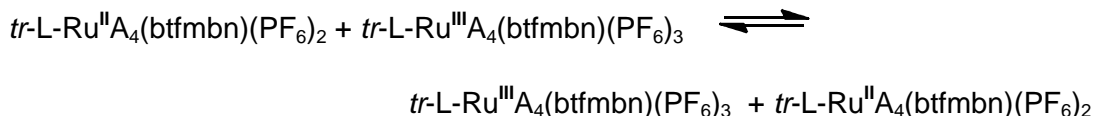
26. Inagaki, M. Master's thesis, University of San Francisco, **2006**.
27. Sista, P. Master's thesis, University of San Francisco, **2009**.

Chapter Two

NMR line broadening measurements of electron transfer self-exchange rates of ruthenium ammine pyridyl complexes and evidence for pyridyl ligand substituent effects on rates

Introduction

The purpose of this work is to determine whether substituent placement on the pyridyl ligands of ruthenium ammine pyridyl complexes will affect the measured electron-transfer self-exchange rates of the complexes as has been suggested from previous work in this lab.^{1,2} For example, the rate constant for the following bimolecular ET self-exchange reaction was measured in d_3 -acetonitrile using ^{19}F NMR linebroadening by Chun,¹

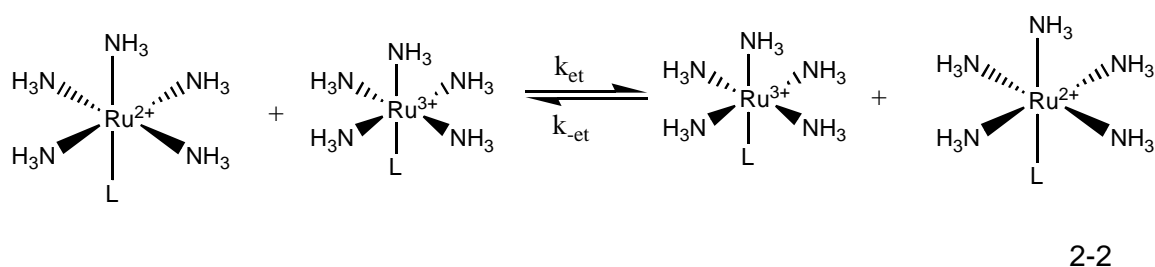


2-1

where L is a pyridyl ligand, A = NH_3 and btfmbn = 3,5-bis-trifluoromethylbenzonitrile. He reported that the rate of reaction for L = 4-Brpy (4-bromopyridine) at 25°C $\ln k_{\text{ex}} = 13.42$, but for L = 3-Brpy (3-bromopyridine) $\ln k_{\text{ex}} = 10.48$. In d_3 -nitromethane as solvent, the $\ln k_{\text{ex}}$ values were 13.60 and 12.12, respectively. Tanaka² also observed this same pattern of 4-substituted halo-pyridines reacting faster than 3-substituted pyridines in her work. She studied the self-exchange reaction between $tr\text{-L-(NH}_3)_4\text{Ru}^{\text{II}}\text{3-tfmpy}$ and $tr\text{-L-(NH}_3)_4\text{Ru}^{\text{III}}\text{3-tfmpy}$ (where 3-tfmpy is 3-

trifluoromethylpyridine). At room temperature in d_3 -acetonitrile, she found $\ln k_{\text{ex}} = 13.70$ for 4-Clpy (4-chloropyridine) and 12.95 for the 3-Clpy ligand (3-chloropyridine).

The studies to be described here were undertaken to investigate the possible existence of substituent effects on ET self-exchange rates in D_2O as solvent, using 15 different pyridyl ligands coordinated to pentaammine complexes of ruthenium (see Table 2-1). The general bimolecular ET self-exchange reaction can be written as follows,



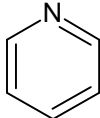
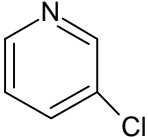
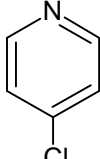
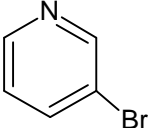
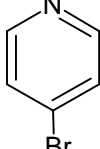
(L= different pyridyl ligands, see Table 2-1)

As introduced in Chapter One, the rates of such bimolecular ET reactions between the $Ru^{II/III}$ complexes can be monitored using the well-known NMR line broadening technique. Unique to this investigation is the fact that many of the rates were measured using line broadening of various peaks arising from the ring protons on the pyridyl ligands. We also did temperature-dependent kinetic measurements of some of the reactions in order to obtain the activation parameters.

Figure 2-1 shows an example of how the peak of aromatic protons broaden upon going from a solution of 5.0 mM $(NH_3)_5Ru^{II}3-Brpy$ in D_2O to a 50:50 mixture of both Ru^{II} and Ru^{III} at 5.0 mM (the Ru^{III} compound was added as its Cl^- salt). Rates were calculated from Peakfit spectral component analysis of the ring proton multiplet peaks (*vide infra*).

In this chapter, we will describe the details of the observed kinetics for complexes of the ligands shown in Table 2-1. While the 3- vs. 4-halo substituent placement effect observed by Chun and Tanaka (in organic solvents) could not be verified in D₂O, we did establish a very robust effect in the case of phenyl groups as substituents. We also uncovered evidence suggestive of a systematic relationship between $E_{1/2}$ for a given complex and its ET self-exchange rate. This will be discussed in the context of possible variations in the Franck-Condon reorganizational barrier to reaction as the electronic structures of complexes are varied according to the pyridyl ligand.

Table 2-1. Pyridyl ligands (names, structures and abbreviations) used in this study

| Name | Structure | Abbreviation |
|------------------|--|--------------|
| Pyridine |  | py |
| 3-Chloropyridine |  | 3-Clpy |
| 4-Chloropyridine |  | 4-Clpy |
| 3-Bromopyridine |  | 3-Brpy |
| 4-Bromopyridine |  | 4-Brpy |

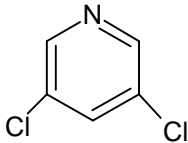
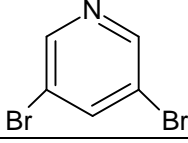
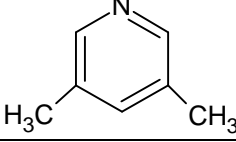
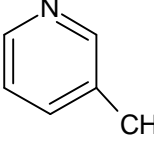
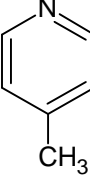
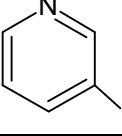
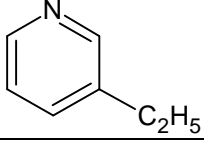
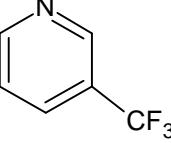
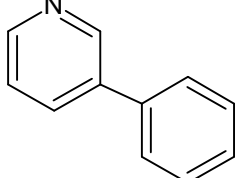
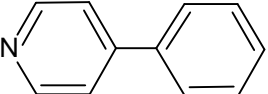
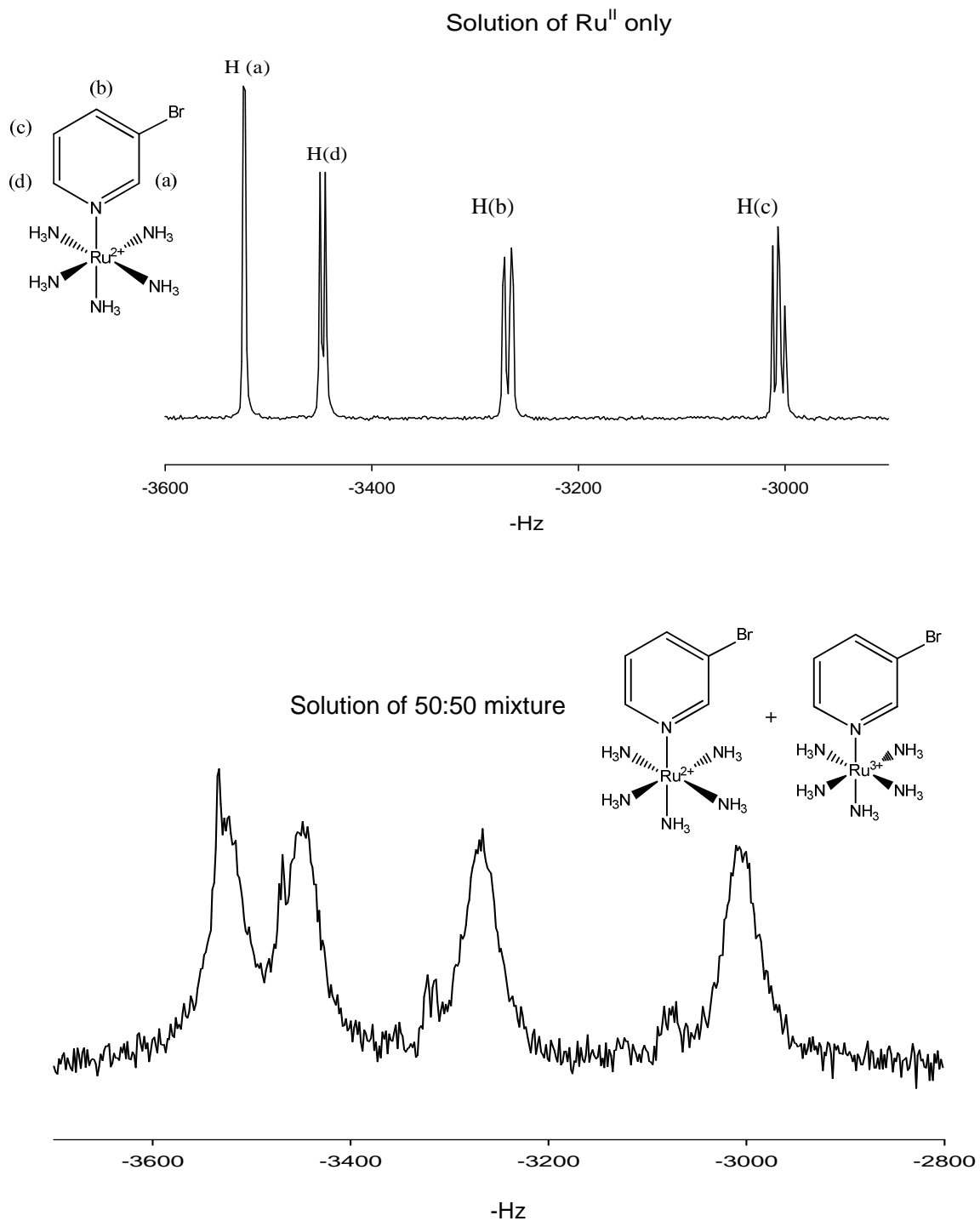
| | | |
|---------------------------------|--|------------------------|
| 3,5-Dichloropyridine |  | 3,5-Cl ₂ py |
| 3,5-Dibromopyridine |  | 3,5-Br ₂ py |
| 3,5-Dimethylpyridine (Lutidine) |  | 3,5-Me ₂ py |
| 3-picoline |  | 3-pic |
| 4-picoline |  | 4-pic |
| 3-Fluoropyridine |  | 3-Fpy |
| 3-Ethylpyridine |  | 3-Etpy |
| 3-Trifluoromethylpyridine |  | 3-tfmpy |
| 3-Phenylpyridine |  | 3-Phpy |
| 4-Phenylpyridine |  | 4-Phpy |

Figure 2-1. Illustration of the line-broadening effect on the 3-Brpy-(NH₃)₅Ru^{II/III} proton NMR spectrum due to electron-transfer self-exchange in the mixture



Experimental

Materials

$\text{RuCl}_3 \cdot x\text{H}_2\text{O}$ was purchased from Sigma Aldrich. All the organic ligands were either from Aldrich or Fluka. Reagent grade acetone was from VWR. The study of salt effects on self-exchange reactions employed both simple salts and more complex salts such as dicarboxylic anions and ferrocyanide. The former ones were purchased from Aldrich, EM Science, JT Baker Chemical or Mallinckrodt and used without further purification. The dicarboxylic species were bought from Aldrich as free acid form and converted to their disodium salts using the procedures described by Inagaki³. Ferrocyanide was from EM Science. All water used in this study was distilled water.

Preparation of the pentaamine Ruthenium Complexes

Preparation of $[(\text{NH}_3)_5\text{Ru}^{\text{III}}\text{Cl}]\text{Cl}_2$ (FW=292g/mol)

$[(\text{NH}_3)_5\text{Ru}^{\text{III}}\text{Cl}]\text{Cl}_2$ was synthesized from commercial $\text{RuCl}_3 \cdot \text{H}_2\text{O}$ using a modification of a method from the literature.⁴ In a typical preparation, 5 g of $\text{RuCl}_3 \cdot \text{H}_2\text{O}$ was added to a round bottom flask containing 62.5 mL distilled water. Next, 62.5 mL of hydrazine was carefully added drop wise with stirring and the flask in the ice bath. The resulting mixture was then stirred for more than 4 hours but less than 24 hours. The solution was a dark red-purple after reaction. The flask was again put into an ice bath and then 125mL of 12M HCl was slowly added over a period of 20 minutes with stirring. The solution was then heated at reflux for 2 hours.

The yellow product was isolated by filtration and washed with 20 mL of 0.1M HCl and followed by 20 mL acetone. Yields at this point were typically 70%.

Recrystallization of $[(\text{NH}_3)_5\text{Ru}^{\text{III}}\text{Cl}]\text{Cl}_2$

Crude $[(\text{NH}_3)_5\text{Ru}^{\text{III}}\text{Cl}]\text{Cl}_2$ (2 g) was added to 125 mL of 0.1 M HCl and heated to about 70 °C or until most of the compound went into the solution. The solution was then chilled gradually to 0°C. Yellow crystalline product was obtained by filtration. The yield was around 85%.

Preparation of $[\text{L}-(\text{NH}_3)_5\text{Ru}^{\text{II}}](\text{PF}_6)_2$

Method 1 (L= py, 3-Clpy, 4-Clpy, 3-Brpy, 4-Brpy, 3-Fpy, 3-tfmpy)

$[(\text{NH}_3)_5\text{Ru}^{\text{III}}\text{Cl}]\text{Cl}_2$ (0.1 g) in 5 mL distilled water acidified with a small amount of trifluoroacetic acid vapor was reduced over ~1 g Zn-Hg amalgam (*vide infra*) for less than 2 minutes. Then a three-fold molar excess of ligand was added to the solution, and it was allowed to react for another 30 minutes. The resulting yellow to orange solution (color depending on the ligand) was filtered into a flask containing a three molar excess of NH_4PF_6 solid. To maximize the yield, the product mixture was chilled at 0°C for half an hour, and then product was isolated by filtration and dried in vacuum.

The 4-Clpy and 4-Brpy ligands were purchased as hydrochloride salts, so they must be neutralized prior to ligation. The deprotonated ligand was prepared as follows. First, 0.18 g of the 4-Clpy hydrochloride salt (or 0.23 g for 4-Brpy ligand) was mixed with 0.5 equivalents of Li_2CO_3 (~0.044 g) and a minimum amount of water

(3-4 drops). The mixture will start to bubble. After 5-10 minutes (no more bubbles), ~1mL of ether was added to extract the neutralized ligand. The mixture separated into two parts with the addition of ether. The bottom layer was the aqueous phase and the top layer was the organic phase which contained the ready-to-use ligand. In the synthesis of $[L-(NH_3)_5Ru^{II}](PF_6)_2$ complex, we usually added all of the organic layer to the $(NH_3)_5RuCl_3/Zn-Hg$ slurry for reaction (the small amount of ether introduced had no effect on this reaction).

Preparation of Zn/Hg amalgam

About 1 g of 20 mesh Zn granules from Aldrich was washed with ~5 mL of 1M HCl to remove the oxide on the zinc surface. Initially, hydrogen bubbles were generated at the Zn surface, to which 3 mg of $HgCl_2$ was added and the solution was swirled until all the bubbles disappeared, indicating the presence of a thin layer of metallic Hg on the Zn particles. The resulting Zn-Hg amalgam was then washed with three small portions of distilled water to remove the remaining HCl. The Zn-Hg amalgam should be sealed from exposure to air and must be used within a few minutes of preparation. It should be removed from frits and flasks immediately after use so as to avoid the formation of ZnO deposits.

Method 2 (L= 3,5-Br₂py, 3,5-Cl₂py, 3-Etpy, 3,5-Me₂py, 3-pic, 4-pic)

This method worked well for ligands that were not water soluble. First, $[(NH_3)_5Ru^{II}OH_2](PF_6)_2$ was synthesized according to the literature method.⁵ In a typical preparation, 0.15g $[(NH_3)_5Ru^{III}Cl]Cl_2$ was reduced over ~1g Zn-Hg amalgam in about 5 mL of deionized water slightly acidified with trifluoroacetic acid. The reaction was allowed to run for about 5-8 minutes with continuous bubbling of argon gas or

until all of the $[(\text{NH}_3)_5\text{Ru}^{\text{III}}\text{Cl}]\text{Cl}_2$ dissolved and the solution became pale yellow in color. The solution containing the $[(\text{NH}_3)_5\text{Ru}^{\text{II}}(\text{OH}_2)]^{2+}$ product was then filtered under argon into 0.4~0.5 g NH_4PF_6 and chilled at 0 °C for half an hour. The ruthenium(II)pentammineaquo-hexafluorophosphate salt was isolated under a blanket of argon and dried in vacuum. The $[(\text{NH}_3)_5\text{Ru}^{\text{II}}\text{OH}_2](\text{PF}_6)_2$ (0.2~0.25 g) obtained from the previous step was dissolved in ~30 mL of argon-degassed acetone (degassing for at least 45 minutes) with a three-fold molar excess of ligand. The solution was stirred in darkness for 40 minutes and filtered into a five-fold volume excess of ether to precipitate out the final product. The product was then isolated by filtration and dried in vacuum. Typical yields were ~80%.

Purification of $[\text{L}-(\text{NH}_3)_5\text{Ru}^{\text{II}}](\text{PF}_6)_2$ (L= py, 3-Clpy, 4-Clpy, 3-Brpy, 4-Brpy, 3-Fpy)

Method 1 (Acetone-Ether Method)

The crude $[\text{L}-(\text{NH}_3)_5\text{Ru}^{\text{II}}](\text{PF}_6)_2$ was dissolved in a minimum amount of acetone and filtered to remove any undissolved solid. A fifteen-fold volume excess of ether was added to the filtrate to precipitate the product. Then the product was isolated via filtration and dried in vacuum. The percentage recovery was typically around 90%. This procedure could be repeated if necessary.

Method 2 (Water Method)

In some cases, the acetone-ether method was insufficient and a more aggressive aqueous method was used. Typically, 2 g of crude $[\text{L}-(\text{NH}_3)_5\text{Ru}^{\text{II}}](\text{PF}_6)_2$ was dissolved in 50 mL of ~0.5 M NH_4PF_6 solution and heated gently (~60 °C) until most of the solid went into the solution. The solution was cooled gradually and then

held at 0°C for two hours. The recrystallized product was then isolated by filtration and dried in vacuum. Typical recovery was 70~80%. This isolation was then followed by one reprecipitation using the acetone-ether method.

Preparation of [L-(NH₃)₅Ru^{II}]Cl₂

[L-(NH₃)₅Ru^{II}](PF₆)₂ (~30 mg) was dissolved in 20mL of acetone and filtered to remove any insoluble impurities. [L-(NH₃)₅Ru^{II}]Cl₂ was then precipitated out by adding 15 drops (~0.75 mL) of 1:8 saturated TEACl (tetra-n-butylammonium chloride) in dry 70:30 acetone/methanol. The orange-colored product was collected by vacuum filtration. If the mother liquid is still orange-colored, a few more drops of TEACl were added to the mother liquid, and the new precipitate was collected into the same frit. The addition of TEACl was repeated several times until the mother liquid was slightly colored but not colorless, indicating no excess amount of TEACl has been added. The final product was dried in vacuum. Yields were typically 75-80%. [L-(NH₃)₅Ru^{II}]Cl₂ salts are only stable for 24 hours.

Preparation of [L-(NH₃)₅Ru^{III}]Cl₃

30mg of [L-(NH₃)₅Ru^{II}](PF₆)₂ was dissolved in 3-4mL acetone and filtered to remove any insoluble impurities. Then 15 drops (~ 0.75 mL) of 1 M HCl and 4 drops (~0.2 mL) of 30% H₂O₂ were added to the solution. Ruthenium (II) was considered oxidized completely when the color of the solution turned orange to pale yellow. [L-(NH₃)₅Ru^{III}]Cl₃ was precipitated by slow addition of a fifteen-fold volume excess of acetone. The product was isolated by filtration and dried in vacuum. Yields were 75-80%. [L-(NH₃)₅Ru^{III}]Cl₃ salts are stable for only 24 hours.

Spectrophotometric Measurements

All the spectrophotometric measurements were performed either on a Cary 5G UV-VIS-NIR Spectrophotometer, a Cary 5000 or an HP 8452A UV-VIS Diode Array Spectrometer. The ruthenium(II) solution was prepared fresh each time before measuring the metal to ligand charge transfer (MLCT) spectrum. As for ruthenium(III) solutions, the purity of these complexes is determined by reducing to ruthenium(II) by addition of a small amount of hydrazine followed by absorbance measurement at the position of the Ru(II) absorption maximum. The typical concentration of ruthenium solution was about 1×10^{-4} M. All MLCT spectra were taken in the UV-visible region (typically from 350-600 nm) so as to determine λ_{\max} and ϵ_{\max} . The extinction coefficient ϵ at λ_{\max} was calculated from the Beer-Lambert Law,

$$A = \epsilon \cdot l \cdot c \quad 2-3^6$$

where l is the cell path length (1 cm) and c is the molar concentration of ruthenium solution. The extinction coefficient, ϵ , and λ_{\max} values can be used to characterize a specific ruthenium complex in a given solvent. A higher extinction coefficient generally indicates a purer compound.

Electrochemical Measurements

An EG & G PARC, Model 270 Voltammetric Analyzer with 270 research electrochemical software was used to perform all electrochemical measurements. The differential pulse voltammetry (DPV) technique was employed to measure the redox potential $E_{1/2}$ of each different ruthenium complex. Typically, about 2 mg of Ru compound (water soluble) was dissolved in ~3 mL of 0.1 M KCl which served as the supporting electrolyte. In the case of Ru PF₆⁻ salts, which are not water soluble, we used 0.1 M TEAPF₆ in acetonitrile/acetone as the supporting electrolyte instead. The measurements were made in a three-compartment cell including a freshly polished (with 0.05 μm alumina) platinum disk as the working electrode and a Pt wire auxiliary electrode. For aqueous measurements, a saturated KCl calomel electrode (SCE) was used as the reference electrode, and for non-water soluble compounds, a Ag/AgCl wire in 0.1 M TEAPF₆ in acetonitrile was the reference electrode. Voltammetric peak positions were determined relative the position of the fc/fc⁺ (fc = ferrocene) couple under the same conditions that day. In DPV, the peak current is proportional to the concentration, but the value of $E_{1/2}$ is independent of Ru concentration. However, if an analyte solution is too diluted, noise in the voltammogram will increase uncertainty in the observed $E_{1/2}$.

Tables 2-2 and 2-3 show the measured spectral data and $E_{1/2}$ values of the series of ruthenium complexes used in this study. Table 2-4 shows the results of the CHN element analyses of the pentaammine ruthenium PF₆⁻ complexes.

Table 2-2. Extinction coefficients and $E_{1/2}$ values of $L-(NH_3)_5Ru^{II}(PF_6)_2$

| Compound | $\lambda_{max}(nm)$ in Acetone | ϵ_{max} | $E_{1/2}(v)$ vs ref. couple fc/fc^+ ^(a) | Solvent for $E_{1/2}$ measurement |
|--|--------------------------------|------------------|--|-----------------------------------|
| 4-pic- $A_5Ru^{II}(PF_6)_2$ | 409 | 8570 | -0.206 | Acetone |
| 3-Etpy- $A_5Ru^{II}(PF_6)_2$ | 415 | 8100 | -0.201 | Acetonitrile |
| 3,5-Me ₂ py- $A_5Ru^{II}(PF_6)_2$ | 413 | 7900 | -0.187 | Acetone |
| 4-Phpy- $A_5Ru^{II}(PF_6)_2$ | 459 | 14110 | -0.164 | Acetone |
| py- $A_5Ru^{II}(PF_6)_2$ | 417 | 8950 | -0.147 | Acetone |
| 3-pic- $A_5Ru^{II}(PF_6)_2$ | 415 | 8780 | -0.145 | Acetone |
| 3-Phpy- $A_5Ru^{II}(PF_6)_2$ | 431 | 7410 | -0.138 | Acetone |
| 3-Clpy- $A_5Ru^{II}(PF_6)_2$ | 440 | 10400 | -0.106 | Acetone |
| 4-Clpy- $A_5Ru^{II}(PF_6)_2$ | 437 | 10260 | -0.099 | Acetone |
| 3-Fpy- $A_5Ru^{II}(PF_6)_2$ | 432 | 9500 | -0.079 | Acetone |
| 4-Brpy- $A_5Ru^{II}(PF_6)_2$ | 439 | 10800 | 0.011 | Acetone |
| 3-tfmpy- $A_5Ru^{II}(PF_6)_2$ | 450 | 9000 | 0.035 | Acetone |
| 3-Brpy- $A_5Ru^{II}(PF_6)_2$ | 441 | 10470 | 0.040 | Acetone |
| 3,5-Cl ₂ py- $A_5Ru^{II}(PF_6)_2$ | 461 | 11050 | 0.080 | Acetone |
| 3,5-Br ₂ py- $A_5Ru^{II}(PF_6)_2$ | 465 | 10880 | 0.095 | Acetone |

(a) the $E_{1/2}$ values were measured against a Ag/AgCl reference electrode and the fc/fc^+ couple was measured against the same Ag/AgCl reference during that same experimental session.

Table 2-3. Spectral data and $E_{1/2}$ values of the $L-(NH_3)_5Ru^{II}Cl_2$ complexes in water

| Compound | $\lambda_{max}(nm)$ in H_2O | ϵ_{max} | $E_{1/2}(v)$ vs SCE in 0.1 M KCl |
|--|-------------------------------|------------------|----------------------------------|
| 3,5-Me ₂ py-A ₅ Ru ^{II} Cl ₂ | 401 | 6380 | 0.025 |
| 4-pic-A ₅ Ru ^{II} Cl ₂ | 399 | 7000 | 0.027 |
| 3-Etpy-A ₅ Ru ^{II} Cl ₂ | 405 | 7060 | 0.032 |
| 3-pic-A ₅ Ru ^{II} Cl ₂ | 404 | 6870 | 0.043 |
| 4-Phpy-A ₅ Ru ^{II} Cl ₂ | 445 | 11020 | 0.054 |
| py-A ₅ Ru ^{II} Cl ₂ | 407 | 7810 | 0.058 |
| 3-Phpy-A ₅ Ru ^{II} Cl ₂ | 418 | 6940 | 0.068 |
| 4-Clpy-A ₅ Ru ^{II} Cl ₂ | 425 | 8950 | 0.090 |
| 4-Brpy-A ₅ Ru ^{II} Cl ₂ | 428 | 8795 | 0.092 |
| 3Clpy-A ₅ Ru ^{II} Cl ₂ | 426 | 8120 | 0.113 |
| 3-Fpy-A ₅ Ru ^{II} Cl ₂ | 422 | 7575 | 0.117 |
| 3-Brpy-A ₅ Ru ^{II} Cl ₂ | 428 | 9390 | 0.119 |
| 3-tfmpy-A ₅ Ru ^{II} Cl ₂ | 436 | 8235 | 0.143 |
| 3,5-Br ₂ py-A ₅ Ru ^{II} Cl ₂ | 449 | 8560 | 0.178 |
| 3,5-Cl ₂ py-A ₅ Ru ^{II} Cl ₂ | 461 | 9580 | 0.188 |

Table 2-4. Elemental analyses of the ruthenium complexes

| Compound | C% observed (theory) | H% observed (theory) | N% observed (theory) |
|---|-------------------------|-------------------------|-------------------------|
| 3,5-Me ₂ py-A ₅ Ru ^{II} (PF ₆) ₂ | 18.00 (18.73) | 4.20 (4.72) | 12.4 (13.1) |
| 4-pic-A ₅ Ru ^{II} (PF ₆) ₂ | 12.95 (12.7) | 3.24 (3.89) | 14.67 (14.8) |
| 3-Etpy-A ₅ Ru ^{II} (PF ₆) ₂ | 15.62 (14.5) | 4.02 (4.14) | 13.84 (14.4) |
| 3-pic-A ₅ Ru ^{II} (PF ₆) ₂ H ₂ O | 12.41 (12.3) | 3.53 (4.09) | 14.48 (14.3) |
| 4-Phpy-A ₅ Ru ^{II} (PF ₆) ₂ | 21.89 (20.92) | 3.64 (3.83) | 12.61 (12.61) |
| py-A ₅ Ru ^{II} (PF ₆) ₂ | 11.16 (10.82) | 3.53 (3.63) | 14.63 (15.14) |
| 3-Phpy-A ₅ Ru ^{II} (PF ₆) ₂ | 20.92 (20.92) | 3.17 (3.83) | 13.02 (13.31) |
| 4-Clpy-A ₅ Ru ^{II} (PF ₆) ₂ | 11.00 (10.1) | 3.11 (3.38) | 13.93 (14.1) |
| 4-Brpy-A ₅ Ru ^{II} (PF ₆) ₂ | 9.82 (9.43) | 2.79 (3.14) | 12.98 (13.2) |
| 3-Clpy-A ₅ Ru ^{II} (PF ₆) ₂ | 10.24 (10.18) | 2.42 (3.24) | 14.06 (14.25) |
| 3-Fpy-A ₅ Ru ^{II} (PF ₆) ₂ | 10.80 (10.48) | 2.58 (3.34) | 14.12 (14.66) |
| 3-Brpy-A ₅ Ru ^{II} (PF ₆) ₂ | 9.33 (9.43) | 3.19 (3.14) | 12.77 (13.20) |
| 3-tfmpy-A ₅ Ru ^{II} (PF ₆) ₂ | 11.71 (11.55) | 3.22 (3.05) | 13.07 (13.48) |
| 3,5-Br ₂ py-A ₅ Ru ^{II} (PF ₆) ₂ H ₂ O | 8.15 (8.20) | 2.34 (2.73) | 11.55 (11.49) |
| 3,5-Cl ₂ py-A ₅ Ru ^{II} (PF ₆) ₂ | 9.72 (9.69) | 2.72 (2.90) | 13.37 (13.46) |

NMR line broadening Measurements

All the NMR experiments in this study were performed on a 400 MHz Bruker DPX FT-NMR. D₂O (99.9%) and d₆-acetone were purchased from Aldrich.

Sample preparation

NMR tubes

The first important step in preparing an NMR sample is the selection of good quality NMR tubes. In this work, (Grade 6) NMR tubes were purchased from Kontes. Previously-used tubes must be cleaned carefully and dried prior to reuse. The cleaning procedure is as follows: (1) wash with H₂O/Acetone (use H₂O if the previous sample compound was water soluble; use acetone if it was soluble in acetone), (2) soak in concentrated nitric acid, (3) rinse with a generous amount of water to remove any acid residue, (4) rinse with acetone, (5) air dry with the tube inverted (DO NOT DRY in OVEN!). Tubes that cannot be cleaned should be discarded. It is highly recommended to clean the tube right away after each experiment. Most problems with cleaning the tube are related to the evaporation of the solvent from the samples whose spectra were taken weeks or even months previously. **IMPORTANT:** Chromic acid should never be used to clean tubes because any paramagnetic chromium ions left on the glass will cause the signals (especially for protons) to broaden for the next sample to be placed in the tube.

Preparation of samples for self-exchange reaction rate studies

Typically, a ruthenium(II) solution of 5.0 mM concentration was prepared as follows: the calculated amount of ruthenium(II) compound was dissolved in 2 mL of D₂O measured and delivered by a micropipette to the NMR tube. After taking the ¹H (or ¹⁹F) spectrum of the Ru^{II} only solution, the solid chloride salt of the Ru^{III} compound (which was calculated to make the mole ratio of [Ru^{II}] : [Ru^{III}] = 1:1) was added directly to the tube. The tube must be shaken and inverted at least 20 times; incomplete dissolution/mixing can result in an inaccurately broadened spectrum. In

the study of salt effects, salts were added to the tube in the same manner as adding the Ru^{III} complex except for Fe(CN)₆⁴⁻, Os(CN)₆⁴⁻ and Ru(CN)₆⁴⁻ which were added in much smaller amounts. Stock solutions of those three solutions were made first (typically at 20 mM) and then added to the Ru^I/Ru^{III} mixture using a P20 micropipette with the smallest aliquots added being 1 µl in volume.

Optimizing NMR signals⁷

Field/Frequency Locking

Since all superconducting magnets are subject to field drift, this effect has to be compensated by electronically locking onto the resonance of a substance contained in the NMR sample. In pulse experiments, we cannot select the same type of nucleus that is being observed as the one to whose signal the magnetic field is to be locked. Therefore, protons ¹H cannot generally be used for field locking, but deuterium is an excellent candidate for locking the field. Most of the solvents that have protons in them can be replaced by perdeuterated analogs, such as D₂O, acetone-d₆ and acetonitrile-d₃. In this work, most of the experiments were done in aqueous conditions where we used D₂O as solvent, thus the deuterons of the D₂O were the nuclei to which the field was locked.

Spectrometer Shimming

It is very important to establish a homogeneous field through the sample volume before any spectrum is taken, especially in kinetics studies of self-exchange reactions, since the rate constant k_{ex} is calculated from the line widths of the peaks. Linewidth is subject to broadening due to the faster dephasing process in the x-y

plane which results if the sample is subjected to an inhomogeneous field (bad shims). Figure 2-2 illustrates how the field changes after loading the sample into the probe (exaggerated).

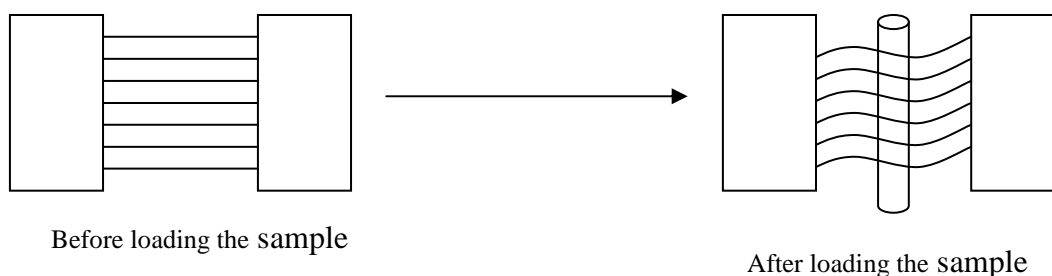


Figure 2-2. Illustration of how the magnetic field changes after loading the sample.

Shimming is a process to correct field homogeneity by adjusting the current flowing in shim coils built into the NMR instrument. Shim coils are available for correcting gradients in all three Cartesian coordinates including the primary gradients, (x , y , and z), as well as higher order (z^2 , z^3 , z^4 , etc.) and combination vectors (xz , yz , x^2-y^2 , etc.). The shimming procedure was carried out by maximizing the lock level as nearly as possible. Before magnet shimming is undertaken, the lock level should be tuned to midrange. The amount of shimming required depends on how the sample is prepared (volume) and the quality of the initial shim file being loaded. For most of the samples in this study, adjusting z and z^2 with spin on was good enough to obtain a good spectrum (as judged by narrow linewidths, *vide infra*). The non-spinning shims (x , y , xz , yz) have to be optimized with the spinning turned off. One way to check the quality of shimming is to take a quick proton spectrum and see whether the spectrum looks good in terms of showing a symmetric line shape and overall

appearance. For ruthenium complexes with a trifluoromethylpyridine ligand attached, a line width of 2-3 Hz in the ^{19}F spectrum indicates good field homogeneity.

Typical ^1H and ^{19}F parameters used

Table 2-5 and 2-6 showed ^1H NMR parameters and ^{19}F NMR parameters, respectively.

Table 2-5. Sample ^1H NMR parameters

| | |
|-----------------------------|-----------------|
| F2 - Acquisition Parameters | |
| Date_ | 20080923 |
| Time | 16.10 |
| INSTRUM | spect |
| PROBHD | 5 mm QNP 1H/1 |
| PULPROG | zg2d |
| TD | 32768 |
| SOLVENT | D2O |
| NS | 64 |
| DS | 2 |
| SWH | 4370.629 Hz |
| FIDRES | 0.133381 Hz |
| AQ | 3.7487092 sec |
| RG | 574.7 |
| DW | 114.400 usec |
| DE | 6.00 usec |
| TE | 300.0 K |
| D1 | 1.00000000 sec |
| ===== CHANNEL f1 ===== | |
| NUC1 | 1H |
| P1 | 9.25 usec |
| PL1 | 0.00 dB |
| SFO1 | 400.1319308 MHz |
| F2 - Processing parameters | |
| SI | 16384 |
| SF | 400.1299598 MHz |
| WDW | EM |
| SSB | 0 |
| LB | 0.10 Hz |
| GB | 0 |
| PC | 1.00 |

Note: PROBHD=probe type; PULPROG= pulse program; TD= number of data points of the FID; NS= Number of data acquisition scans; DS= Number of dummy scan (Dummy scans pulse the sample in exactly the same manner as the data acquisition scans (NS), except that the receiver is switched off. This allows the sample to respond to the pulse program and relax before data is acquired.) SWH=sweep width (Hz); FIDRES= FID resolution; AQ= Acquisition time of one scan in seconds; RG=Receiver gain; DW= Dwell time (the time difference between two data points of the FID); DE= Pre-scan delay; TE= Probe temperature; D1= relaxation delay between pulses; NUC1= type of nucleus being observed; P1= Pulse length; PL1= Power level of main pulse; SFO1= Spectrum scanning range; SI= zero filling point; SF= Spectrometer frequency; LB= line broadening parameter.

Table 2-6. Sample ¹⁹F NMR parameters

| | |
|---------------------------|-----------------|
| F2-Acquisition Parameters | |
| Date_ | 20090315 |
| Time | 15.26 |
| INSTRUM | spect |
| PROBHD | 5 mm QNP 1H/1 |
| PULPROG | zgflqn |
| TD | 32768 |
| SOLVENT | D2O |
| NS | 64 |
| DS | 0 |
| SWH | 7530.121 Hz |
| FIDRES | 0.229801 Hz |
| AQ | 2.1758451 sec |
| RG | 2896.3 |
| DW | 66.400 usec |
| DE | 6.00 usec |
| TE | 300.0 K |
| D1 | 0.60000002 sec |
| ===== CHANNEL f1 ===== | |
| NUC1 | 19F |
| P1 | 15.00 usec |
| PL1 | 0.00 dB |
| SFO1 | 376.4725441 MHz |

| | |
|----------------------------|-----------------|
| F2 - Processing parameters | |
| SI | 32768 |
| SF | 376.4715406 MHz |
| WDW | EM |
| SSB | 0 |
| LB | 5.00 Hz |
| GB | 0 |
| PC | 1.00 |

Exporting NMR spectra

NMR raw data were exported as a text file from the Xwinnmr program by either commands “smail” or “tojdx”. The Xwinnmr command “smail” offers an easy way to send data by email.

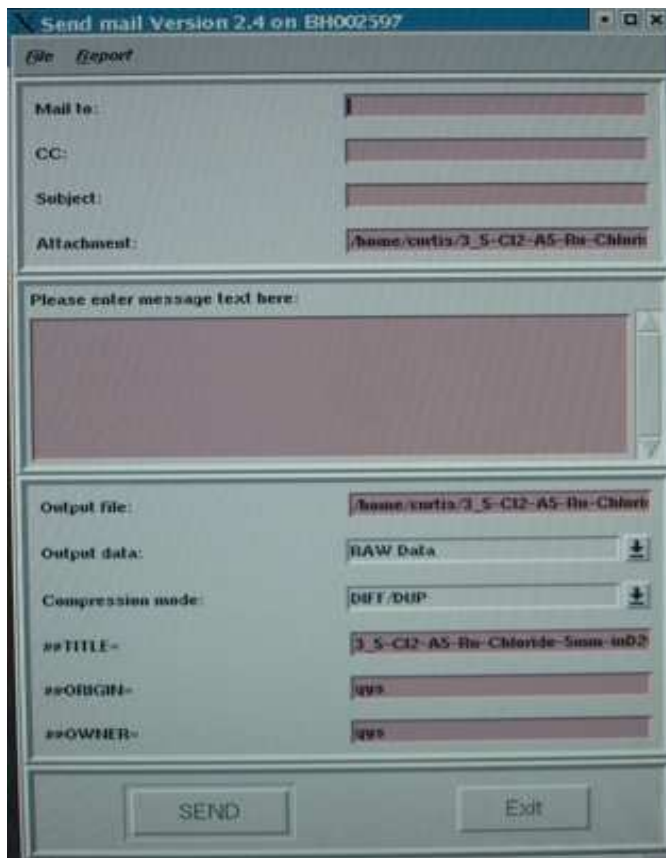


Figure 2-3. the “smail” window

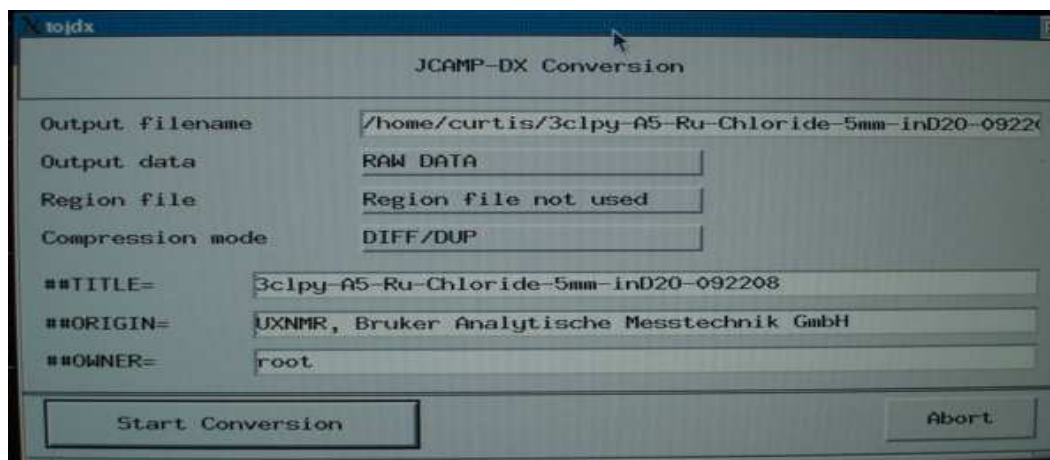
To use this utility,

1. start the Xwinnmr program
2. go to the data set you want to send (e.g. with “search” command)
3. type “smail”
4. enter the email address in the field Mail to
5. click on the field Output data, enter the data mode (see “tojdx” command for more details)
6. optionally fill out the fields message, subject and CC1
7. click on “send”

Note: When typing the file name, no spaces are allowed (otherwise, raw data exporting will fail).

The other method is to type “tojdx”. This command works similarly to “smail”. The only difference is the destination of the raw data text file. The data text file is received by email when using “smail” while it is saved on the pc if one executes “tojdx”.

Figure 2-4. the “tojdx” window



To use the tojdx utility,

1. start the Xwinmr Program
2. go to the data set you want to send (use the “search” command)
3. type “tojdx”
4. input the parameters as follows,

output file: name of the output file

output type: FID, Real spectrum & complex spectrum (we use “real spectrum”)

compression mode: Fix(table format), Packed(no spaces between y values), squeezed(sign coded into the first digit of the value, no spaces), Diff/Dup (coding the differences of subsequent values in the squeezed format with compression of repeated values) (we use “Fix” mode)

Title: the text specified here appears as ##TITLE=... in the output file. The processing parameter TI is taken as default. If TI is not specified, the current data set parameter NAME is used.

Origin: The text specified here appears as ##ORIGIN=... in the output file.

Owner: The text specified here appears as ##OWNER=... in the output file.

On the receiving end, the Internet Explorer (IE) web browser was used to open the output data file which was then further processed using Wordpad, Excel and Sigmaplot before it was ready to be imported to the Peakfit program. The detailed procedure was as follows,

1. Open the data file by using IE web browser
2. Copy and paste all data to Wordpad and save as MS-DOS. format file

3. Open Excel and import the text file from step 2 →choose “Delimited” as the original data type→select “tab” and “space” for delimiters→copy all the spectrum x y points. Do not include unnecessary information such as NMR parameters. We only need the spectrum data in order to regraph the NMR spectrum in the Peakfit program. Eight columns (the first column is data for the X axis; the rest of the columns are all data for the Y axis) will be generated if using “sma1” or “tojdx” command.

Finally, all 8 useful columns are copied to a new worksheet of Sigmaplot. The data points in the first column have to be transformed within Sigmaplot into Hz units using a transformation file. The following is an example of the transformation file,

```
col(1)=((col(1)-Di)*((RP-LP)/(Df-Di)))+LP
RP=214
LP=-4156
Di=16384
Df=6
```

“Col” stands for column. “(1)” refers to the first column. “RP”: the far right point of X data from the original NMR spectrum in Xwinnmr. “LP”: the far left point of X data from the original NMR spectrum in Xwinnmr. “Di”: value the first data point in the first column. “Df”: value of the last data point in the first column. The values of “RP”,

“LP”, “Di” and “Df” can be obtained from the output file generated by “sma1l” or “tojdx” command.

More copy and paste work was done to place all X data in column 1 and all Y data in column 2. Then these two columns were copied and saved in Wordpad as an MS-DOS file for export to the SPSS “Peakfit” program. A graph of intensity vs. – Hz can be plotted in Sigmaplot using X (-Hz) and Y (intensity) data.

Using the Peakfit Program for Spectral Analysis

After the raw NMR spectral data were obtained, it was necessary to use the SPSS Peakfit program (version 4.12 for Windows) to obtain the best-fit peak positions and line widths for the self-exchange rate calculations. The procedure for using Peakfit program was as follows,

1. Open the Peakfit program. Click “import” under the file menu or  to select the two-column text file which was saved in the previous step in Wordpad.
2. Use Peakfit’s non-parametric digital filter to reduce the number of final data points for fitting (2000-5000). This produces a smaller table that can be more rapidly fitted.
3. Click the  button and choose the best fitted baseline. (It’s very important to set a good baseline because this will affect the final fitting of the spectrum and the linewidths which will be used to calculate the self-exchange rate.)
4. Click the  button (Autofit peaks | Residuals. This is the most basic of the options since it first identifies peaks by identifying local maxima in a smoothed data stream.).

5. The program will generate a rough fit for the NMR spectrum as shown in Figure 2-5. The peak type for the fitting should be “Lorentzian Area”. The “vary width” should be selected in order to change the width of each peak.
6. Move the dots on the peak (one on the top of the peak, two on the half height, see Figure 2-5) to adjust peak height and width until the two lines (the yellow line is the actual spectrum and the white line is the fitting line) fitted the best in the top graph.
7. Click the  button and the program will then perform a least-squares graphic fitting.

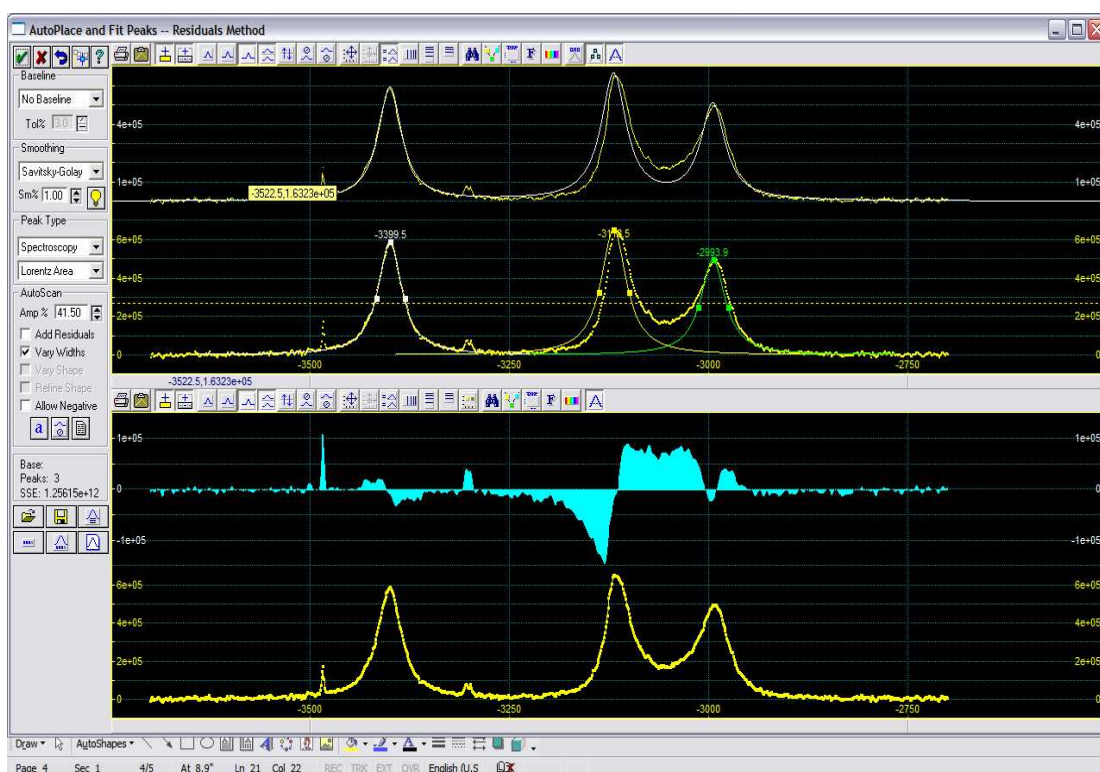


Figure 2-5. Rough fitting performed by the Peakfit program after clicking the “Autofit peaks I Residuals” button.

8. Click “Review fit” and then select “Numeric”. The program will then display the analysis results. Table 2-7 is an example of the Peakfit numerical result output.

Table 2-7. Sample Peakfit numerical result output

Description: C:\Documents and Settings\Angela\My Documents\thesis\4-Clpy 4-Brpy 3-Phpy 100608\4c
 File Source: c:\documents and settings\angela\my documents\thesis\4-Clpy 4-Brpy 3-Phpy 100608\4-Clpy-a5-ruiii-cl3-first-5.0mM-ind2o-100608 ready for pf.txt

Fitted Parameters

| r ² | Coef Det | DF | Adj r ² | Fit Std Err | F-value |
|----------------|--------------|------------|--------------------|-------------|-----------|
| 0.99593732 | 0.99592508 | 10405.5935 | | 10405.5935 | 1.222e+05 |
| Peak | Type | a0 | a1 | a2 | |
| 1 | Lorentz Area | 3.177e+07 | -2980.4437 | 5.81106822 | |

Measured Values

| Peak | Type | Amplitude | Center | FWHM | Asym50 | FW Base |
|------|--------------|-------------|------------|------------|------------|----------|
| 1 | Lorentz Area | 1.7402e+06 | -2980.4437 | 11.6221364 | 1.00000000 | |
| | Asym10 | 38.7404548 | 1.00000000 | | | |
| Peak | Type | Anlytc Area | % Area | Int Area | % Area | Centroid |
| 1 | Lorentz Area | 3.177e+07 | 100.000000 | 3.1534e+07 | 100.000000 | - |
| | Moment2 | 2980.5966 | 1830.71892 | | | |
| | Total | 3.177e+07 | 100.000000 | 3.1534e+07 | 100.000000 | |

Parameter Statistics

Peak 1 Lorentz Area

| Parm | Value | Std Error | t-value | 95 |
|------|------------|------------|------------|-----------------------|
| Area | 3.177e+07 | 88988.3608 | 357.009920 | 3.1595e+07 3.1944e+07 |
| Ctr | -2980.4437 | 0.01627701 | -1.831e+05 | -2980.4757 -2980.4118 |
| Wid | 5.81106822 | 0.02301923 | 252.444051 | 5.76589652 5.85623993 |

Analysis of Variance

| r ² | Coef Det | DF | Adj r ² | Fit Std Err |
|----------------|----------------|------------|--------------------|-------------|
| 0.99593732 | 0.99592508 | 10405.5935 | | 10405.5935 |
| Source | Sum of Squares | DF | Mean Square | F |
| Regr | 2.6463555e+13 | 2 | 1.3231778e+13 | 122203.74 |
| Error | 1.0795155e+11 | 997 | 1.0827638e+08 | |
| Total | 2.6571507e+13 | 999 | | |

Details of Fit

| Set Convergence | State | Iterations | Minimization | Extent |
|------------------|--------------------------|------------|---------------|----------|
| 1E-6 | Converged | 8 | Least Squares | 1/1 |
| Curvature Matrix | Constraints | | | Violated |
| Sparse-Roots | 25.0000-5.00000-50.0000- | None | - None | 0 |

The numerical summary consists of the following items:

1. Fitted parameters: this section shows how good is the fit with Peakfit's four sum of squares which are r^2 coefficient of determination, a degree of freedom adjusted r^2 , the standard error for the fit and the F-statistic for the fit.
2. Measured values: this area reports amplitude, center, full width at half-maxima (FWHM), asymmetry at half-maxima (Asym 50), full width at base (FW base) and asymmetry at 10% of maxima (Asym 10) measured values. The information needed (for most cases, FWHM in Hz, see boxed area in Table 2-7) to calculate the self-exchange rate are found in this area.
3. Parameter statistics: this section is a peak by peak display of parameter statistics which are each parameter's value, standard error, t-value (parameter value/std error) and confidence limits.
4. Analysis of variance: it includes a standard analysis of variance table and also reports the r^2 coefficient of determination, the degree of freedom adjusted r^2 and the standard error for the fit.
5. Details of fit: this area includes convergence state, iterations and fit settings which are helpful for subsequently referencing how a fit was made and its success or failure relative to convergence.

Calibration of the variable temperature controller used in the NMR experiments

For accurate determination of kinetic activation parameters (*vide infra*), it is very important to know that the temperature controller/sensor of the NMR provides an accurate temperature reading of the actual temperature in the sample. Therefore, for each NMR probe, the actual sample temperature vs. the set value of the console and the reported value from the probe thermocouple must be calibrated before data

collected for real samples can be properly interpreted. A typical method for temperature calibration over the range of -20 to 50°C is to observe the chemical shift difference ($\Delta\delta$ in ppm) between the two peaks (the OH protons and protons in the methyl group, respectively, see Figure 2-6) of a standard methanol sample (Wilmad company, 99.97% CH₃OH + 0.03% of HCl). A trace amount (0.03% by volume) of concentrated aqueous hydrochloric acid was added, so that a complete collapse of the methyl group multiplet structure and sharp lines will be obtained at all temperatures. The addition of HCl does not affect the chemical shift at any temperature.⁸ Teng⁹ has given an empirical expression for the relationship between the observed $\Delta\delta$ and temperature:

$$T(^{\circ}C) = 130.00 - 29.53\Delta\delta - 23.87\Delta\delta^2 \quad 2-4$$

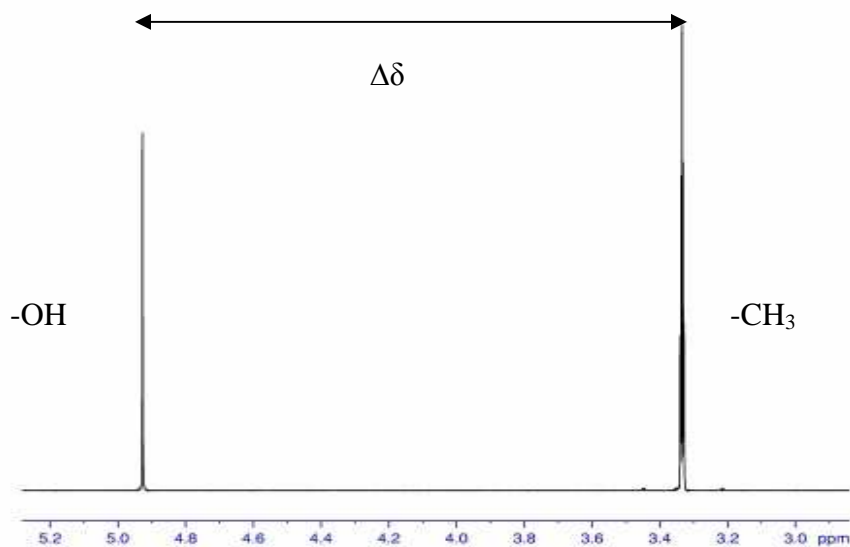


Figure 2-6. Illustration of chemical shift difference between -OH and -CH₃ in methanol

For temperature calibration over 50°C, 100% ethylene glycol should be used. Now the chemical shift difference of the two peaks has a temperature dependence given by,

$$T(^{\circ}C) = 193.0 - 101.6\Delta\delta \quad 2-5^9$$

Since the accuracy of the measurement is somewhat dependent on the line shapes of the peaks, the sample should be well-shimmed before the calibration. It is impossible to shim using the ^2H lock level by the conventional shimming method because the calibration samples do not contain any portion of deuterated solvents. Gradient shimming on ^1H is the best way to do the z shimmings.⁹ Since the instrument used in this study had no gradient capability, we simply shimmed on D_2O of the same volume (thus the height in the tube is the same) and then ran the sample with the same shimming. The thermocouple read-out temperature was obtained from the "EDTE" panel in the Xwinnmr program. The actual temperature was then calculated by Equation 2-4. Figure 2-7 and 2-8 shows the point-by-point calibration data. The Figure 2-7 data are also listed in Table 2-8.

Figure 2-7. Graph of NMR read-out temperature vs actual temperature calculated from Equation 2-4 (The regression line is shown as reference only.)

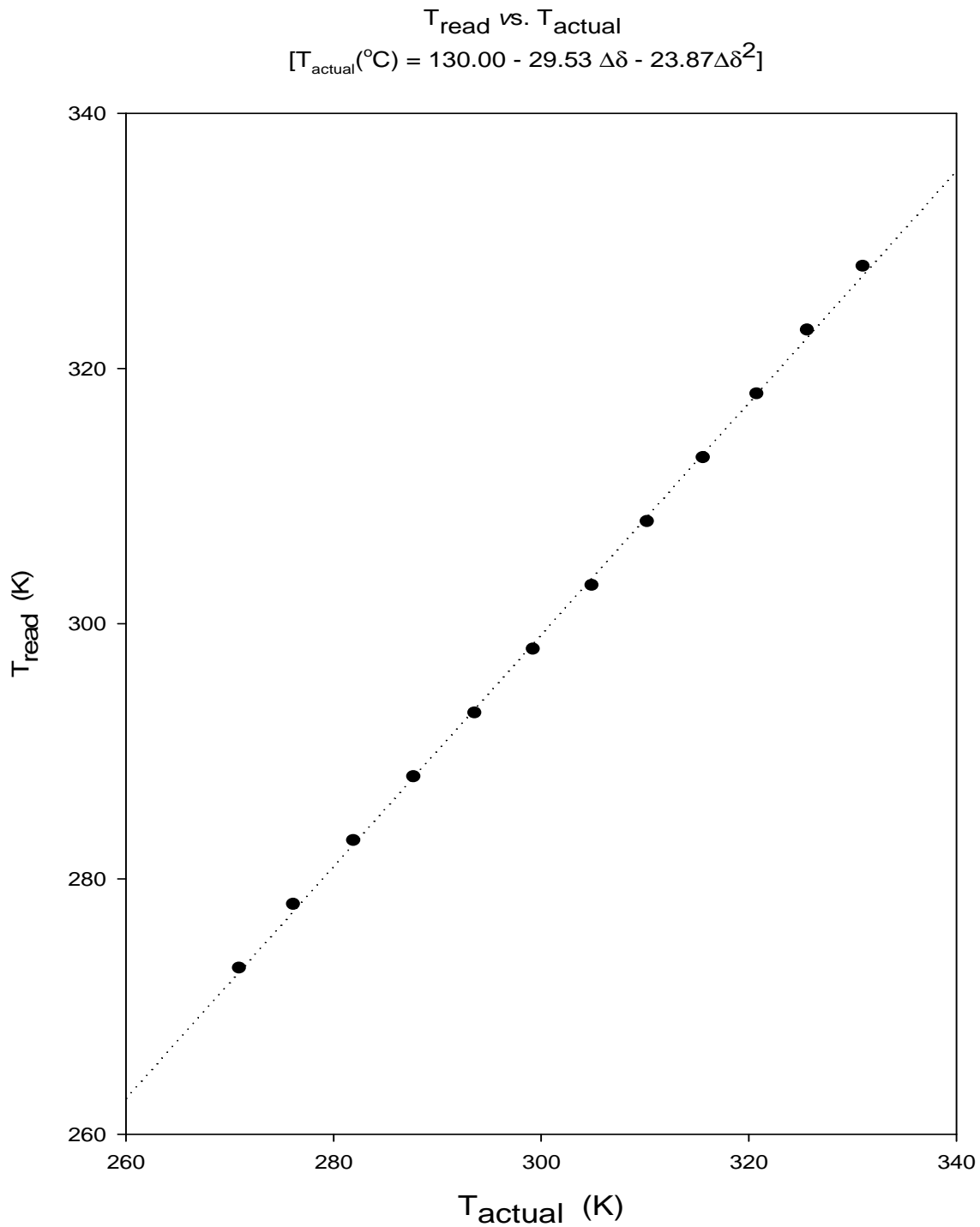


Figure 2-8. Graph of instrument temperature error, $(T_{\text{actual}} - T_{\text{read}})$ vs T_{read} (these values can be directly added to T_{read} in order to arrived at T_{actual})

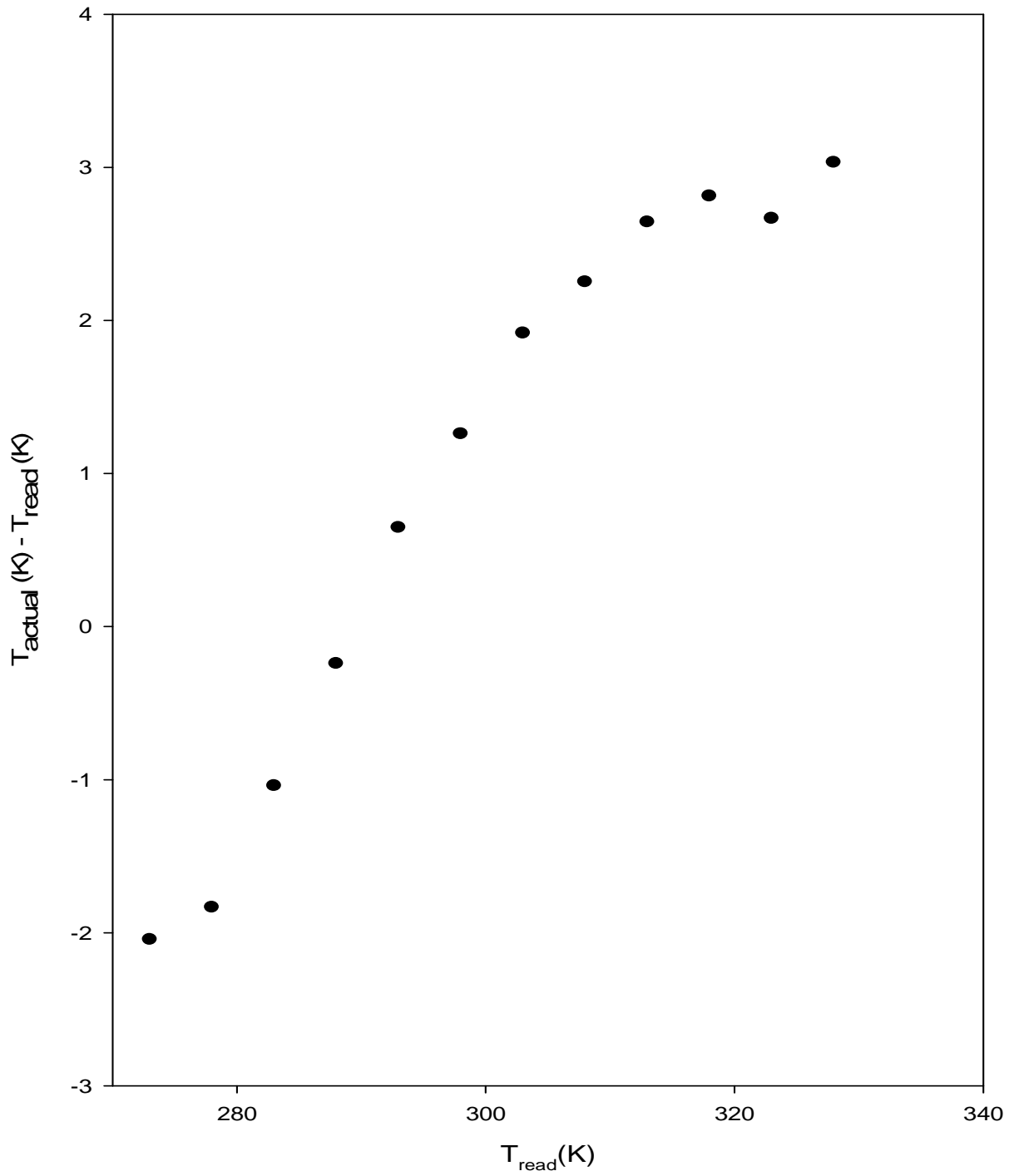


Table 2-8. NMR read-out temperature and actual temperature calibrated from Equation 2-4

| NMR Read-out Temperature | | Actual Temperature(Calibrated) | |
|--------------------------|-----|--------------------------------|-------|
| °C | K | °C | K |
| 0 | 273 | -2.0 | 271.0 |
| 5 | 278 | 3.2 | 276.2 |
| 10 | 283 | 9.0 | 282.0 |
| 15 | 288 | 14.8 | 287.8 |
| 20 | 293 | 20.6 | 293.6 |
| 25 | 298 | 26.3 | 299.3 |
| 30 | 303 | 31.9 | 304.9 |
| 35 | 308 | 37.3 | 310.3 |
| 40 | 313 | 42.6 | 315.6 |
| 45 | 318 | 47.8 | 320.8 |
| 50 | 323 | 52.7 | 325.7 |
| 55 | 328 | 58.0 | 331.0 |

From Figure 2-8, we conclude that it is indeed necessary to calibrate the temperature in the NMR because the complex functional form of the T_{actual} vs. T_{read} relationship. For convenience, we can crudely assume a linear dependence of T_{actual} on T_{read} . From the regression line in Figure 2-8, we obtain the following equation to approximately calculate the actual temperature,

$$T_{\text{actual}} = 1.1008T_{\text{read}} - 29.29 \quad 2-6$$

With Equation 2-4, a reliable first-order correction can be applied at any temperature in the range of 0°C to 55°C, but the more accurate corrections available from Figure 2-8 or Table 2-8 were used in our kinetic activation analyses.

Results and Discussion

Rates of Self-exchange Electron Transfer Reactions

Most of the rates of the electron-transfer self-exchange reactions between the pentaammine ruthenium complexes studied in this work fall into the slow-exchange region (see Chapter One Figure 1-9), and therefore the rates could be calculated by Equation 1-31. Theoretically, since Ru^{II} and Ru^{III} are equally populated, W_0 and W^* can be determined from peaks on either Ru^{II} or Ru^{III} (see Equation 1-31). In ¹H NMR however, due to the paramagnetic property of the 4d⁵ Ru^{III} complex, the proton NMR spectra of the Ru^{III} complexes are generally not observable except for some of the 4-substituted pyridine ligands such as 4-Clpy, 4-Brpy, 4-pic and 4-Phpy. See Figure 2-9(b), 2-10(b), 2-12(b), 2-13(b) and 2-14(b) for an illustration of this paramagnetic broadening effect at Ru^{III}. For the 3-substituted pyridine ligands, the proton peaks on the pyridine ring were not observable at all.

Because of the paramagnetic broadening, we made our kinetic measurements using the peaks observed for Ru^{II} species. In some cases, the Ru^{II} ¹H peaks are broadened enough by chemical exchange (in the Ru^{II/III} mixtures, see Figures 2-13(c), 2-15(b), 2-16(b), 2-23(b) and 2-24(b)) to cause significant peak overlap. In these cases the Peakfit spectral deconvolution program (Seaside Software) was used to obtain the peak widths. Figures 2-9 through Figure 2-24 show the detailed ¹H (or ¹⁹F) NMR spectra of the various Ru^{II} and/or Ru^{III} complexes alone and the 50:50 Ru^{II/III} mixture. The resulting self-exchange rates computed by equations are listed in Table 2-9.

Figure 2-9(a). ^1H NMR spectrum of $\text{A}_5\text{Ru}^{\text{II}}$ (4-Clpy) $^{2+}$ complex in D_2O , $[\text{Ru}^{\text{II}}] = 5.0$ mM

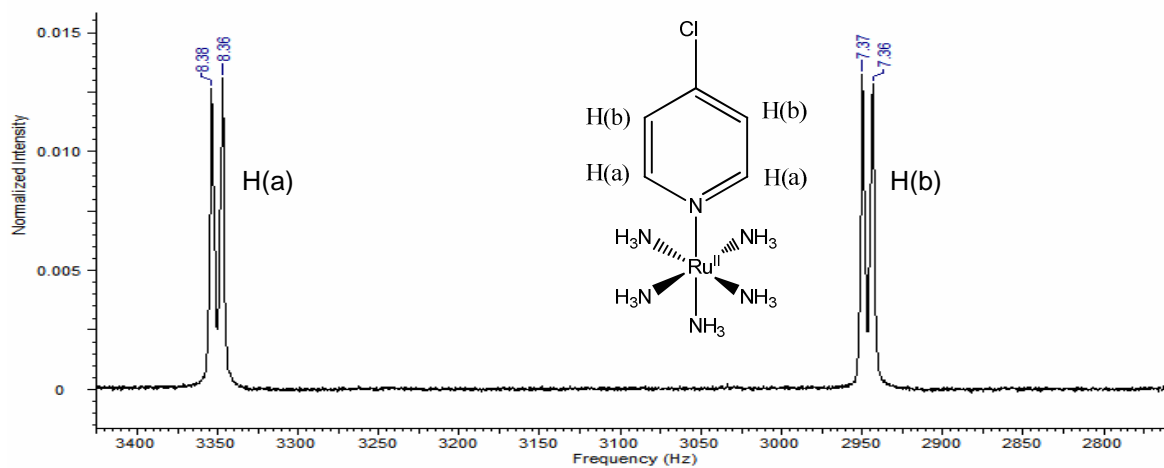


Figure 2-9(b). ^1H NMR spectrum of $\text{A}_5\text{Ru}^{\text{III}}$ (4-Clpy) $^{3+}$ complex in D_2O , $[\text{Ru}^{\text{III}}] = 5.0$ mM

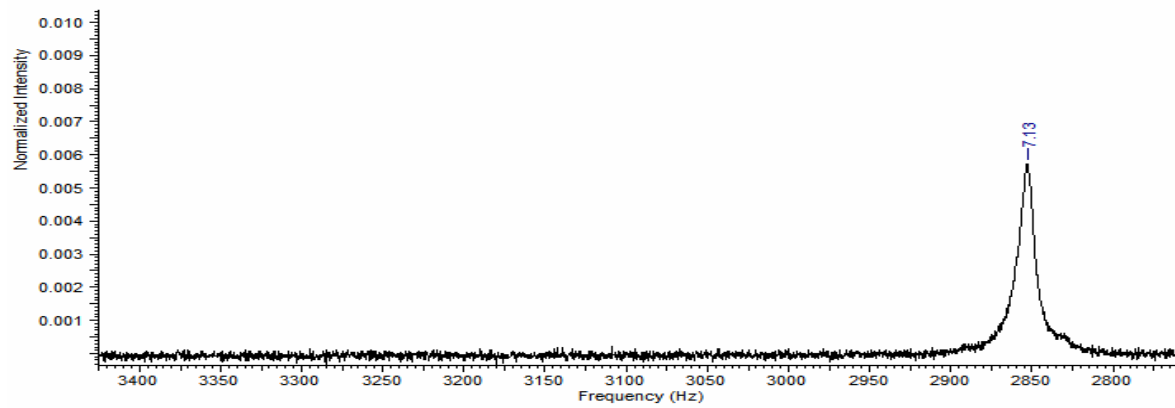


Figure 2-9(c). ^1H NMR spectrum of $\text{A}_5\text{Ru}^{\text{II/III}}$ (4-Clpy) $^{2+/3+}$ mixture in D_2O , $[\text{Ru}^{\text{II}}] = [\text{Ru}^{\text{III}}] = 5.0$ mM

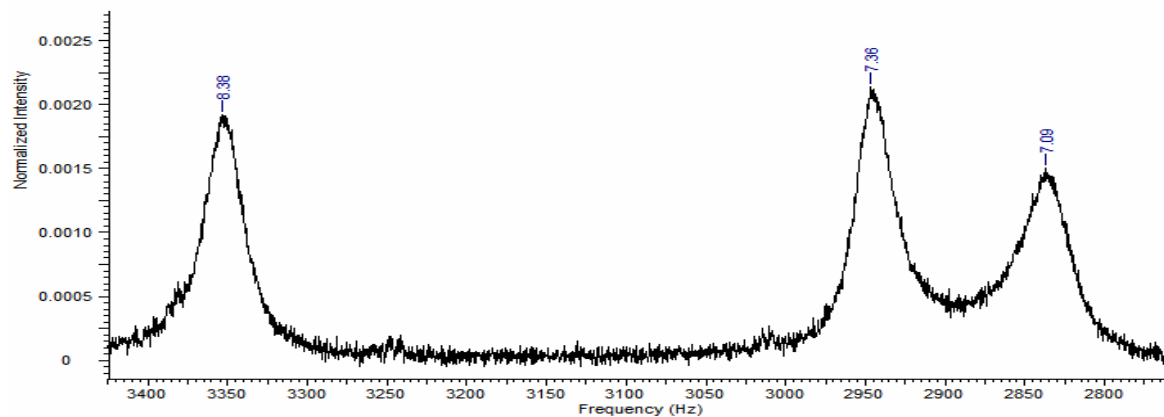


Figure 2-10(a). ^1H NMR spectrum of $\text{A}_5\text{Ru}^{\text{II}}$ (4-Brpy) $^{2+}$ complex in D_2O , $[\text{Ru}^{\text{II}}] = 5.0$ mM

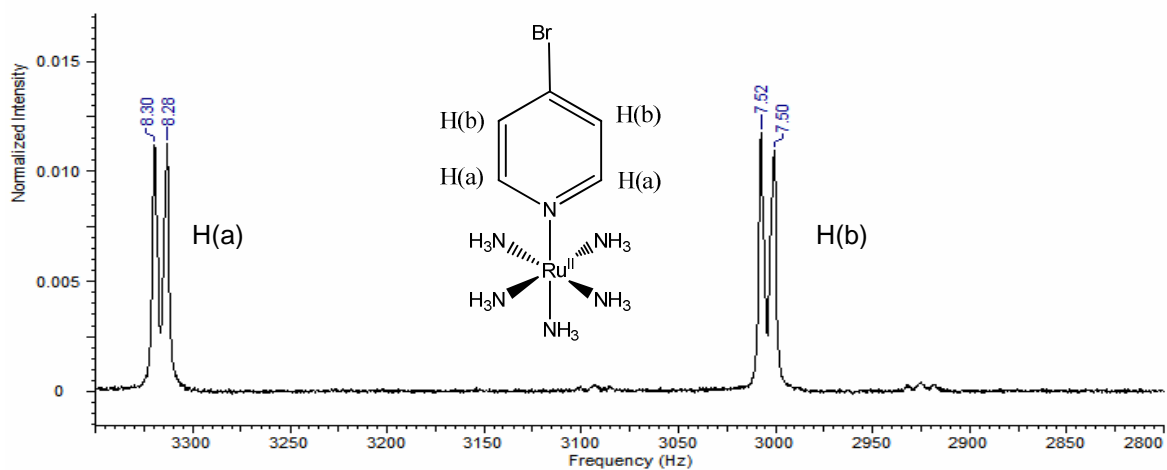


Figure 2-10(b). ^1H NMR spectrum of $\text{A}_5\text{Ru}^{\text{III}}$ (4-Brpy) $^{3+}$ complex in D_2O , $[\text{Ru}^{\text{III}}] = 5.0$ mM

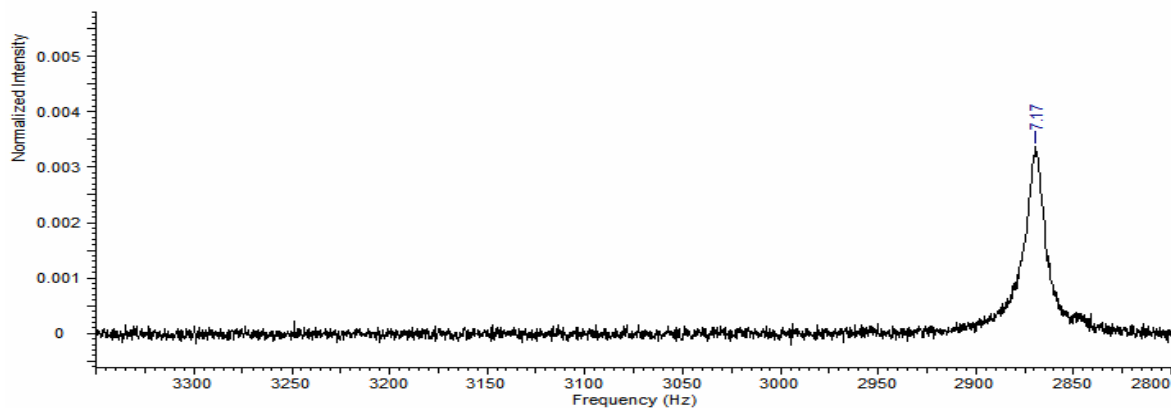


Figure 2-10(c). ^1H NMR spectrum of $\text{A}_5\text{Ru}^{\text{II/III}}$ (4-Brpy) $^{2+/3+}$ mixture in D_2O , $[\text{Ru}^{\text{II}}] = [\text{Ru}^{\text{III}}] = 5.0$ mM

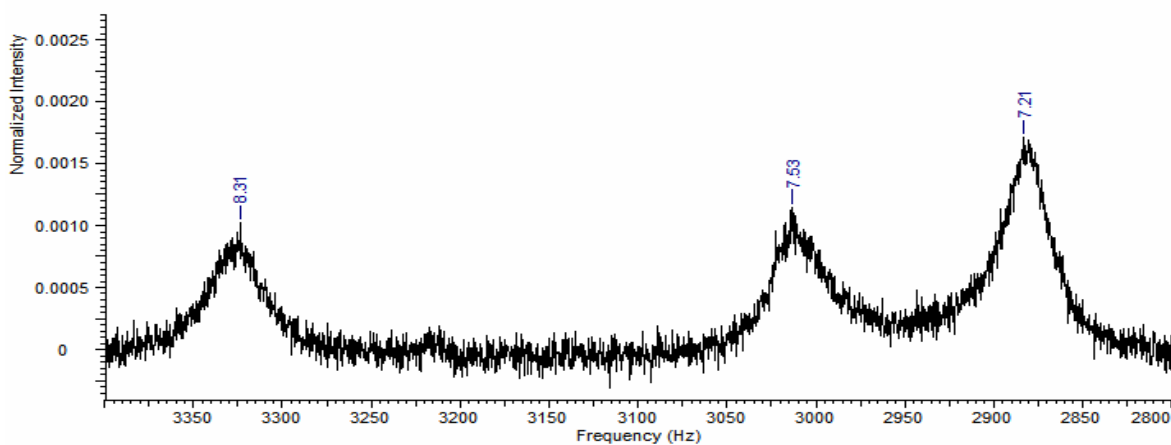


Figure 2-11(a). ^1H NMR spectrum of $\text{A}_5\text{Ru}^{\text{II}}$ (4-pic) $^{2+}$ complex in D_2O , $[\text{Ru}^{\text{II}}] = 5.0\text{mM}$

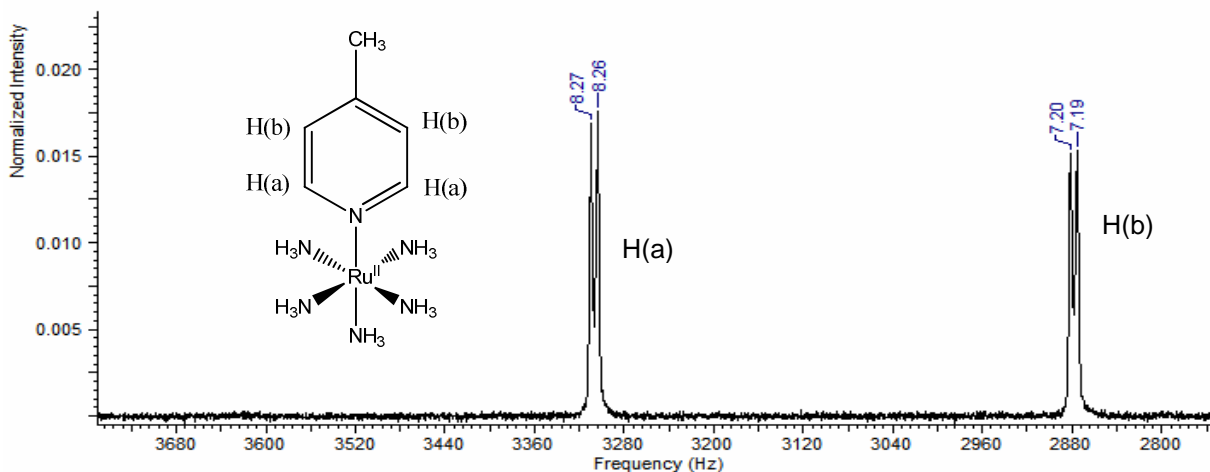


Figure 2-11(b). ^1H NMR spectrum of $\text{A}_5\text{Ru}^{\text{III}}$ (4-pic) $^{3+}$ complex in D_2O , $[\text{Ru}^{\text{III}}] = 5.0\text{mM}$

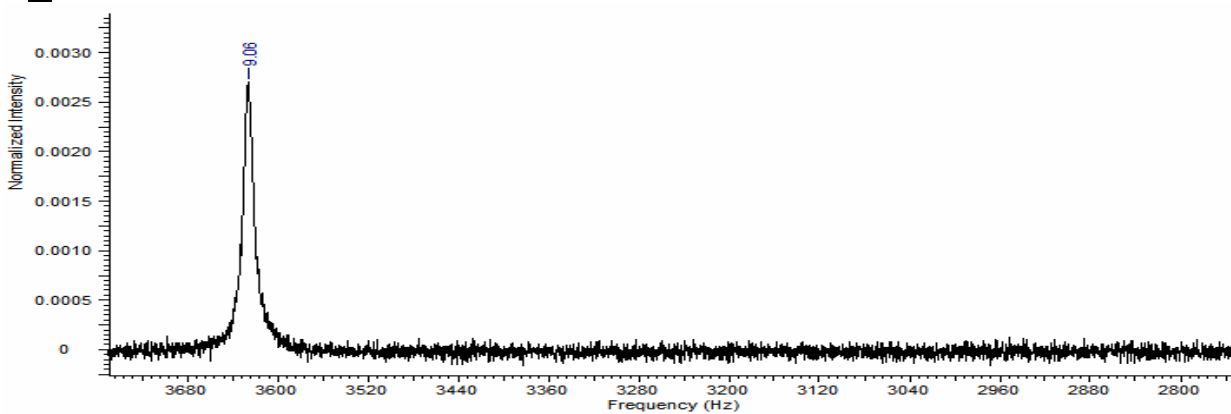


Figure 2-11(c). ^1H NMR spectrum of $\text{A}_5\text{Ru}^{\text{II/III}}$ (4-pic) $^{2+/3+}$ mixture in D_2O , $[\text{Ru}^{\text{II}}] = [\text{Ru}^{\text{III}}] = 5.0\text{mM}$

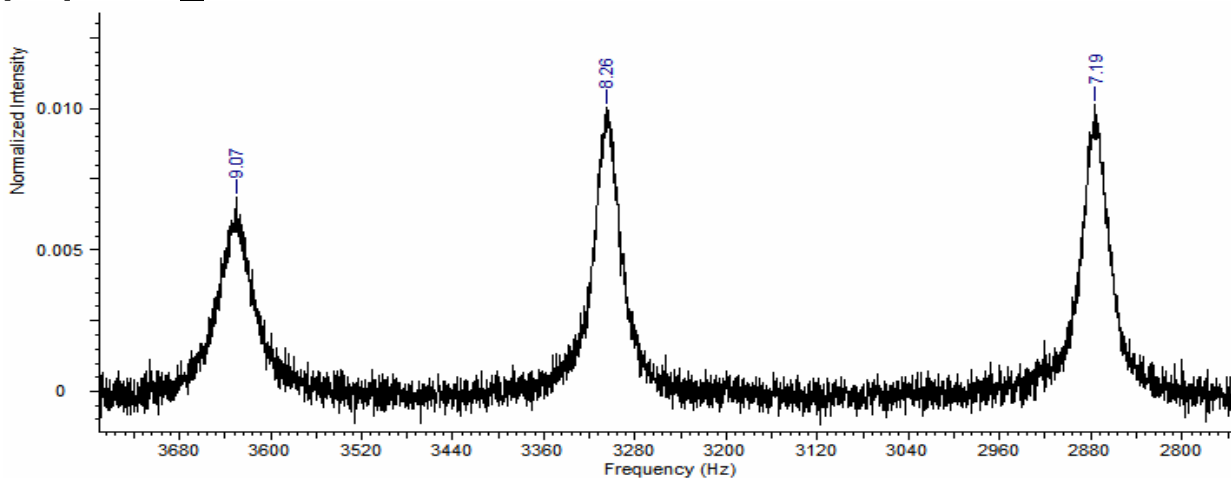


Figure 2-12(a). ^{19}F NMR spectrum of $\text{A}_5\text{Ru}^{\text{II}}$ (3-tfmpy) $^{2+}$ complex in D_2O , $[\text{Ru}^{\text{II}}] = 5.0$ mM

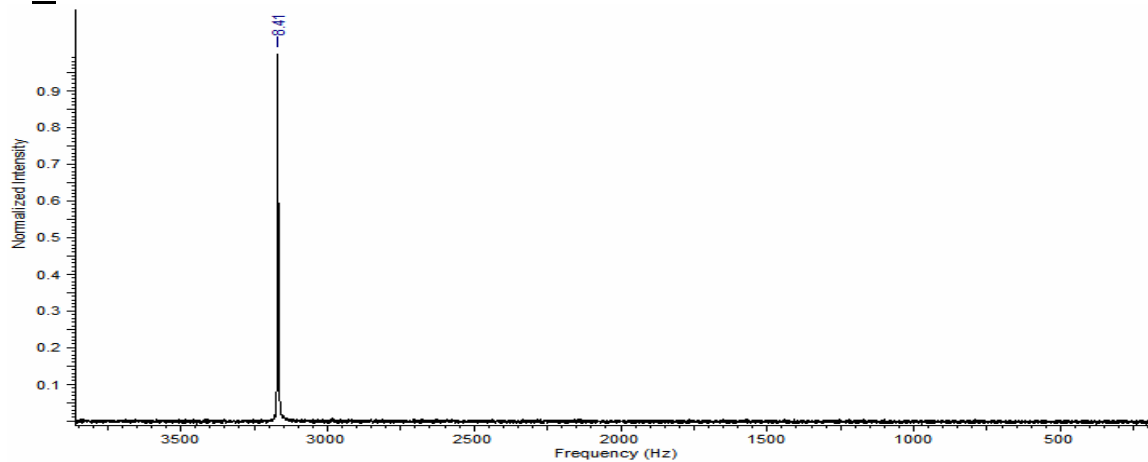


Figure 2-12(b). ^{19}F NMR spectrum of $\text{A}_5\text{Ru}^{\text{III}}$ (3-tfmpy) $^{3+}$ complex in D_2O , $[\text{Ru}^{\text{III}}] = 5.0$ mM

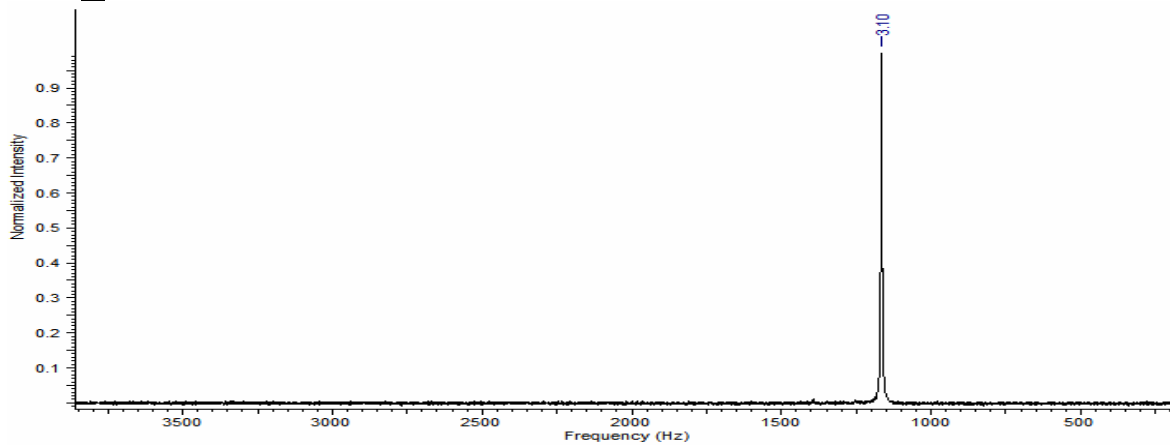


Figure 2-12(c). ^{19}F NMR spectrum of $\text{A}_5\text{Ru}^{\text{II/III}}$ (3-tfmpy) $^{2+/3+}$ mixture in D_2O , $[\text{Ru}^{\text{II}}] = [\text{Ru}^{\text{III}}] = 5.0$ mM

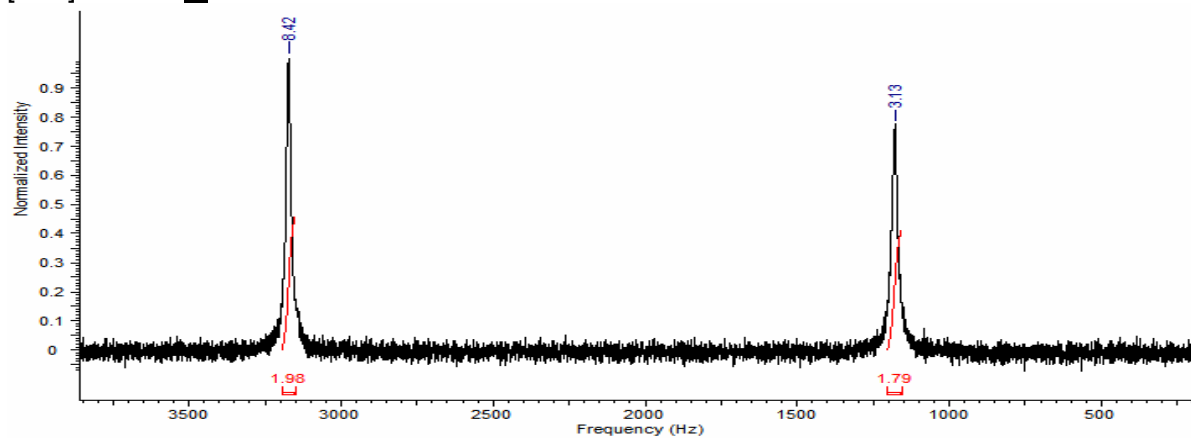


Figure 2-13(a). ^1H NMR spectrum of $\text{A}_5\text{Ru}^{\text{II}}$ (4-Phpy) $^{2+}$ complex in D_2O , $[\text{Ru}^{\text{II}}] = 5.0$ mM

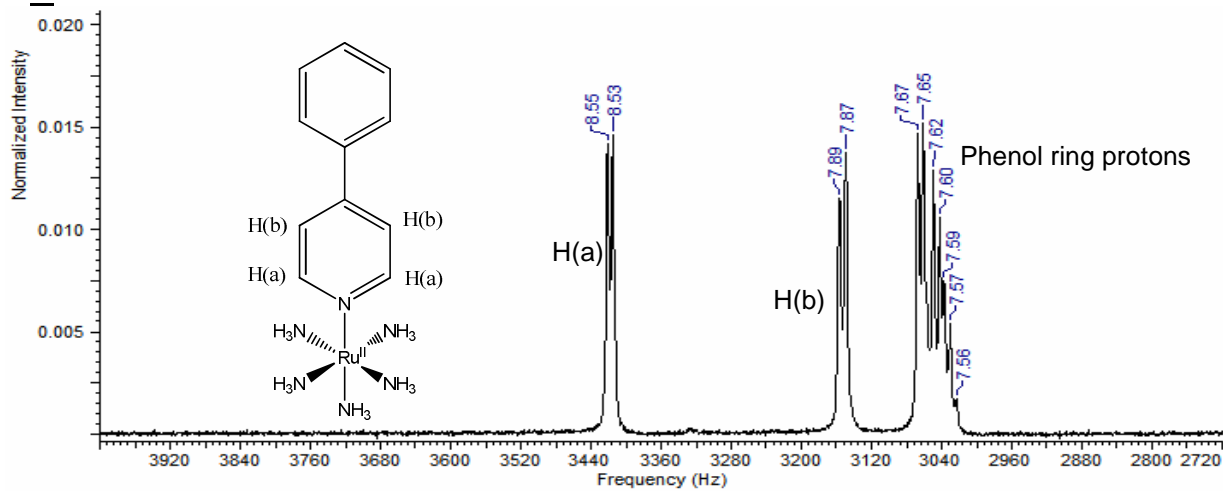


Figure 2-13(b). ^1H NMR spectrum of $\text{A}_5\text{Ru}^{\text{III}}$ (4-Phpy) $^{3+}$ complex in D_2O , $[\text{Ru}^{\text{III}}] = 5.0$ mM

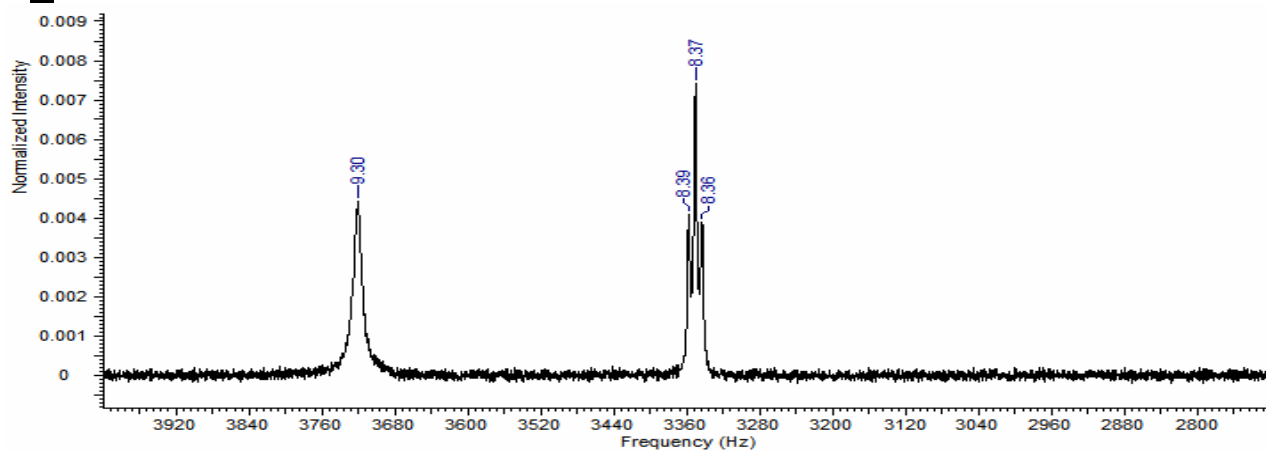


Figure 2-13 (c). ^1H NMR spectrum of $\text{A}_5\text{Ru}^{\text{II/III}}$ (4-Phpy) $^{2+/3+}$ mixture in D_2O , $[\text{Ru}^{\text{II}}] = [\text{Ru}^{\text{III}}] = 5.0$ mM

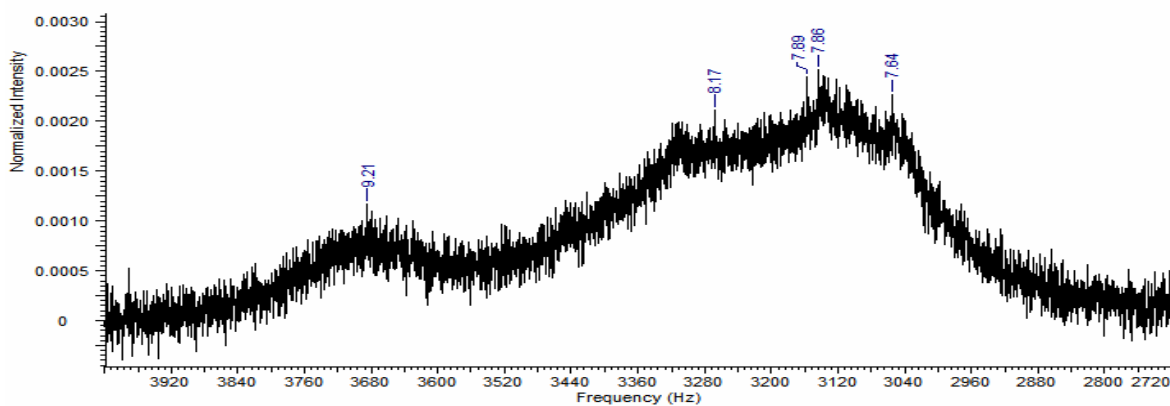


Figure 2-14(a). ^1H NMR spectrum of $\text{A}_5\text{Ru}^{\text{II}}\text{py}^{2+}$ complex in D_2O , $[\text{Ru}^{\text{II}}] = 5.0 \text{ mM}$

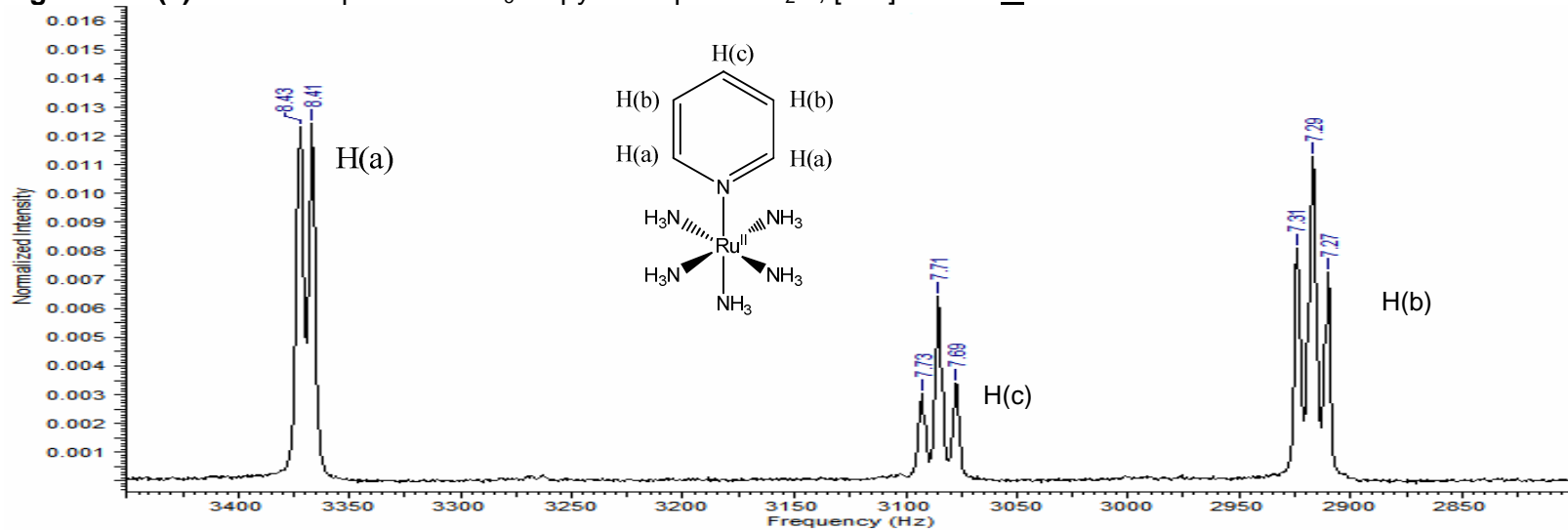


Figure 2-14(b). ^1H NMR spectrum of $\text{A}_5\text{Ru}^{\text{II/III}}\text{py}^{2+/3+}$ mixture in D_2O , $[\text{Ru}^{\text{II}}] = [\text{Ru}^{\text{III}}] = 5.0 \text{ mM}$

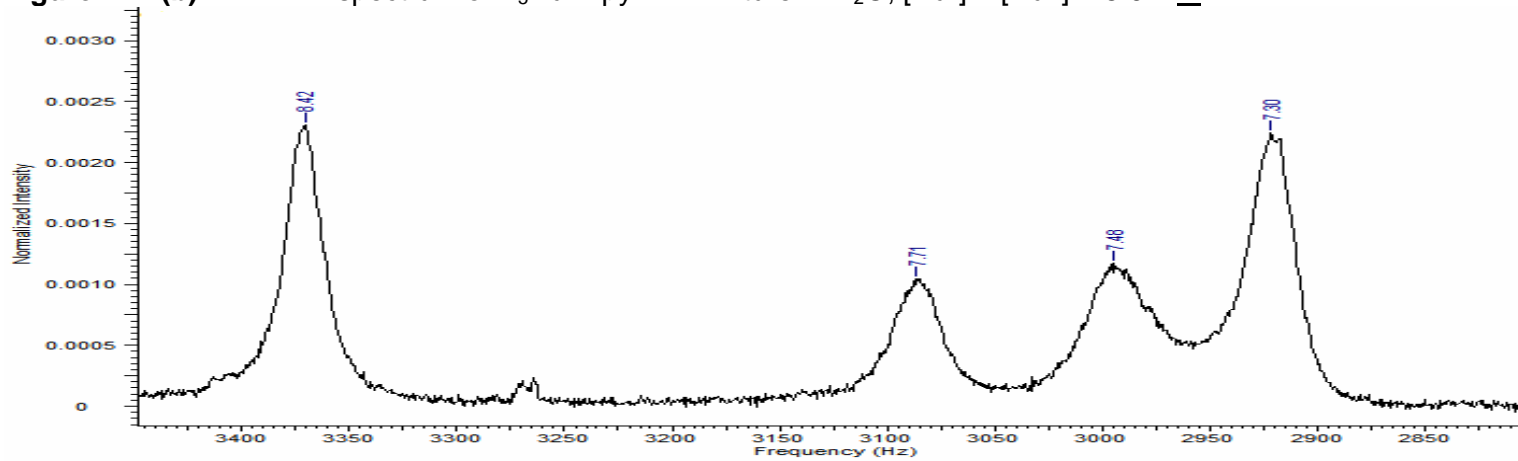


Figure 2-15(a). ^1H NMR spectrum of $\text{A}_5\text{Ru}^{\text{II}}(\text{3-Clpy})^{2+}$ complex in D_2O , $[\text{Ru}^{\text{II}}] = 5.0 \text{ mM}$

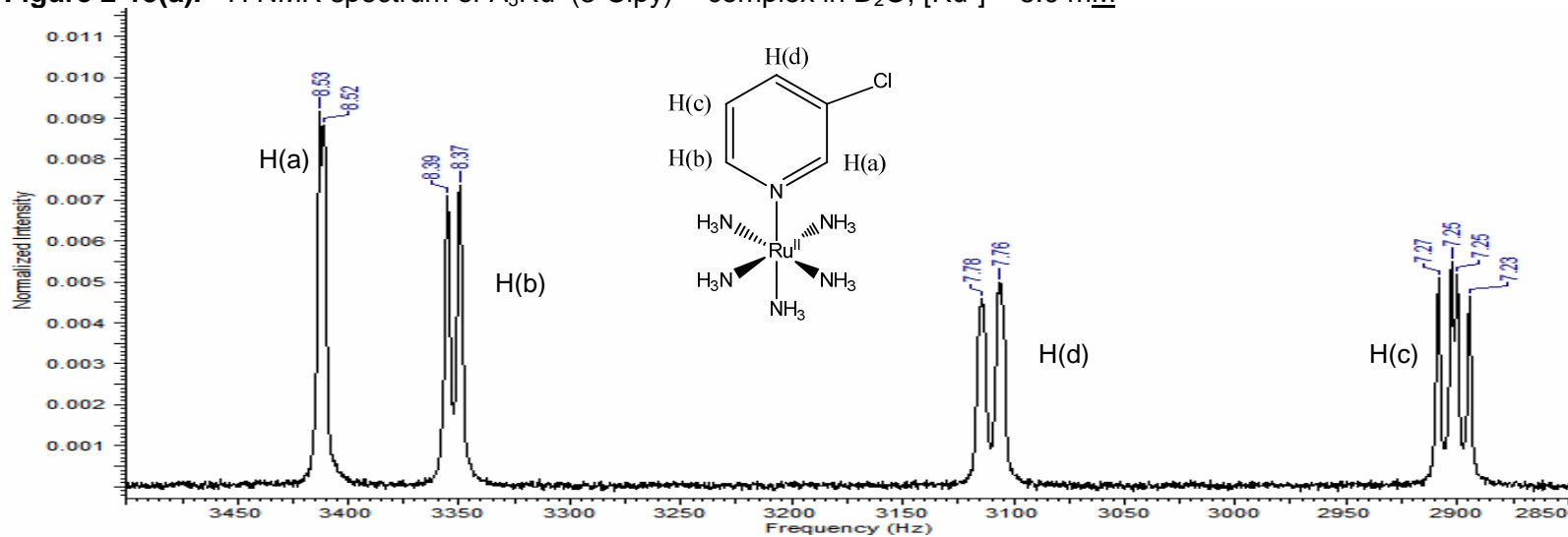


Figure 2-15(b). ^1H NMR spectrum of $\text{A}_5\text{Ru}^{\text{II/III}}(\text{3-Clpy})^{2+/3+}$ mixture in D_2O , $[\text{Ru}^{\text{II}}] = [\text{Ru}^{\text{III}}] = 5.0 \text{ mM}$

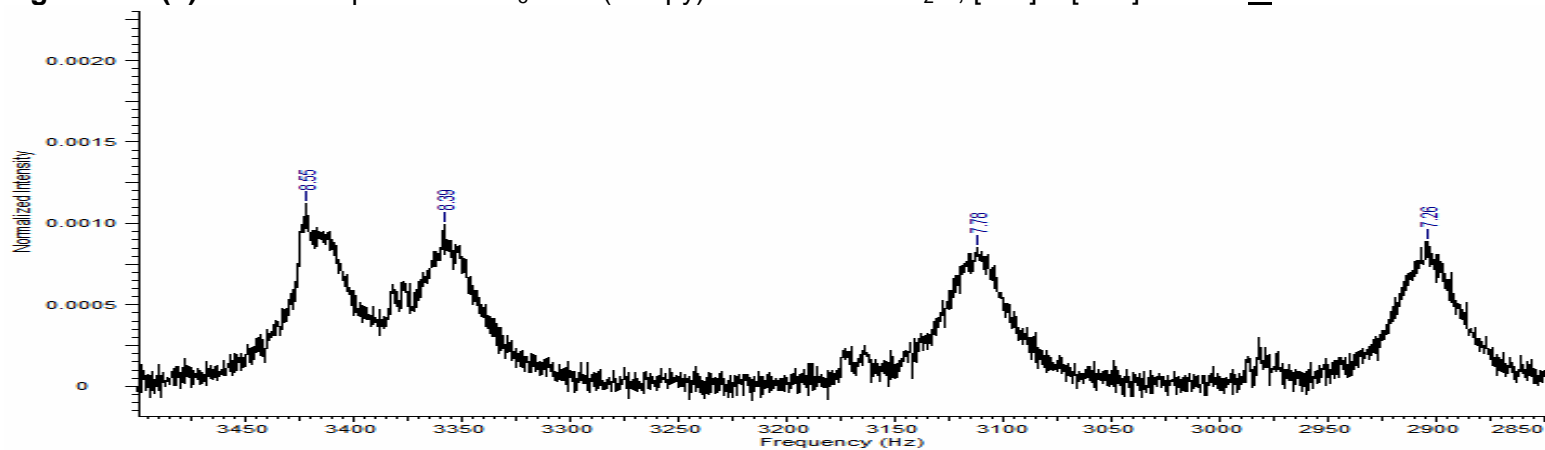


Figure 2-16(a). ^1H NMR spectrum of $\text{A}_5\text{Ru}^{\text{II}}(3\text{-Brpy})^{2+}$ complex in D_2O , $[\text{Ru}^{\text{II}}] = 5.0 \text{ mM}$

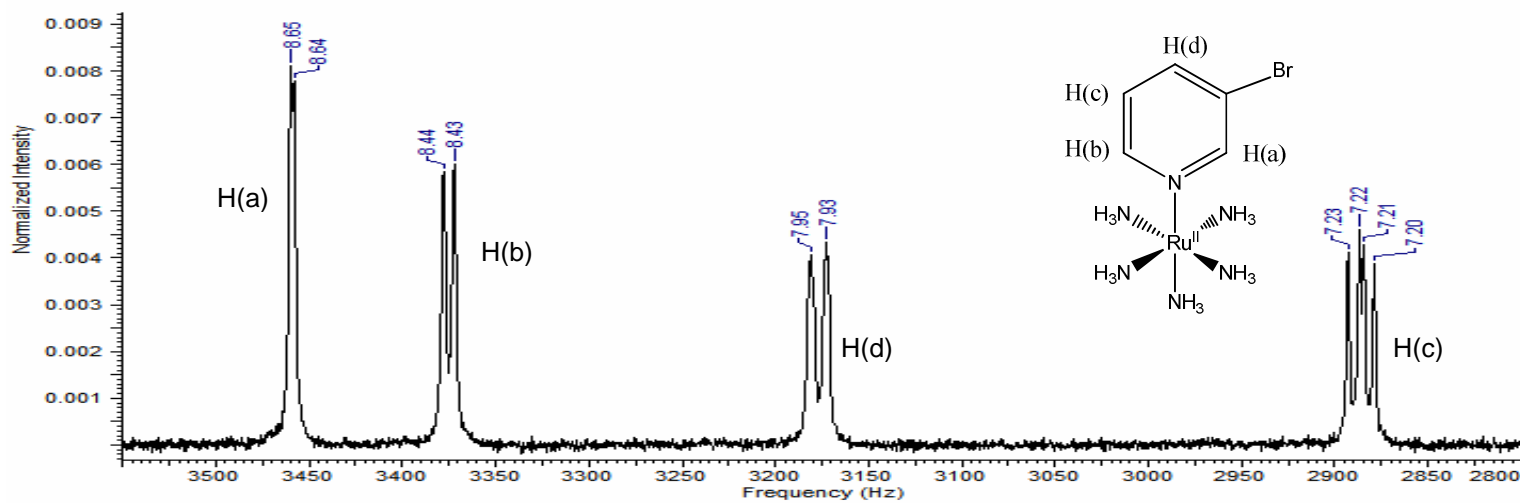


Figure 2-16(b). ^1H NMR spectrum of $\text{A}_5\text{Ru}^{\text{II/III}}(3\text{-Brpy})^{2+/3+}$ mixture in D_2O , $[\text{Ru}^{\text{II}}] = [\text{Ru}^{\text{III}}] = 5.0 \text{ mM}$

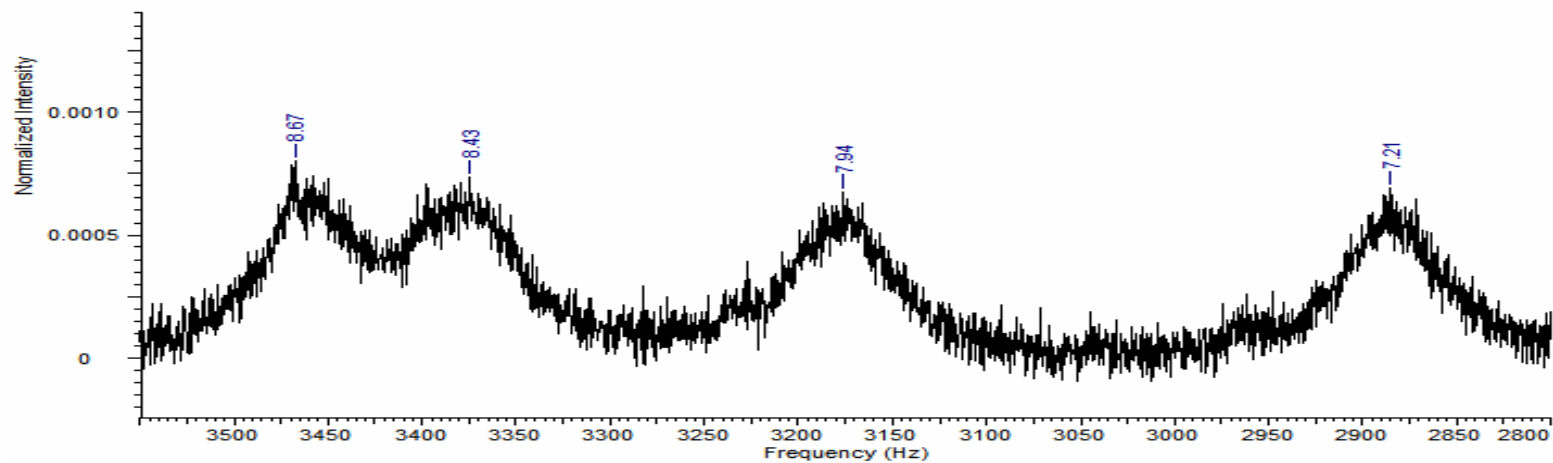


Figure 2-17(a). ^1H NMR spectrum of $\text{A}_5\text{Ru}^{\text{II}}(\text{3-Fpy})^{2+}$ complex in D_2O , $[\text{Ru}^{\text{II}}] = 5.0 \text{ mM}$

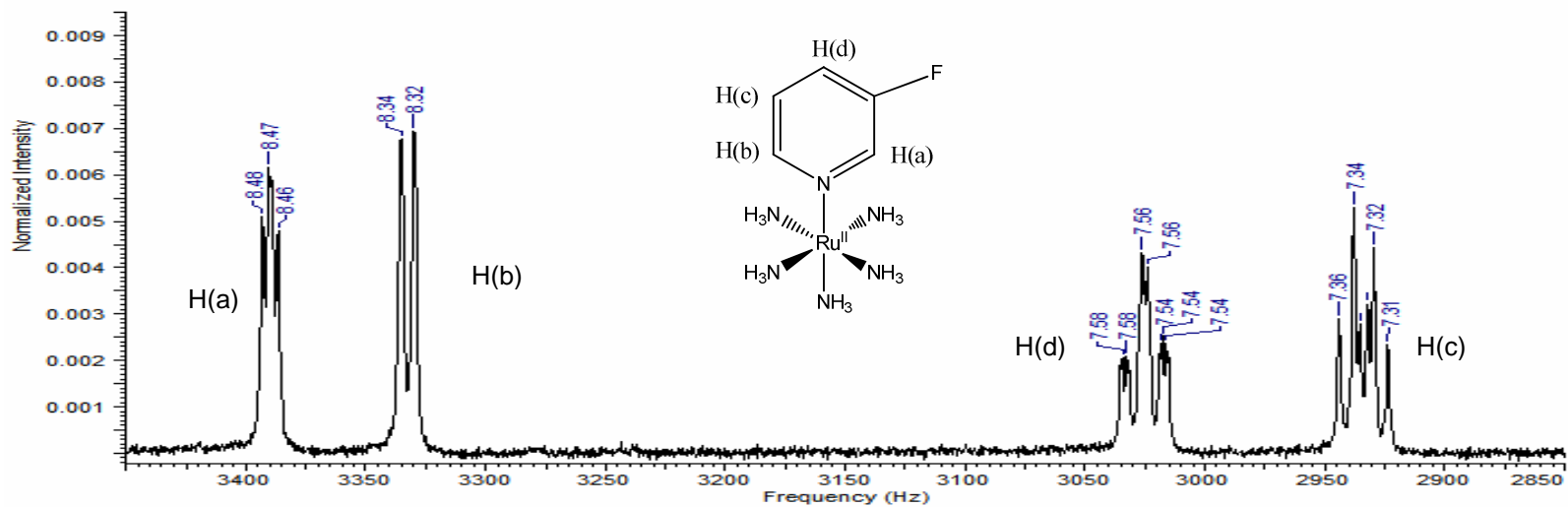


Figure 2-17(b). ^1H NMR spectrum of $\text{A}_5\text{Ru}^{\text{II/III}}(\text{3-Fpy})^{2+/3+}$ mixture in D_2O , $[\text{Ru}^{\text{II}}] = [\text{Ru}^{\text{III}}] = 5.0 \text{ mM}$

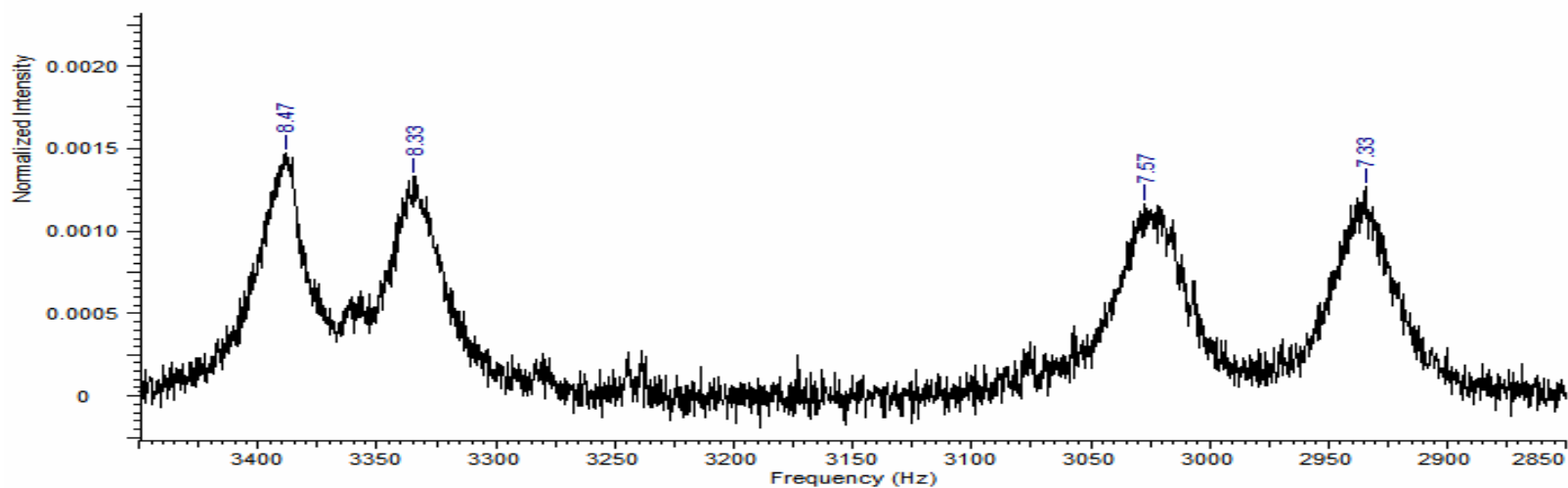


Figure 2-18(a). ^1H NMR spectrum of $\text{A}_5\text{Ru}^{\text{II}}$ (3-pic) $^{2+}$ complex in D_2O , $[\text{Ru}^{\text{II}}] = 5.0 \text{ mM}$

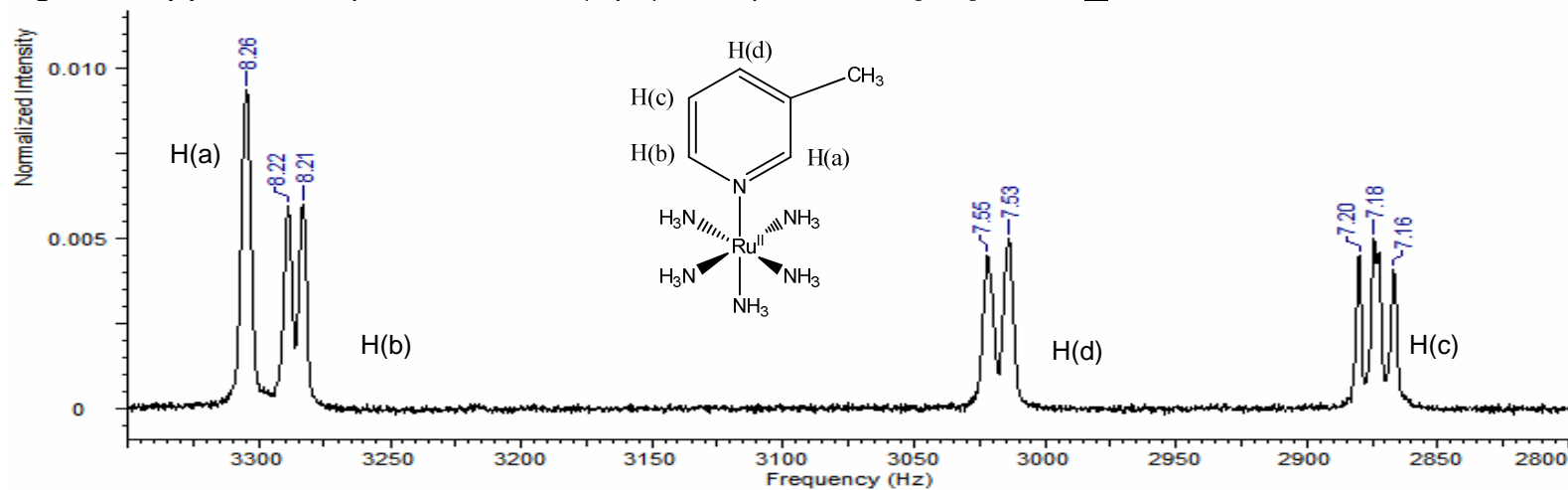


Figure 2-18(b). ^1H NMR spectrum of $\text{A}_5\text{Ru}^{\text{II/III}}$ (3-pic) $^{2+/3+}$ mixture in D_2O , $[\text{Ru}^{\text{II}}] = [\text{Ru}^{\text{III}}] = 5.0 \text{ mM}$

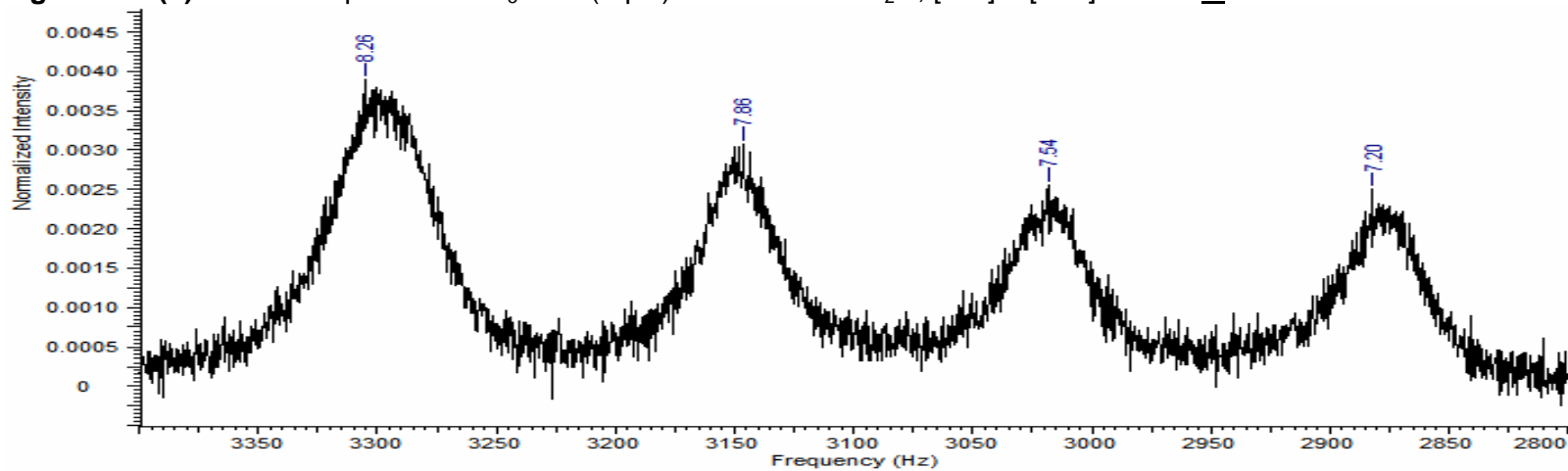


Figure 2-19(a). ^1H NMR spectrum of $\text{A}_5\text{Ru}^{\text{II}}$ (3-Etpy) $^{2+}$ complex in D_2O , $[\text{Ru}^{\text{II}}] = 5.0 \text{ mM}$

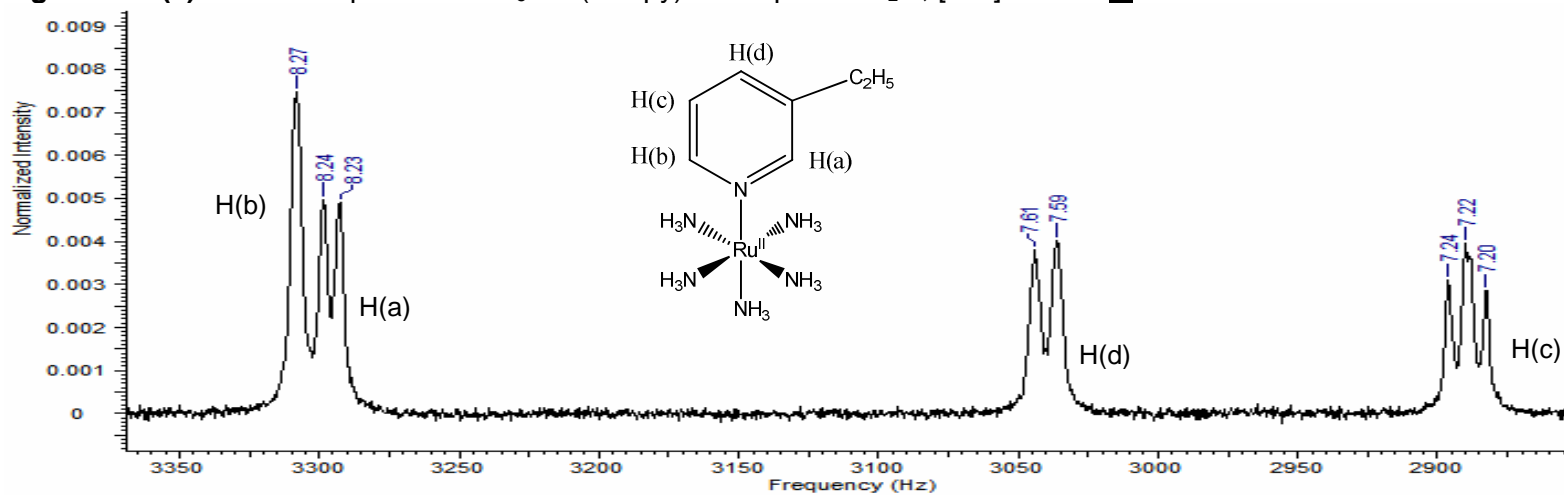


Figure 2-19(b). ^1H NMR spectrum of $\text{A}_5\text{Ru}^{\text{II/III}}$ (3-Etpy) $^{2+/3+}$ mixture in D_2O , $[\text{Ru}^{\text{II}}] = [\text{Ru}^{\text{III}}] = 5.0 \text{ mM}$

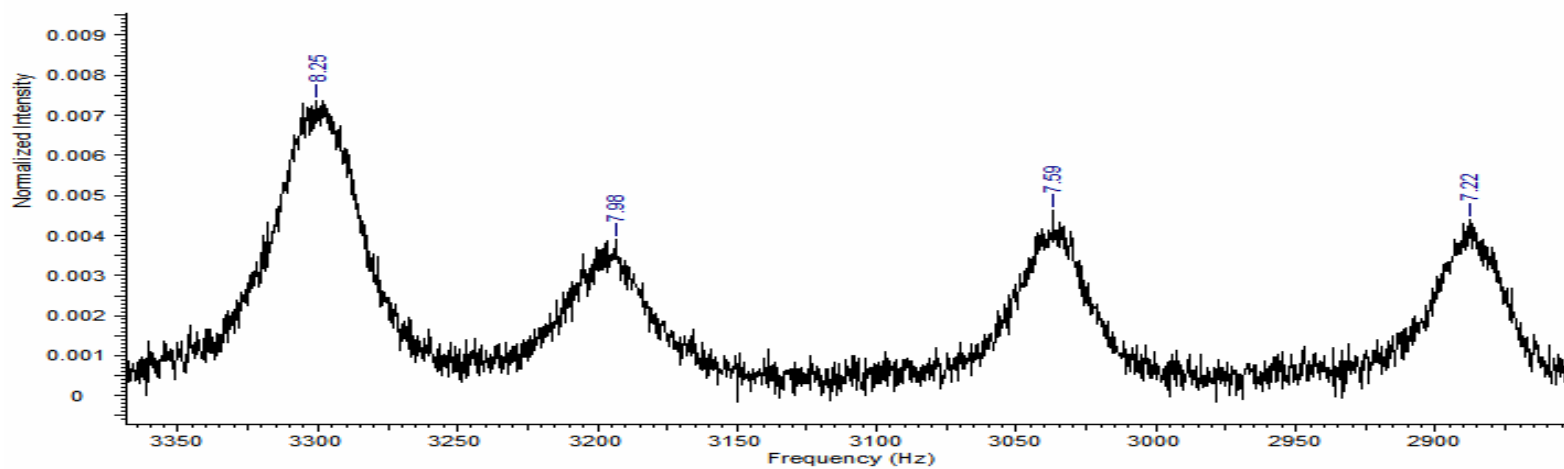


Figure 2-20(a). ^1H NMR spectrum of $\text{A}_5\text{Ru}^{\text{II}}$ (3,5- Cl_2py) $^{2+}$ complex in D_2O , $[\text{Ru}^{\text{II}}] = 5.0 \text{ mM}$

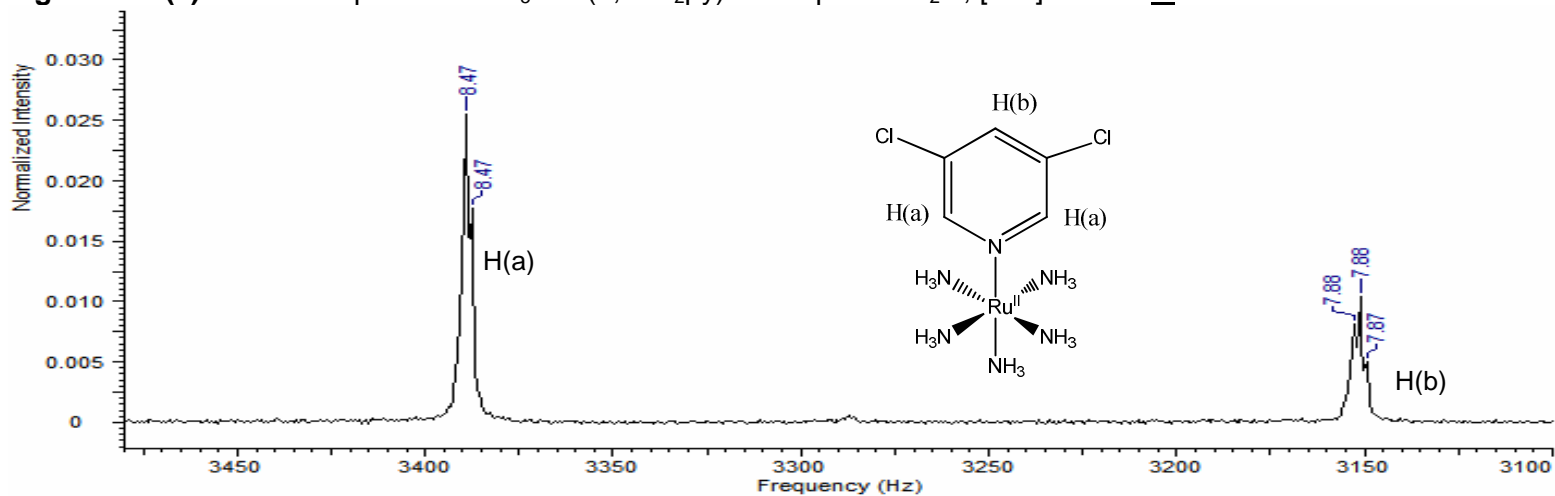


Figure 2-20(b). ^1H NMR spectrum of $\text{A}_5\text{Ru}^{\text{II/III}}$ (3,5- Cl_2py) $^{2+/3+}$ mixture in D_2O , $[\text{Ru}^{\text{II}}] = [\text{Ru}^{\text{III}}] = 5.0 \text{ mM}$

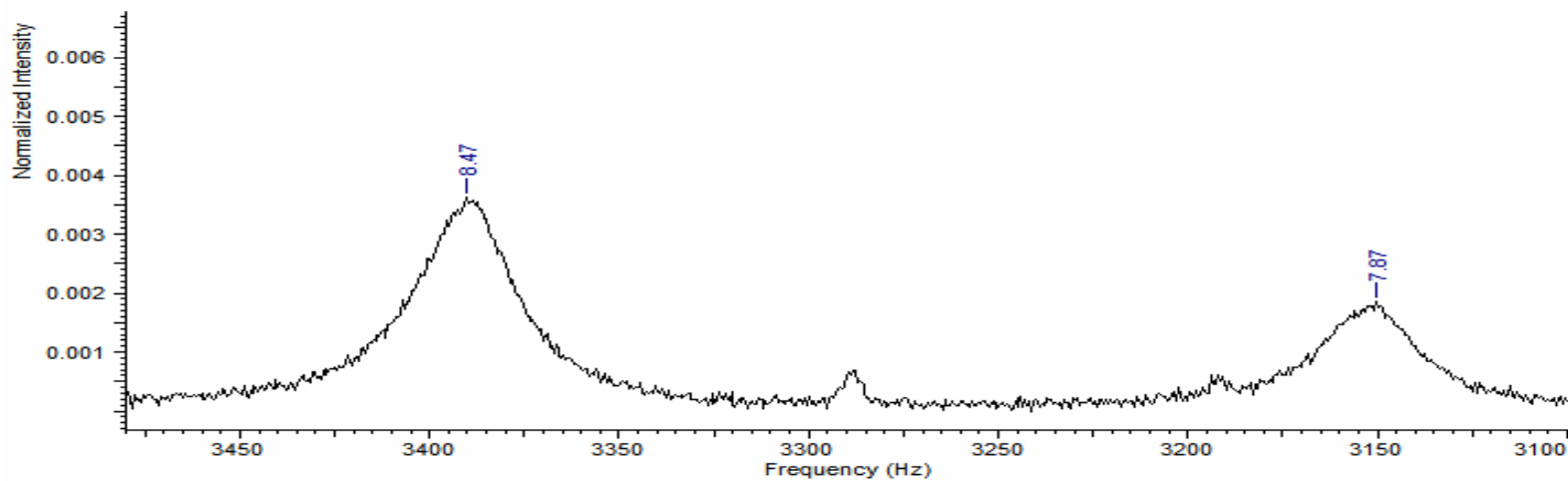


Figure 2-21(a). ^1H NMR spectrum of $\text{A}_5\text{Ru}^{\text{II}}(3,5\text{-Br}_2\text{py})^{2+}$ complex in D_2O , $[\text{Ru}^{\text{II}}] = 5.0 \text{ mM}$

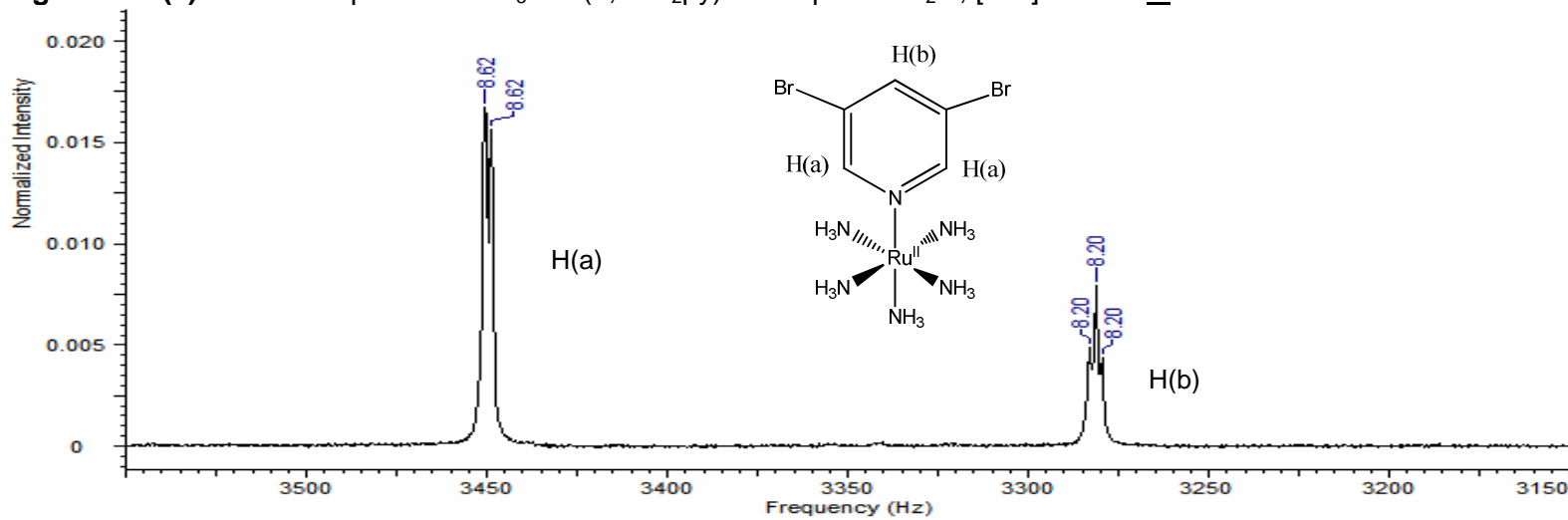


Figure 2-21(b). ^1H NMR spectrum of $\text{A}_5\text{Ru}^{\text{II/III}}(3,5\text{-Br}_2\text{py})^{2+/3+}$ mixture in D_2O , $[\text{Ru}^{\text{II}}] = [\text{Ru}^{\text{III}}] = 5.0 \text{ mM}$

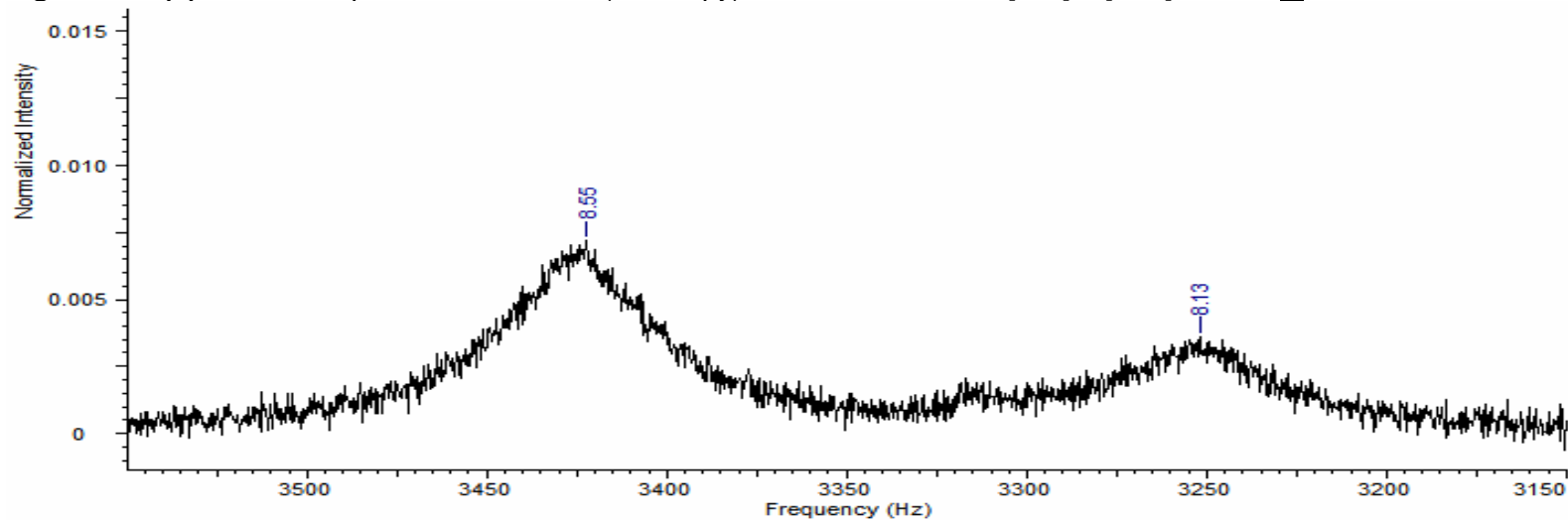


Figure 2-22(a). ^1H NMR spectrum of $\text{A}_5\text{Ru}^{\text{II}}$ (3,5-Me₂py)²⁺ complex in D₂O, $[\text{Ru}^{\text{II}}] = 5.0 \text{ mM}$

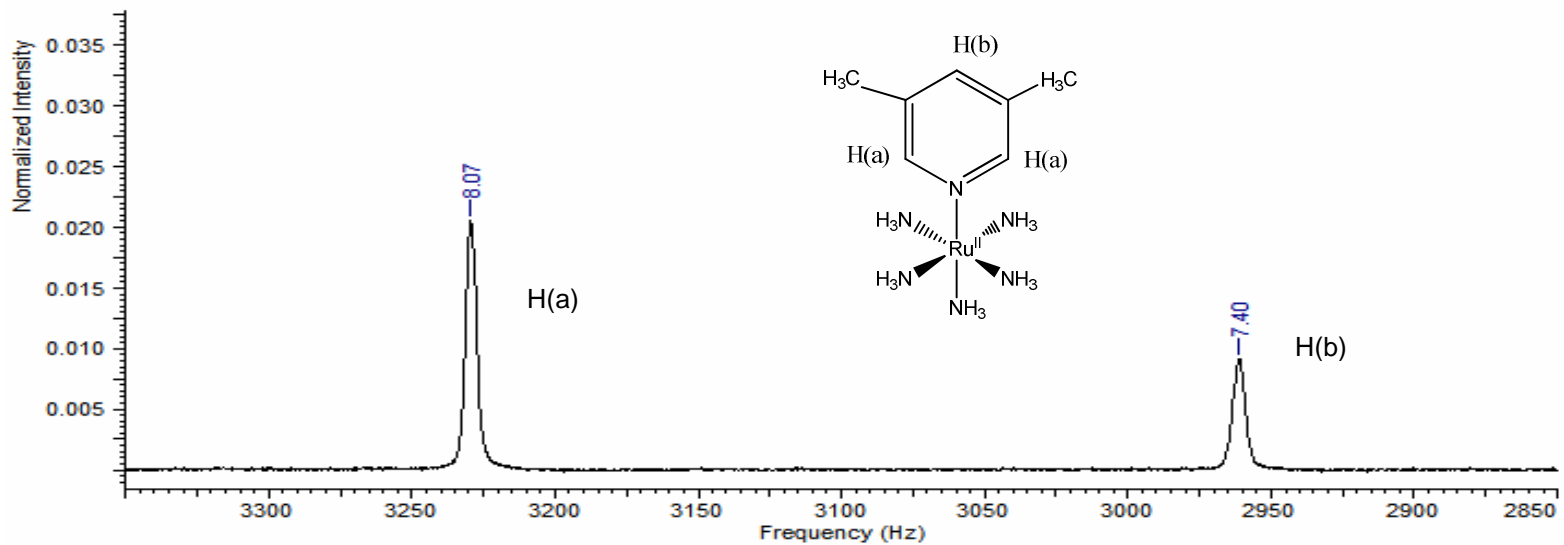


Figure 2-22(b). ^1H NMR spectrum of $\text{A}_5\text{Ru}^{\text{II/III}}$ (3,5-Me₂py)^{2+/3+} mixture in D₂O, $[\text{Ru}^{\text{II}}] = [\text{Ru}^{\text{III}}] = 5.0 \text{ mM}$

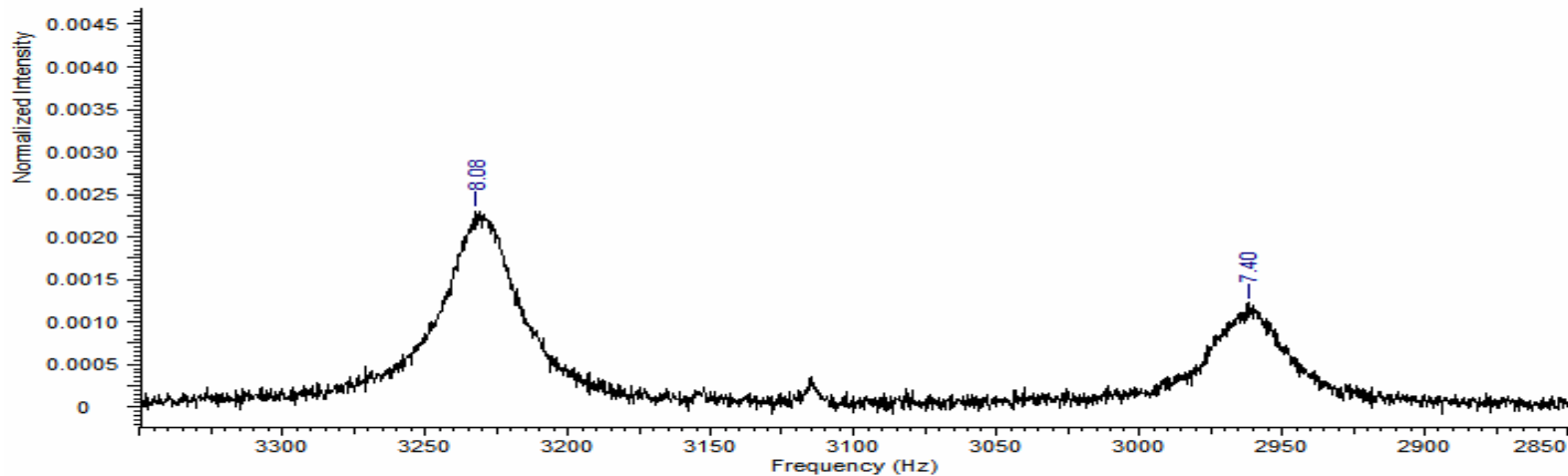


Figure 2-23(a). ^1H NMR spectrum of $\text{A}_5\text{Ru}^{\text{II}}$ (3-tfmpy) $^{2+}$ complex in D_2O , $[\text{Ru}^{\text{II}}] = 5.0 \text{ mM}$

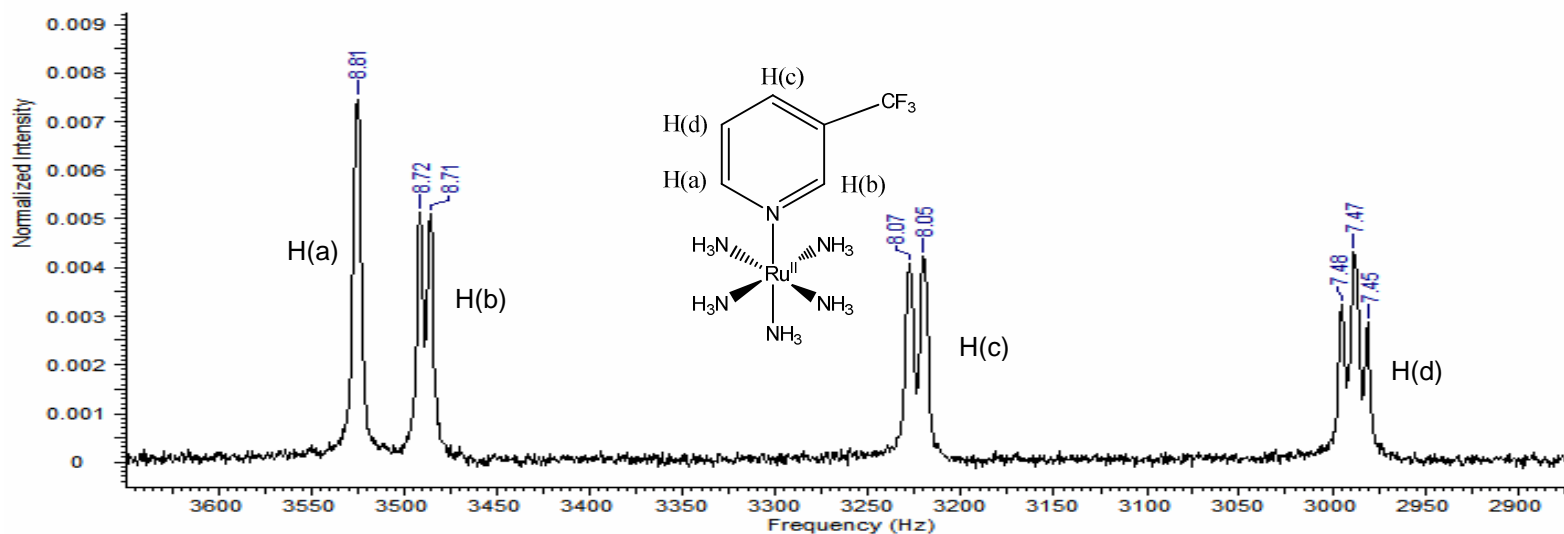


Figure 2-23(b). ^1H NMR spectrum of $\text{A}_5\text{Ru}^{\text{II/III}}$ (3-tfmpy) $^{2+/3+}$ mixture in D_2O , $[\text{Ru}^{\text{II}}] = [\text{Ru}^{\text{III}}] = 5.0 \text{ mM}$

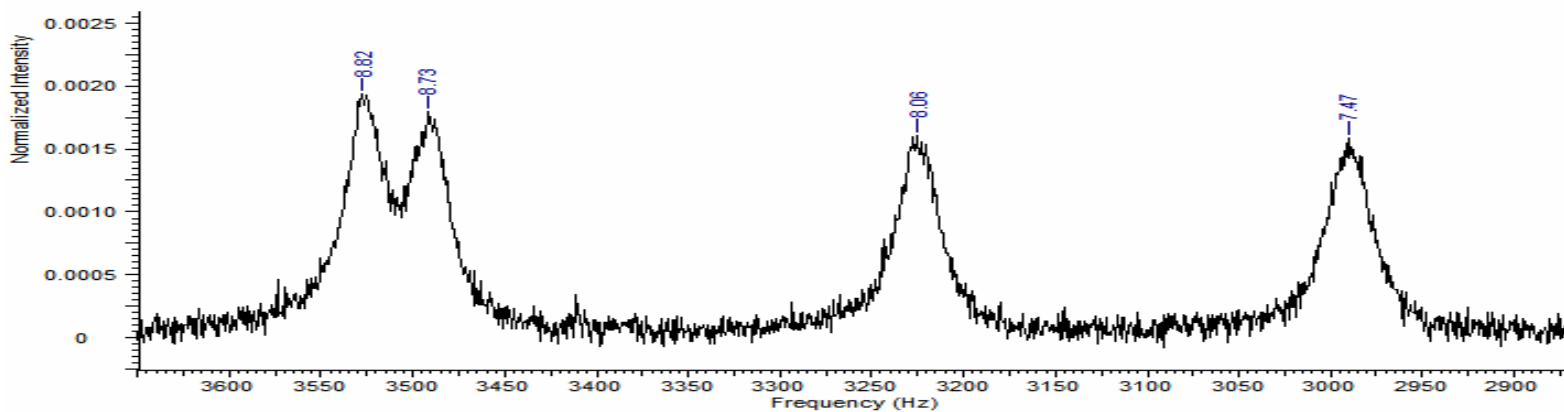


Figure 2-24(a). ^1H NMR spectrum of $\text{A}_5\text{Ru}^{\text{II}}$ (3-Phpy) $^{2+}$ complex in D_2O , $[\text{Ru}^{\text{II}}] = 5.0 \text{ mM}$

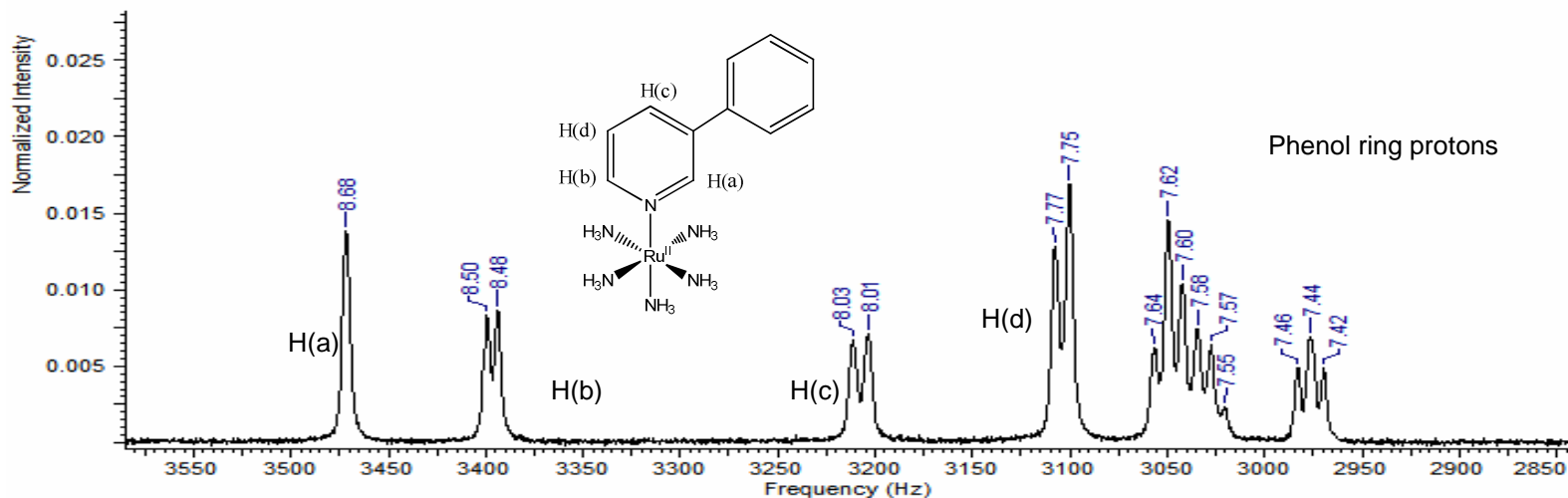


Figure 2-24(b). ^1H NMR spectrum of $\text{A}_5\text{Ru}^{\text{II/III}}$ (3-Phpy) $^{2+/3+}$ mixture in D_2O , $[\text{Ru}^{\text{II}}] = [\text{Ru}^{\text{III}}] = 5.0 \text{ mM}$

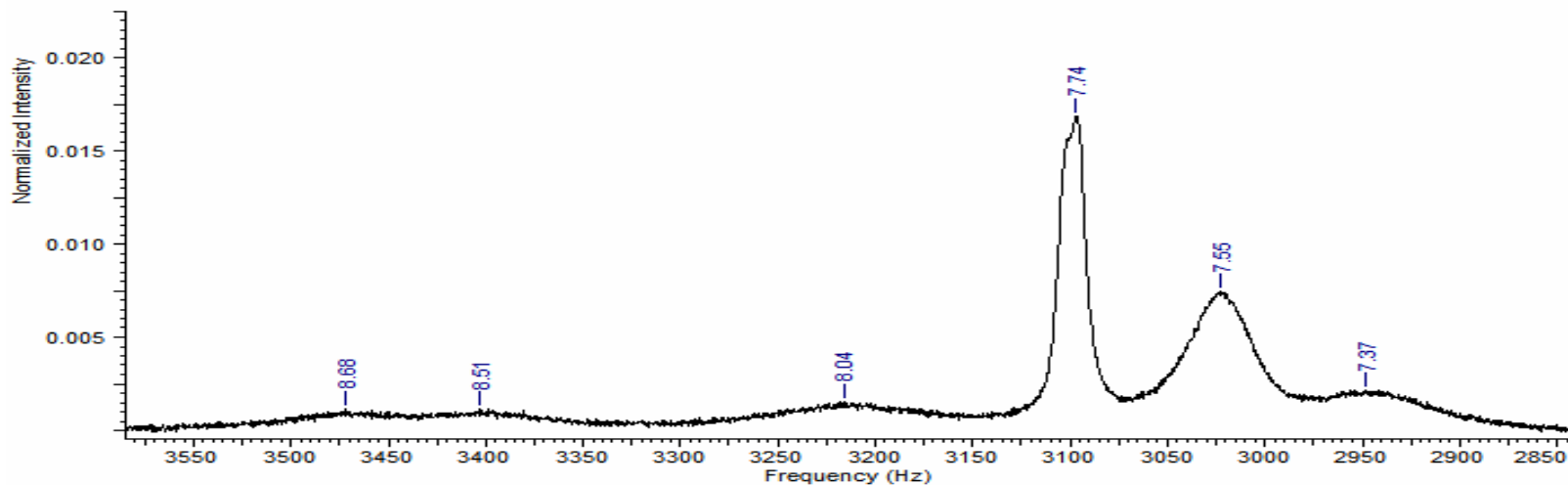


Table 2-9. Rates of self-exchange for L-A₅Ru^{II/III} in D₂O monitored by ¹H or ¹⁹F NMR at room temperature (L= various pyridyl ligands, see Table 2-1 for structures)

| Ligand | E _{1/2} vs SCE in 0.1M KCl | Positions and widths of peaks used in calculation of k _{ex} (Ru ^{II} except where noted) | | | | log k _{ex} ^(a) |
|------------------------|---|---|----------------------|----------------------------------|----------------|------------------------------------|
| | | Hz (before broadening) | Width in Hz | Hz (in mixture) | Width in Hz | |
| 3,5-Me ₂ py | 0.025 | 3229 | 4.30 | 3231 | 29.89 | 4.14 ± 0.01 |
| 4-pic | 0.027 | 3304 3309 | 2.78 3.00 | 3305 | 26.85 | 4.00 ± 0.05 |
| 3-Etpy | 0.032 | 3036 3044 | 4.53 4.48 | 3037 | 24.40 | 4.07 ± 0.05 |
| 3-pic | 0.043 | 3014 3022 | 3.89 3.78 | 3018 | 39.93 | 4.02 ± 0.02 |
| 4-Phpy ^(b) | 0.054 | 3721 (Ru ^{III} peak) | 10.25 | 3685 (Ru ^{III} peak) | 194.01 | 5.06 ± 0.06 ^(c) |
| Py | 0.058 | 3372 3367 | 3.34 3.30 | 3371 | 21.08 | 4.10 ± 0.07 |
| 3-Phpy | 0.068 | 3472 | 4.71 | 3471 | 63.60 | 4.59 ± 0.04 ^(c) |
| 4-Clpy | 0.090 | 3353 3347 | 3.00 3.04 | 3353 | 30.39 | 4.18 ± 0.10 |
| 4-Brpy | 0.092 | 3313 3320 | 3.19 3.11 | 3325 | 40.06 | 4.30 ± 0.11 |
| 3Clpy | 0.113 | 3411 3413 | 2.18 2.11 | 3421 | 33.25 | 4.17 ± 0.02 ^(c) |
| 3-Fpy | 0.117 | 3386 3390 3393 | 1.93 3.10 1.84 | 3389 | 22.46 | 4.04 ± 0.04 ^(c) |
| 3-Brpy | 0.119 | 3458 3460 | 2.28 2.22 | 3467 | 36.74 | 4.29 ± 0.10 ^(c) |
| 3-tfmpy (1H) | 0.143 | 3220 3228 | 5.14 5.14 | 3224 | 29.21 | 4.15 ± 0.06 |
| 3-tfmpy (19F) | 0.143 | 3168 | 3.30 | 3171 | 18.47 | |
| 3,5-Br ₂ py | 0.178 | 3449 3451 | 1.18 1.26 | 3423 | 45.43 | 4.42 ± 0.01 |
| 3,5-Cl ₂ py | 0.188 | 3387 3389 | 1.43 1.55 | 3390 | 34.28 | 4.37 ± 0.07 |

(a) Equation 1-31 used in rate calculation except where noted. (b) In 4-Phpy case, Ru^{III} peak is used since Ru^{II} peak has broadened too wide/complicated to perform Peakfit deconvolution (see Figure 2-13) (c) Equation 1-31 used after Peakfit deconvolution.

The rates listed in Table 2-9 were obtained from the single peak indicated in the table, but we also checked for consistency in two favorable cases (L = 3-Clpy and 3,5-Cl₂py) where the rate could be obtained from two peaks in the spectrum. As shown in Table 2-10, the consistency is very good.

Table 2-10. Illustration of rate variations in two cases where rates could be calculated from different pyridyl ring protons.

| Ligand | Pyridine ring proton selected to obtain log k _{ex} | log k _{ex} |
|------------------------|---|---------------------|
| 3Clpy | ortho (at 3484 Hz) | 4.18 |
| | ortho (at 3430 Hz) | 4.18 |
| | para (at 3112 Hz) | 4.20 |
| | meta (at 3021 Hz) | 4.13 |
| | Ave log k _{ex} | 4.17 ± 0.03 |
| 3,5-Cl ₂ py | ortho (at 3494 Hz) | 4.42 |
| | meta (at 3340 Hz) | 4.41 |
| | Ave log k _{ex} | 4.42 ± 0.01 |

Figure 2-25 displays the rate data from Table 2-9 graphically (y-axis) vs. the E_{1/2} value of the complex (in H₂O vs. SCE) along the x-axis. The most striking aspect of the figure is the dramatic rate accelerations observed for the 3-Phpy and 4-Phpy complexes relative to the others. We note that the rate constant is plotted here in log units, meaning that these complexes really are undergoing significantly faster self-exchange than the others compared to the experimental uncertainty.

One possible explanation for the 3-Phpy and 4-Phpy deviations could be favorable π - π stacking interactions between the phenyl groups on Ru^{II} and Ru^{III} as

illustrated in Figure 2-26. It is known that extended π -systems can exhibit stacking patterns due to favorable Van der Waals interactions in crystals,¹⁰ and it would not be surprising if such interactions also occurred in solution. This could be especially true in aqueous solution where the large phenyl group substituents would be expected to be hydrophobically solvated. It is known that hydrophobically-solvated alkylammonium cations will associate to some degree in aqueous solution due to the fact that, upon doing so, they are able to release some of the water from their individual (strained) hydration spheres by forming a single, larger one.¹¹ A similar effect may be happening here, and if so, it (along with any favorable π - π stacking) would be expected to increase the K_A term in Equation 1-12 and thus lead to faster self-exchange.

A second possible explanation is that the phenyl substituents might serve as electron-transfer "antenna groups" when they are brought into near proximity in the encounter complex. There is significant delocalization of electron density from Ru(II) out onto the pyridyl rings in the HOMO levels of these complexes due to the well-known π -backbonding interaction (*vide infra*), between the d^6 Ru^{II} center and the π^* levels on pyX.¹² In this case, we might expect the resulting electron density on the distal rings to make the electron-transfer reaction become more adiabatic if these extended HOMOs were to give rise to an increase in H_{ab} at the transition state. We note that theoretical work indicates that ET reactions across Ru-NH₃ interfaces in complexes such as these are probably just below the adiabatic limit.¹³ Any increased adiabaticity would show up experimentally as an increase κ_{el} in Equation 1-22 and also lead to an increase in rate.

Table 2-9 and Figure 2-25 also show that the 4-Phpy complex self-exchange is significantly faster than that of the 3-Phpy complex. This may simply be related to how steric crowding in the 3-Phpy complex inhibits the associative/solvational effects already mentioned above, but it may also reflect details of the orbital structures since one might expect the meta-substituted aromatic rings to provide less efficient coupling than para-substituted ones.¹⁴

A second feature we see in Figure 2-25 is a possible trend of increasing self-exchange electron transfer rate with increasing redox potential $E_{1/2}$ of each complex ranging from the lowest at 4-pic to the highest at the 3,5-Cl₂py ligand (excluding now the points for 3-Phpy and 4-Phpy which are clearly off the line as discussed above). A linear regression through these data indicates a slope of 1.8 ± 0.1 . One possible explanation of this effect could be related to the extent of π -backbonding and a resulting systematic variation in the reorganizational barrier λ . The increase in the measured $E_{1/2}$ value over the series of pyridyl ligands is due to the electron withdrawing ability of the ligand substituents. More electron-withdrawing substituents cause the extent of π -backbonding to increase such that more electron density flows from the Ru(II) $d\pi$ orbitals out onto the ring (see Figure 2-27). This electron density shift away from the Ru^{II} center would be expected to render the Ru^{II} center more like the Ru^{III} product species in an electrostatic sense. This could cause the overall nuclear reorganization energy λ to drop since, for a complex with greater π -back donation, the effective change in charge at the ruthenium will drop. Since much of λ_{inner} and λ_{outer} in these complexes has to do with reorganization at the ammine groups (and their solvation layer),¹⁵ any such decrease in Δe (change in charge at

the metal) would be expected to lessen λ . *Ab initio* computational work in order to test this idea against theory is currently underway.¹⁶

Figure 2-25. Rates for ET self-exchange in D₂O ($[Ru^{II}] = [Ru^{III}] = 5.0 \text{ mM}$) vs the measured $E_{1/2}$ value of the Ru^{II/III} couple

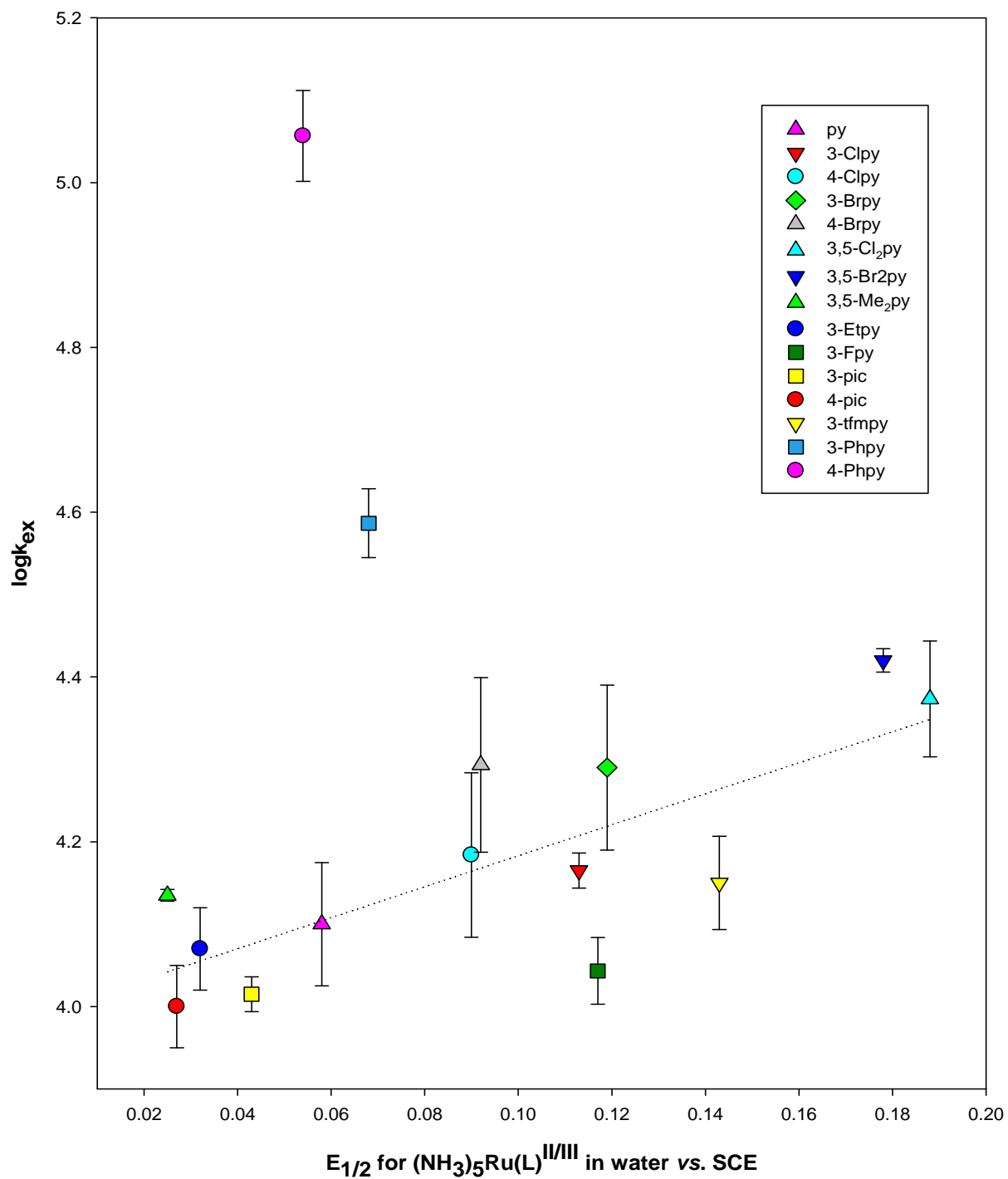


Figure 2-26. Illustration of possible π - π stacking interactions between the 4-Phpy and 3-Phpy ligands.

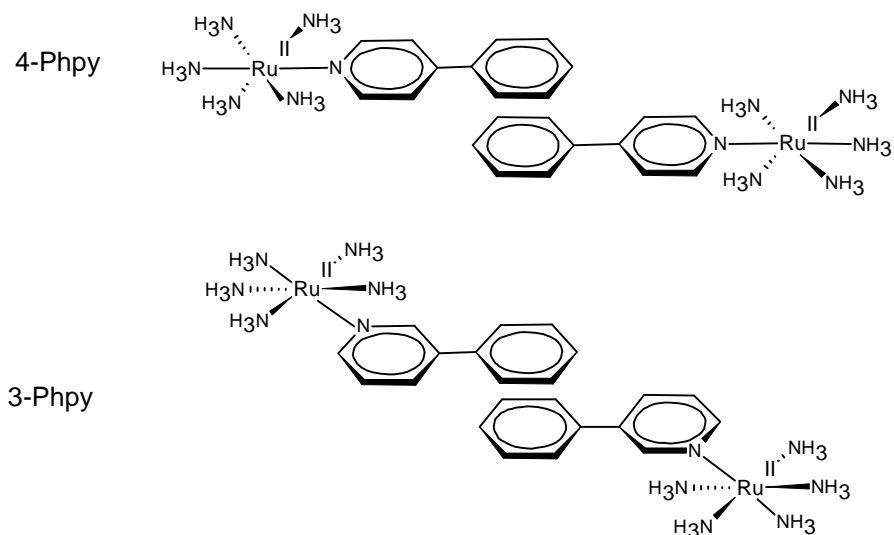
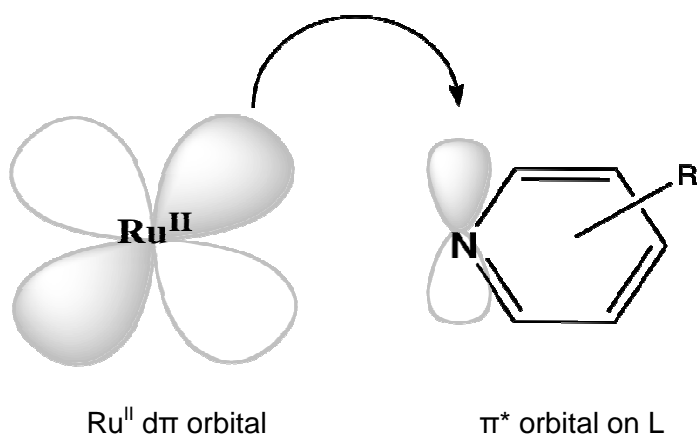


Figure 2-27. Illustration of π -backbonding. The electron density from the Ru^{II} d π orbital can be partially donated to the empty π^* orbital of the pyridyl ligand to an extent depending on the electron-withdrawing ability of the substituent group R.



Activation Parameters and Mechanistic Interpretation

To probe more deeply into the ET self-exchange mechanism, we performed temperature-dependent rate studies so as to obtain the activation parameters for a subset of the reactions reported in Table 2-9. Based on the transition state model, the general form of Eyring equation is

$$k = \frac{k_B T}{h} \exp(-\Delta G^\ddagger / RT) \quad 2-7^{17}$$

where ΔG^\ddagger is the Gibbs energy of activation, k_B is Boltzmann's constant, R is the gas constant, T is absolute temperature and h is Planck's constant. ΔG^\ddagger can be partitioned into its enthalpic (\sim work against forces) and entropic (probabilistic) components according to,

$$\Delta G^\ddagger = \Delta H^\ddagger - T\Delta S^\ddagger \quad 2-8^{18}$$

where ΔH^\ddagger is enthalpy of activation and ΔS^\ddagger is entropy of activation. Equation 2-7 can be then rewritten as,

$$k = \left(\frac{k_B T}{h} \right) \exp\left(\frac{\Delta S^\ddagger}{R} \right) \exp\left(-\frac{\Delta H^\ddagger}{RT} \right) \quad 2-9$$

To get the linear form of the Eyring equation, we take the ln of both sides of this equation,

$$\ln \frac{k}{T} = \frac{-\Delta H^\ddagger}{R} \cdot \frac{1}{T} + \ln \frac{k_B}{h} + \frac{\Delta S^\ddagger}{R} \quad 2-10$$

Thus, we can now obtain ΔH^\ddagger and ΔS^\ddagger from a plot of $\ln(k/T)$ versus $1/T$. The slope is $-\Delta H^\ddagger/R$, and the y-intercept is $\ln(k_B/h) + \Delta S^\ddagger/R$.

The motivation behind the Eyring experiments was to see whether it was primarily the enthalpy or entropy contributions to ΔG^\ddagger which were giving rise to our measured rate variations.

The ligands involved in reactions from Figure 2-25 chosen for Eyring experiments were: tfmpy, 4-pic (lowest $E_{1/2}$), 3,5-Cl₂py (highest $E_{1/2}$), 3-Fpy (below the trend line), 3-Phpy (above the trend line) and 4-Phpy (above the trend line). Table 2-11 and Figure 2-28 show the Eyring experiment results.

Technically, the Ru^{II} and Ru^{III} peaks are broadened in the same way by ET self-exchange and rates obtained from either peak should be the same. In order to prove this, the 4-pic complex was chosen since the pure 4-pic-A₅Ru^{III} complex shows a peak at 9.06 ppm (3628 Hz) (see Figure 2-11 for illustration). In the relevant Eyring experiment (see Figure 2-29), rates (see Table 2-12) were calculated from both the Ru^{II} and Ru^{III} peaks and compared. Table 2-13 shows the activation parameters extracted from the Eyring plots.

Table 2-11. Results of Eyring experiments for reaction 2-1 with selected ligands (in all cases $[Ru^{II}] = [Ru^{III}] = 5.0 \text{ mM}$)

3-Fpy (measured from Ru^{II} peak at 8.47ppm 1H -NMR)

| T(K) | 1/T | k_{ex} | $\ln(k_{ex}/T)$ |
|------|----------|----------|-----------------|
| 284 | 0.003516 | 5850 | 3.02 |
| 288 | 0.003475 | 6800 | 3.16 |
| 293 | 0.00341 | 9180 | 3.44 |
| 299 | 0.003347 | 12520 | 3.74 |
| 304 | 0.003287 | 14730 | 3.88 |
| 310 | 0.003228 | 20830 | 4.21 |
| 315 | 0.003172 | 26150 | 4.42 |
| 321 | 0.003118 | 28130 | 4.47 |

4-pic (measured from Ru^{II} peak at 8.26ppm 1H -NMR)

| T(K) | 1/T | k_{ex} | $\ln(k_{ex}/T)$ |
|------|----------|----------|-----------------|
| 279 | 0.003584 | 8010 | 3.36 |
| 281 | 0.003559 | 8730 | 3.44 |
| 284 | 0.003521 | 9000 | 3.46 |
| 288 | 0.003472 | 9660 | 3.51 |
| 293 | 0.003413 | 10700 | 3.60 |
| 298 | 0.003356 | 13300 | 3.80 |
| 303 | 0.0033 | 16410 | 3.99 |
| 308 | 0.003247 | 18800 | 4.11 |
| 313 | 0.003195 | 21630 | 4.24 |
| 318 | 0.003145 | 25360 | 4.38 |
| 323 | 0.003096 | 29470 | 4.51 |

3,5-Cl₂py (measured from Ru^{II} peak at 8.47 ppm ¹H-NMR)

| T(K) | 1/T | k _{ex} | lnk _{ex} /T |
|------|----------|-----------------|----------------------|
| 282 | 0.003546 | 15990 | 4.04 |
| 284 | 0.003521 | 16690 | 4.07 |
| 288 | 0.003472 | 17980 | 4.13 |
| 293 | 0.003413 | 20760 | 4.26 |
| 298 | 0.003356 | 25690 | 4.46 |
| 303 | 0.0033 | 27480 | 4.51 |
| 308 | 0.003247 | 35190 | 4.74 |
| 313 | 0.003195 | 40940 | 4.87 |
| 318 | 0.003145 | 46400 | 4.98 |
| 323 | 0.003096 | 54470 | 5.13 |

3-Phpy (measured from Ru^{II} peak at 8.68 ppm ¹H-NMR)

| T(K) | 1/T | k _{ex} | lnk _{ex} /T |
|------|----------|-----------------|----------------------|
| 281 | 0.003559 | 30160 | 4.68 |
| 283 | 0.003534 | 33930 | 4.79 |
| 288 | 0.003472 | 36440 | 4.84 |
| 293 | 0.003413 | 41470 | 4.95 |
| 298 | 0.003356 | 51520 | 5.15 |
| 303 | 0.0033 | 54660 | 5.20 |
| 308 | 0.003247 | 62200 | 5.31 |
| 313 | 0.003195 | 64090 | 5.32 |
| 318 | 0.003145 | 78540 | 5.51 |
| 323 | 0.003096 | 93620 | 5.67 |

4-Phpy (measured from Ru^{III} peak at 9.30 ppm in ¹H-NMR)

| T(K) | 1/T | k _{ex} | lnk _{ex} /T |
|------|----------|-----------------|----------------------|
| 281 | 0.003559 | 91740 | 5.79 |
| 284 | 0.003521 | 99900 | 5.86 |
| 288 | 0.003472 | 102420 | 5.87 |
| 293 | 0.003413 | 129430 | 6.09 |
| 298 | 0.003356 | 148910 | 6.21 |
| 303 | 0.0033 | 137600 | 6.12 |
| 308 | 0.003247 | 167760 | 6.30 |
| 313 | 0.003195 | 179070 | 6.35 |
| 318 | 0.003145 | 203580 | 6.46 |
| 323 | 0.003096 | 214260 | 6.50 |

3-tfmpy (measured from Ru^{II} peak at 8.41 ppm in ¹⁹F-NMR)

| T(K) | 1/T | k _{ex} | ln(k _{ex} /T) |
|------|----------|-----------------|------------------------|
| 277 | 0.003614 | 6300 | 3.13 |
| 280 | 0.003571 | 6420 | 3.13 |
| 283 | 0.003529 | 7880 | 3.32 |
| 288 | 0.003475 | 8890 | 3.43 |
| 293 | 0.00341 | 10240 | 3.55 |
| 299 | 0.003347 | 11050 | 3.61 |
| 304 | 0.003287 | 15030 | 3.90 |
| 310 | 0.003228 | 16350 | 3.97 |
| 315 | 0.003172 | 19390 | 4.12 |
| 321 | 0.003118 | 23730 | 4.30 |
| 326 | 0.003065 | 29430 | 4.50 |
| 277 | 0.003614 | 5760 | 3.04 |
| 280 | 0.003571 | 6330 | 3.12 |
| 283 | 0.003529 | 7170 | 3.23 |
| 288 | 0.003475 | 7850 | 3.31 |
| 293 | 0.00341 | 10310 | 3.56 |
| 299 | 0.003347 | 12050 | 3.70 |
| 304 | 0.003287 | 14330 | 3.85 |
| 310 | 0.003228 | 16640 | 3.98 |
| 315 | 0.003172 | 19210 | 4.11 |
| 321 | 0.003118 | 23150 | 4.28 |
| 326 | 0.003065 | 27120 | 4.42 |

Table 2-12. Eyring plots data for 4-pic ligand (rates were calculated from both Ru^{II} and Ru^{III} peaks).

| measurements from Ru ^{II} (at 8.26 ppm) | | | | measurements from Ru ^{III} (at 9.06 ppm) | | | |
|--|----------|-----------------|------------------------|---|----------|-----------------|------------------------|
| T(K) | 1/T | k _{ex} | ln(k _{ex} /T) | T(K) | 1/T | k _{ex} | ln(k _{ex} /T) |
| 278 | 0.003599 | 8010 | 3.36 | 278 | 0.003599 | 10120 | 3.59 |
| 280 | 0.003571 | 8730 | 3.44 | 280 | 0.003571 | 10760 | 3.65 |
| 283 | 0.003529 | 9000 | 3.46 | 283 | 0.003529 | 11090 | 3.67 |
| 288 | 0.003475 | 9660 | 3.51 | 288 | 0.003475 | 11220 | 3.66 |
| 293 | 0.00341 | 10690 | 3.60 | 293 | 0.00341 | 12250 | 3.73 |
| 299 | 0.003347 | 13300 | 3.80 | 299 | 0.003347 | 15260 | 3.93 |
| 304 | 0.003287 | 16410 | 3.99 | 304 | 0.003287 | 16170 | 3.97 |
| 310 | 0.003228 | 18800 | 4.11 | 310 | 0.003228 | 19370 | 4.14 |
| 315 | 0.003172 | 21630 | 4.23 | 315 | 0.003172 | 21230 | 4.21 |
| 321 | 0.003118 | 25360 | 4.37 | 321 | 0.003118 | 24940 | 4.35 |
| 326 | 0.003065 | 29470 | 4.50 | 326 | 0.003065 | 25850 | 4.37 |
| 277 | 0.003614 | 6400 | 3.14 | 277 | 0.003614 | 8320 | 3.40 |
| 282 | 0.003543 | 8260 | 3.38 | 282 | 0.003543 | 10240 | 3.59 |
| 288 | 0.003475 | 10950 | 3.64 | 288 | 0.003475 | 11520 | 3.69 |
| 293 | 0.00341 | 12270 | 3.73 | 293 | 0.00341 | 11570 | 3.68 |
| 299 | 0.003347 | 13320 | 3.80 | 299 | 0.003347 | 13800 | 3.83 |
| 304 | 0.003287 | 14790 | 3.88 | 304 | 0.003287 | 13900 | 3.82 |
| 310 | 0.003228 | 19790 | 4.16 | 310 | 0.003228 | 17640 | 4.04 |
| 315 | 0.003172 | 22300 | 4.26 | 315 | 0.003172 | 21570 | 4.23 |
| 321 | 0.003118 | 25560 | 4.38 | 321 | 0.003118 | 23310 | 4.29 |
| 277 | 0.003614 | 7780 | 3.34 | 277 | 0.003614 | 10470 | 3.63 |
| 282 | 0.003543 | 9430 | 3.51 | 282 | 0.003543 | 11070 | 3.67 |
| 288 | 0.003475 | 10730 | 3.62 | 288 | 0.003475 | 12030 | 3.73 |
| 293 | 0.00341 | 11010 | 3.63 | 293 | 0.00341 | 12880 | 3.78 |
| 299 | 0.003347 | 13840 | 3.84 | 299 | 0.003347 | 15440 | 3.95 |
| 304 | 0.003287 | 17400 | 4.05 | 304 | 0.003287 | 17650 | 4.06 |
| 310 | 0.003228 | 20110 | 4.17 | 310 | 0.003228 | 19370 | 4.14 |
| 315 | 0.003172 | 23600 | 4.32 | 315 | 0.003172 | 23690 | 4.32 |
| 321 | 0.003118 | 25320 | 4.37 | 321 | 0.003118 | 26360 | 4.41 |

Figure 2-28 (a). Eyring plots for complexes of selected ligands; full temperature range

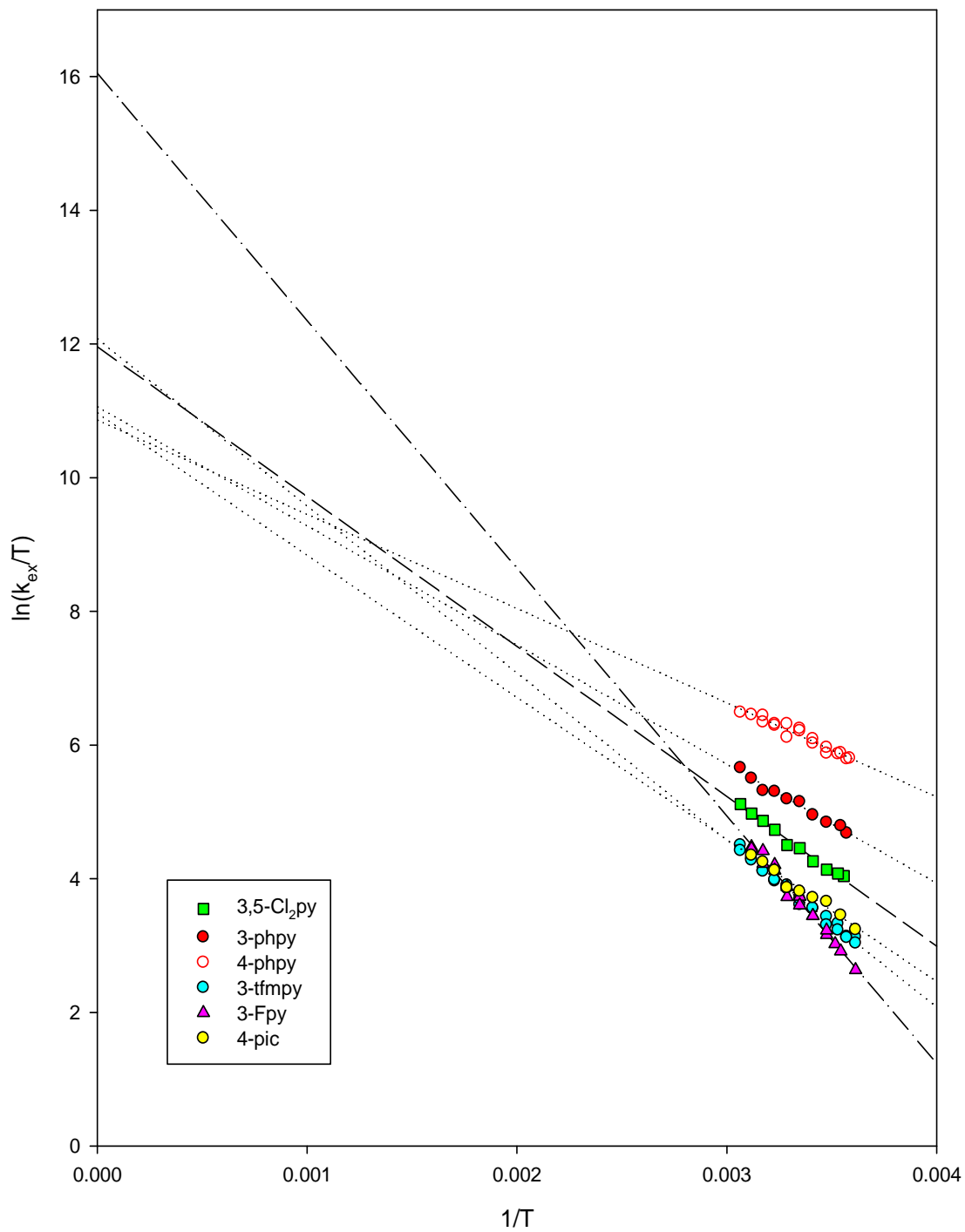


Figure 2-28 (b). Eyring plots for complexes of selected ligands; experimental temperature range

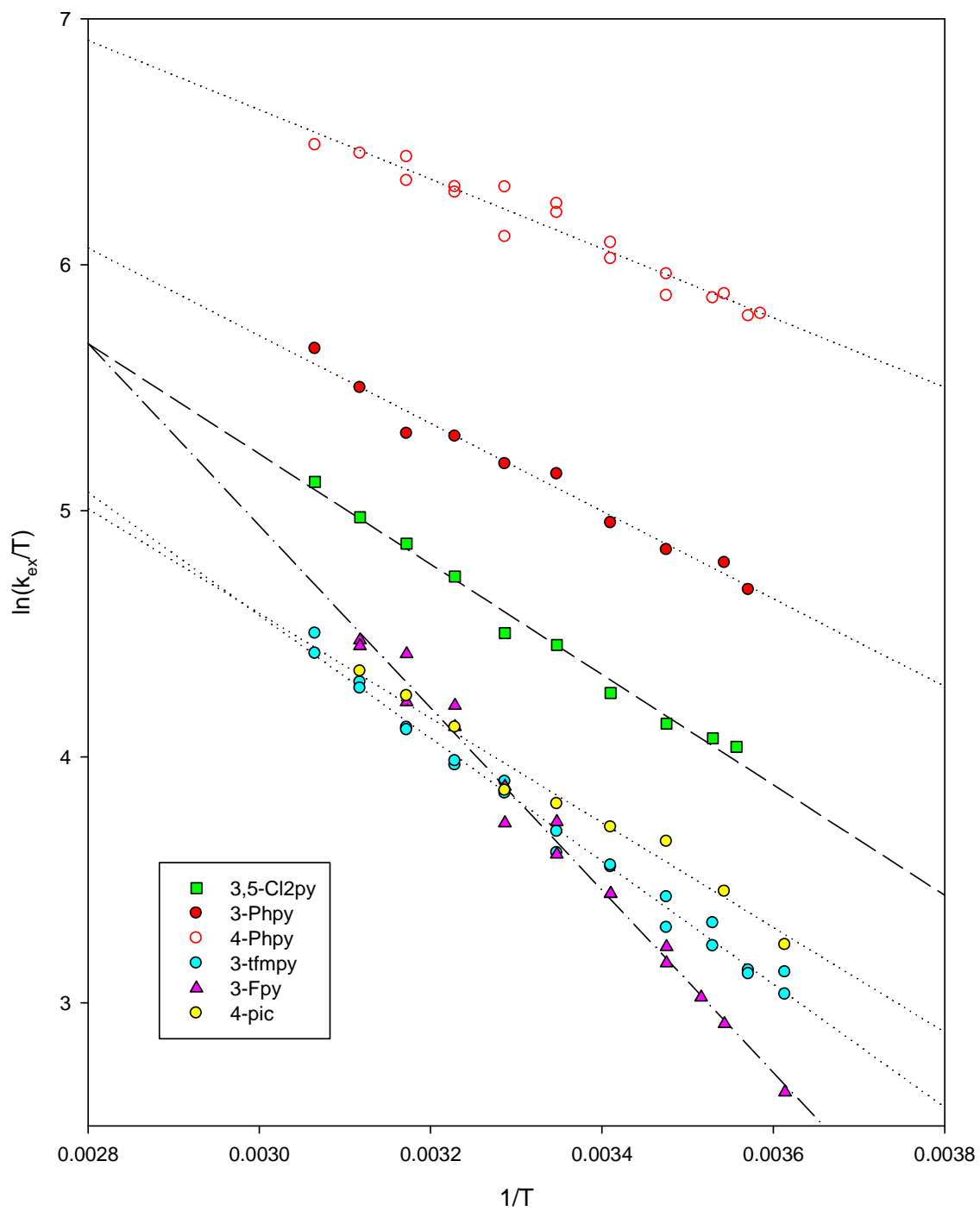


Figure 2-29. Eyring plots for the $(\text{NH}_3)_5\text{Ru}^{\text{II}}$ and Ru^{III} complex of the 4-pic ligand in D_2O ($[\text{Ru}^{\text{II}}] = [\text{Ru}^{\text{III}}] = 5.0 \text{ mM}$, rates were calculated from both Ru^{II} and Ru^{III} peaks)

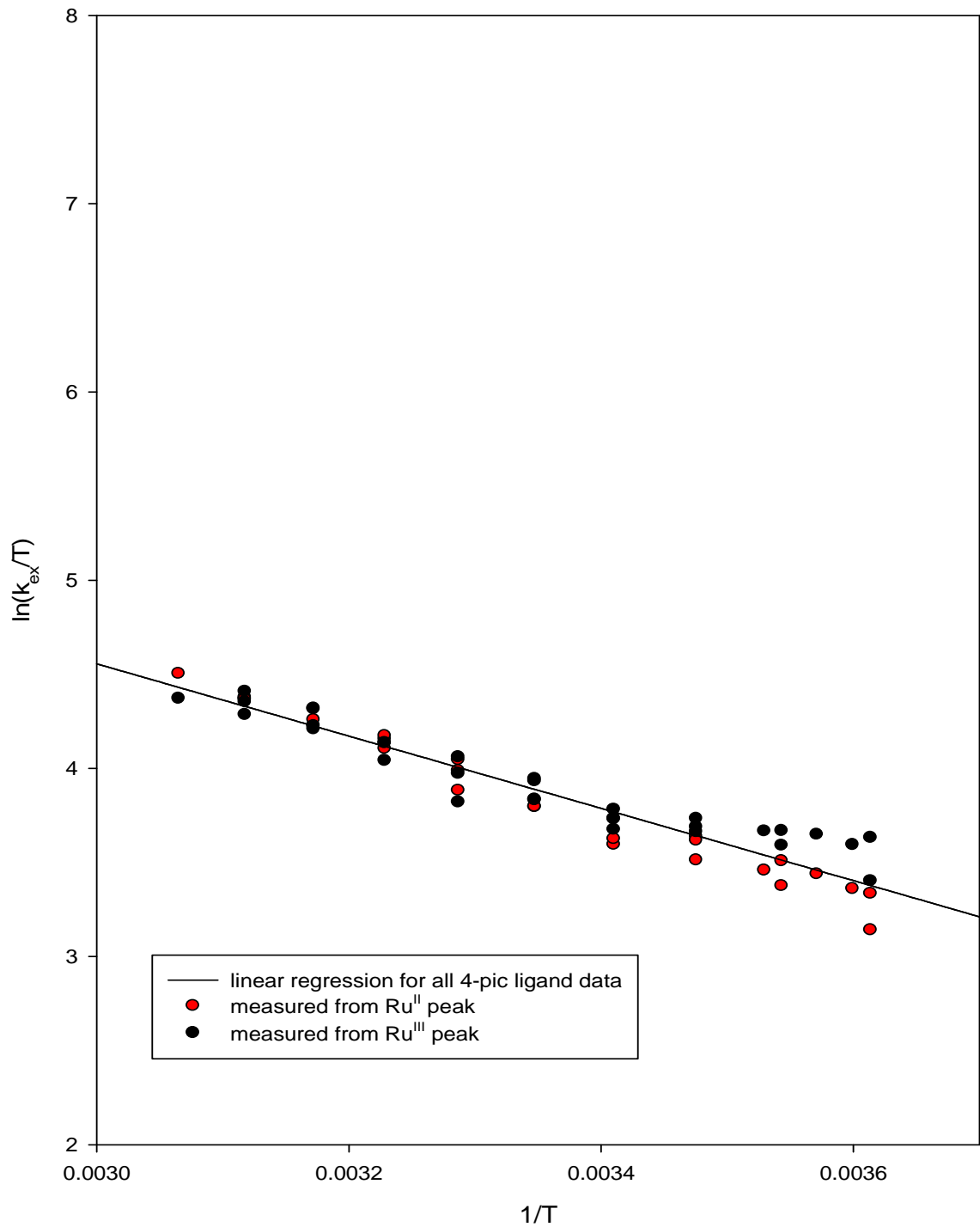


Table 2-13. ET activation parameters calculated for selected complexes as shown in Figures 2-28 and 2-29

| ligand | $E_{1/2}$ vs SCE in 0.1M KCl | slope | intercept | ΔH^\ddagger (kJ/mol) | ΔS^\ddagger (J/mol·K) |
|------------------------|---------------------------------|-----------------------|------------------|---------------------------------|----------------------------------|
| 4-pic* | 0.027 | -2126.93 ± 99.97 | 11.10 ± 0.33 | 17.7 ± 0.8 | -105.2 ± 2.8 |
| 4-Phpy | 0.054 | -1410.00 ± 88.61 | 11.38 ± 0.30 | 11.7 ± 0.7 | -102.9 ± 2.5 |
| 3-Phpy | 0.068 | -1782.46 ± 92.25 | 11.06 ± 0.31 | 14.8 ± 0.8 | -105.6 ± 2.6 |
| 3-Fpy | 0.117 | -3703.00 ± 113.00 | 16.05 ± 0.38 | 30.8 ± 0.9 | -64.1 ± 3.2 |
| 3-tfmpy** | 0.143 | -2499.87 ± 56.85 | 12.07 ± 0.19 | 20.8 ± 0.5 | -97.2 ± 1.6 |
| 3,5-Cl ₂ py | 0.188 | -2241.86 ± 88.36 | 11.96 ± 0.29 | 18.6 ± 0.7 | -98.1 ± 2.4 |

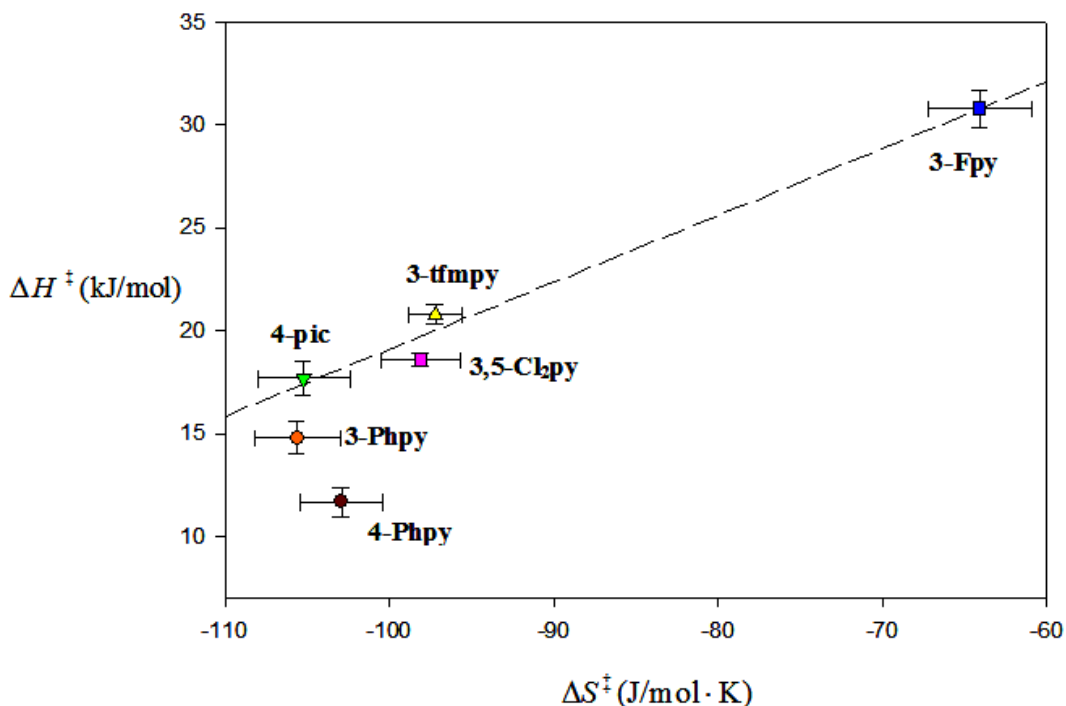
* Since rates calculated from Ru^{II} peak and Ru^{III} peak didn't show much difference, activation parameters were derived from Ru^{II} and Ru^{III} data combined.

** Measured by ¹⁹F NMR on the Ru^{II} peak

As listed in the table and as is visible in Figure 2-28, the 4-Phpy complex has the lowest values of enthalpy of activation (11.7 ± 0.7 kJ/mol) and a significantly large negative entropy of activation (-102.9 ± 2.5 J/mol·K). The 3-Phpy complex also exhibits a relatively low enthalpy of activation value (14.8 ± 0.8 kJ/mol) and an even more negative entropy value (-105.6 ± 2.6 J/mol·K). According to Equation 2-4 and 2-5, smaller ΔH^\ddagger and more negative ΔS^\ddagger values will result in a smaller activation free energy and thus faster rates. In contrast to the 4-Phpy/3-Phpy complexes, 3-Fpy shows the biggest ΔH^\ddagger value (30.8 ± 0.9 KJ/mol) and the least negative ΔS^\ddagger (-64.1 ± 3.2 J/mol·K) of all the complexes studied in the Eyring experiments. 3,5-Cl₂py, 4-pic and 3-tfmpy complexes show moderate $\Delta H^\ddagger / \Delta S^\ddagger$ values.

Taken together, the complexes of this subset of ligands shows a linear relationship between their enthalpic and entropic barriers. Such behavior is known as “enthalpy-entropy compensation”¹⁹ and the plot is shown in Figure 2-30. The line in the plot is drawn through the points for the 4-pic, 3,5-Cl₂py, 3-tfmpy and 3-Fpy complexes since these complexes presumably exhibit no “antenna” or peculiar reorganizational energy effects.

Figure 2-30. ΔH^\ddagger in kJ/mol vs. ΔS^\ddagger in J/mol·K



The 4-Phpy complex clearly deviates from the line in a way which implicates the enthalpic barrier as being uniquely small (in that the ΔS^\ddagger values is unremarkable). The 3-Phpy complex shows a similar deviation, but the significance relative to uncertainty is less clear.

Since all the reactions in this study follow the outer-sphere electron transfer mechanism, the activation enthalpy necessarily contains the enthalpic component of the energy barrier to bring the reactants together to form the precursor complex and allow the electron-transfer event to occur. This association requires a partial break up of the hydration shell of the reactants,²⁰ and such rearrangements of the solvent molecules are known to contribute to entropies of activation.²¹ The exact mechanisms underlying entropy-enthalpy compensation behaviors such as this (the trend line in Figure 2-30) are a matter of on-going investigation and debate,²² and we are unable to settle that issue here. However, it is clear that these ET reactions in water (where solvent-solute interactions with our complexes are especially strong) should provide a useful starting point for further work and comparisons. As for the low ΔH^\ddagger values obtained with the 3- and 4-Phpy ligands, on-going computational work in our lab seeks to discover whether ab-initio calculations of the reorganizational energy λ (both in gas phase and in explicitly-solvated cases) predict variations in electronic structure which might cause a drop in λ for the two Ph-py cases as well as the gradual trend observed in Figure 2-25. Gas-phase calculations carried out thus far at the B3LYP/6-31+ g (d, p) level (with the SDD effective core potential on Ru) have failed to do so, but higher-level calculations are now in progress.^{23,24}

An early hypothesis in this work was that the fast rates encountered with 4-Phpy as ligand might be related to a combination of π - π stacking effects (see Figure 2-26) and/or an electronic coupling enhancement by an “antenna” effect operating through the phenyl substituent. In the former case, we would expect favorable π - π interactions to increase the K_a term in Equation 1-12. Such an interaction would

probably have the effect of lowering the measured ΔH^\ddagger to some extent, but the effect on ΔS^\ddagger is difficult to assess. If the “antenna effect” were to be important, this would show up as an increase in κ_{el} (the transmission coefficient, see page 15), and this would show up as a less negative ΔS^\ddagger . Since Figure 2-30 clearly indicates no unusual downward fluctuation in ΔS^\ddagger for the Phpy cases, we can at least conclude that any variations in κ_{el} are small relative to the more dominating variations which combine to make up the measured ΔH^\ddagger .

References

1. Chun, J., Masters Thesis, University of San Francisco, **2001**.
2. Tanaka, M., Masters Thesis, University of San Francisco, **2004**.
3. Inagaki, M. Master's Thesis, University of San Francisco, **2006**.
4. Allen, A. D.; Bottomley, F.; Harris, R. O.; Reinsalu, V. P.; Senoff, C.V. *J. Am. Chem. Soc.* **1967**, 89, 5595.
5. Curtis, J.C.; Sullivan, B.P.; Meyer, T. J. *Inorg. Chem.* **1983**, 22(2), 224.
6. Harris, D.C. *Exploring Chemical Analysis*, 3rd Edition. W. H Freeman and Company, New York, **2005**, p 308.
7. Lambert, J.B., Mazzola, E. P., *Nuclear magnetic resonance spectroscopy: An introduction to principles, applications, and experimental methods*. Pearson Education Inc. **2004**, p 32.
8. Van Geet A. L. *Analy. Chem.* **1970**, 42, 6, 679-680.
9. Teng, Q. *Structural biology: practical NMR applications*, Birkhauser, **2005**, p 106.
10. Bao, Z. Locklin; J. J. *Organic Field-Effect Transistors*. CRC Press, **2007**, p 278.
11. Tadros, T. F. *Applied Surfactants: Principles and Applications*. Wiley-VCH, **2005**, p 33.
12. Wieder, N.L; Gallagher, M; Carroll, P.J.; Berry, D.H. *J. Am. Chem. Soc.*, **2010**, 132 (12), 4107-4109.
13. Newton, M.D. *Chem. Rev.* **1991**, 91, 767-792.
14. Richardson, D.E.; Taube, H. *J. Am. Chem. Soc.* **1983**, 105, 40-51.
15. Brown, G.M.; Sutin, N. *J. Am. Chem. Soc.*, **1979**, 101 (4), 883-892
16. Curtis, J. C. Work in progress.

17. (a) Eyring, H. *J. Chem. Phys.* **1935**, 3, 107.
(b) Laidler, K.J.; King M.C. *J. Phys. Chem.* **1983**, 87, 2657–2664.
18. Mascetta, J. A. *Chemistry the Easy Way*, 4th Edition, Barron's Educational Series, Inc, **2003**, p 193.
19. Anslyn, E.V.; Dougherty, D.A. *Modern Physical Organic Chemistry*, University Science Books, **2006**, p 469.
20. Inoue, Y. *Chiral Photochemistry*. CRC Press, **2004**, p 297.
21. Karlin, K.D. *Progress in Inorganic Chemistry*, Volum 55. Wiley-Interscience. **2007**, 11.
22. Liu, L.; Guo, Q.X. *Chem. Rev.*, **2001**, 101 (3), 673–696.
23. Curtis, J. C. Work in progress.
24. Frisch, M. J.; Trucks, G. W.; Schlegel, H. B.; Scuseria, G. E.; Robb, M. A.; Cheeseman, J. R.; Scalmani, G.; Barone, V.; Mennucci, B.; Petersson, G. A.; Nakatsuji, H.; Caricato, M.; Li, X.; Hratchian, H. P.; Izmaylov, A. F.; Bloino, J.; Zheng, G.; Sonnenberg, J. L.; Hada, M.; Ehara, M.; Toyota, K.; Fukuda, R.; Hasegawa, J.; Ishida, M.; Nakajima, T.; Honda, Y.; Kitao, O.; Nakai, H.; Vreven, T.; Montgomery, Jr., J. A.; Peralta, J. E.; Ogliaro, F.; Bearpark, M.; Heyd, J. J.; Brothers, E.; Kudin, K. N.; Staroverov, V. N.; Kobayashi, R.; Normand, J.; Raghavachari, K.; Rendell, A.; Burant, J. C.; Iyengar, S. S.; Tomasi, J.; Cossi, M.; Rega, N.; Millam, N. J.; Klene, M.; Knox, J. E.; Cross, J. B.; Bakken, V.; Adamo, C.; Jaramillo, J.; Gomperts, R.; Stratmann, R. E.; Yazyev, O.; Austin, A. J.; Cammi, R.; Pomelli, C.; Ochterski, J. W.; Martin, R. L.; Morokuma, K.; Zakrzewski, V. G.; Voth, G. A.; Salvador, P.; Dannenberg, J. J.; Dapprich, S.;

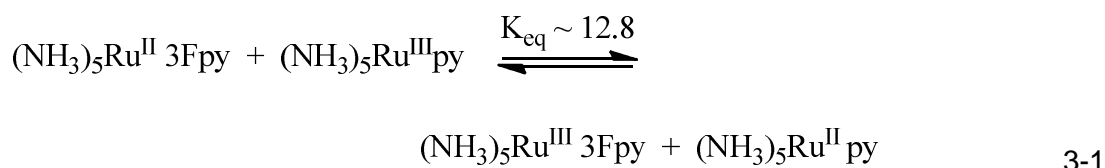
Daniels, A. D.; Farkas, Ö.; Foresman, J. B.; Ortiz, J. V.; Cioslowski, J.; Fox, D.
J. Gaussian 09, Revision A.1, Gaussian, Inc., Wallingford CT, **2009**.

Chapter Three Kinetic Studies of Salt Effects on Self-exchange Electron Transfer Reactions Monitored by ^{19}F NMR Spectroscopy

Introduction

In Chapter Two, we discussed pyridyl ligand substituent effects on the kinetics of bimolecular electron-transfer self-exchange reactions. In this chapter, we will discuss kinetic salt effects on these same reactions. Added salts have long been known to affect the rates of reactions between charged species in solution.¹⁻³

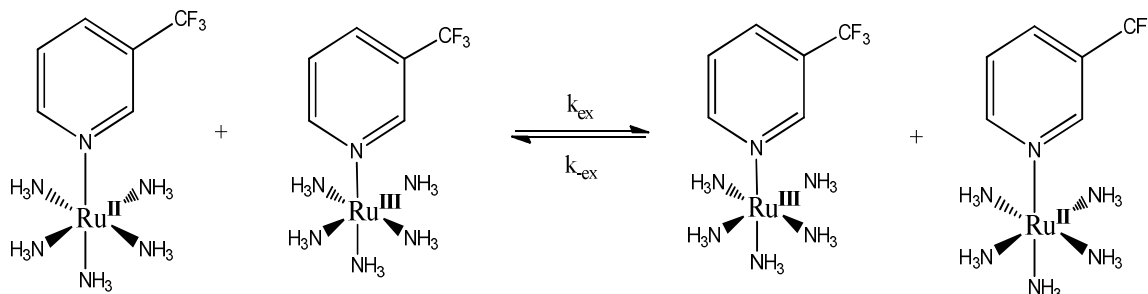
Previous studies⁴⁻⁷ in this lab have focused on various aspects of salt effects on the kinetics of the low-driving force pseudo-self exchange reaction shown below (as monitored by stopped-flow),



Their studies showed that some added salts, such as NaF and NaCl lead to kinetic effects which quantitatively follow the predictions of the Debye-Huckel theory of ionic atmospheres reasonably well, while others, such as NaI, $\text{Na}_2(\text{muc})$ or $\text{Na}_2(\text{tere})$ deviate strongly in a positive, accelerating direction (where muc is the dianionic muconate and tere is terephthalate). These deviations were interpreted as possible evidence of an individual anion's ability to catalyze ET by modulating the degree of superexchange coupling between electron donor (Ru^{II}) and electron acceptor (Ru^{III}) taking place in the encounter complex. Reactant concentrations in the stopped-flow work were in the range of $5 \times 10^{-5} \text{ M} \sim 3.0 \times 10^{-4} \text{ M}$ in both $\text{Ru}(\text{II})$ and $\text{Ru}(\text{III})$.⁴⁻⁷

To extend the study of salt effects to a "true" ET self-exchange (zero driving force), we chose to study the reaction between ruthenium(II) and (III)

pentaammine(3-trifluoromethylpyridine) preliminarily investigated by Chun,⁴ Tanaka,⁸ and Inagaki⁵.



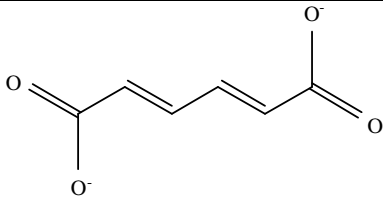
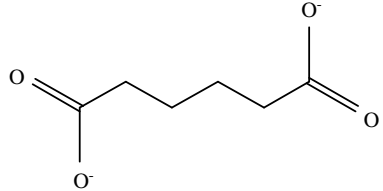
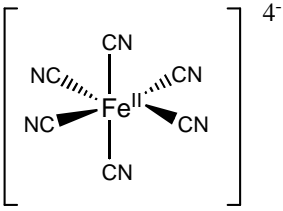
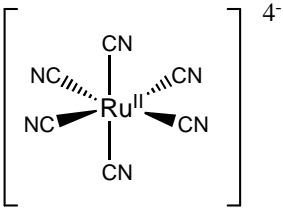
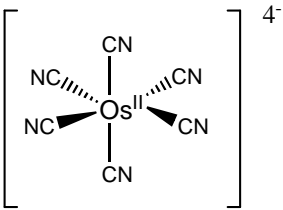
3-2

This complex is especially advantageous because the 3-trifluoromethylpyridine ligand gives rise to a strong, singlet ¹⁹F resonance which can be measured with better precision than was found to be the case using proton NMR (see Chapter One). Importantly, this ¹⁹F NMR “tag” gives a very sharp singlet for *both* Ru^{II} and Ru^{III}. As mentioned in Chapter Two, paramagnetic broadening by Ru^{III} tends to obscure ¹H NMR signals from near-lying hydrogens (even out on the pyridyl ligands). ¹⁹F is nearly as sensitive in NMR as ¹H and is about 86 times more sensitive than ²H.^{9, 10} Being able to see sharp, singlet peaks from both redox states of the complex makes it easy to verify the desired 50:50 redox state distribution in kinetic line broadening experiments, and also allows rates to be calculated from either the Ru^{II} peak or the Ru^{III} peak.

Preliminary NMR investigations of reaction 3-2 by Inagaki indicated that the magnitudes of both the “Debye-Huckel” (simple salt) and “catalytic” (muc²⁻, tere²⁻) kinetic salt effects were much less than those observed by stopped-flow.⁵ This was explained as possibly being due to the significantly-higher reactant concentrations necessary in order to measure ET rates by NMR (Inagaki used [Ru^{II}] = [Ru^{III}] = 3 mM

in her NMR work⁵ as opposed to 1.0×10^{-4} M used by Sista⁷). The work to be described here was undertaken in order to verify Inagaki's observations as well to extend the range of salts investigated and apply detailed kinetic modeling to the results. The salts used in this work included the simple salts NaF, NaBr, NaCl, NaOAc and Na₂SO₄, the disodium dicarboxylic dianions Na₂Muc and Na₂adip, and the complex metal-cyano salts K₄[Fe^{II}(CN)₆], K₄[Os^{II}(CN)₆] and K₄[Ru^{II}(CN)₆]. See Table 3-1 for the structures of these salts.

Table 3-1. Dicarboxylic dianions and $M(\text{CN})_6^{4-}$ complexes used as added salts in this study.

| Name | Structure | Abbreviation |
|----------------|---|--------------------|
| Muconate |  | muc ²⁻ |
| Adipate |  | adip ²⁻ |
| Ferrocyanide |  | ---- |
| Ruthenocyanide |  | ---- |
| Osmiocyanide |  | ---- |

The effect of ionic strength on ET rates

Ionic strength has long been known to have an influence on kinetic rate constants between charged reactants.^{1-3, 11} The effect of ionic strength on rate can be understood by considering the ratio of activity coefficients as suggested by Bronsted,

$$k = k_0 \frac{\gamma_A \gamma_B}{\gamma_{AB}^\ddagger} \quad 3-3^{12}$$

where k_0 is the rate constant for some reaction at infinite dilution (zero ionic strength) in a given solvent, and the γ_A , γ_B and γ_{AB}^\ddagger are the activity coefficients for reactant ions A, B and their presumed encounter complex AB^\ddagger which goes onto become products. According to Debye-Huckel theory,^{13,14} the relationship between the activity coefficient γ_i and the ionic strength μ for dilute solutions (less than ~0.01M) can be expressed by the “extended” Debye-Huckel equation,

$$-\log \gamma_i = \frac{Z_i^2 \alpha \sqrt{\mu}}{1 + \beta a_i \sqrt{\mu}} \quad 3-4^{11}$$

where a_i is the distance of approach of some ion in solution to the i^{th} reactant ion, and α and β are the Debye-Huckel constants for a given solvent and temperature ($\alpha=0.51$ and $\beta=0.329$ in water at 25 °C)¹¹, Z_i is the charge on ion i and μ is the ionic strength of the solution. Physically, at low concentration (≤ 0.1 M), the observable decrease of γ_i with added ionic strength results from the fact that an “atmosphere” of ions in the solution builds up around any charged reactant ion and this “screens” its charge from the rest of the solution, including any other charged reactant species in solution with which it might be capable of reacting. In other

words, the ionic atmosphere built up around any given ion decreases electrostatic interactions generally between it and other ions in the solution, and this leads to a decreased γ_i value with respect to any equilibrium that ion might participate in, including encounter between A and B to form AB^\ddagger in Equation 3-3.¹⁵

If Equations 3-3 and 3-4 are combined, we obtain,

$$\log k = \log k_0 - \frac{Z_A^2 \alpha \sqrt{\mu}}{1 + \beta a_A \sqrt{\mu}} - \frac{Z_B^2 \alpha \sqrt{\mu}}{1 + \beta a_B \sqrt{\mu}} + \frac{(Z_A + Z_B)^2 \alpha \sqrt{\mu}}{1 + \beta a_{AB} \sqrt{\mu}} \quad 3-5$$

or, if a mean value of a is taken for the distance of approach of the centers of the reactants, Equation 3-5 can be simplified as follows,

$$\log k = \log k_0 + \frac{2Z_A Z_B \alpha \sqrt{\mu}}{1 + \beta a \sqrt{\mu}} \quad 3-6^{16}$$

and this has come to be known as the Debye-Huckel-Bronsted equation. Since the product of a and β ($\beta = 0.329$ in water at 25 °C) is approximately equal to 1 for many ions,¹⁷ Equation 3-6 can usually be approximated as,

$$\log k = \log k_0 + \frac{2Z_A Z_B \alpha \sqrt{\mu}}{1 + \sqrt{\mu}} \quad 3-7$$

It is then convenient to define the “Guggenheim parameter” GP as,

$$GP = \frac{\sqrt{\mu}}{1 + \sqrt{\mu}} \quad 3-8^{18,19}$$

and then Equation 3-7 becomes,

$$\log k = \log k_0 + 2Z_A Z_B \alpha (GP) \quad 3-9$$

If we collect kinetic data as a function of total ionic strength and then plot $\log k$ vs GP , the predicted slope of the line would be $2Z_A Z_B \alpha \approx Z_A Z_B$ (since $\alpha = 0.51$ in

water at 25 °C and $2\alpha \cong 1$), which is simply the product of the charges of reactant ions A and ion B (in a situation where the assumptions of Debye-Huckel theory hold).

Superexchange

As mentioned earlier, the conjugated dicarboxylic muconate dianion showed a strong catalytic effect on ET rates in previous work, and this is thought to be due to its ability to act as a “bridge” in a non-covalent context of quantum “superexchange” ET coupling mediation.^{4,5,7,20} The “superexchange” concept and terminology were originally used in the context of magnetic spin exchange where electron spins on two paramagnetic elements interact with each other through a virtual intermediate state provided by a nonmagnetic element or bridging group in between.²¹ It was McConnell who first introduced the idea of superexchange into considerations of the quantum mechanism underlying long-range electron transfer.²² In his work, McConnell investigated the intramolecular electron transfer between the two phenyl groups in α,ω -diphenylalkanes anions, $[\phi-(\text{CH}_2)_n-\phi]^-$, involving the interactions of the redox-active ends with the virtual excited state which places an electron on the methylene bridge. He suggested that virtual bridge states intervening between the donor and acceptor sites could facilitate the electron-transfer process by lowering the energetic height of the relevant tunneling barrier.

To understand the quantum superexchange process, we need to review the concept of electron tunneling. Suppose in a double square-well potential field (see Figure 3-1), electron donor D is on the left side and electron acceptor A is on the right side. The potential energy in the area between D and A represents the relevant tunneling energy barrier that will modulate the “tunneling frequency” at which an

electron initially on D oscillates back and forth to A.²³ In the simplest case, the distance between D and A is treated as being fixed. The wave function of the system is denoted by $\psi(D, A)$ when the electron is localized on D, or by $\psi(D^+, A^-)$ when it is on A. Both wavefunctions decay exponentially, and the conceptual basis of tunneling is that ψ never goes to zero under the finite rectangular potential barrier (see Figure 3-2 for a graphic depiction of how the D and A⁻ wavefunctions decay).

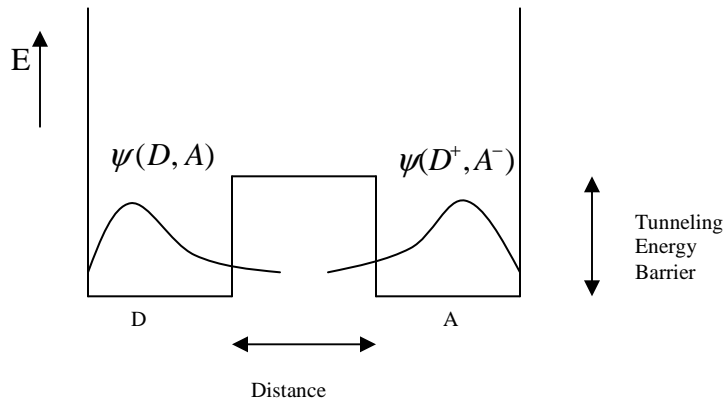


Figure 3-1. Illustration of double square-well potential function. $\psi(D, A)$ would represent the case when the electron is in the left well and $\psi(D^+, A^-)$ would be the case when the electron is in the right well. The wavefunction of the exchanging electron in both cases extends underneath the potential barrier due to the known ability of quantum particles to “tunnel”.²⁴

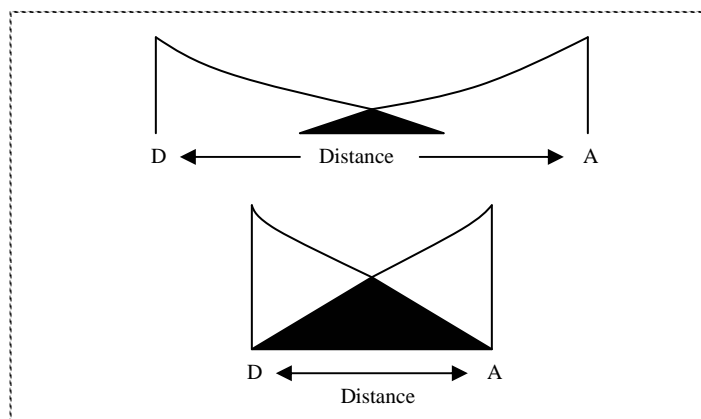


Figure 3-2. A schematic illustration of how the region of overlap between the $\psi(D, A)$ and $\psi(D^+, A^-)$ wavefunctions depends on the distance between the D and A groups. The size of the black “overlap” area can be related to the magnitude of the tunneling matrix element H_{ab} (see Chapter One).

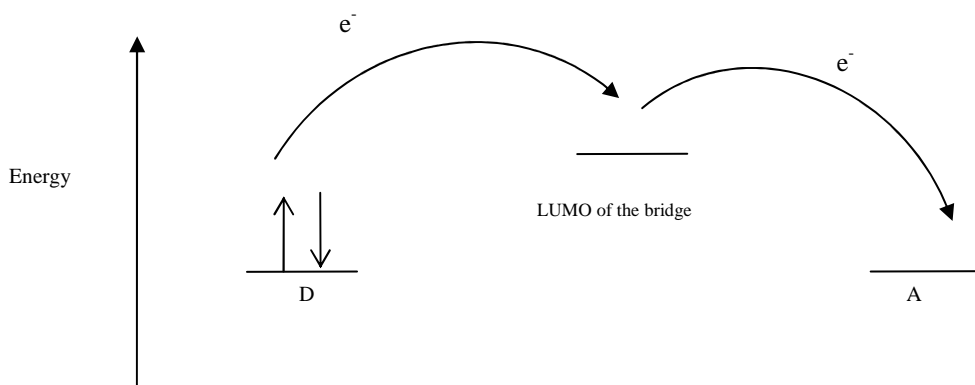
In Figure 3-2, the dark area of overlap between the decaying wavefunctions centered on D and A⁻ is proportional to the size of H_{ab} , the electronic coupling matrix element which modulates the quantum interaction between donor and acceptor (see Equations 1-23 and 1-24 in Chapter One). If D and A are barely coupled, then $\nu_{\text{tunneling}}(e^-) < \nu_{\text{nuclear}}$ (the frequency of electron tunneling through the energy barrier is smaller than the effective frequency of nuclear motion on the reaction coordinate) and the transmission coefficient $\kappa_{el} < 1$ in Equation 1-23. Such electron-transfer reactions are said to be in the “non-adiabatic” regime described in Chapter One (meaning that the nuclear sub-system can vibrate through the intersection region of the Marcus curves and stay on the reactant’s surface without any electron transfer happening such that the system transits to the product’s surface). On the other hand,

if the overlap is large enough, then $v_{\text{tunneling}}(e^-) \gg v_{\text{nuclear}}$, and there is strong enough coupling between D and A to assure that $\kappa_{el} = 1$; then the reaction is in the “adiabatic” regime. In this case, the reaction system can move smoothly from the reactant surface to the product surface by thermal activation over the barrier at the intersection region as well as by nuclear tunneling underneath the Marcus barrier under low-temperature conditions (which is possible because the nuclear/vibrational wavefunctions also extend some distance past the classically-allowed parabolic potential functions).^{25,26}

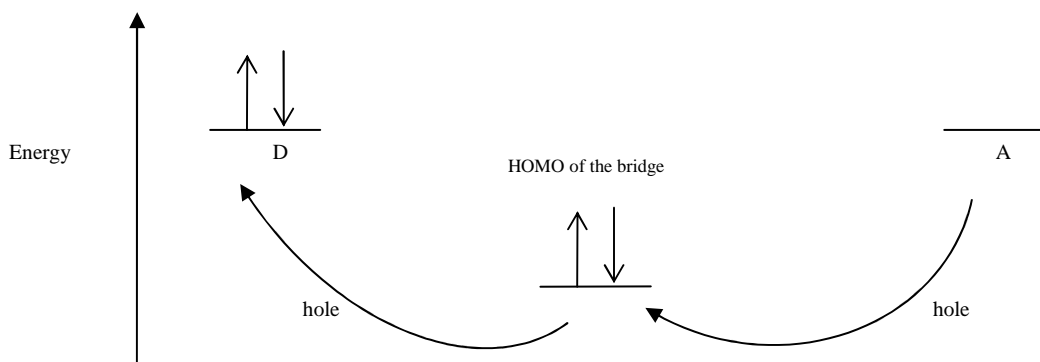
A key concept in understanding superexchange is that of the so-called “virtual state”. Superexchange-electron transfer mediation is due to the indirect mixing of the donor and acceptor wave functions provided through the intervening bridge orbitals between D and A.²⁷ The energy necessary to reach an intermediate bridge state, or “virtual state” in which either an electron or a hole is localized on the bridge will determine the effective tunneling barrier height and thus tunneling frequency, but it is important to note that these bridge states are never actually realized at typical thermal energies. In other words, the electron transfer happens in only one concerted step in superexchange, there is no discrete “hopping” of an electron (or hole) “onto” the bridge where it resides for some finite and definable lifetime.

We can readily identify two types of virtual states relevant to electron transfer superexchange (see Figure 3-3 for illustration).²⁸ In the first pathway, an electron tunnels from donor to acceptor according to the energy barrier defined by the high-lying empty bridge orbitals (LUMO 0, LUMO +1, LUMO +2...). This is referred to as the “electron transfer” superexchange pathway. In the second pathway, the energy of the virtual state is defined by the energy necessary for a “hole” to be localized on

the bridge by moving an electron from a low-lying fully occupied bridge orbital (HOMO 0, HOMO -1, HOMO -2...) onto A (which would be a Ru(III) center in our case).



(1) Schematic illustration of the virtual state relevant to the “electron transfer” superexchange pathway



(2) Schematic illustration of the virtual state relevant to “hole transfer” superexchange pathway

Figure 3-3. Illustration of the virtual states which establish the two pathways of superexchange mediation

In Figure 3-3, we see that “electron-transfer” superexchange is the pathway in which an electron is transferred from D through the virtual state involving the LUMO (lowest unoccupied molecular orbital) or possibly LUMO +1 or LUMO +2 of the bridge group and then onto A (again, in a concerted tunneling process). The energy which would be required to elevate the electron from D to an empty anti-bonding orbital of the bridge is thus the energy which defines the height of the tunneling barrier (the magnitude of this energy gap would be roughly comparable to typical metal-to-ligand charge-transfer (MLCT) energies of our family of $A_5Ru^II L$ complexes). In the lower panel, we see that “hole-transfer” superexchange happens when an electron vacancy is transferred from A (the lowest and singly occupied molecular orbital of the ground state of the system, in our case the “hole” in the t_{2g} orbital set on Ru(III)) through the virtual state involving the removal of an electron from the HOMO 0 (or possibly HOMO -1 or HOMO -2) of the bridge. An electron is transferred from the HOMO of the bridge to the hole on A, leaving a hole on the bridge which is then filled by an electron from D (from the t_{2g} set on Ru(II) in our case). The magnitude of the hole-transfer tunneling barrier will now roughly correspond to typical ligand-to-metal charge-transfer (LMCT) energies.

Rate constants for reactant association/dissociation

As explained in Chapter One, a key step in any bimolecular ET reaction is the diffusion of the reactant ions together to form the precursor complex. The equilibrium constant for this association, K_a , can be treated by using the Eigen-Fuoss equation which is derived on the basis of thermodynamic considerations,

$$K_a = \frac{4\pi N a^3}{3000} \exp\left(-\frac{z_1 z_2 e_0^2}{D_s a RT}\right) \quad 3-10^{29,30}$$

where N is Avogadro's number, a is the center-to-center distance of the ions in a pair, z_1 and z_2 are the charges on the reactants, e_0 is the unit electron charge, D_s is dielectric constant, R is gas constant and T is absolute temperature.

For purposes of analyzing our ET kinetic data, however, it is helpful for us to specifically consider how ionic strength affects the association and dissociation rates of the reactant ions to form and destroy precursor and successor complexes relevant to the bimolecular ET mechanism.

The Debye-Smoluchowski treatment of the diffusional association of charged particles in solution gives the following expression,

$$k_a = \frac{2k_B T N}{3000 \eta} \left(2 + \frac{r_A}{r_B} + \frac{r_B}{r_A} \right) \frac{1}{d \int_d^\infty r^{-2} e^{\left(\frac{w(r,\mu)}{k_B T}\right)} dr} \quad 3-11^{31}$$

where the "work term", $w(r,\mu)$ is defined by,

$$w(r,\mu) = \frac{e^2 z_A z_B}{4\pi \epsilon_0 D_s d} \left(\frac{1}{1 + \beta d \sqrt{\mu}} \right) \quad 3-12$$

here r_A and r_B are the radii of the ions, z_A and z_B are the charges of the ions, D_s is the dielectric constant of the solvent, and d is the distance of closest approach ($d = r_A + r_B$).

A parallel equation for the rate constant of dissociation is given by Eigen's treatment of the diffusional separation of (ionic) encounter pairs as

$$k_d = \frac{k_B T}{2\pi\eta d^2} \left(\frac{1}{r_A} + \frac{1}{r_B} \right) \frac{e^{\left(\frac{w(d,\mu)}{k_B T}\right)}}{d \int_d^\infty r^{-2} e^{\left(\frac{w(r,\mu)}{k_B T}\right)} dr} \quad 3-13^{30}$$

Equations 3-11 and 3-13 thus form the basics for kinetic modeling studies, which will allow us to predict how added electrolytes should affect the bimolecular ET rate for reaction 3-2 in cases where the assumptions of the extended Debye-Huckel theory hold. We will describe how the kinetic effects due to the various added electrolytes studied compare to these predictions and suggest explanations, based on the ideas of superexchange coupling, for the observed deviations from theory (some of which are found to be quite spectacular, involving anomalous rate accelerations of up to two orders of magnitude).

Experimental

Materials

The studies of salt effects on self-exchange reactions employed both “simple” salts (such as NaF, NaCl and NaBr *etc.*), and more “complex” salts such as dicarboxylic anions and the group 8b hexacyanide complexes (see Table 3-1). The former salts were purchased from Aldrich, EM Science, JT Baker Chemical or Mallinckrodt and used without further purification. The dicarboxylic species (see Table 3-1) were from Aldrich in free acid form and converted to their disodium salts using the procedures described by Inagaki.⁵ $\text{RuCl}_3 \cdot \text{H}_2\text{O}$ used to prepare $\text{K}_4\text{Ru}^{\text{II}}(\text{CN})_6$ was purchased from Aldrich. Potassium ferrocyanide was purchased from EM Science and recrystallized once from water prior to use. The $(\text{NH}_4)_2\text{OsCl}_6$ used to prepare $\text{K}_4[\text{Os}(\text{CN})_6]$ was purchased from Baker. The $(3\text{-tfmpy})\text{A}_5\text{Ru}^{\text{II}}(\text{PF}_6)_2$, $(3\text{-tfmpy})\text{A}_5\text{Ru}^{\text{II}}\text{Cl}_2$ and $(3\text{-tfmpy})\text{A}_5\text{Ru}^{\text{III}}\text{Cl}_3$ complexes were prepared as described in Chapter Two.

Preparation of $\text{K}_4\text{Ru}^{\text{II}}(\text{CN})_6$ (MW=413g/mol)

$\text{K}_4\text{Ru}^{\text{II}}(\text{CN})_6$ was synthesized using the method described by Howe.³² In a typical preparation, 2 g of $\text{RuCl}_3 \cdot \text{H}_2\text{O}$ was heated at reflux in 50 mL saturated aqueous KCN solution for 24 hours. Upon cooling of the solution to 0°C overnight, a brownish-white microcrystalline precipitate was produced. The crude product was then isolated by filtration, washed with methanol and dried in vacuum. Yields were ~70%.

The crude $\text{K}_4\text{Ru}^{\text{II}}(\text{CN})_6$ product was purified by dissolving it in 75 mL of water at room temperature, followed by the slow addition of an equal volume of methanol

to yield the white product. The purification process was carried out twice (upon aging, this material develops a trace bluish-colored impurity which can be eliminated by repeating this procedure).

Preparation of $K_4Os^{II}(CN)_6$ (MW= 502g/mol)

$K_4Os^{II}(CN)_6$ was synthesized and purified analogously to $K_4Ru^{II}(CN)_6$ except using $(NH_4)_2OsCl_6$ as the starting material.

Table 3-2 shows the microanalytical data obtained (Columbia Analytical Laboratories) for $K_4Os(CN)_6$ and $K_4Ru(CN)_6$.

Table 3-2. Elemental analysis data for $K_4M(CN)_6$ (M = Os, Ru)

| Compound | C% Observed (Theory) | H% Observed (Theory) | N% Observed (Theory) |
|--------------------------|-------------------------|-------------------------|-------------------------|
| $K_4Os(CN)_6 \cdot H_2O$ | 14.44 (13.84) | 0.95 (0.38) | 15.87 (16.15) |
| $K_4Ru(CN)_6 \cdot H_2O$ | 17.09 (16.71) | 0.87 (0.46) | 19.61 (19.49) |

Preparation of sodium muconate, Na_2Muc^5

Muconic acid (~1.0g) was added to a flask containing 100 mL distilled water. Concentrated NaOH was then used to titrate the muconic acid until the pH was about 6.5. During the process of titration the muconic acid slowly dissolved. The resulting solution was filtered and ~ 4 volumes of reagent grade acetone were added in order to precipitate the sodium muconate salt. The final product was filtered and dried in vacuum. This compound was used in experiments without further purification.

Preparation of sodium adipate, Na₂adip

Sodium adipate was synthesized in the same way as sodium muconate.

Calculation of μ and GP in the reactant solutions

In the study of salt effects on rates, the total ionic strength μ due to the charges of the Ru^{II} and Ru^{III} complexes, their counter ions and any added salts is an important quantity and must be known in order to calculate the GP function relevant to the extended Debye-Huckel theory. For example, in the solution of [(NH₃)₅Ru^{II}py]Cl₂ and [(NH₃)₅Ru^{III}py]Cl₃, the former complex will contribute one (NH₃)₅Ru^{II}py²⁺ ion of +2 charge and two Cl⁻ ions of -1 charge; similarly, the latter will contribute one (NH₃)₅Ru^{III}py³⁺ of +3 charge and three Cl⁻ of -1 charge. In order to calculate the total ionic strength and GP in a mixture of [(NH₃)₅Ru^{II}py]Cl₂ and [(NH₃)₅Ru^{III}py]Cl₃ complexes at 5.0 mM, we first employ the definition of ionic strength,

$$\mu = \frac{1}{2} \sum Z_i^2 C_i \quad 3-14^{33}$$

and arrive at,

$$\begin{aligned} \mu &= \frac{1}{2} \left\{ (+2)^2 \times [Ru^{II}] + 2 \times (-1)^2 \times [Cl^-] + (+3)^2 \times [Ru^{III}] + 3 \times (-1)^2 \times [Cl^-] \right\} \\ &= \frac{1}{2} \left[(+2)^2 \times 0.005 + 2 \times (-1)^2 \times 0.005 + (+3)^2 \times 0.005 + 3 \times (-1)^2 \times 0.005 \right] \\ &= 0.045 \end{aligned}$$

According to Equation 3-8, the resulting GP value is then,

$$GP = \frac{\sqrt{\mu}}{1 + \sqrt{\mu}} = \frac{\sqrt{0.045}}{1 + \sqrt{0.045}} = 0.175$$

Methods of addition of salts used in the NMR line broadening experiments

In the NMR experiments, all simple salts and disodium dicarboxylic salts were directly added as solids into the NMR tube containing the verified mixture of Ru^{II} and Ru^{III} pentaammine(3-trifluoromethylpyridine) (verified by noting the peak heights of the Ru(II) and Ru(III) resonances at 2.0 ppm and 2.2 ppm in D₂O, respectively). The amount of salt to be added was simply calculated based on the desired total GP value.

Due to the highly-catalytic nature of the M^{II} hexacyanide salts, however, the salts had to be added as small volumes of precisely-controlled solutions. Stock solutions (20 mM) of K₄M(CN)₆ (M=Fe, Os, Ru) were made just prior to the experiment. These were then added to the Ru^{II/III} mixture in the NMR tube using a Gilson P10 micropipette in order to reach the desired total GP values. The smallest addition volume used was 1.0 μL and the typical volume of [Ru^{II}] = [Ru^{III}] = 5 mM solution in D₂O was 2.0 mL.

Measurement of the ion-pair formation constant K_{ip} between the $[\text{NH}_3]_5\text{Ru(III)(3-tfmpy)}]^{3+}$ cation and the $[\text{M}^{\text{II}}(\text{CN})_6]^{4-}$ anions

Stock solutions of both $[\text{NH}_3]_5\text{Ru(III)(3-tfmpy)}]^{3+}$ and $\text{M}^{\text{II}}(\text{CN})_6^{4-}$ were prepared at 0.020M and 0.002M right before the experiment. $[\text{NH}_3]_5\text{Ru(III)(3-tfmpy)}]^{3+}$ was transferred using a Gilson P1000 micropipette to a 1 cm (or 5 cm) cell and quickly mixed with an appropriate amount of H₂O and $[\text{M}^{\text{II}}(\text{CN})_6]^{4-}$ to reach a desired concentration ($[\text{Ru}^{\text{III}}] : [\text{M}^{\text{II}}(\text{CN})_6]^{4-} = 1:1$ and total filled volume = 2 mL). For example (calculation will be similar if 5cm cell is used),

0.60 mL 0.020M Ru^{III} + 0.80 mL H₂O + 0.60mL 0.020 M^{II} → a 2.00 mL solution with [A₅Ru^{III}(3-tfmpy)]³⁺ = 6 x 10⁻³ M and [M^{II}(CN)₆]⁴⁻ = 6 x 10⁻³ M. Similarly, 0.90 mL 0.002M Ru^{III} +0.20 mL H₂O + 0.90 mL 0.002 M^{II} → a 2.00 mL solution with [A₅Ru^{III}(3-tfmpy)]³⁺ = 9 x 10⁻⁴ M and [M^{II}(CN)₆]⁴⁻ = 9 x 10⁻⁴ M.

The maximum absorbance in the VIS-NIR spectral region and λ_{max} values must be obtained as quickly as possible after mixing (typically within 30 seconds). This will minimize any error resulting from the slow formation of the more highly-absorbing cyano-bridged species *trans*-(3-tfmpy)(NH₃)₄Ru^{III}NC-M^{II}(CN)₆⁻¹.³⁴

The spectral data and graphical analyses based on them will be shown in the following section (Table 3-14, Figures 3-22 through 3-24).

Results and Discussions

Kinetic salt effect data

In the salt effect studies, we observed that in all cases, the self-exchange ET rate of reaction 3-2 was enhanced by the addition of salts. Figures 3-4 through 3-7 show examples of the ^{19}F NMR spectra for $[\text{NH}_3]_5\text{Ru}(\text{III})(3\text{-tfmpy})]^{2+/3+}$ in the presence of the different added salts, NaF, NaCl, NaBr and $\text{K}_4\text{Fe}(\text{CN})_6$ (from the slow-exchange to the fast-exchange limiting kinetic regimes).

Figure 3-4. ^{19}F NMR spectra of equimolar $[(\text{NH}_3)_5(3\text{-tfmpy})\text{yRu}^{\text{II/III}}]^{2+/3+}$ mixture ($[\text{Ru}^{\text{II}}] = [\text{Ru}^{\text{III}}] = 5.0 \text{ mM}$ in D_2O) as a function of added NaF concentration (all spectra exhibit slow-exchange limit here).

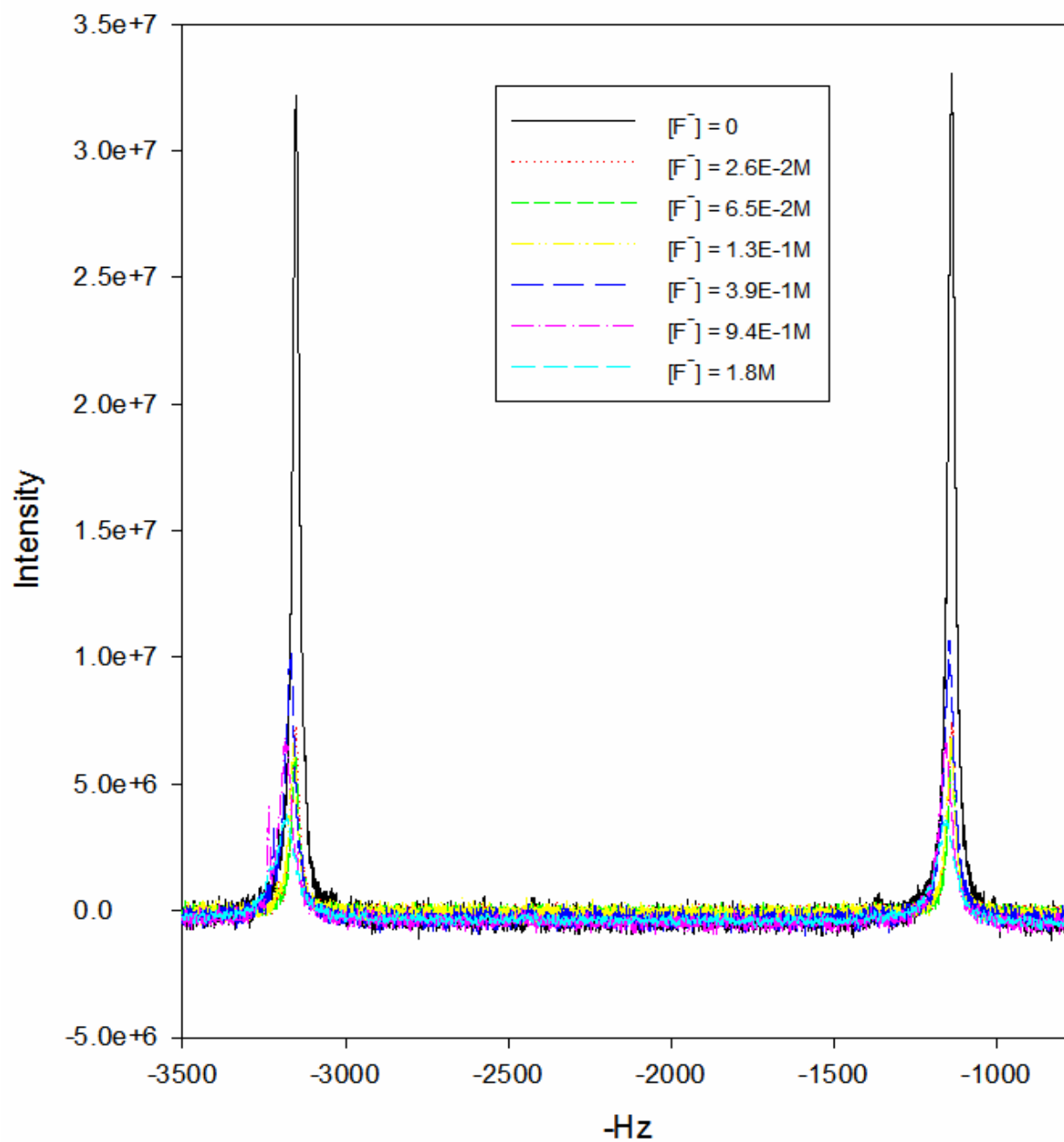


Figure 3-5. ^{19}F NMR spectra of the equimolar $[(\text{NH}_3)_5(3\text{-tfmpy})\text{Ru}^{\text{II/III}}]^{2+/3+}$ mixture ($[\text{Ru}^{\text{II}}] = [\text{Ru}^{\text{III}}] = 5.0 \text{ mM}$ in D_2O) as a function of added NaCl concentration (slow exchange limit at $[\text{NaCl}] < \sim 0.66 \text{ M}$ but intermediate exchange seen at $[\text{NaCl}] > \sim 0.13 \text{ M}$).

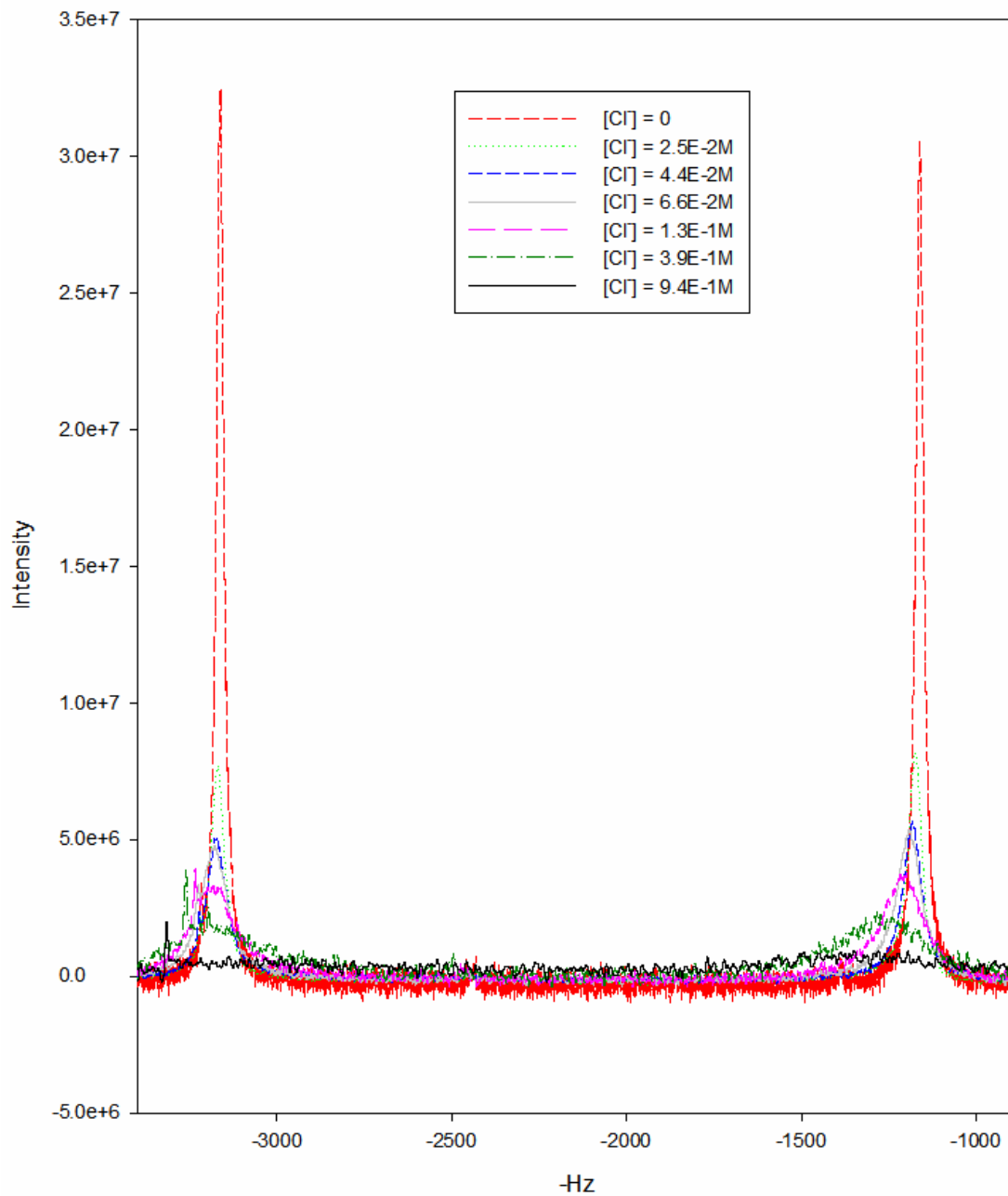


Figure 3-6. ^{19}F NMR spectra of the equimolar $[(\text{NH}_3)_5(3\text{-tfmpy})\text{Ru}^{\text{II/III}}]^{2+/3+}$ mixture ($[\text{Ru}^{\text{II}}] = [\text{Ru}^{\text{III}}] = 5.0 \text{ mM}$ in D_2O) as a function of NaBr (intermediate exchange rate region.)

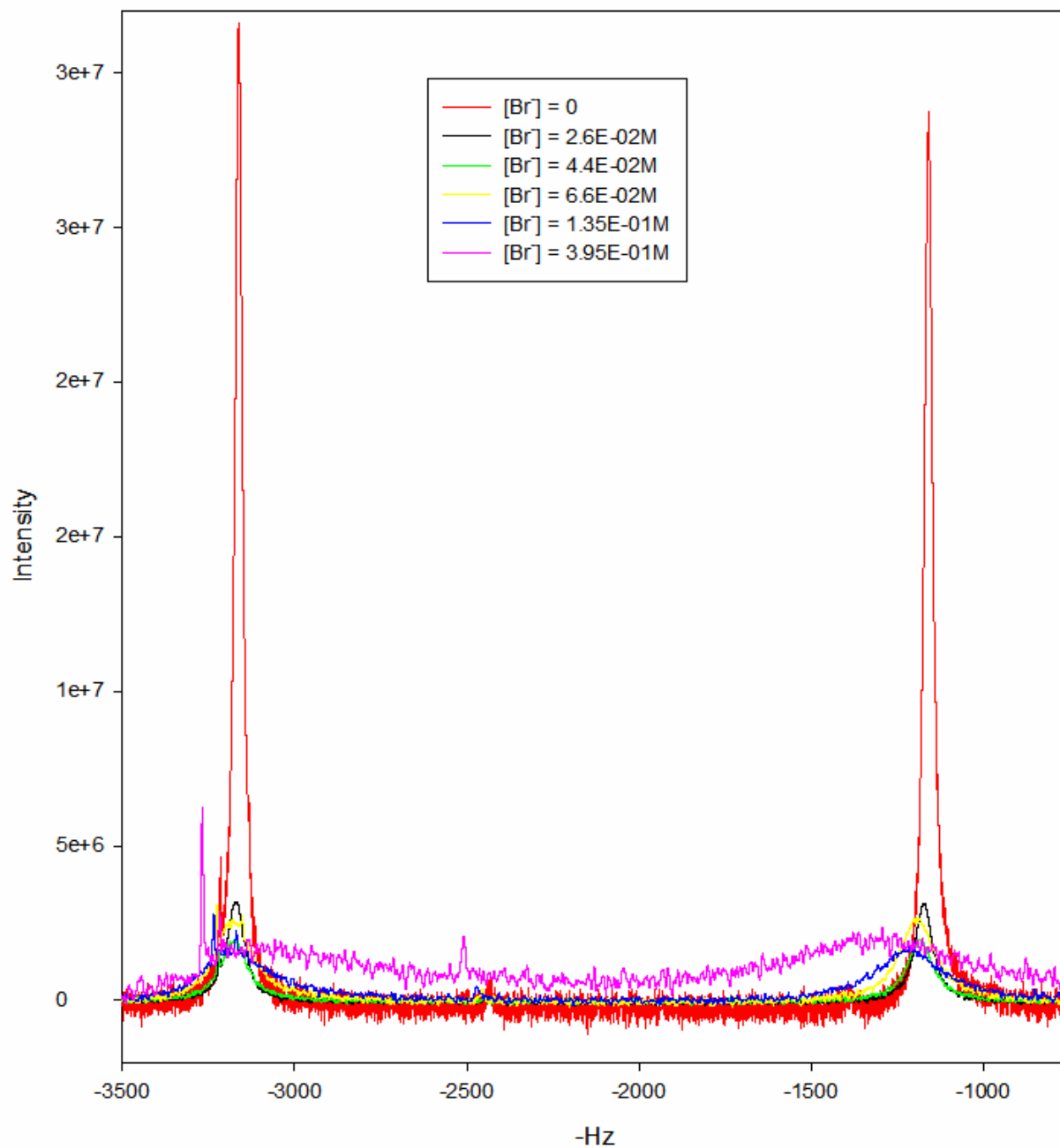
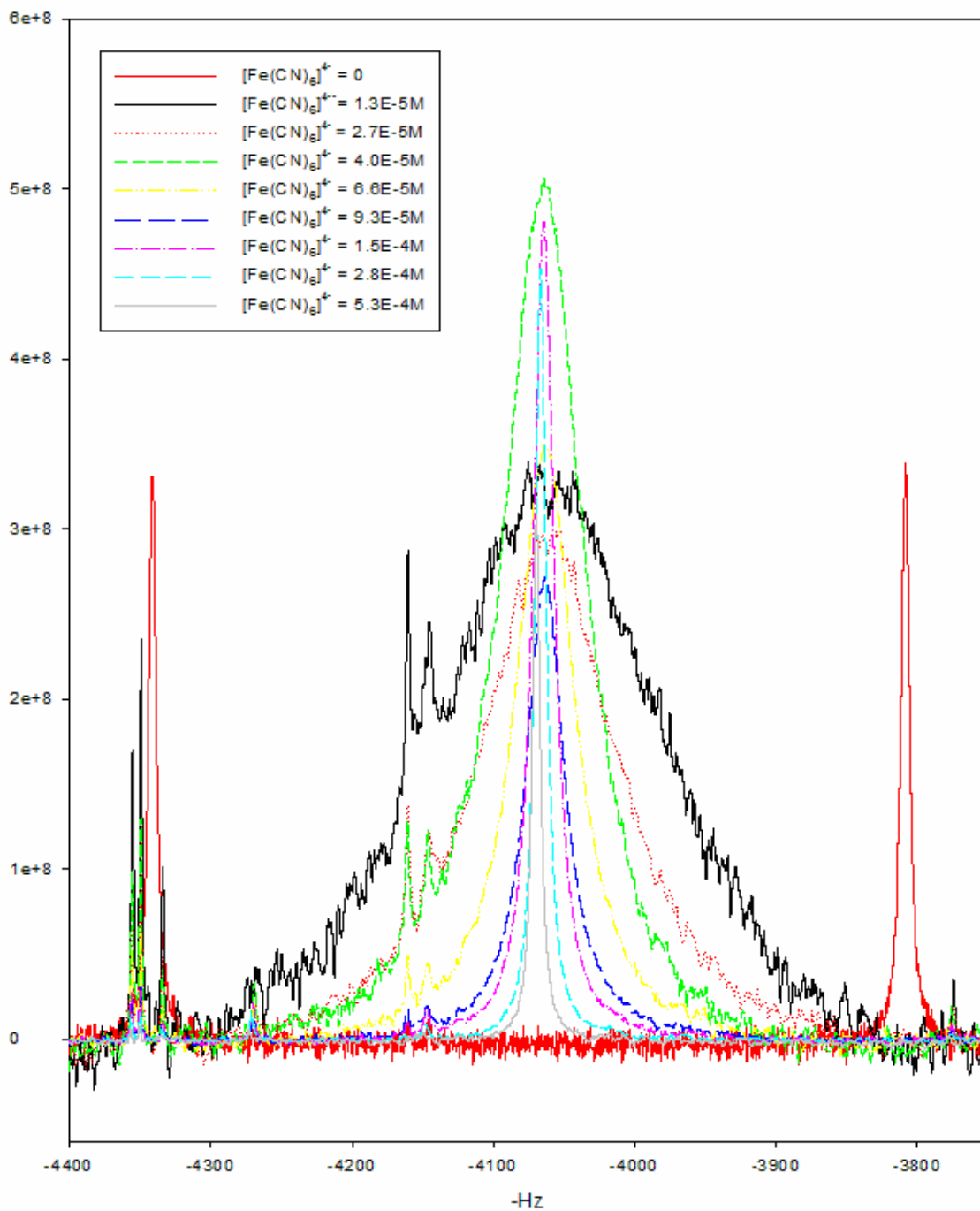


Figure 3-7. ^{19}F NMR spectra of the equimolar $[(\text{NH}_3)_5(3\text{-tfmpy})\text{Ru}^{\text{II/III}}]^{2+/3+}$ mixture ($[\text{Ru}^{\text{II}}] = [\text{Ru}^{\text{III}}] = 5.0 \text{ mM}$ in D_2O) as a function of $\text{K}_4\text{Fe}(\text{CN})_6$ (fast exchange rate region reached at $[\text{Fe}(\text{CN})_6^{4-}] > \sim 1.3 \times 10^{-5} \text{ M}$).



The measured rate constants were calculated by Equation 1-31 when the rate was within the slow chemical exchange limit (with Peakfit deconvolution being required once significant peak overlap/shifting became evident). In the case of added $K_4Fe(CN)_6$, however, the rate was in the fast exchange limit very soon into the additions, and Equation 1-36 was used for the rate calculation after $[Fe(CN)_6]^{4-} > 1.3 \times 10^{-2} \text{ mM}$. Tables 3-3 and 3-4 list the measured rate constant data vs. total GP for the salts investigated. The initial rate reported in all cases is at the μ value of 0.04 (GP = 0.18) which corresponds to no added salt and $[A_5Ru^{II}(3\text{-tfmpy})]^{2+} = [A_5Ru^{III}(3\text{-tfmpy})]^{3+} = 5 \text{ mM}$.

Table 3-3. Measured variations in the rates of the $[(\text{NH}_3)_5(3\text{-tfmpy})\text{Ru}^{\text{II/III}}]^{2+/3+}$ self-exchange ET due to the addition of various simple and dicarboxylate salts (based on the width of the Ru^{II} peak and Equation 1-31)

| NaF | | | | NaCl | | | | NaBr | | | |
|---------------------|------|-------------------|---------------------|---------------------|------|--------------------|---------------------|---------------------|------|--------------------|---------------------|
| μ | GP | [F ⁻] | log k_{ex} | μ | GP | [Cl ⁻] | log k_{ex} | μ | GP | [Br ⁻] | log k_{ex} |
| 0.04 ^(a) | 0.18 | 0.00 | 4.12 ± 0.02 | 0.04 ^(a) | 0.18 | 0.00 | 4.12 ± 0.02 | 0.04 ^(a) | 0.18 | 0.00 | 4.12 ± 0.02 |
| 0.07 | 0.21 | 0.03 | 4.15 | 0.07 | 0.21 | 0.03 | 4.42 | 0.07 | 0.21 | 0.03 | 4.56 |
| 0.11 | 0.25 | 0.07 | 4.17 | 0.09 | 0.23 | 0.04 | 4.60 | 0.09 | 0.23 | 0.04 | 4.75 |
| 0.18 | 0.30 | 0.14 | 4.24 | 0.11 | 0.25 | 0.07 | 4.71 | 0.11 | 0.25 | 0.07 | 4.92 |
| 0.44 | 0.40 | 0.40 | 4.31 | 0.18 | 0.30 | 0.14 | 4.93 | 0.18 | 0.30 | 0.14 | 5.14 |
| 1.00 | 0.50 | 0.96 | 4.43 | 0.44 | 0.40 | 0.40 | 5.33 | 0.44 | 0.40 | 0.40 | 5.69 |
| | | | | 1.00 | 0.50 | 0.96 | 5.70 | | | | |

| NaOAc | | | | Na ₂ SO ₄ | | | | Na ₂ Muc | | | | Na ₂ Adip | | | |
|---------------------|------|---------------------|---------------------|---------------------------------|------|----------------------------------|---------------------|---------------------|------|----------------------|---------------------|----------------------|------|-----------------------|---------------------|
| μ | GP | [OAc ⁻] | log k_{ex} | μ | GP | [SO ₄ ²⁻] | log k_{ex} | μ | GP | [muc ²⁻] | log k_{ex} | μ | GP | [adip ²⁻] | log k_{ex} |
| 0.04 ^(a) | 0.18 | 0.00 | 4.12 ± 0.02 | 0.04 ^(a) | 0.18 | 0.00 | 4.12 ± 0.02 | 0.04 ^(a) | 0.18 | 0.00 | 4.12 ± 0.02 | 0.04 ^(a) | 0.18 | 0.00 | 4.12 ± 0.02 |
| 0.07 | 0.21 | 0.03 | 4.11 | 0.06 | 0.20 | 0.01 | 4.70 | 0.07 | 0.21 | 0.01 | 4.34 | 0.07 | 0.21 | 0.009 | 4.17 |
| 0.09 | 0.23 | 0.04 | 4.12 | 0.08 | 0.22 | 0.01 | 4.88 | 0.09 | 0.23 | 0.01 | 4.40 | 0.09 | 0.23 | 0.015 | 4.25 |
| 0.11 | 0.25 | 0.07 | 4.13 | 0.11 | 0.25 | 0.02 | 5.01 | 0.11 | 0.25 | 0.02 | 4.42 | 0.11 | 0.25 | 0.022 | 4.31 |
| 0.18 | 0.30 | 0.14 | 4.17 | 0.15 | 0.28 | 0.04 | 5.07 | 0.18 | 0.30 | 0.05 | 4.55 | 0.18 | 0.30 | 0.046 | 4.33 |
| 0.44 | 0.40 | 0.40 | 4.26 | 0.20 | 0.31 | 0.05 | 5.11 | 0.44 | 0.40 | 0.13 | 4.79 | 0.44 | 0.40 | 0.133 | 4.39 |
| 1.00 | 0.50 | 0.96 | 4.40 | 0.29 | 0.35 | 0.08 | 5.10 | 1.00 | 0.50 | 0.32 | 4.89 | 1.00 | 0.50 | 0.318 | 4.51 |
| | | | | 0.44 | 0.40 | 0.13 | 5.11 | | | | | | | | |
| | | | | 1.00 | 0.50 | 0.32 | 5.14 | | | | | | | | |

a) the initial ionic strength of 0.04 was due to the initial concentration of $\text{Ru}^{\text{II/III}} = 5.0 \text{ mM}$

Table 3-4. Rates of $[(\text{NH}_3)_5(3\text{-tfmpy})\text{Ru}^{\text{II/III}}]^{2+/3+}$ self-exchange ET due to the addition of $\text{K}_4\text{M}(\text{CN})_6$, M= Ru, Os, Fe (based on Ru^{II} peak)

| $\text{K}_4\text{Ru}(\text{CN})_6$ | | | | $\text{K}_4\text{Os}(\text{CN})_6$ | | | | $\text{K}_4\text{Fe}(\text{CN})_6$ | | | |
|------------------------------------|---------------------------------|---------|----------------------------|------------------------------------|---------------------------------|---------|----------------------------|------------------------------------|---------------------------------|---------|----------------------------|
| μ | $[\text{Ru}(\text{CN})_6^{4-}]$ | GP | $\log k_{\text{ex}}^{(a)}$ | μ | $[\text{Os}(\text{CN})_6^{4-}]$ | GP | $\log k_{\text{ex}}^{(a)}$ | μ | $[\text{Fe}(\text{CN})_6^{4-}]$ | GP | $\log k_{\text{ex}}^{(b)}$ |
| 0.04500 | 0.00000 | 0.17501 | 4.12 ± 0.02 | 0.04500 | 0.00000 | 0.17501 | 4.12 ± 0.02 | 0.045 | 0.00000 | 0.17501 | 4.12 ± 0.02 |
| 0.04510 | 0.00001 | 0.17517 | 4.15 | 0.04510 | 0.00001 | 0.17517 | 4.41 | 0.04510 | 0.00001 | 0.17517 | 5.77 |
| 0.04521 | 0.00003 | 0.17534 | 4.22 | 0.04521 | 0.00003 | 0.17534 | 4.61 | 0.04521 | 0.00003 | 0.17534 | 6.25 |
| 0.04551 | 0.00007 | 0.17583 | 4.43 | 0.04551 | 0.00007 | 0.17583 | 4.84 | 0.04531 | 0.00004 | 0.17550 | 6.48 |
| 0.04582 | 0.00011 | 0.17632 | 4.56 | 0.04582 | 0.00011 | 0.17632 | 5.03 | 0.04551 | 0.00007 | 0.17583 | 6.70 |
| 0.04623 | 0.00016 | 0.17696 | 4.71 | 0.04623 | 0.00016 | 0.17696 | 5.15 | 0.04572 | 0.00009 | 0.17616 | 6.84 |
| 0.04704 | 0.00026 | 0.17823 | 4.86 | 0.04704 | 0.00026 | 0.17823 | 5.34 | 0.04613 | 0.00015 | 0.17681 | 7.03 |
| 0.04804 | 0.00039 | 0.17978 | 4.98 | 0.04804 | 0.00039 | 0.17978 | 5.43 | 0.04714 | 0.00028 | 0.17839 | 7.30 |
| 0.05000 | 0.00065 | 0.18274 | 5.28 | | | | | 0.04912 | 0.00053 | 0.18143 | 7.59 |
| 0.05377 | 0.00113 | 0.18824 | 5.55 | | | | | 0.05106 | 0.00078 | 0.18432 | 7.73 |

(a) Rates of the self-exchange reaction in the presence of $\text{K}_4\text{Ru}(\text{CN})_6$ and $\text{K}_4\text{Os}(\text{CN})_6$ were obtained from the width of Ru^{II} peaks and application of Equation 1-31 (and deconvolution of the line widths using PeakFit when necessary).

(b) Rates of the self-exchange reaction in the presence of $\text{K}_4\text{Fe}(\text{CN})_6$ were obtained from the widths of both the Ru^{II} and Ru^{III} peaks and application of Equation 1-36.

As explained earlier, Debye-Huckel theory provides a theoretical prediction (Equation 3-9) for how k_{ex} should respond to GP under sufficiently-dilute conditions. Figures 3-8 and Figure 3-9 show the rate vs. GP plots obtained for the simple and dicarboxylate salts and then the $K_4M(CN)_6$ (M= Fe, Os, Ru) family of salts, respectively. The early slopes of all the curves in Figure 3-8 and Figure 3-9 are listed in Table 3-5.

Figure 3-8. Rates ($\log k_{\text{ex}}$ vs GP) for the $[(\text{NH}_3)_5(3\text{-tfmpy})\text{Ru}^{\text{II/III}}]^{2+/3+}$ self-exchange reaction in D_2O with addition of various simple sodium salts (Based on Ru^{II} peak, $[\text{Ru}^{\text{II}}] = [\text{Ru}^{\text{III}}] = 5.0 \text{ mM}$)

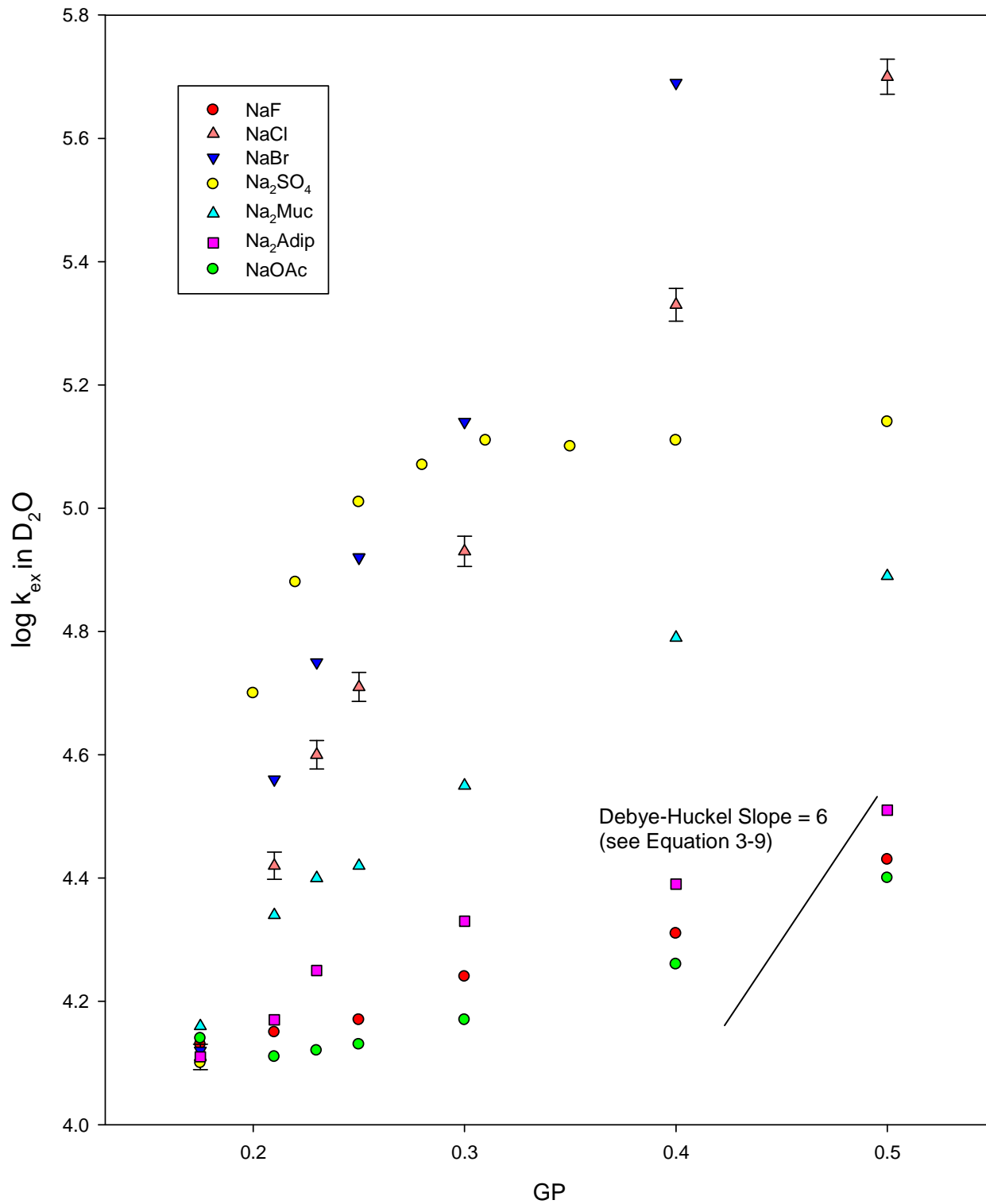


Figure 3-9. Rates ($\log k_{\text{ex}}$ vs GP) for the $[(\text{NH}_3)_5(3\text{-tfmpy})\text{Ru}^{\text{II/III}}]^{2+/3+}$ self-exchange in D_2O with addition of $\text{K}_4\text{M}^{\text{II}}(\text{CN})_6$ effect ($\text{M}=\text{Fe, Os, Ru}$; $[\text{Ru}^{\text{II}}] = [\text{Ru}^{\text{III}}] = 5.0 \text{ mM}$)

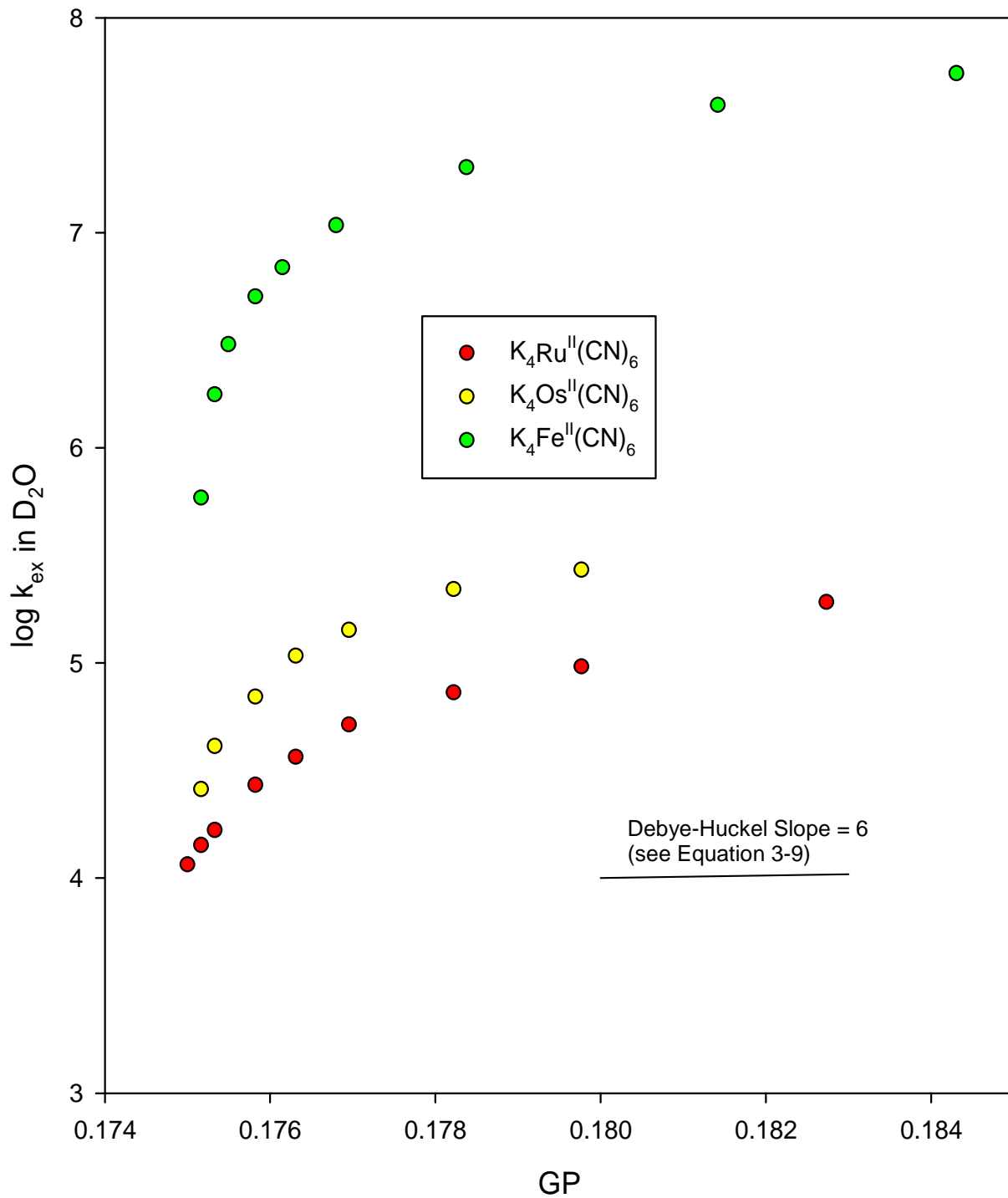


Table 3-5. Early and late slopes in the log k_{ex} vs GP plots shown in Figures 3-7 and 3-8 for reaction 3-2 in D₂O due to the addition of various salts at 25 °C ($[R^{II}] = [R^{III}] = 5.0$ mM)

| Salt | Early Slope | Late Slope |
|------------------------------------|-------------------------------|------------------------------|
| NaF | 0.92 ± 0.05 (GP 0.175-0.500) | 0.92 ± 0.05 (GP 0.175-0.500) |
| NaCl | 8.2 ± 0.6 (GP 0.175-0.23) | 4.0 ± 0.1 (GP 0.25-0.50) |
| NaBr | 10.7 ± 0.7 (GP 0.175-0.25) | 5.2 ± 0.3 (GP 0.25-0.40) |
| NaOAc | 0.5 ± 0.0 (GP 0.21-0.25) | 1.07 ± 0.05 (GP 0.25-0.50) |
| Na ₂ SO ₄ | 6.1 ± 0.8 (GP 0.20-0.25) | 0.25 ± 0.07 (GP 0.28-0.5) |
| Na ₂ Muc | 3.6 ± 0.7 (GP 0.175-0.25) | 1.9 ± 0.3 (GP 0.25-0.5) |
| Na ₂ adip | 2.7 ± 0.0 (GP 0.175-0.25) | 0.8 ± 0.1 (GP 0.25-0.5) |
| K ₄ Ru(CN) ₆ | 539 ± 41 (GP 0.1750-0.1782) | 118 ± 11 (GP 0.1782-0.1882) |
| K ₄ Os(CN) ₆ | 832 ± 119 (GP 0.1751-0.1770) | 186 ± 32 (GP 0.1770-0.1798) |
| K ₄ Fe(CN) ₆ | 2180 ± 440 (GP 0.1751-0.1762) | 170 ± 27 (GP 0.1760-0.1843) |

According to Equation 3-9, the idealized Debye-Huckel slope of all the curves in Figure 3-8 and Figure 3-9 should be 6 (since $Z_A Z_B = 2 \times 3 = 6$ for the Ru^{III} self-exchange reaction studied here). What we observe, however, is that all the curves have the early slopes different than 6 except for the early portion for Na₂SO₄ as the added salt. Importantly, only NaF showed the predicted *linear* behavior over the entire GP range, and it had the very shallow slope of 0.92 ± 0.05. Previous work by Sista⁷ has shown that NaF and KF behave as nearly-ideal added salts in pseudo-self exchange ET reactions carried out by stopped-flow at reactants concentrations of ~10⁻⁴ M. All other salts, NaCl, NaBr, Na₂SO₄, Na₂muc and Na₂adip exhibited curvature in their behavior with a higher slope in the low GP range and followed by a shallower slope in the high GP range (with much higher values than the ones seen here by NMR at 5.0 mM reactants).

In our work, NaOAc as added salts results in the smallest early slope 0.50 ± 0.00 and at GP 0.25 - 0.50, and the slope increased a little bit to 1.07 ± 0.05 at high GP. In Inagaki's ^{19}F NMR work⁵ (done with $\text{Ru}^{\text{II/III}} = 3 \text{ mM}$), she also observed a falling slope for NaOAc (slope = 5.1 ± 1.5 for GP = 0.141 - 0.230 and slope = 0.1 ± 0.5 for GP = 0.230-0.480) in the higher GP range which was thought to be possibly due to increased pH of the solutions at high GP due to the basicity of OAc^- . There is a well-known decomposition disproportionation of Ru^{III} to Ru^{II} and Ru^{IV} in water at $\text{pH} > \sim 7.5$,³⁵ and loss of some fraction of the Ru^{III} complex by this route would affect the measured rates. In this current study, however, all experiments were conducted at the higher reactants concentration of $\text{Ru}^{\text{II/III}} = 5.0 \text{ mM}$, which may be enough to suppress the Ru^{III} disproportionation process.

The results for NaBr, NaCl and Na_2SO_4 agree well with Inagaki's study, even though the reactants' concentrations were different. NaBr and NaCl showed the same trends in their curvature with the early slope in the lower GP range being slightly more than doubled compared to the later slope at higher GP (the slope of NaBr went from 10.7 to 5.2 and the slope of NaCl went from 8.2 to 4.0). As for Na_2SO_4 , the lower GP part (slope = 6.1 ± 0.8) of the curve is much steeper than the later part (slope = 0.25 ± 0.07). In the case of the dicarboxylic dianions, they did not show any of the striking large catalytic rate enhancements seen in the stopped-flow experiments reported by Inagaki and others.⁴⁻⁷ However, at $[\text{Ru}^{\text{II}}] = [\text{Ru}^{\text{III}}] = 5.0 \text{ mM}$ our NMR results here do agree with her NMR results reported from experiments done at 3 mM reactants concentration. We found that both Na_2muc and Na_2adip showed moderate (early/late) slopes which were $3.6 \pm 0.7 / 1.9 \pm 0.3$ and $2.7 \pm 0.0 / 0.8 \pm 0.1$, respectively. Inagaki⁵ found $4.8 \pm 0.7 / 2.5 \pm 1.0$ and $2.7 \pm 0.3 / -5.2\text{E}-15$. The slightly steeper early slope for muconate seen in our work does not quite exceed the measurement uncertainty.

The rate effects due to added $\text{K}_4\text{Fe}(\text{CN})_6$, $\text{K}_4\text{Os}(\text{CN})_6$ and $\text{K}_4\text{Ru}(\text{CN})_6$ are plotted in a separate graph (Figure 3-9) since now the rates increase so much that if they were on the same graph Figure 3-8, they would essentially look like a straight line perpendicular to the x-axis. $\text{K}_4\text{Fe}(\text{CN})_6$ showed the fastest rate increase of the three, followed by $\text{K}_4\text{Os}(\text{CN})_6$ and then by $\text{K}_4\text{Ru}(\text{CN})_6$ which was the slowest but still much faster than any of the simple salts or dicarboxylate salts shown in Figure 3-8.

Interpretation of the observed kinetic salt effects

One possible origin of the rate enhancements in the presence of added “simple” salts could be the ion-atmosphere effect predicted by the Debye-Huckel-Bronsted model as shown in Equation 3-6. However, this would not explain the clear deviations from linearity exhibited for all but the fluoride salts, and it also leaves open the question of why the measured $\log k_{\text{ex}}$ vs. GP slopes are so low (for the simple salts) as compared to the theoretical slope value of 6.1 and to the large body of previous stopped-flow work.

A competing explanation for the rate enhancement is that they might be related simply to the concentration of the anion of the added salt as would be predicted by the “Olson-Simonson” effect.³⁶ Long ago, Olsen and Simonson observed that for reactions between ions of the same charge sign, the kinetic effect of added “spectator” salts on ionic reactions was in some cases most closely related to (*i.e.*, linearly-correlated with) the concentration and identity of the added ions of opposite sign from the reactant ions rather than to the total ionic strength of the solution change or the resulting change in GP. Their interpretation of the simple concentration-correlated salt effects was that a counter ion (or other ion charge opposite to the reactants) must be ion pairing or specially interacting with the reactive transition state.

In order to check for this effect, we plotted our rates vs. μ (total ionic strength) and vs. concentration of added anion, respectively. The results are shown in Figures 3-

10 through 3-13. Even though the rates were plotted against the total ionic strength and [anion], essentially the same curvature was seen as in the GP plots (similar to the lines in Figure 3-8 and 3-9). Therefore, it is hard for us to say whether the classic “Olson-Simonson” effect is playing a dominant or even a definitive role in these salt effect experiments. It would appear that neither of the simplest, limiting cases (linear in GP or linear in [anions]) is able to explain our observed behavior.

Figure 3-10. Rates ($\log k_{\text{ex}}$ vs μ) for the $[(\text{NH}_3)_5(3\text{-tfmpy})\text{Ru}^{\text{II/III}}]^{2+/3+}$ self-exchange reaction in D_2O with addition of various simple and dicarboxylic sodium salts (Based on Ru^{II} peak, $[\text{Ru}^{\text{II}}] = [\text{Ru}^{\text{III}}] = 5.0 \text{ mM}$)

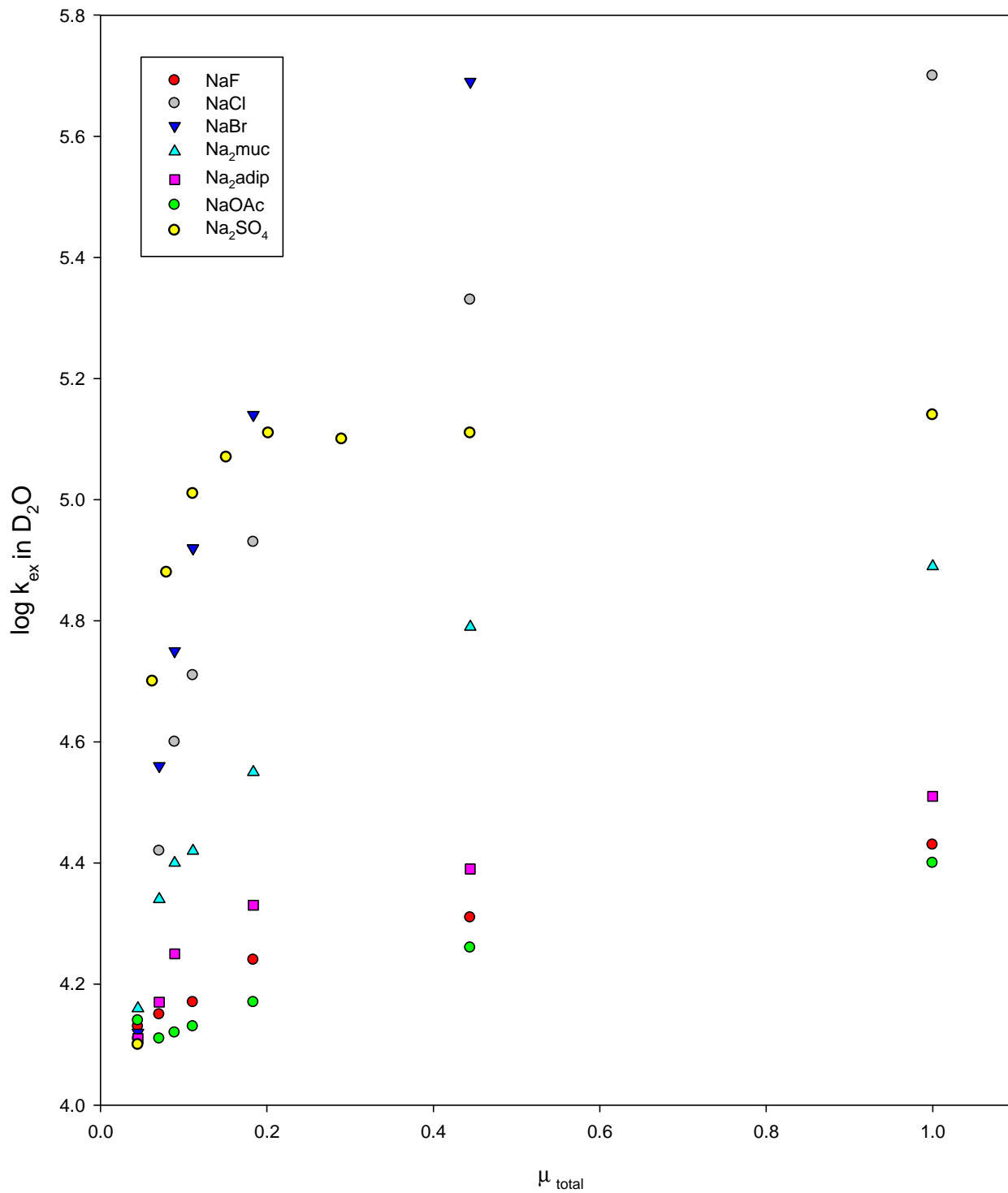


Figure 3-11. Rates ($\log k_{\text{ex}}$ vs [anion]) for the $[(\text{NH}_3)_5(3\text{-tfmpy})\text{Ru}^{\text{II/III}}]^{2+/3+}$ self-exchange reaction in D_2O with addition of various simple and dicarboxylic sodium salts (Based on Ru^{II} peak, $[\text{Ru}^{\text{II}}] = [\text{Ru}^{\text{III}}] = 5.0 \text{ mM}$)

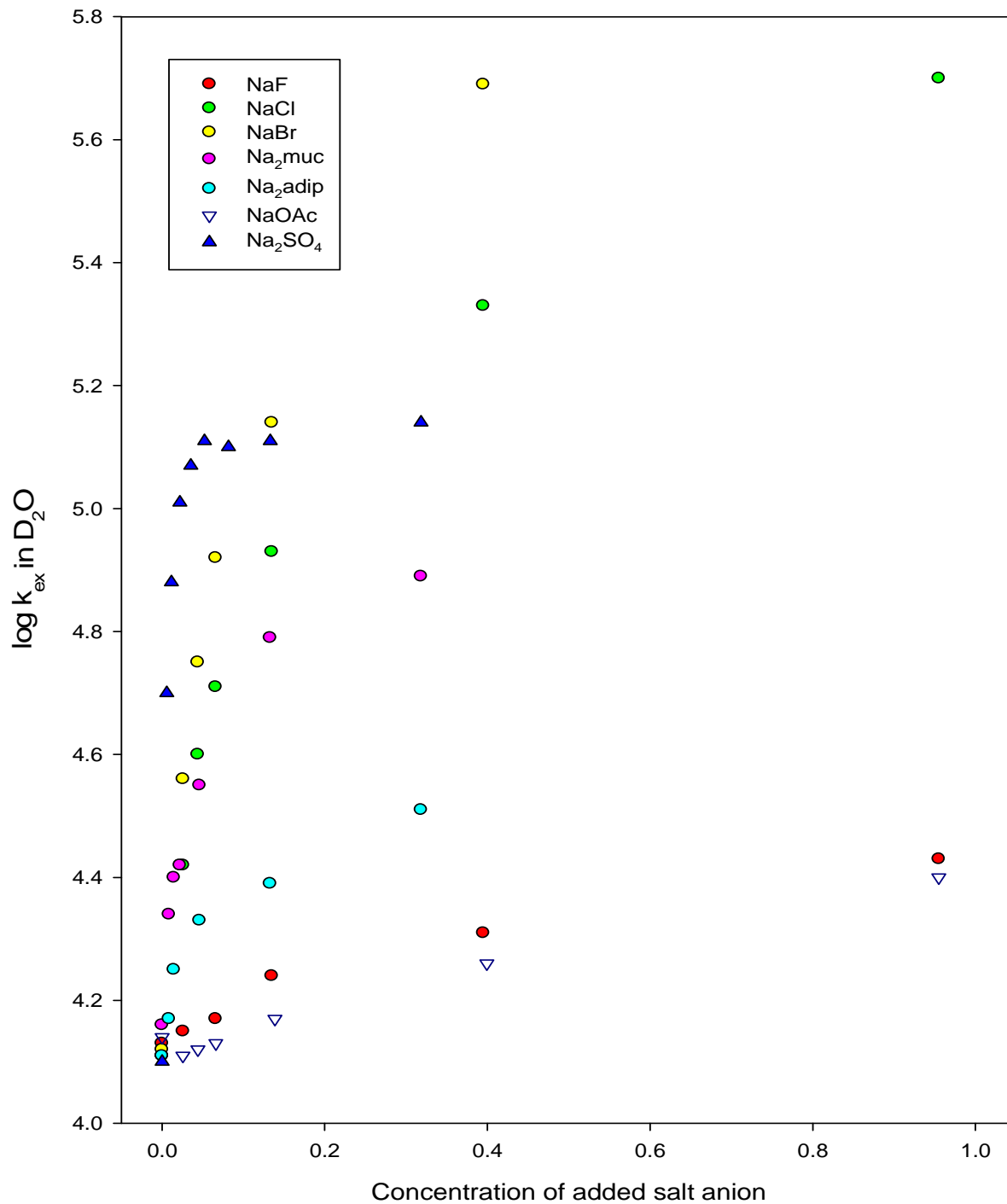


Figure 3-12. Rates ($\log k_{\text{ex}}$ vs μ_{total}) for the $[(\text{NH}_3)_5(3\text{-tfmpy})\text{Ru}^{\text{II/III}}]^{2+/3+}$ self-exchange reaction in D_2O with addition of $\text{K}_4\text{M}(\text{CN})_6$ ($\text{M}=\text{Ru}, \text{Os}$ and Fe) (Based on Ru^{II} peak, $[\text{Ru}^{\text{II}}] = [\text{Ru}^{\text{III}}] = 5.0 \text{ mM}$)

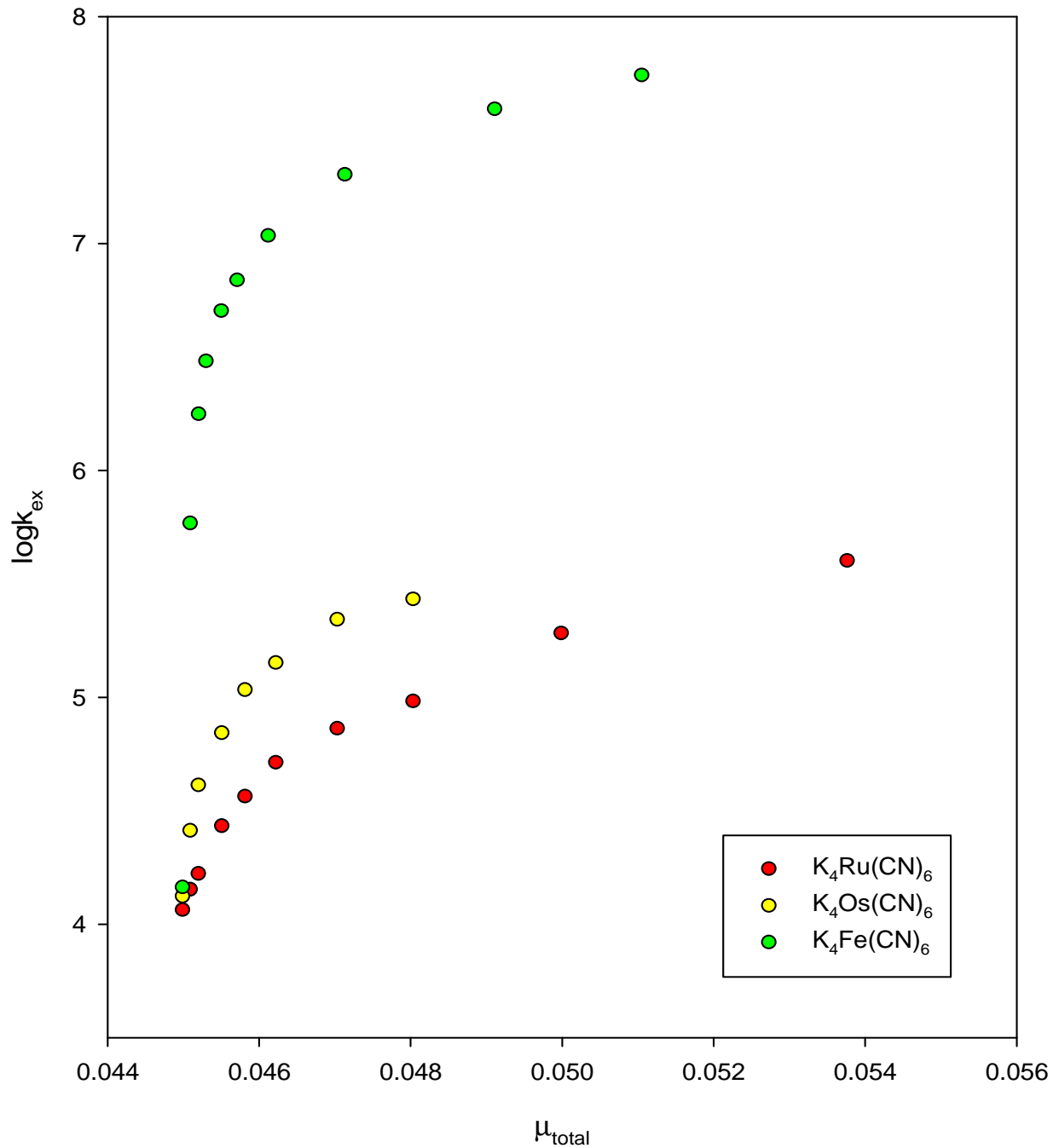
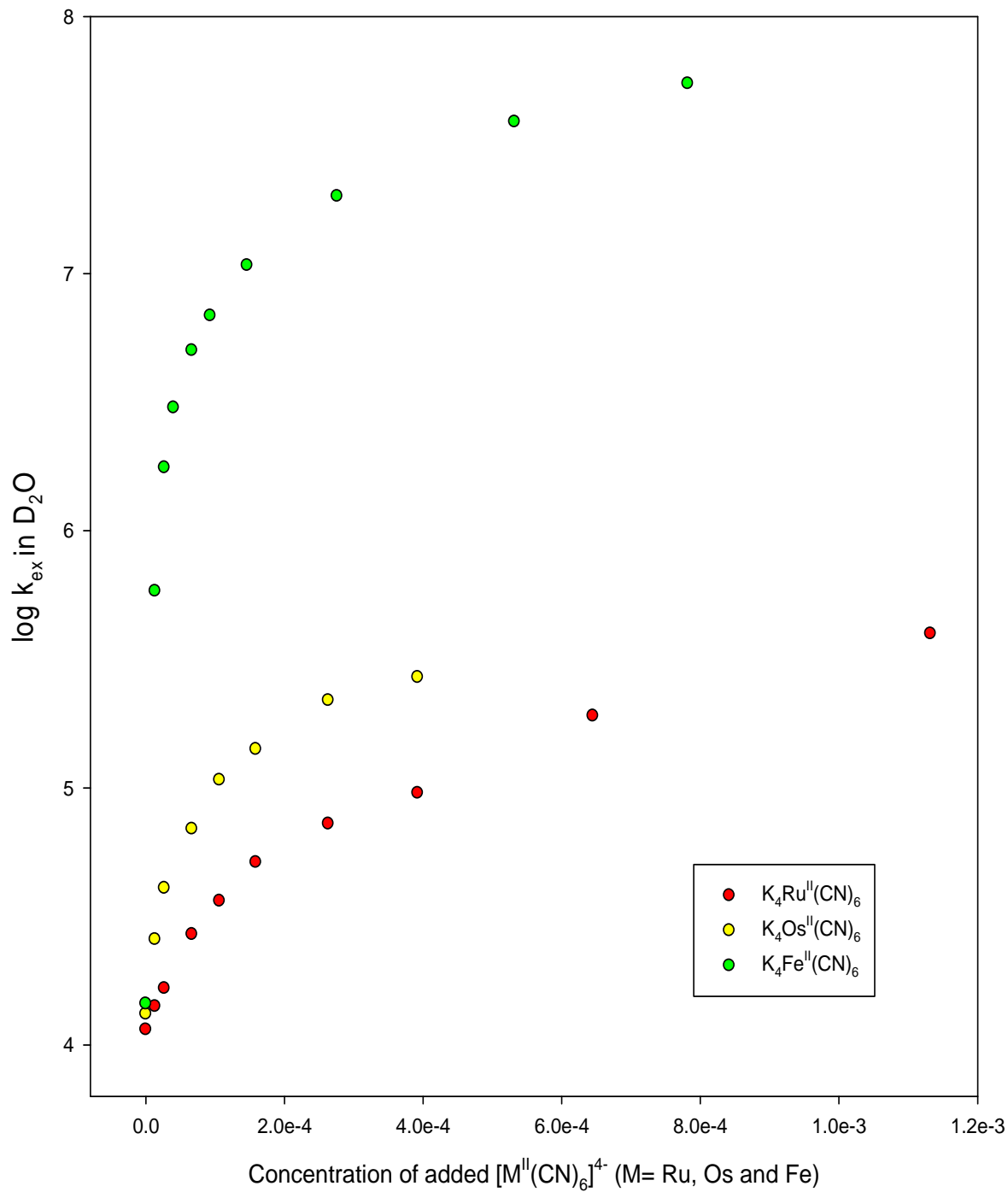


Figure 3-13. Rates ($\log k_{\text{ex}}$ vs $[K^+]$) for the $[(\text{NH}_3)_5(3\text{-tfmpy})\text{Ru}^{\text{II/III}}]^{2+/3+}$ self-exchange reaction in D_2O with addition of $\text{K}_4\text{M}(\text{CN})_6$ ($\text{M}=\text{Ru}, \text{Os}$ and Fe) (Based on Ru^{II} peak, $[\text{Ru}^{\text{II}}] = [\text{Ru}^{\text{III}}] = 5.0 \text{ mM}$)



From the curvatures seen in all these plots, it is clear that no simple relationship can explain the observed behaviors over our data ranges. For this reason we turned to kinetic modeling studies based on detailed calculation of rates of association / dissociation of relevant ion pairs and encounter complexes using Equations 3-11 to 3-13. These calculations will be described in the next section.

The origin of the dramatic rate increases seen upon addition of very small amounts of the $K_4M(CN)_6$ salts is probably related to the known thermodynamically favored (and presumably kinetically rapid) ion pair formation between $M(CN)_6^{4-}$ and $(NH_3)_5Ru^{III}L^{3+}$ in water.³⁴ There is sufficient $Ru^{III}-M^{II}(CN)_6^{4-}$ electronic coupling to allow for a clearly-resolved IPCT (ion-pair charge transfer) absorption band in their systems, and this might be expected here to facilitate strong superexchange catalysis of the thermal ET self-exchange reaction due to enhanced donor/acceptor electronic coupling in the (presumed) ternary association complex $[(NH_3)_5(3\text{-tfmpy})Ru^{II}, M^{II}(CN)_6, Ru^{III}(NH_3)_5(3\text{-tfmpy})]^+$ leading to the transition state for the self-exchange reaction.

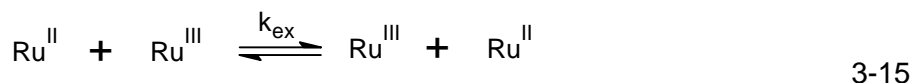
If “hole transfer” superexchange³⁷ were to happen inside a ternary association complex, it would be expected to depend upon the ease of hole creation on any $M^{II}(CN)_6^{4-}$ bridging species which might be present. In the case of the $K_4M(CN)_6$ salts, the Fe^{II} and Os^{II} species could both provide an energetically lower-lying HOMO between $(NH_3)_5(3\text{-tfmpy})Ru^{II}$ and $(NH_3)_5(3\text{-tfmpy})Ru^{III}$ reactant ions than the $Ru^{II}(CN)_6^{4-}$ would since the redox potentials for $M = Fe, Os$ and Ru in $M^{II}(CN)_6^{4-}$ are 0.187, 0.395 and 0.701 (V vs. SCE), respectively.³⁴ In fact, we see in Figure 3-9 that $Fe^{II}(CN)_6^{4-}$ gives the greatest rate enhancement, then Os and lastly Ru . An alternative explanation might be that there is stronger ion pairing between $Fe^{II}(CN)_6^{4-}$ and $(NH_3)_5(3\text{-tfmpy})Ru^{III}$ than with Os and $Ru(CN)_6^{4-}$. More ion pairing could also lead to faster ET, and attempts were made to measure and compare the ion-pair formation constants of the three $M(CN)_6^{4-}$

species with $(\text{NH}_3)_5(3\text{-tfmpy})\text{Ru}^{\text{III}}$. The results from these will be discussed later in this chapter.

Kinetic Modeling

As seen in Figure 3-8, only the sodium fluoride, acetate, and adipate salts give the linear behavior for $\log k_{\text{ex}}$ vs. GP which would be expected on the basis of simple or “innocent” ion-atmosphere effects as described by Debye-Huckel theory. However, the slopes here are again much lower than the Debye-Huckel prediction as was also reported by Inagaki (working at 3 mM reactants concentration). Following the kinetic formalism already employed by Inagaki⁵ and Sista,⁷ we infer that those salts which give rise to curved lines in Figures 3-7 and 3-8 must be providing some degree of “extra” catalysis to the reaction above and beyond simple ionic strength effects.

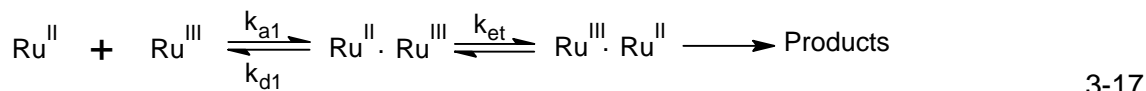
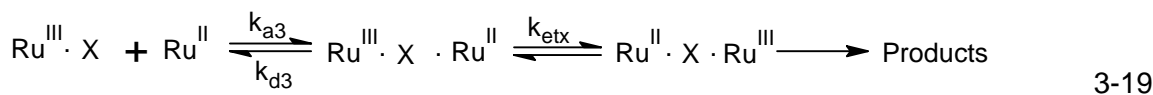
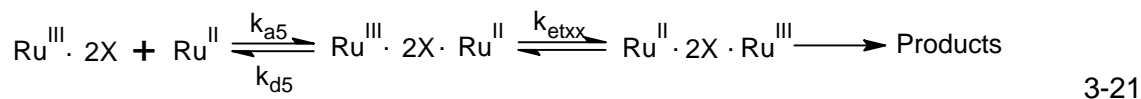
In order to arrive at a plausible mechanism behind the salt catalysis effect on the $(\text{NH}_3)_5\text{Ru}^{\text{II/III}}(3\text{-tfmpy})^{2+/3+}$ reaction, we built a 3-channel kinetic model for how the simple salts such as NaF, NaCl, NaBr and NaI, might be affecting the reaction rate. The model is as shown below,



For convenience, we will henceforth denote the two rutheniumamine pyridyl reactants in reaction 3-2 simply as Ru^{II} and Ru^{III} respectively. X is the anion of the added salt. According to the second-order rate law,³⁸ we know that the observed rate will vary with concentration as,

$$\text{Rate} = k_{\text{ex}}[\text{Ru}_0^{\text{II}}][\text{Ru}_0^{\text{III}}] \quad 3-16$$

In order to incorporate salt effects into a model for the observed overall rate, we follow Inagaki⁴ and Sista⁷ by considering different reactive “Channels” as shown below,

Channel 1 (no specific catalysis)**Channel 2** (catalysis by one specifically-interacting X)**Channel 3** (catalysis by two X)

Channel 1 will be assumed to respond to added salt *only* in so far as the k_{a1} , k_{d1} and k_{et} rate constants depend on ionic strength (*i.e.*, no specific catalysis by X). The magnitudes of the first two of these vary according to Equation 3-11 and 3-12 discussed previously. The value of k_{et} (the rate of ET within the encounter or “precursor” complex) will be assumed here to have negligible dependence on ionic strength, although there is a body of work which would suggest a very small inverse dependence on μ since rearrangement of the ion-atmosphere around charged reactants can result in a small additional reorganizational barrier as compared to pure solvent.³⁹ Thus in Channel 1, the only adjustable parameter is k_{et} and kinetic simulations (*vide infra*) allow straightforward determination of k_{et} from kinetic data obtained on k_{ex} with no added salt

and/or relatively low-GP portions of the experimental log k_{ex} vs. GP (see Figures 3-8 and 3-9).

Channels 2 and 3 sequentially incorporate specific ion-pairing events first with one then with two of the added salt's anion, X^- . Here again we can rely on Equation 3-11 and 3-12 (and calculated volumes, *vide infra*) to compute the k_{ai} and k_{di} for all the various species involved. Only k_{etx} and k_{etxx} are adjusted to bring the simulated kinetic predictions into agreement with experiment. The ion-pairing step between Ru^{II} and X^- to form $Ru^{II} \cdot X$ was not considered in Channels 2 and 3 because the association of Ru^{III} and X^- is more favorable than with Ru^{II} due to the more acidic nature of Ru^{III} ammine protons. Moreover, analyses of stopped-flow data by Sista⁷ has shown that incorporation of the equilibrium to form $Ru^{II} \cdot X$ has negligible effect on the best-fit value of k_{etxx} .⁴⁰

Based on Channels 1 and 2, the rate equation can be written as,

$$Rate = \frac{k_{a1}}{k_{d1}} k_{et} [Ru_0^{II}] ([Ru_0^{III}] - [Ru^{III} \cdot X]) \quad (CH1)$$

$$+ [Ru^{III} \cdot X] [Ru_0^{II}] \frac{k_{a3}}{k_{d3}} k_{etx} \quad (CH2)$$

3-22

where $[Ru^{III} \cdot X] = \frac{k_{a2}}{k_{d2}} [X] [Ru_0^{III}]$

and X is $Fe(CN)_6^{4-}$, $Os(CN)_6^{4-}$ or $Ru(CN)_6^{4-}$. If Equation 3-22 is expanded and compared to Equation 3-16, we obtain the expression for k_{ex} from the two-channel model as follows,

$$k_{ex} = \frac{k_{a1}}{k_{d1}} k_{et} \left(1 - \frac{k_{a2}}{k_{d2}} [X]\right) + \frac{k_{a2}}{k_{d2}} \frac{k_{a3}}{k_{d3}} k_{etx} [X] \quad 3-23$$

Based on all three channels, the overall rate equation can be written as,

$$Rate = \frac{k_{a1}}{k_{d1}} k_{et} [Ru_0^{II}] ([Ru_0^{III}] - [Ru^{III} \cdot X]) \quad (CH1)$$

$$+ ([Ru_0^{III} \cdot X] - [Ru_0^{III} \cdot 2X]) \frac{k_{a3}}{k_{d3}} k_{etx} [Ru_0^{II}] \quad (CH2)$$

$$+ [Ru_0^{III} \cdot 2X] [Ru_0^{II}] \frac{k_{a5}}{k_{d5}} k_{etxx} \quad (CH3)$$

3-24

where $[Ru^{III} \cdot X] = \frac{k_{a2}}{k_{d2}} [X] [Ru_0^{III}]$ and $[Ru^{III} \cdot 2X] = \frac{k_{a4}}{k_{d4}} [Ru^{III} \cdot X] [X]$.

If Equation 3-24 is expanded and compared with Equation 3-16, the following equation is obtained for the overall second-order rate constant k_{ex} , which would be observed in a kinetics experiment.

$$k_{ex} = \frac{k_{a1}}{k_{d1}} k_{et} \left(1 - \frac{k_{a2}}{k_{d2}} [X]\right) + \frac{k_{a2}}{k_{d2}} \frac{k_{a3}}{k_{d3}} \left(1 - \frac{k_{a4}}{k_{d4}} [X]\right) [X] k_{etx} + \frac{k_{a2}}{k_{d2}} \frac{k_{a4}}{k_{d4}} \frac{k_{a5}}{k_{d5}} [X]^2 k_{etxx} \quad 3-25$$

In performing these kinetic rate predictions as a function of reactants' concentrations and total solution ionic strength (used as GP in our final plots), the relevant association/dissociation rate constants k_{a1} , k_{d1} , k_{a2} , k_{d2} , k_{a3} , k_{d3} , k_{a4} , k_{d4} , k_{a5} and k_{d5} were calculated using MathCad 14.0 (Parametric Technology Corporation) to implement Equations 3-11 and 3-13. The radii needed for Equations 3-11 and 3-13 are listed in Table 3-6. Tables 3-7 to 3-9 give the k_{ai} and k_{di} values as a function of GP (and μ) for NaF, NaCl and NaBr.

Best-fit simulation results are listed in Tables 3-10 to 3-12 and shown in Figures 3-14 to 3-16. From the figures, we see how the best-fit values of k_{et} , k_{etx} and k_{etxx} allow our three-channel model to follow the experimental accelerations due to added NaF, NaCl and NaBr. Apparently, the two-channel model didn't provide a good fit to the

experimental data as the three-channel model. This is probably due to the high concentration of added salts (0.026 M to 0.995 M) and the third channel cannot be simply neglected as in the cases of added $\text{M}(\text{CN})_6^{4-}$ (1.33×10^5 M to 1.13×10^{-3} M) that will be discussed later.

Table 3-6. Radii of the ions, complexes and ion pairs used in calculation of the association/dissociation constants ^a

| | Ion | Radius(Å) |
|----|---|-----------|
| 1 | $(\text{NH}_3)_5\text{Ru}^{\text{II}}(3\text{-tfmpy})$ | 4.64 |
| 2 | $(\text{NH}_3)_5\text{Ru}^{\text{III}}(3\text{-tfmpy})$ | 4.49 |
| 3 | F^- | 1.5 |
| 4 | Cl^- | 1.90 |
| 5 | Br^- | 2.00 |
| 6 | $\text{Ru}^{\text{III}}\cdot\text{F}^-$ | 4.55 |
| 7 | $\text{Ru}^{\text{III}}\cdot 2\text{F}^-$ | 4.60 |
| 8 | $\text{Ru}^{\text{III}}\cdot\text{Cl}^-$ | 4.60 |
| 9 | $\text{Ru}^{\text{III}}\cdot 2\text{Cl}^-$ | 4.70 |
| 10 | $\text{Ru}^{\text{III}}\cdot\text{Br}^-$ | 4.62 |
| 11 | $\text{Ru}^{\text{III}}\cdot 2\text{Br}^-$ | 4.74 |

a) The radii of ions 1 to 5 were calculated by Dr. Curtis using B3LYP density functional method and the SDD/6-31+g(d,p) basis set using the “PCM” (polarizable continuum model and volume = tight keyword) contained within Gaussian 03 for windows.⁴¹ The radii of complex ions 6-11 were obtained by finding the radius of a sphere with equivalent volume. For example,

$$V_{\text{Ru}^{\text{III}} \cdot \text{F}^-} = \frac{4}{3} \pi (r_{\text{Ru}^{\text{III}}}^3 + r_{\text{F}^-}^3) = \frac{4}{3} \pi (4.49^3 + 1.50^3) \Rightarrow r_{\text{Ru}^{\text{III}} \cdot \text{F}^-} = 4.55$$

where $V_{\text{Ru}^{\text{III}} \cdot \text{F}^-}$ is the volume of ion $[\text{Ru}^{\text{III}} \cdot \text{F}^-]$ and we assume it is the sum of $V_{\text{Ru}^{\text{III}}}$ and V_{F^-} .

Table 3-7. Association and dissociation rate constants calculated for application of Equation 3-25 to reaction 3-2 in the presence of added NaF ^a

| GP | μ | [F ⁻] | k_{a1} | k_{d1} | k_{a2} | k_{d2} | k_{a3} | k_{d3} | k_{a4} | k_{d4} | k_{a5} | k_{d5} |
|------|-------|-------------------|----------|----------|----------|----------|----------|----------|----------|----------|----------|----------|
| 0.18 | 0.05 | 0.000 | 1.53E+09 | 1.44E+10 | | | | | | | | |
| 0.21 | 0.07 | 0.026 | 1.85E+09 | 1.35E+10 | 2.04E+10 | 3.51E+09 | 1.41E+09 | 2.68E+10 | 1.67E+10 | 6.28E+09 | 5.02E+09 | 5.99E+09 |
| 0.25 | 0.11 | 0.066 | 2.23E+09 | 1.24E+10 | 1.91E+10 | 3.99E+09 | 1.72E+09 | 2.53E+10 | 1.59E+10 | 6.80E+09 | 5.27E+09 | 5.75E+09 |
| 0.30 | 0.18 | 0.135 | 2.71E+09 | 1.12E+10 | 1.79E+10 | 4.65E+09 | 2.13E+09 | 2.34E+10 | 1.51E+10 | 7.47E+09 | 5.54E+09 | 5.48E+09 |
| 0.40 | 0.44 | 0.395 | 3.64E+09 | 9.20E+09 | 1.58E+10 | 6.12E+09 | 3.04E+09 | 1.96E+10 | 1.38E+10 | 8.85E+09 | 5.98E+09 | 5.04E+09 |
| 0.50 | 1.00 | 0.955 | 4.49E+09 | 7.63E+09 | 1.43E+10 | 7.80E+09 | 4.01E+09 | 1.63E+10 | 1.28E+10 | 1.03E+10 | 6.33E+09 | 4.68E+09 |

a) calculations made using complex and other radius values listed in Table 3-6

Table 3-8. Association and dissociation rate constants calculated for application of Equation 3-25 to reaction 3-2 in the presence of added NaCl ^a

| GP | μ | [Cl] | k_{a1} | k_{d1} | k_{a2} | k_{d2} | k_{a3} | k_{d3} | k_{a4} | k_{d4} | k_{a5} | k_{d5} |
|------|-------|-------|----------|----------|----------|----------|----------|----------|----------|----------|----------|----------|
| 0.18 | 0.045 | 0.000 | 1.53E+09 | 1.44E+10 | | | | | | | | |
| 0.21 | 0.071 | 0.026 | 1.85E+09 | 1.35E+10 | 1.74E+10 | 3.01E+09 | 3.21E+09 | 9.06E+09 | 1.44E+10 | 5.05E+09 | 5.06E+09 | 5.76E+09 |
| 0.23 | 0.089 | 0.044 | 2.04E+09 | 1.29E+10 | 1.69E+10 | 3.20E+09 | 3.39E+09 | 8.76E+09 | 1.41E+10 | 5.24E+09 | 5.18E+09 | 5.64E+09 |
| 0.25 | 0.111 | 0.066 | 2.23E+09 | 1.24E+10 | 1.64E+10 | 3.40E+09 | 3.58E+09 | 8.48E+09 | 1.38E+10 | 5.43E+09 | 5.30E+09 | 5.53E+09 |
| 0.30 | 0.184 | 0.135 | 2.71E+09 | 1.12E+10 | 1.53E+10 | 3.92E+09 | 4.01E+09 | 7.82E+09 | 1.31E+10 | 5.93E+09 | 5.57E+09 | 5.28E+09 |
| 0.40 | 0.444 | 0.395 | 3.64E+09 | 9.20E+09 | 1.37E+10 | 5.06E+09 | 4.77E+09 | 6.73E+09 | 1.20E+10 | 6.94E+09 | 6.01E+09 | 4.85E+09 |
| 0.50 | 1.000 | 0.955 | 4.49E+09 | 7.63E+09 | 1.24E+10 | 6.31E+09 | 5.40E+09 | 5.88E+09 | 1.12E+10 | 7.96E+09 | 6.35E+09 | 4.51E+09 |

a) calculations made using complex and other radius values listed in Table 3-6

Table 3-9. Association and dissociation rate constant values calculated for application of Equation 3-25 to reaction 3-2 in the presence of added NaBr ^a

| GP | μ | [Br ⁻] | k_{a1} | k_{d1} | k_{a2} | k_{d2} | k_{a3} | k_{d3} | k_{a4} | k_{d4} | k_{a5} | k_{d5} |
|------|-------|--------------------|----------|----------|----------|----------|----------|----------|----------|----------|----------|----------|
| 0.18 | 0.045 | 0.000 | 1.53E+09 | 1.44E+10 | | | | | | | | |
| 0.21 | 0.071 | 0.026 | 1.85E+09 | 1.35E+10 | 1.68E+10 | 2.91E+09 | 3.22E+09 | 8.98E+09 | 1.40E+10 | 4.80E+09 | 5.07E+09 | 5.67E+09 |
| 0.23 | 0.089 | 0.044 | 2.04E+09 | 1.29E+10 | 1.63E+10 | 3.09E+09 | 3.40E+09 | 8.69E+09 | 1.37E+10 | 4.98E+09 | 5.20E+09 | 5.56E+09 |
| 0.25 | 0.111 | 0.066 | 2.23E+09 | 1.24E+10 | 1.59E+10 | 3.28E+09 | 3.59E+09 | 8.41E+09 | 1.34E+10 | 5.16E+09 | 5.32E+09 | 5.45E+09 |
| 0.30 | 0.184 | 0.135 | 2.71E+09 | 1.12E+10 | 1.48E+10 | 3.78E+09 | 4.02E+09 | 7.75E+09 | 1.27E+10 | 5.63E+09 | 5.58E+09 | 5.20E+09 |
| 0.40 | 0.444 | 0.395 | 3.64E+09 | 9.20E+09 | 1.33E+10 | 4.85E+09 | 4.78E+09 | 6.67E+09 | 1.17E+10 | 6.56E+09 | 6.02E+09 | 4.78E+09 |

a) calculations made using complex and other radius values listed in Table 3-6

Table 3-10. Best-fit simulation data for reaction 3-2 at $[Ru^{II}] = [Ru^{III}] = 5.0 \text{ mM}$ in the presence of added NaF

| GP | $\log k_{ex}$ (experimental) | CH1-2 with $k_{et} = 1.20 \times 10^5$ and $k_{etx} = 1.85 \times 10^5$ | CH 1-3 with $k_{et} = 1.20 \times 10^5$, $k_{etx} = 1.00 \times 10^4$ and $k_{etxx} = 2.89 \times 10^4$ |
|------|---------------------------------|---|---|
| 0.21 | 4.15 | 4.19 | 4.15 |
| 0.25 | 4.17 | 4.27 | 4.21 |
| 0.30 | 4.24 | 4.35 | 4.27 |
| 0.40 | 4.31 | 4.45 | 4.33 |
| 0.50 | 4.43 | 4.43 | 4.44 |

Table 3-11. Best-fit simulation data for reaction 3-2 at $[Ru^{II}] = [Ru^{III}] = 5.0 \text{ mM}$ in the presence of added NaCl

| GP | $\log k_{ex}$ (experimental) | CH1-2 with $k_{et} = 1.20 \times 10^5$ and $k_{etx} = 1.50 \times 10^5$ | CH 1-3 with $k_{et} = 1.20 \times 10^5$, $k_{etx} = 2.40 \times 10^4$ and $k_{etxx} = 2.00 \times 10^4$ |
|------|---------------------------------|---|---|
| 0.21 | 4.42 | 4.34 | 4.44 |
| 0.23 | 4.60 | 4.45 | 4.59 |
| 0.25 | 4.71 | 4.54 | 4.71 |
| 0.30 | 5.93 | 4.73 | 4.97 |
| 0.40 | 5.33 | 5.04 | 5.37 |
| 0.50 | 5.70 | 5.29 | 5.70 |

Table 3-12. Best-fit simulation data for reaction 3-2 at $[Ru^{II}] = [Ru^{III}] = 5.0 \text{ mM}$ in the presence of added NaBr

| GP | $\log k_{ex}$ (experimental) | CH1-2 with $k_{et} = 1.20 \times 10^5$ and $k_{etx} = 4.40 \times 10^5$ | CH 1-3 with $k_{et} = 1.20 \times 10^5$, $k_{etx} = 3.90 \times 10^4$ and $k_{etxx} = 4.00 \times 10^4$ |
|------|---------------------------------|---|---|
| 0.21 | 4.56 | 4.58 | 4.57 |
| 0.23 | 4.75 | 4.74 | 4.75 |
| 0.25 | 4.92 | 4.87 | 4.90 |
| 0.30 | 5.14 | 5.13 | 5.20 |
| 0.40 | 5.69 | 5.53 | 5.67 |

Figure 3-14(a). $\log k_{\text{ex}}$ for the $(\text{NH}_3)_5\text{Ru}^{\text{II/III}}(3\text{-tfmpy})^{2+/3+}$ ($[\text{Ru}^{\text{II}}] = [\text{Ru}^{\text{III}}] = 5.0 \text{ mM}$) in D_2O with addition of NaF : experimental data and the best-fit simulation from the 2-channel fitting using Equation 3-23 with $k_{\text{et}} = 1.20 \times 10^5$, $k_{\text{etx}} = 1.85 \times 10^5$

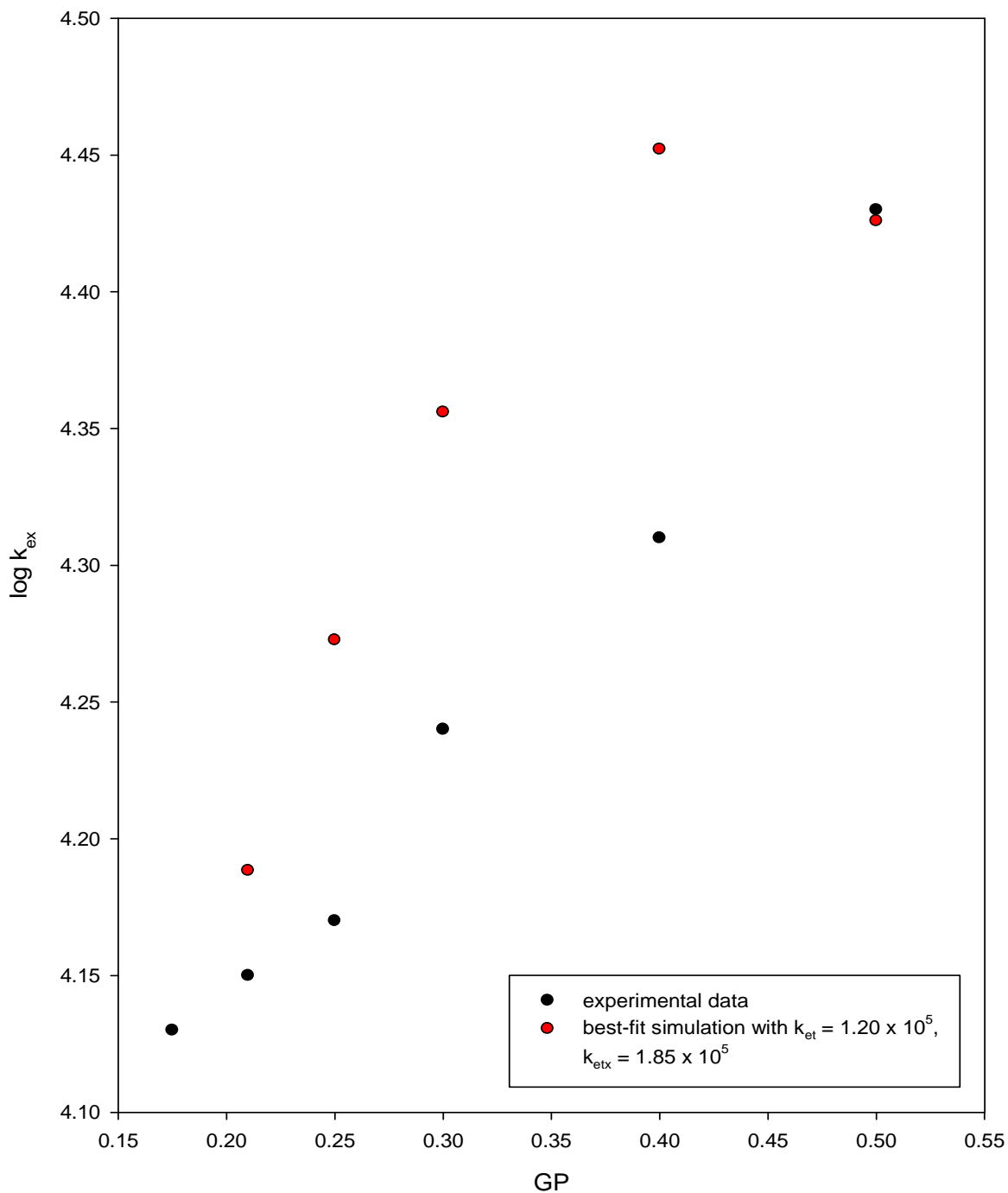


Figure 3-14(b). $\log k_{\text{ex}}$ for the $(\text{NH}_3)_5\text{Ru}^{\text{I/III}}(\text{3-tfmpy})^{2+/3+}$ ($[\text{Ru}^{\text{I}}] = [\text{Ru}^{\text{III}}] = 5.0 \text{ mM}$) in D_2O with addition of NaF : experimental data and the best-fit simulation from 3-channel fitting using Equation 3-25 with $k_{\text{et}} = 1.20 \times 10^5$, $k_{\text{etx}} = 1.00 \times 10^4$ and $k_{\text{etxx}} = 2.89 \times 10^4$

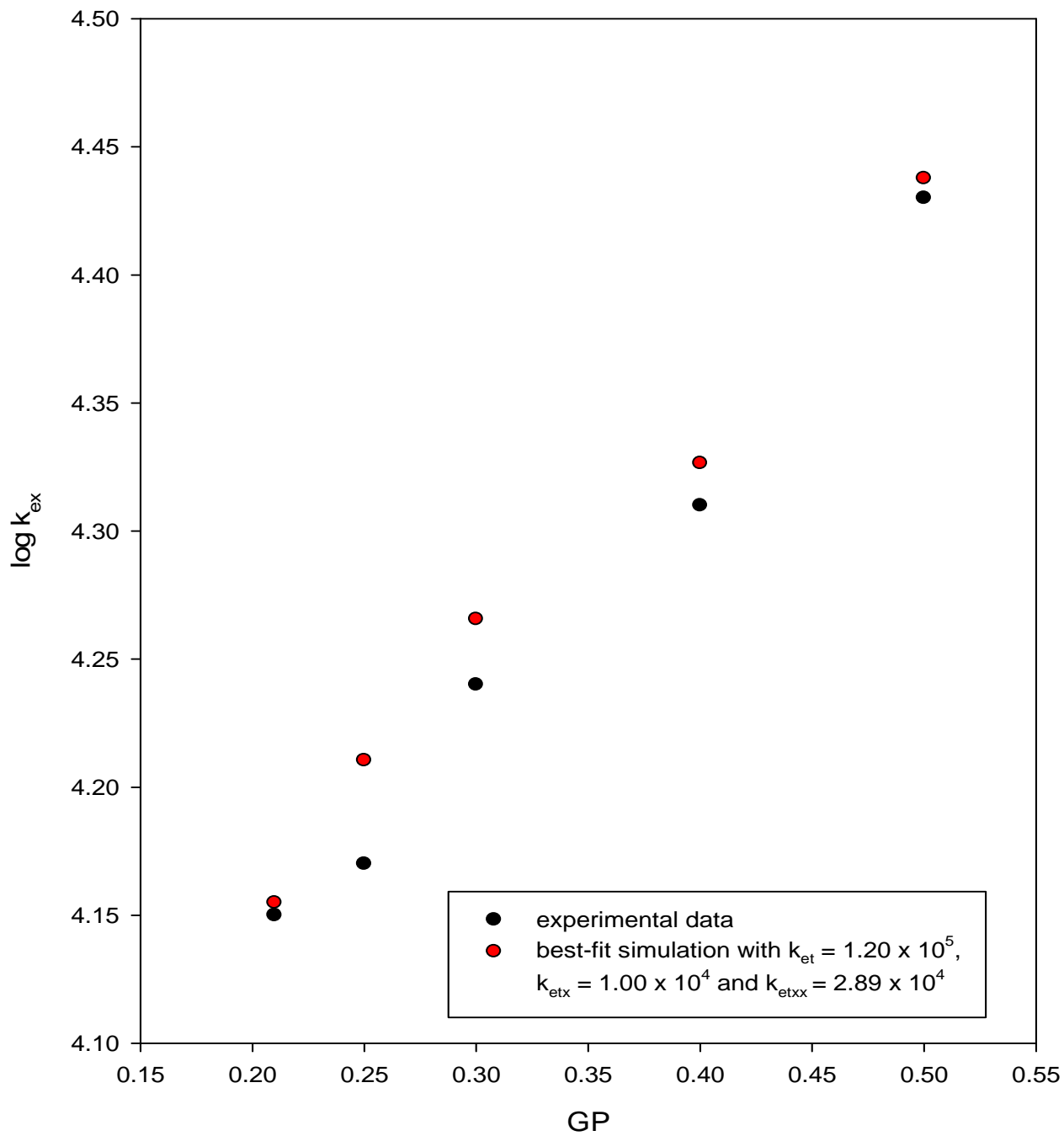


Figure 3-15(a). $\log k_{\text{ex}}$ for the $(\text{NH}_3)_5\text{Ru}^{\text{II/III}}(\text{3-tfmpy})^{2+/3+}$ ($[\text{Ru}^{\text{II}}] = [\text{Ru}^{\text{III}}] = 5.0 \text{ mM}$) in D_2O with addition of NaCl : experimental data and the best-fit simulation from the 2-channel fitting using Equation 3-23 with $k_{\text{et}} = 1.20 \times 10^5$, $k_{\text{etx}} = 1.50 \times 10^5$

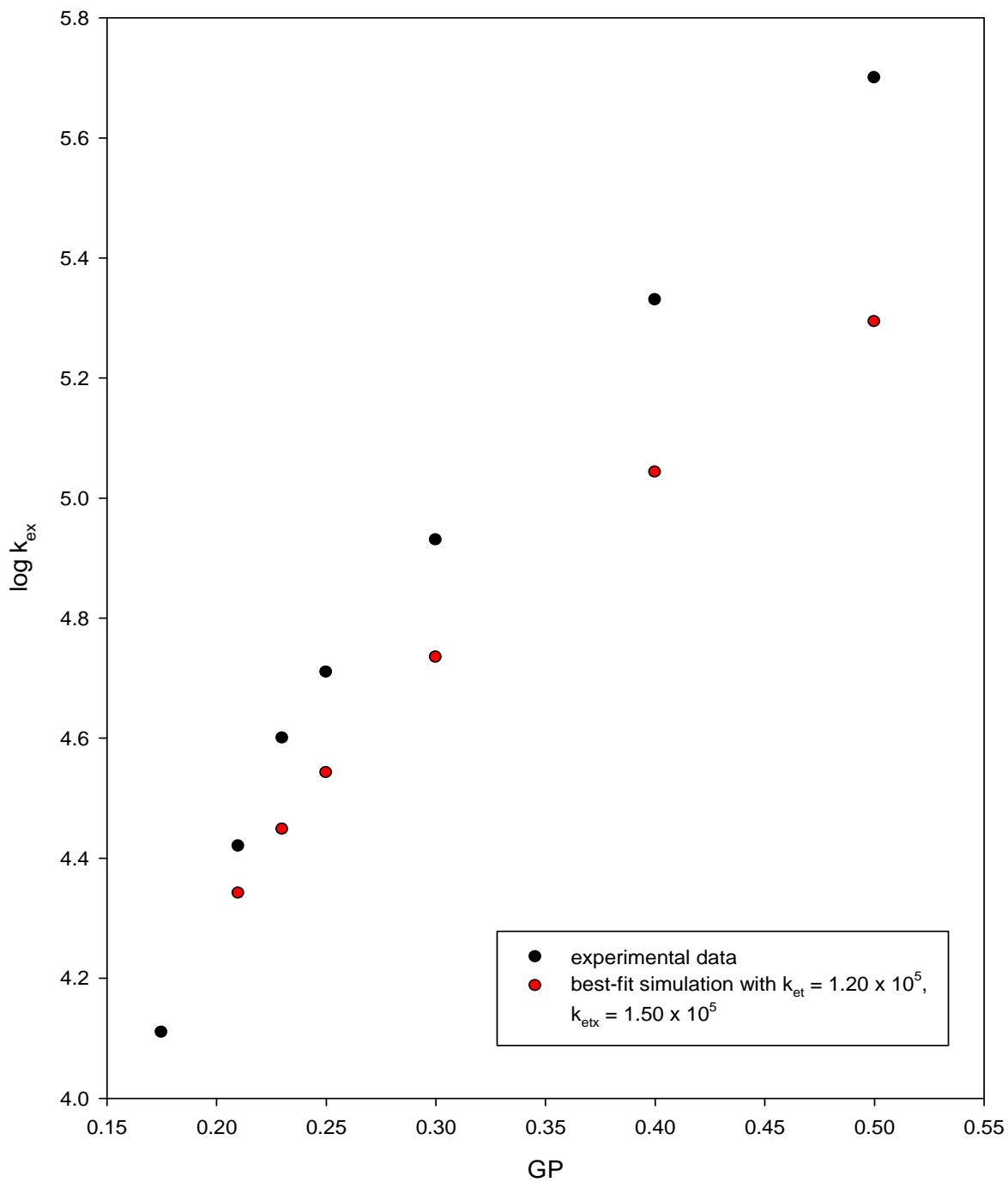


Figure 3-15(b). $\log k_{\text{ex}}$ for the $(\text{NH}_3)_5\text{Ru}^{\text{I/III}}(3\text{-tfmpy})^{2+/3+}$ ($[\text{Ru}^{\text{I}}] = [\text{Ru}^{\text{III}}] = 5.0 \text{ mM}$) in D_2O with addition of NaCl : experimental data and the best-fit simulation from the 2-channel model using Equation 3-25 with $k_{\text{et}} = 1.20 \times 10^5$, $k_{\text{etx}} = 2.40 \times 10^5$ and $k_{\text{etxx}} = 2.00 \times 10^5$

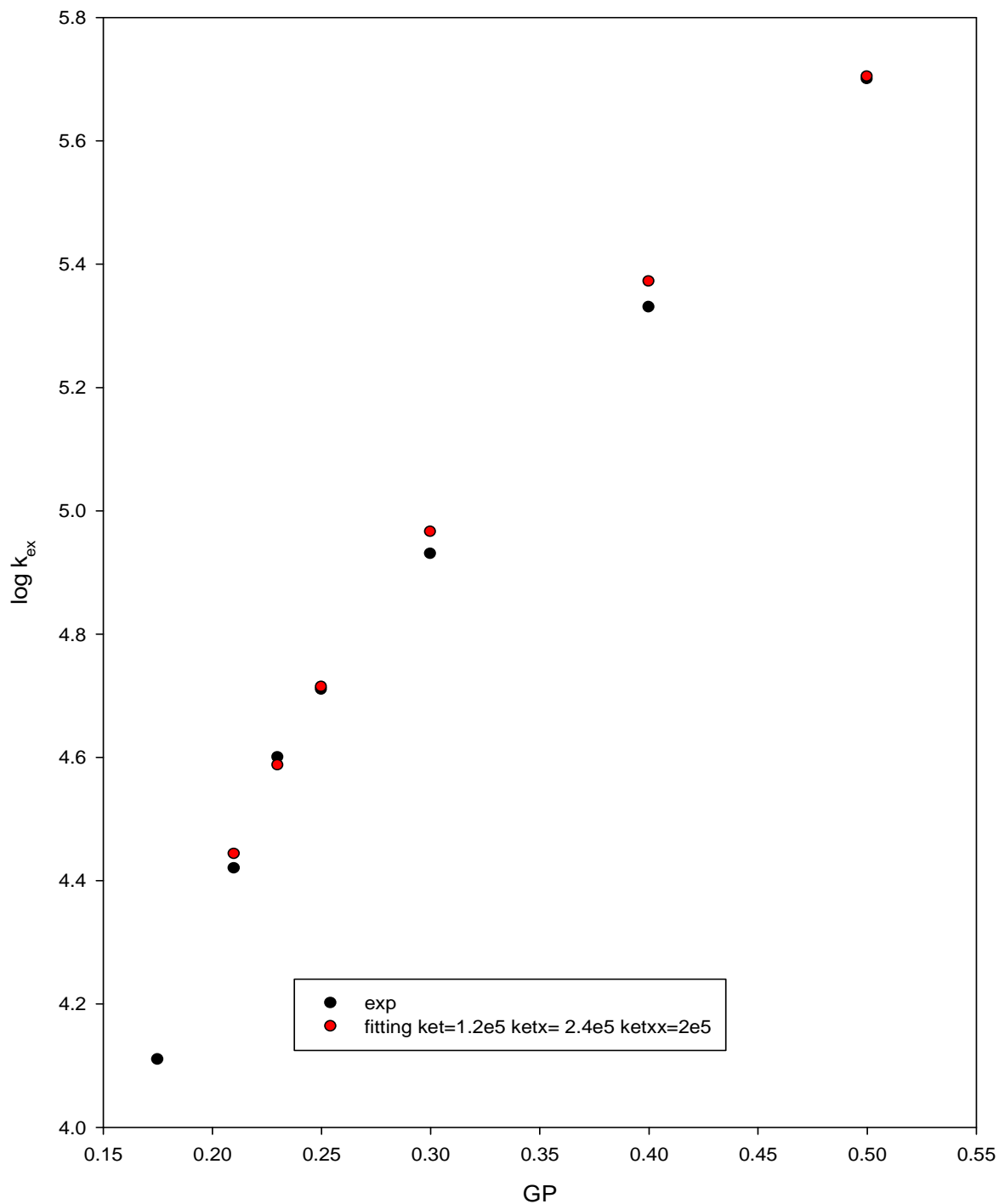


Figure 3-16(a). $\log k_{\text{ex}}$ for the $(\text{NH}_3)_5\text{Ru}^{\text{II/III}}(3\text{-tfmpy})^{2+/3+}$ ($[\text{Ru}^{\text{II}}] = [\text{Ru}^{\text{III}}] = 5.0 \text{ mM}$) in D_2O with addition of NaBr: experimental data and the best-fit simulation from the 2-channel fitting using Equation 3-23 with $k_{\text{et}} = 1.20 \times 10^5$, $k_{\text{etx}} = 4.40 \times 10^5$

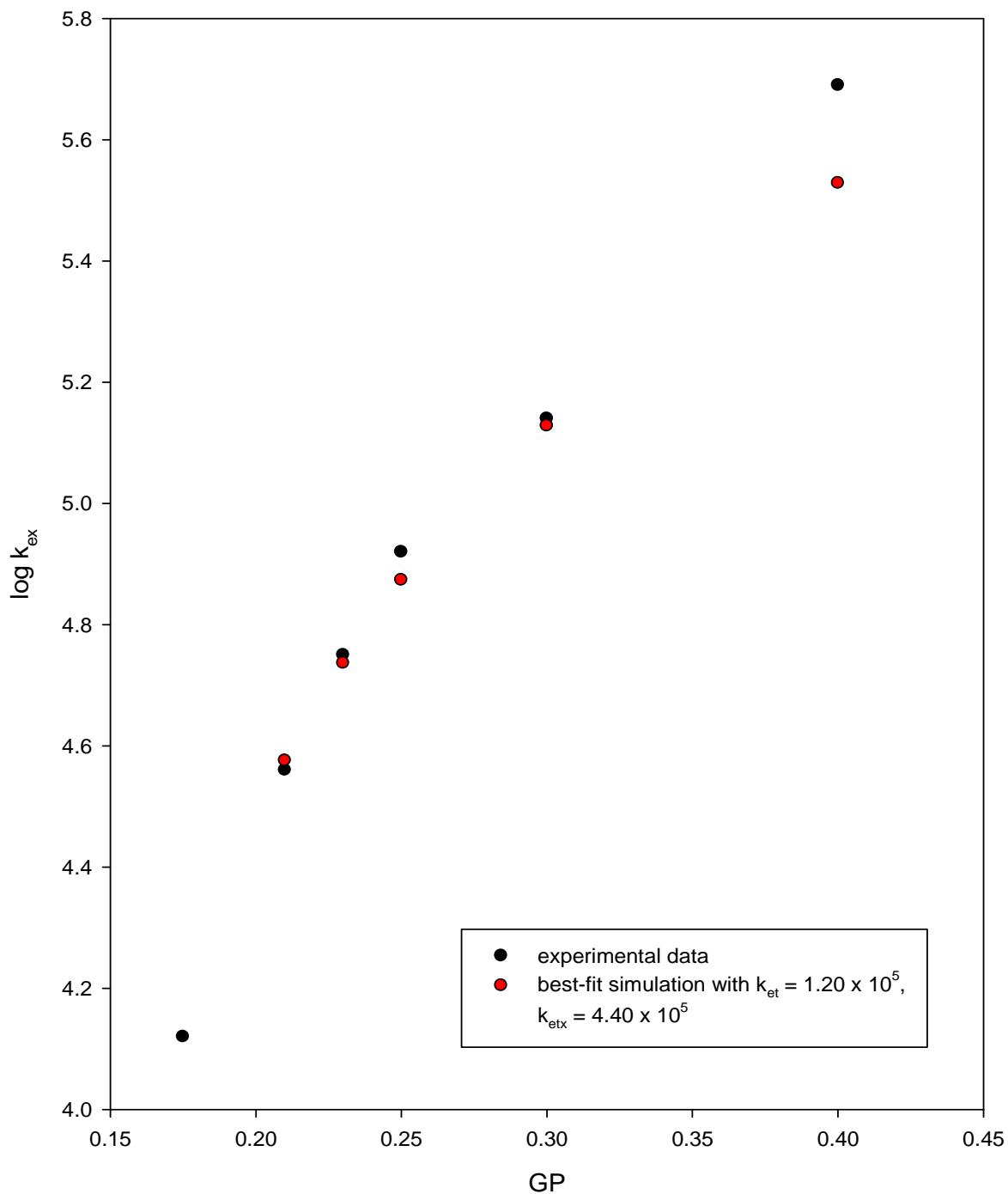
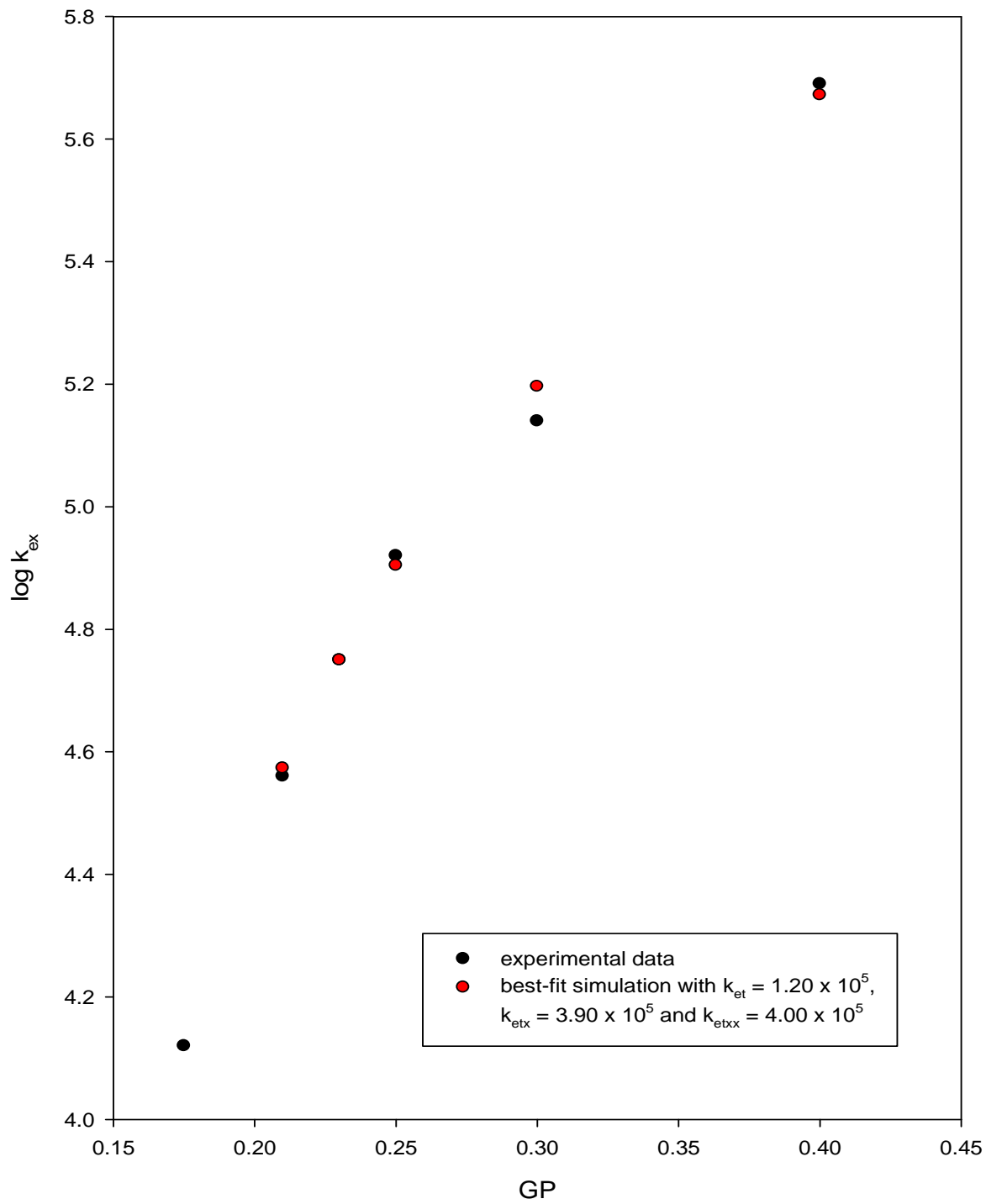


Figure 3-16(b). $\log k_{\text{ex}}$ for the $(\text{NH}_3)_5\text{Ru}^{\text{I/III}}(\text{3-tfmpy})^{2+/3+}$ ($[\text{Ru}^{\text{I}}] = [\text{Ru}^{\text{III}}] = 5.0 \text{ mM}$) in D_2O with addition of NaBr: experimental data and the best-fit simulation from 3-channel model using Equation 3-25 with $k_{\text{et}} = 1.20 \times 10^5$, $k_{\text{etx}} = 3.90 \times 10^5$ and $k_{\text{etxx}} = 4.00 \times 10^5$



From Figures 3-14 through 3-16, we see that the early parts of $\log k_{\text{ex}}$ vs. GP curves are quite well-fit if we use a value of 1.2×10^5 for k_{et} with the halide salts and then (k_{etx} , k_{etxx}) values of (1.0×10^4 , 2.89×10^4), (2.4×10^5 , 2.0×10^5) and (3.9×10^5 , 4.0×10^5) for the halide series, $X^- = \text{F}^-$, Cl^- , Br^- respectively (see Table 3-13). The estimated error in the averaged (over many trials) value of k_{et} is $\pm 1.2\%$ and the error in k_{etx} is about 10%. The value of k_{etxx} is much more uncertain and cannot be interpreted quantitatively. The fitted value of k_{etxx} has no effect on the best-fit value of k_{et} (because k_{et} was calculated from experimental rates with no added salt) and it has only a small effect on k_{etx} (since the value of k_{etx} is primarily determined from the fit quality in the $\text{GP} \cong 0.20 - 0.33$ region). The value of the $k_{\text{etx}}/k_{\text{et}}$ ratio follows a clear progression from 0.083 to 2.00 to 3.25 as we compare the F^- , Cl^- and Br^- data, respectively. This progression captures the essential rate acceleration provided by F^- , Cl^- and Br^- above (or below as with F^-) the value of k_{et} for the “uncatalyzed” pathway in which only Debye-Huckel ion atmosphere type (ionic-strength-only dependent) acceleration happens due to added salt. Possible interpretations of this set of ratios will be discussed later in this chapter.

Table 3-13. Best-fit values of k_{et} , k_{etx} and k_{etxx} for added halide and values of $k_{\text{etx}}/k_{\text{et}}$

| X^- | $k_{\text{et}}^{(a)}$ | $k_{\text{etx}}^{(b)}$ | k_{etxx} | $k_{\text{etx}}/k_{\text{et}}$ |
|---------------|-----------------------|------------------------|--------------------|--------------------------------|
| F^- | 1.20×10^5 | 1.00×10^4 | 2.89×10^4 | 0.083 |
| Cl^- | 1.20×10^5 | 2.40×10^5 | 2.00×10^5 | 2.00 |
| Br^- | 1.20×10^5 | 3.90×10^5 | 4.00×10^5 | 3.25 |

a) error estimate represents 95% confidence based on $n \cong 20$

b) uncertainty in k_{etx} is $\sim 10\%$

Catalysis by $M(CN)_6^{4-}$ ($M = Fe, Os, Ru$)

In a manner similar to our modeling of the simple salt effect, the two-channel model (Equations 3-17 to 3-19) was used in our fitting analyses of data from the self-exchange experiments with added $M(CN)_6^{4-}$ salts. Since the added amount of $M(CN)_6^{4-}$ salts necessary to cause large rate accelerations were very small (the added $M(CN)_6^{4-}$ concentration range being from $1.33 \times 10^{-5} \text{ M}$ up to a maximum of $1.13 \times 10^{-3} \text{ M}$), we will make the simplifying assumption here that channel three (Equations 3-20 and 3-21) can be neglected. The k_{ai} , k_{di} association /dissociation rate constants of the reactants (see Equation 3-2) with added $M(CN)_6^{4-}$ were calculated using Mathcad to compute Equations 3-11 and 3-13 using the radii listed in Table 3-14. Tables 3-15 through 3-17 list all the association/dissociation rate constants as a function of GP.

Table 3-14. Radii of the ions, complexes and ion pairs used in calculation of association/dissociation rate constants (for added $K_4M(CN)_6$ salts, $M= Fe, Os$ and Ru)^a

| | Ion | Radius(Å) |
|---|--------------------------------|-----------|
| 1 | Ru^{II} | 4.64 |
| 2 | Ru^{III} | 4.49 |
| 3 | $Fe(CN)_6^{4-}$ | 4.32 |
| 4 | $Os(CN)_6^{4-}$ | 4.39 |
| 5 | $Ru(CN)_6^{4-}$ | 4.38 |
| 6 | $Ru^{III} \cdot Fe(CN)_6^{4-}$ | 5.55 |
| 7 | $Ru^{III} \cdot Os(CN)_6^{4-}$ | 5.57 |
| 8 | $Ru^{III} \cdot Ru(CN)_6^{4-}$ | 5.59 |

a) see Table 3-6 captions

Table 3-15. Association and dissociation rate constants calculated for application of Equation 3-23 to reaction 3-2 in the presence of $K_4[Fe(CN)_6]^a$

| GP | u | $[Fe(CN)_6]^{4-}$ | ka1 | kd1 | ka2 | kd2 | ka3 | kd3 |
|---------|---------|-------------------|----------|----------|----------|----------|----------|----------|
| 0.17501 | 0.04500 | 0 | 1.53E+09 | 1.44E+10 | --- | --- | --- | --- |
| 0.17517 | 0.04510 | 1.33E-05 | 1.53E+09 | 1.44E+10 | 2.62E+10 | 3.47E+07 | 9.94E+09 | 1.63E+09 |
| 0.17534 | 0.04521 | 2.66E-05 | 1.53E+09 | 1.44E+10 | 2.62E+10 | 3.48E+07 | 9.94E+09 | 1.63E+09 |
| 0.17550 | 0.04531 | 3.99E-05 | 1.53E+09 | 1.44E+10 | 2.62E+10 | 3.48E+07 | 9.94E+09 | 1.63E+09 |
| 0.17583 | 0.04551 | 6.64E-05 | 1.54E+09 | 1.44E+10 | 2.62E+10 | 3.50E+07 | 9.94E+09 | 1.63E+09 |
| 0.17616 | 0.04572 | 9.29E-05 | 1.54E+09 | 1.44E+10 | 2.62E+10 | 3.52E+07 | 9.93E+09 | 1.63E+09 |
| 0.17681 | 0.04613 | 1.46E-04 | 1.55E+09 | 1.44E+10 | 2.61E+10 | 3.55E+07 | 9.93E+09 | 1.63E+09 |
| 0.17839 | 0.04714 | 2.76E-04 | 1.56E+09 | 1.43E+10 | 2.60E+10 | 3.62E+07 | 9.91E+09 | 1.64E+09 |
| 0.18143 | 0.04912 | 5.32E-04 | 1.59E+09 | 1.42E+10 | 2.58E+10 | 3.77E+07 | 9.88E+09 | 1.64E+09 |
| 0.18432 | 0.05106 | 7.82E-04 | 1.61E+09 | 1.42E+10 | 2.56E+10 | 3.92E+07 | 9.85E+09 | 1.65E+09 |

a) calculations made using complex and other radius values listed in Table 3-14

Table 3-16. Association and dissociation rate constants calculated for application of Equation 3-23 to reaction 3-2 in the presence of added $K_4[Os(CN)_6]^{4-}$ ^a

| GP | u | $[Os(CN)_6]^{4-}$ | ka_1 | kd_1 | ka_2 | kd_2 | ka_3 | kd_3 |
|---------|---------|-------------------|----------|----------|----------|----------|----------|----------|
| 0.17501 | 0.04500 | 0 | 1.53E+09 | 1.44E+10 | --- | --- | --- | --- |
| 0.17517 | 0.04510 | 1.33E-05 | 1.53E+09 | 1.44E+10 | 2.60E+10 | 3.59E+07 | 9.94E+09 | 1.62E+09 |
| 0.17534 | 0.04521 | 2.66E-05 | 1.53E+09 | 1.44E+10 | 2.60E+10 | 3.60E+07 | 9.94E+09 | 1.62E+09 |
| 0.17583 | 0.04551 | 6.65E-05 | 1.54E+09 | 1.44E+10 | 2.60E+10 | 3.62E+07 | 9.93E+09 | 1.62E+09 |
| 0.17632 | 0.04582 | 1.06E-04 | 1.54E+09 | 1.44E+10 | 2.60E+10 | 3.65E+07 | 9.93E+09 | 1.62E+09 |
| 0.17696 | 0.04623 | 1.59E-04 | 1.55E+09 | 1.44E+10 | 2.59E+10 | 3.68E+07 | 9.92E+09 | 1.63E+09 |
| 0.17823 | 0.04704 | 2.63E-04 | 1.56E+09 | 1.43E+10 | 2.58E+10 | 3.74E+07 | 9.91E+09 | 1.63E+09 |
| 0.17978 | 0.04804 | 3.92E-04 | 1.57E+09 | 1.43E+10 | 2.57E+10 | 3.82E+07 | 9.89E+09 | 1.63E+09 |

a) calculations made using complex and other radius values listed in Table 3-14

Table 3-17. Association and dissociation rate constants calculated for application of Equation 3-23 to reaction 3-2 in the presence of added $K_4[Ru(CN)_6]^{4-}$ ^a

| GP | u | $[Ru(CN)_6]^{4-}$ | ka_1 | kd_1 | ka_2 | kd_2 | ka_3 | kd_3 |
|---------|---------|-------------------|----------|----------|----------|----------|----------|----------|
| 0.17501 | 0.04500 | 0 | 1.53E+09 | 1.44E+10 | --- | --- | --- | --- |
| 0.17517 | 0.04510 | 1.33E-05 | 1.53E+09 | 1.44E+10 | 2.60E+10 | 3.57E+07 | 9.93E+09 | 1.62E+09 |
| 0.17534 | 0.04521 | 2.66E-05 | 1.53E+09 | 1.44E+10 | 2.60E+10 | 3.58E+07 | 9.93E+09 | 1.62E+09 |
| 0.17583 | 0.04551 | 6.65E-05 | 1.54E+09 | 1.44E+10 | 2.60E+10 | 3.60E+07 | 9.93E+09 | 1.62E+09 |
| 0.17632 | 0.04582 | 1.06E-04 | 1.54E+09 | 1.44E+10 | 2.60E+10 | 3.63E+07 | 9.92E+09 | 1.62E+09 |
| 0.17696 | 0.04623 | 1.59E-04 | 1.55E+09 | 1.44E+10 | 2.59E+10 | 3.66E+07 | 9.92E+09 | 1.62E+09 |
| 0.17823 | 0.04704 | 2.63E-04 | 1.56E+09 | 1.43E+10 | 2.58E+10 | 3.72E+07 | 9.90E+09 | 1.62E+09 |
| 0.17978 | 0.04804 | 3.92E-04 | 1.57E+09 | 1.43E+10 | 2.57E+10 | 3.80E+07 | 9.89E+09 | 1.63E+09 |
| 0.18274 | 0.05000 | 6.45E-04 | 1.60E+09 | 1.42E+10 | 2.55E+10 | 3.95E+07 | 9.86E+09 | 1.63E+09 |
| 0.18824 | 0.05377 | 1.13E-03 | 1.65E+09 | 1.41E+10 | 2.52E+10 | 4.24E+07 | 9.81E+09 | 1.64E+09 |

a) calculations made using complex and other radius values listed in Table 3-14

Proceeding as before with the halides, we then computed the overall rate predicted by Equation 3-23 vs. GP (in the form of μ_{tot}) and found the best-fit values of k_{et} and k_{etx} so as to reproduce the observed $\log k_{ex}$ vs. GP behavior. Tables 3-18 to 3-20 listed the best-fit simulation data. Figures 3-17 to 3-19 give the comparison between the experimental catalyzed rates and best-fit rates computed using the two-channel model and adjusting only k_{etx} (since k_{et} was obtained from a large number of no-added salt measurements previously, see Table 3-13). The resulting best-fit k_{etx} (and k_{etx}/k_{et} ratios) are listed in Table 3-21.

Table 3-18. Best-fit simulation data for reaction 3-2 at $[Ru^{II}] = [Ru^{III}] = 5.0 \text{ mM}$ in the presence of added $K_4Fe(CN)_6$

| GP | $\log k_{ex}$ (experimental) | CH1-2 with $k_{et} = 1.20 \times 10^5$ and $k_{etx} = 1.51 \times 10^7$ |
|---------|------------------------------|--|
| 0.17517 | 5.77 | 5.97 |
| 0.17534 | 6.25 | 6.27 |
| 0.17550 | 6.48 | 6.44 |
| 0.17583 | 6.70 | 6.66 |
| 0.17616 | 6.84 | 6.80 |
| 0.17681 | 7.03 | 6.99 |
| 0.17839 | 7.30 | 7.26 |
| 0.18143 | 7.59 | 7.52 |
| 0.18432 | 7.73 | 7.66 |

Table 3-19. Best-fit simulation data for reaction 3-2 at $[Ru^{II}] = [Ru^{III}] = 5.0 \text{ mM}$ in the presence of added $K_4Os(CN)_6$

| GP | $\log k_{ex}$ (experimental) | CH1-2 with $k_{et} = 1.20 \times 10^5$ and $k_{etx} = 1.80 \times 10^5$ |
|---------|------------------------------|--|
| 0.17517 | 4.41 | 4.37 |
| 0.17534 | 4.61 | 4.53 |
| 0.17583 | 4.84 | 4.81 |
| 0.17632 | 5.03 | 4.98 |
| 0.17696 | 5.15 | 5.13 |
| 0.17823 | 5.34 | 5.32 |
| 0.17978 | 5.43 | 5.47 |

Table 3-20. Best-fit simulation data for reaction 3-2 at $[Ru^{II}] = [Ru^{III}] = 5.0 \text{ mM}$ in the presence of added $K_4Ru(CN)_6$

| GP | $\log k_{ex}$ (experimental) | CH1-2 with $k_{et} = 1.20 \times 10^5$ and $k_{etx} = 5.50 \times 10^4$ |
|---------|------------------------------|--|
| 0.17517 | 4.15 | 4.20 |
| 0.17534 | 4.22 | 4.28 |
| 0.17583 | 4.43 | 4.45 |
| 0.17632 | 4.56 | 4.57 |
| 0.17696 | 4.71 | 4.69 |
| 0.17823 | 4.86 | 4.85 |
| 0.17978 | 4.98 | 4.98 |
| 0.18274 | 5.28 | 5.16 |
| 0.18824 | 5.60 | 5.35 |

Figure 3-17. $\log k_{\text{ex}}$ for the $(\text{NH}_3)_5\text{Ru}^{\text{II/III}}(3\text{-tfmpy})^{2+/3+}$ ($[\text{Ru}^{\text{II}}] = [\text{Ru}^{\text{III}}] = 5.0 \text{ mM}$) in D_2O with addition of $\text{K}_4\text{Fe}(\text{CN})_6$: experimental data and the best-fit simulation from the 2-channel model using Equation 3-23 with $k_{\text{et}} = 1.20 \times 10^5$ and $k_{\text{etx}} = 1.51 \times 10^7$

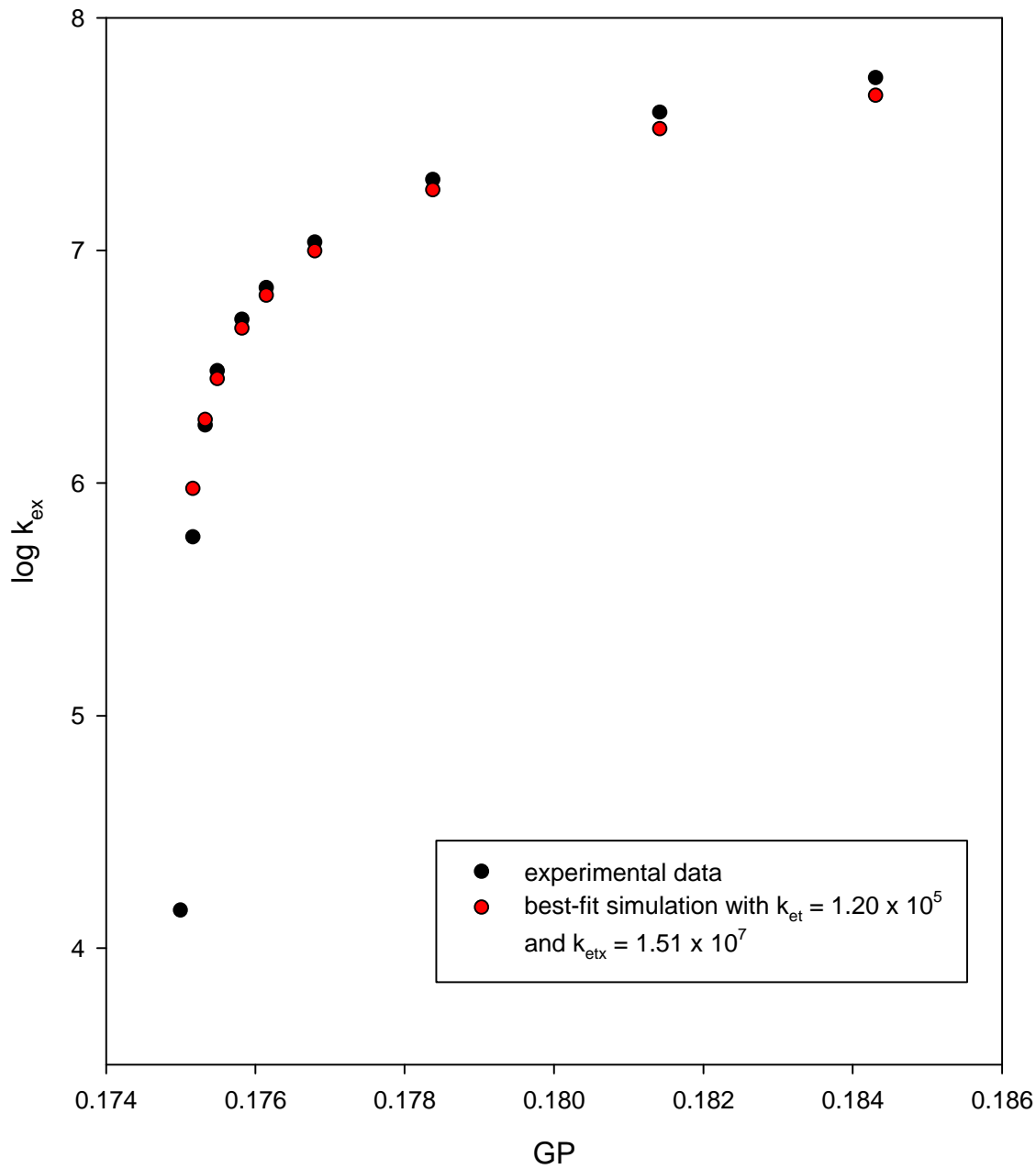


Figure 3-18. $\log k_{\text{ex}}$ for the $(\text{NH}_3)_5\text{Ru}^{\text{II/III}}(3\text{-tfmpy})^{2+/3+}$ ($[\text{Ru}^{\text{II}}] = [\text{Ru}^{\text{III}}] = 5.0 \text{ mM}$) in D_2O with addition of $\text{K}_4\text{Os}(\text{CN})_6$: experimental data and the best-fit simulation from the 2-channel model using Equation 3-23 with $k_{\text{et}} = 1.20 \times 10^5$ and $k_{\text{etx}} = 1.80 \times 10^5$

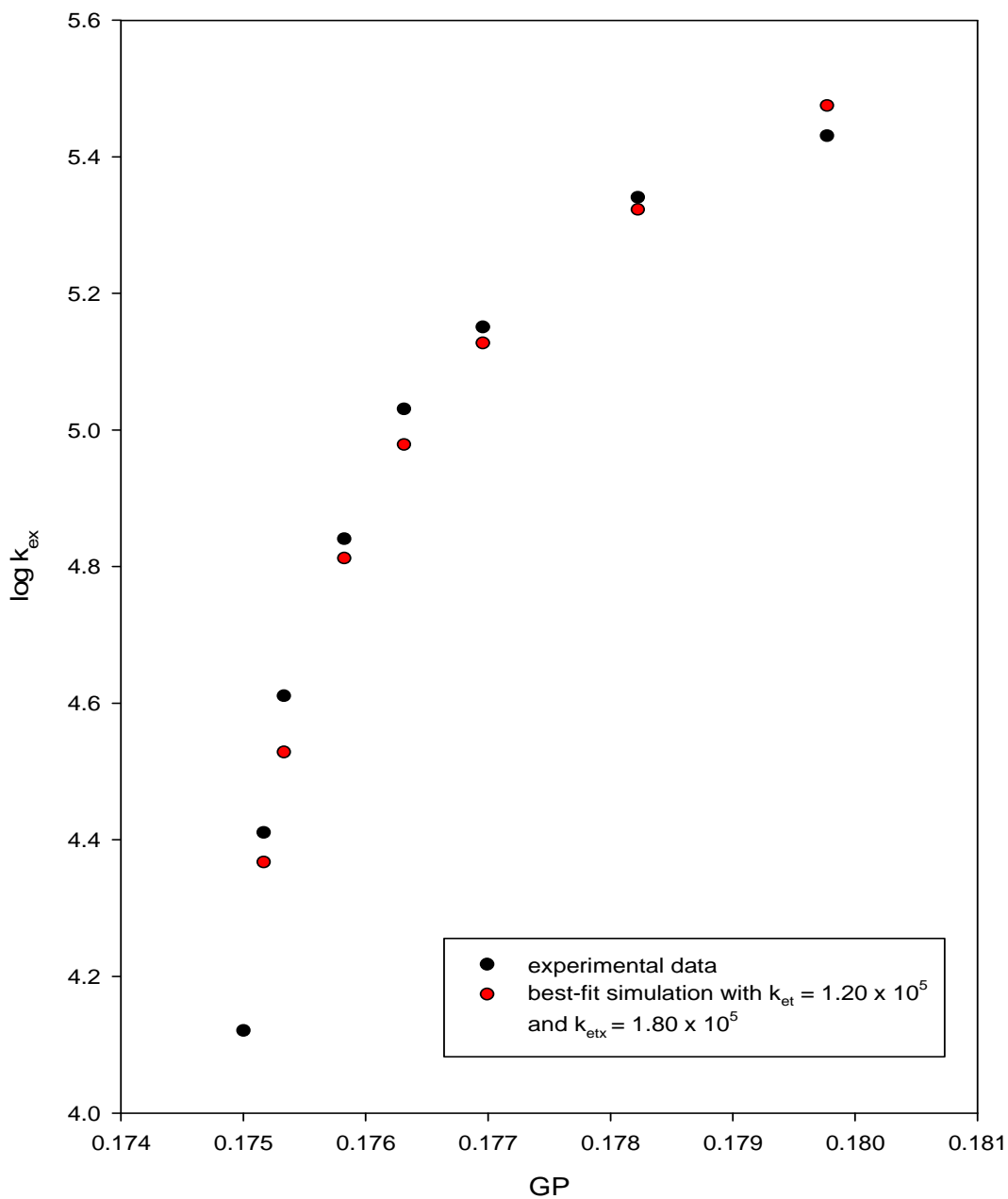
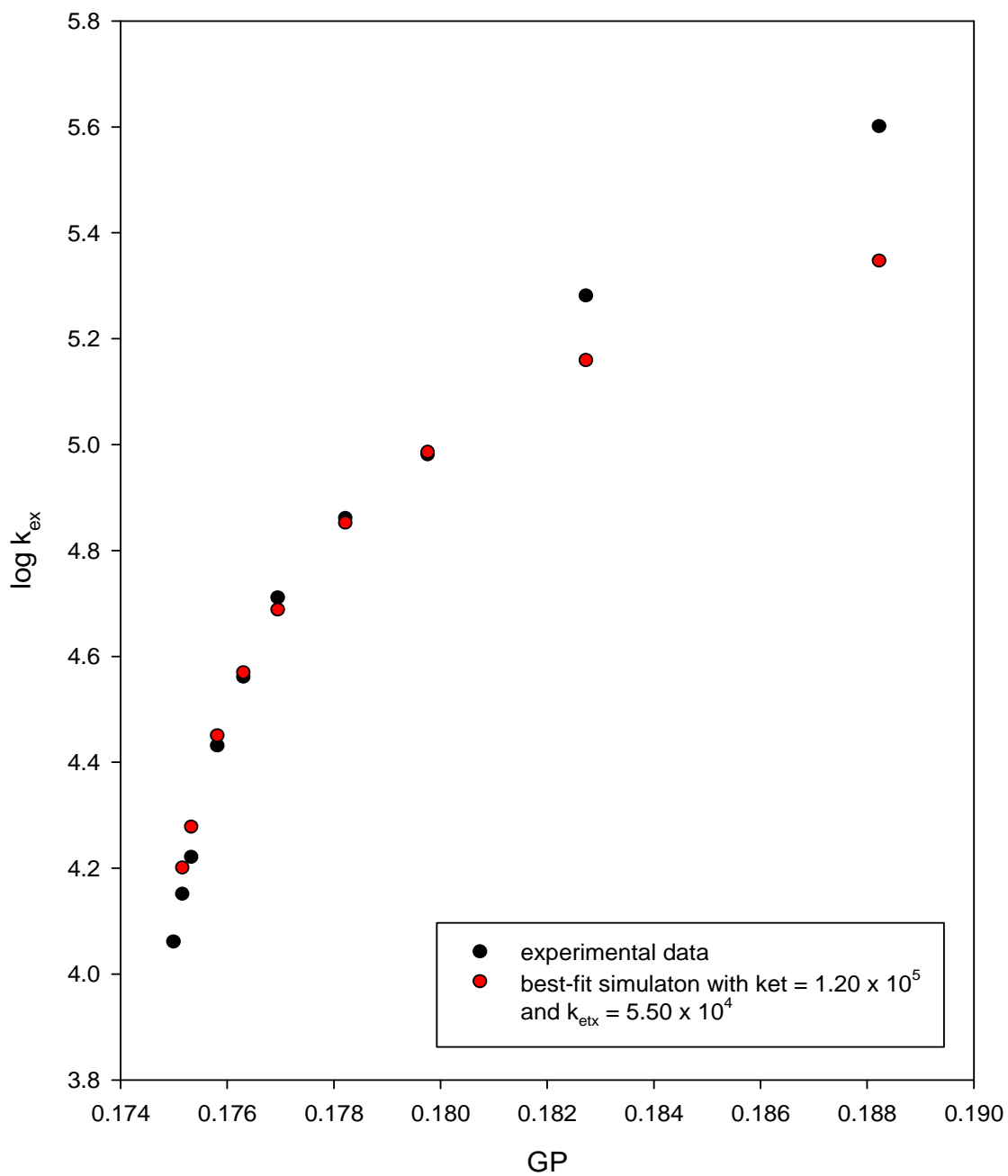


Figure 3-19. $\log k_{\text{ex}}$ for the $(\text{NH}_3)_5\text{Ru}^{\text{II/III}}(3\text{-tfmpy})^{2+/3+}$ ($[\text{Ru}^{\text{II}}] = [\text{Ru}^{\text{III}}] = 5.0 \text{ mM}$) in D_2O with addition of $\text{K}_4\text{Ru}(\text{CN})_6$: experimental data and the best-fit simulation from the 2-channel model using Equation 3-23 with $k_{\text{et}} = 1.20 \times 10^5$ and $k_{\text{etx}} = 5.50 \times 10^4$



Figures 3-17 to 3-19, Table 3-13 and Table 3-21 show that $K_4Fe(CN)_6$ gives by far largest rate acceleration, as indexed by the ratio of k_{etx}/k_{et} , and $M = Os$ and $M = Ru$ give a sharp drop off.

Table 3-21. k_{etx}/k_{et} ratios for $K_4M(CN)_6$ ($M = Ru, Os$ and Fe)

| Salt | k_{et}^a | k_{etx}^b | k_{etx}/k_{et} |
|---------------|--------------------|--------------------|-----------------------|
| $K_4Ru(CN)_6$ | 1.20×10^5 | 5.50×10^4 | 4.58×10^{-1} |
| $K_4Os(CN)_6$ | 1.20×10^5 | 1.80×10^5 | 1.50 |
| $K_4Fe(CN)_6$ | 1.20×10^5 | 1.51×10^7 | 1.26×10^2 |

a) error estimate represents 95% confidence based on $n \cong 20$

b) uncertainty in k_{etx} is ~10%

According to our kinetic model, if the value of k_{etx}/k_{et} is large, then the anion of the added salt is playing a role in accelerating the ET reaction above and beyond the μ and GP effects calculated using Equation 3-11 through 3-13 (with individual k_{ai} , k_{di} inputted at each GP) values using Equation 3-23 or 3-25) or, alternatively, some variable-slope version of Equation 3-9. The sharp drop off in k_{etx}/k_{et} agrees well a “hole-transfer” superexchange catalysis mechanism and will be discussed in detail later.

Ion-pair formation constants between Ru^{III} ammine complexes and $M^{II}(CN)_6^{4-}$ based on outer-sphere charge-transfer absorption measurements

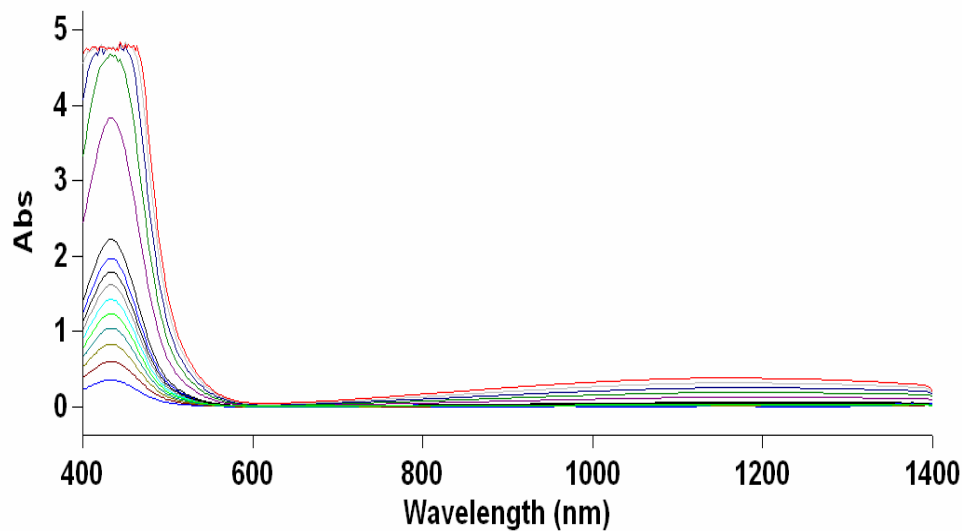
It is well-known from earlier work by Navon et.al.,⁴² Sexton et.al.⁴³ and Han⁴⁴ in this lab that ruthenium(III) hexaammine and pentaammine species form spectroscopically-identifiable and reasonably stable ion pairs in solution with added

halide ions. The spectroscopic transition of interest is an ion-pair charge-transfer (IPCT) band in which electron density is shifted from X^- and placed on the Ru(III) center. Similar absorptions, now with an intervalence-transfer type aspect, are known to arise in the even more stable ion pairs formed with $M(CN)_6^{4-}$.³⁴ To further characterize this behavior, an attempt was made to measure this K_{IP} value and see if any differences in the ion-pairing behaviors of $Fe^{II}(CN)_6^{4-}$, $Os^{II}(CN)_6^{4-}$ and $Ru^{II}(CN)_6^{4-}$ could be resolved.

Because of the direct relevance to some of the steps in our kinetic modeling schemes, we undertook to measure the K_{IP} values for the specific $[(NH_3)_5Ru^{III}(3\text{-tfmpy}), M^{II}(CN)_6^{4-}]$ ion-pairs of our work using the IPCT (also known as "OSIT" for outer-sphere intervalence-transfer) bands of these species. This was done by applying Beer's law to the IPCT band absorbance. Figures 3-20 through 3-22 show the individual IPCT spectra obtained at a series of concentrations where $[(NH_3)_5Ru^{III}(3\text{-tfmpy})^{3+}] = [M^{II}(CN)_6^{4-}]$ (M= Fe, Os, Ru).

Figure 3-20. (a) Vis-NIR Spectrum of the ion pair $[(\text{NH}_3)_5\text{Ru}^{\text{III}}(3\text{-tfmpy}), \text{Fe}^{\text{II}}(\text{CN})_6]^-$ in 1cm cell ($[\text{Fe}(\text{II})] = [\text{Ru}(\text{III})]$, concentration from 0.1 mM to 9 mM) (b) a close look at λ_{max} area

(a)



(b) OSIT $\lambda_{\text{max}} = 1160\text{nm}$

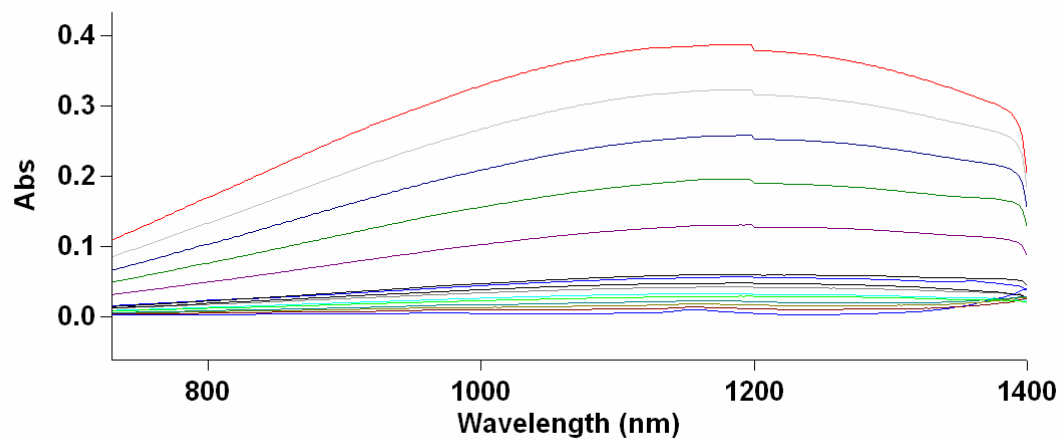


Figure 3-21. Vis-NIR Spectrum of the ion pair $[(\text{NH}_3)_5\text{Ru}^{\text{III}}(3\text{-tfmpy}), \text{Os}^{\text{II}}(\text{CN})_6]^-$ in 1cm cell ($[\text{Os}(\text{II})] = [\text{Ru}(\text{III})]$, concentrations range from 0.2 mM to 6 mM)

OSIT $\lambda_{\text{max}} = 703 \text{ nm}$

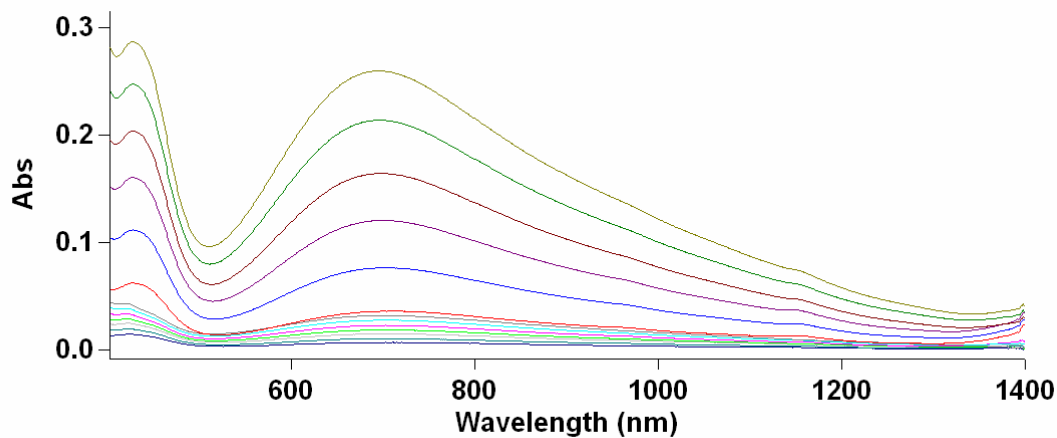
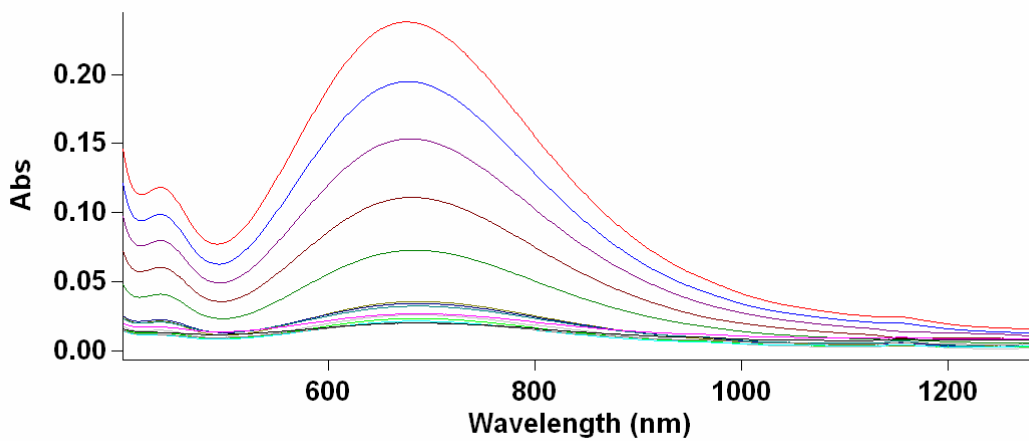


Figure 3-22. Vis-NIR Spectrum of the ion pair $[(\text{NH}_3)_5\text{Ru}^{\text{III}}(3\text{-tfmpy}), \text{Ru}^{\text{II}}(\text{CN})_6]^-$ in 1cm cell ($[\text{Ru}(\text{II})] = [\text{Ru}(\text{III})]$, concentrations range from 0.2mM to 6mM)

OSIT $\lambda_{\text{max}} = 686 \text{ nm}$



Figures 3-23 to 3-25 show Beer's law plot of ion pairs $[(\text{NH}_3)_5\text{Ru}^{\text{III}}(3\text{-tfmpy}), \text{M}^{\text{II}}(\text{CN})_6]^-$ (M= Fe, Os, Ru). In a typical Beer's law plot, for example, in plot of ion pair $[(\text{NH}_3)_5\text{Ru}^{\text{III}}(3\text{-tfmpy}), \text{Fe}^{\text{II}}(\text{CN})_6]^-$ (at $\lambda_{\text{max}} = 1160\text{nm}$), it is found to consist of two parts: a lower concentration non-linear part and a higher concentration linear part. In the range of the low concentration part (curved part), from $0.1 \text{ mM} - 1 \text{ mM}$, Ru^{III} and M^{II} have not reached 100% ion-pairing and the plot does not follow Beer's law. However, the linearity in the high concentration part, where Ru^{III} and M^{II} are 100% ion paired, allows us to use a linear regression to fit the slope and thus determine the extinction coefficient of the ion pair according to Beer's law.

Figure 3-23. Beer's law plot for the ion pair $[(\text{NH}_3)_5\text{Ru}^{\text{III}}(3\text{-tfmpy}), \text{Fe}^{\text{II}}(\text{CN})_6]^-$ at 25°C in water

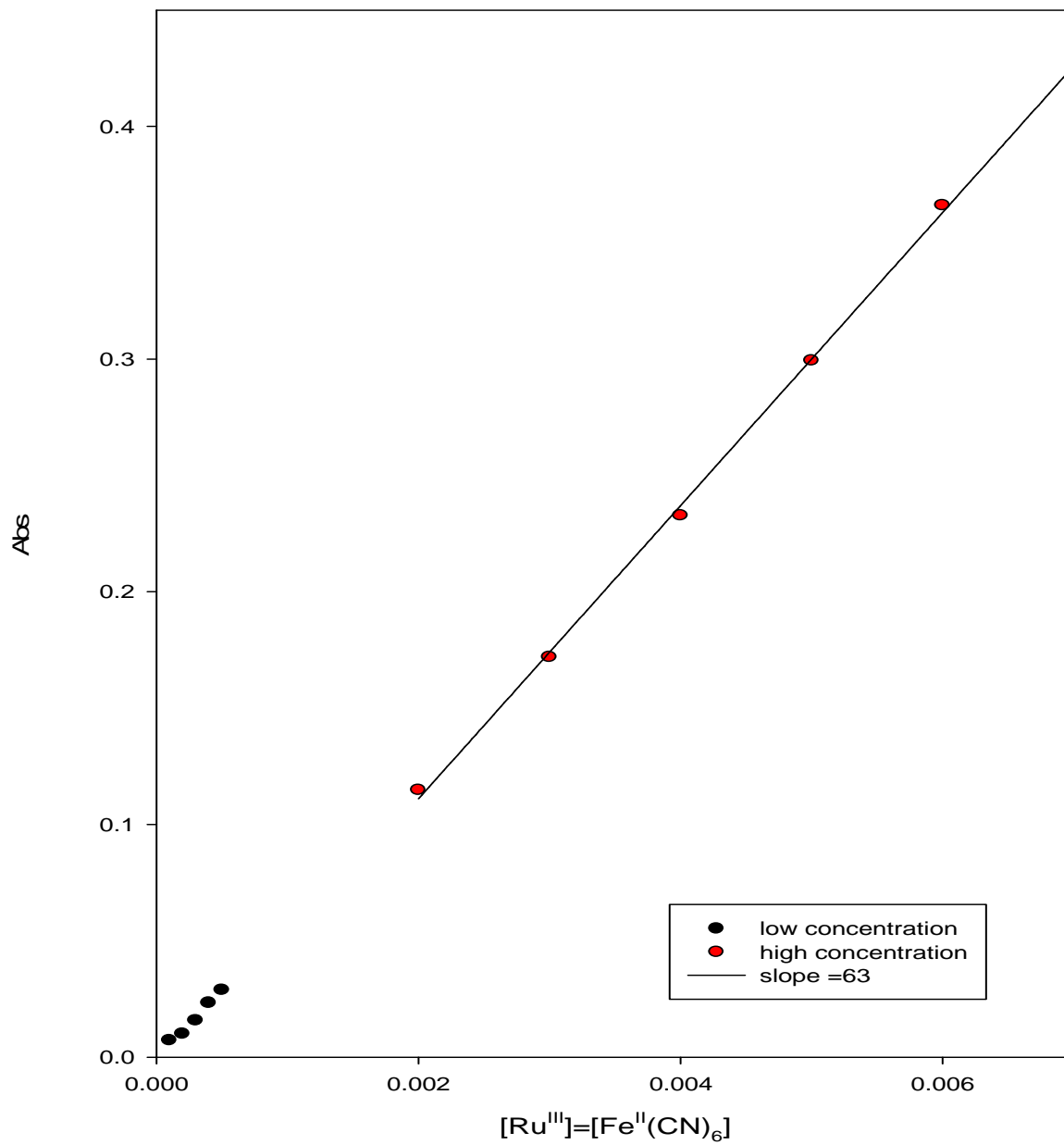


Figure 3-24. Beer's law plot for the ion pair $[(\text{NH}_3)_5\text{Ru}^{\text{III}}(3\text{-tfmpy}), \text{Os}^{\text{II}}(\text{CN})_6]^-$ at 25°C in water

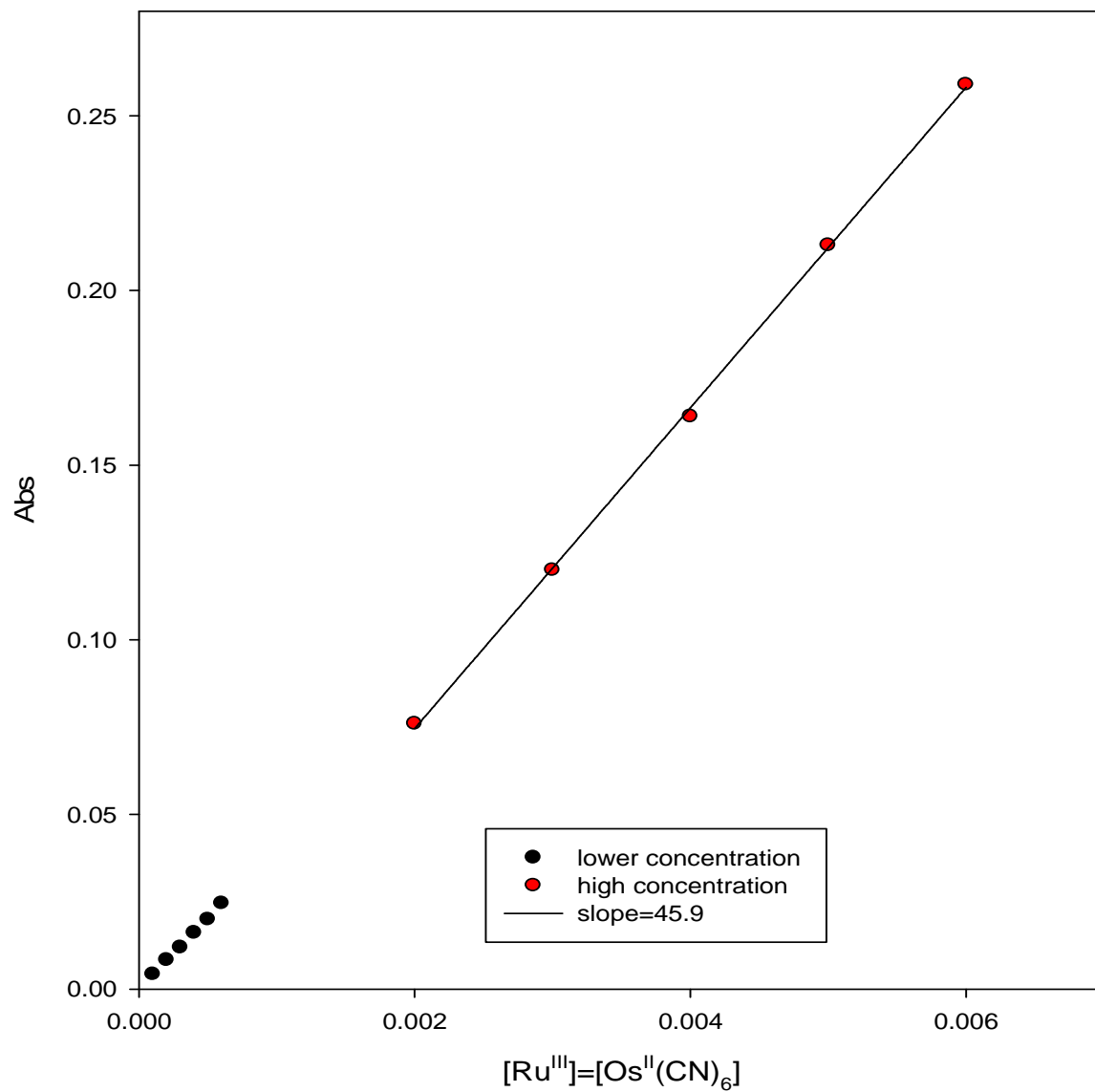
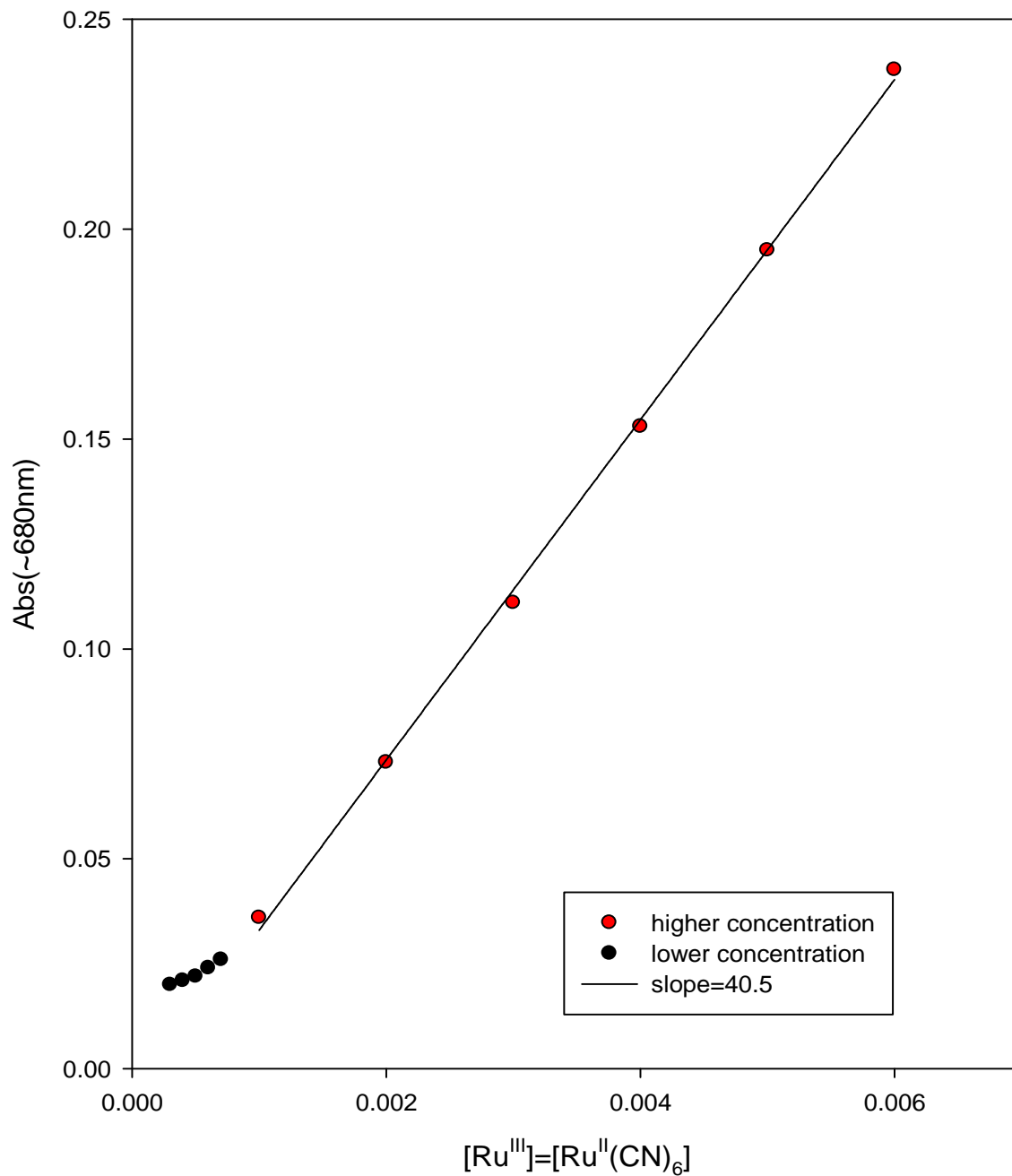


Figure 3-25. Beer's law plot for the ion pair $[(\text{NH}_3)_5\text{Ru}^{\text{III}}(3\text{-tfmpy}), \text{Ru}^{\text{II}}(\text{CN})_6]^-$ at 25°C in water



Once the extinction coefficient for a given ion pair is known from the linear (Beer's law) part of the plots, it is possible to analyze spectrophotometrically for the ion-pair concentration in the region of less than 100% ion pair formation,



where M=Fe, Os, Ru and IP is $[Ru^{III} \cdot M^{II} (CN)_6^{4-}]$

The ion pair formation constant K_a is defined as follows,

$$K_a = \frac{[IP]}{([Ru^{III}]_0 - [IP])([M^{II}]_0 - [IP])} \quad 3-27$$

where $[Ru^{III}]_0$ and $[M^{II}]_0$ are the concentration of added $(NH_3)_5(3\text{-tfmpy})Ru^{III}$ and $M^{II}(CN)_6^{4-}$. Since $[Ru^{III}]_0 = [M^{II}]_0$, Equation 3-27 can be simplified to

$$K_a = \frac{[IP]}{([Ru^{III}]_0 - [IP])^2} \quad 3-$$

28

At any point in added $[Ru^{III}]_0 = [M^{II}(CN)_6]_0$, we can calculate $[IP]$ from the measured absorbance at λ_{max} and the known ϵ_{max} via,

$$[IP] = \frac{Abs(\lambda_{max})}{\epsilon_{max} \cdot l} \quad 3-29$$

where l is the path length in cm (in most experiments 1.0cm but also $l=5.0$ cm in some, where noted). We can also calculate the fraction of ion-paired species in the solution at any point in the non-linear (<100% ion-paired) portion of the Beer's law plot using,

$$\text{fraction ion-paired} = \frac{[IP]}{[Ru^{III}]_0} \quad 3-30$$

Applying Equations 3-29 and 3-30 to the non-linear (early) portion of the Beer's law plots in Figures 3-23 through 3-25, we are able to compute values for K_a at those concentrations.

Table 3-22 lists the formation constants, so obtained, for the ion pairs $[A_5Ru^{III}(3\text{-tfmpy}), M^{II}(\text{CN})_6]^-$. From the data, we see that the three different hexacyanides of Fe, Os and Ru result in K_a values of very similar magnitudes of 1.9×10^5 , 1.4×10^5 , 2.8×10^5 for $M = \text{Fe}$, Os and Ru , respectively. These yield an average value of 2.0×10^5 .

Table 3-22. Ion-pair spectral and formation constant data for $[(\text{NH}_3)_5\text{Ru}^{\text{III}}(3\text{-tfmpy})]$, $\text{M}^{\text{II}}(\text{CN})_6^-$ (M=Fe, Os, Ru)

| $[(\text{NH}_3)_5\text{Ru}^{\text{III}}(3\text{-tfmpy}), \text{Fe}^{\text{II}}(\text{CN})_6^-]$ | | $\lambda_{\text{max}} = 1160 \text{ nm}$ Extinction coefficient $\epsilon = 63.1 \text{ M}^{-1} \text{ cm}^{-1}$ | |
|---|------------------------------|---|-------------------|
| $[\text{Ru}^{\text{III}}]=[\text{Fe}^{\text{II}}]$ | Abs (~1160nm) in 5cm cell | % ion pair | K_{ip} |
| 2.00×10^{-4} | 0.0500 | 79.4 | 9.4×10^4 |
| 3.00×10^{-4} | 0.0788 | 83.4 | 1.0×10^5 |
| 4.00×10^{-4} | 0.117 | 92.5 | 4.1×10^5 |
| 5.00×10^{-4} | 0.145 | 91.8 | 2.7×10^5 |
| 6.00×10^{-4} | 0.160 | 84.4 | 5.8×10^4 |
| Ave $K_{\text{a}} = 1.9 \times 10^5$ | | | |
| $[(\text{NH}_3)_5\text{Ru}^{\text{III}}(3\text{-tfmpy}), \text{Os}^{\text{II}}(\text{CN})_6^-]$ | | $\lambda_{\text{max}} = 703 \text{ nm}$ Extinction coefficient $\epsilon = 45.9 \text{ M}^{-1} \text{ cm}^{-1}$ | |
| $[\text{Ru}^{\text{III}}]=[\text{Os}^{\text{II}}]$ | Abs (~703nm) in 5cm cell | % ion pair | K_{a} |
| 3.00×10^{-4} | 0.0598 | 86.8 | 1.7×10^5 |
| 4.00×10^{-4} | 0.0805 | 87.7 | 1.5×10^5 |
| 5.00×10^{-4} | 0.0998 | 86.9 | 1.0×10^5 |
| 6.00×10^{-4} | 0.123 | 89.3 | 1.3×10^5 |
| Ave $K_{\text{a}} = 1.4 \times 10^5$ | | | |
| $[(\text{NH}_3)_5\text{Ru}^{\text{III}}(3\text{-tfmpy}), \text{Ru}^{\text{II}}(\text{CN})_6^-]$ | | $\lambda_{\text{max}} = 686 \text{ nm}$ Extinction coefficient $\epsilon = 40.5 \text{ M}^{-1} \text{ cm}^{-1}$ | |
| $[\text{Ru}^{\text{III}}]=[\text{Ru}^{\text{II}}]$ | Abs (~686nm) in 5cm cell | % ion pair | K_{a} |
| 3.00×10^{-4} | 0.0552 | 90.9 | 3.6×10^5 |
| 4.00×10^{-4} | 0.0726 | 89.6 | 2.1×10^5 |
| 5.00×10^{-4} | 0.0928 | 91.7 | 2.6×10^5 |
| 6.00×10^{-4} | 0.113 | 92.7 | 2.9×10^5 |
| Ave $K_{\text{a}} = 2.8 \times 10^5$ | | | |

Given the scatter in the data we can really only conclude that the formation constants between Ru^{III} and the $\text{M}(\text{CN})_6^{2-}$ ions (M = Fe, Os, Ru) are approximately

equal. Importantly, $\text{Fe}(\text{CN})_6^{2-}$ didn't show any obvious difference from the other two. This is in agreement with the assumptions underlying how we calculated the individual k_{a2} , k_{d2} (and thus inferred $K_{\text{IP}} = k_{a2}/k_{d2}$) in our kinetic modeling. In other words, from these data it would appear that ion-pair formation is indeed dominated by the sizes and charge types of the relevant species rather than by possible electronic effects (such as resonance stabilization of the ion pairs, *vide infra*) in accord with the assumptions underlying Equations 3-10 through 3-13.

We note, however, that the stoichiometric ratio of $[\text{M}(\text{CN})_6^{2-}]/[\text{Ru}^{\text{III}}]$ in the NMR solutions studied kinetically is quite different from the $[\text{Ru}^{\text{III}}]_0 = [\text{M}(\text{CN})_6^{4-}]_0$ condition used in the K_{IP} determinations. The biggest $[\text{M}(\text{CN})_6^{2-}]/[\text{Ru}^{\text{III}}]$ ratio is ~ 0.15 in the ^{19}F NMR experiment, and the strong ET catalysis by $\text{M}(\text{CN})_6^{4-}$ is clearly evident much before this at $[\text{M}(\text{CN})_6^{4-}]/[\text{Ru}^{\text{III}}]$ as low as 0.0027. It is known from the work of Taube and Vania⁴⁵ that multi-ion clusters of species similar to ours can form, and thus our analysis in terms of binary ion pairs will be to some extent overly-simple for our NMR conditions. The near-constancy of the simple K_{IP} values measured, however, indicates that the striking variation in ET catalytic efficacy as we go from Ru^{II} to Os^{II} to Fe^{II} hexacyanide is most likely related to some fundamental electronic property of the $\text{M}(\text{CN})_6^{4-}$ ion rather than variations in ion-association equilibria.

From the $k_{\text{etx}}/k_{\text{et}}$ ratios summarized in Tables 3-13 and 3-21, we see two cases of a clear and regular progression in ET catalytic efficacy; one as the added salt's anion goes from F^- to Cl^- to Br^- , and a much stronger effect as $\text{M}(\text{CN})_6^{4-}$ goes from $\text{M} = \text{Ru}^{\text{II}}$ to Os^{II} to Fe^{II} . A similar ordering of the halides has been established by Sista's work⁷ in this lab in the context of reaction 3-1 (including I^- as well) as measured using the stopped-flow, and the probable role of enhanced hole-transfer

superexchange as the halide ionization potential decreases down the halide group was discussed there in detail. Figure 3-26 below (from Sista's thesis) shows how the $k_{\text{etx}}/k_{\text{et}}$ ratio for reaction 3-1 varies with the ionization potential of the added X^- anion, and Figure 3-27 below shows the analogous graph using our ^{19}F NMR kinetic data for reaction 3-2.

Figure 3-26. $k_{\text{etx}}/k_{\text{et}}$ values for halide catalysis of reaction 3-1 obtained from Specfit simulations of stopped-flow data⁷ plotted against the ionization potentials of the halides⁴⁶

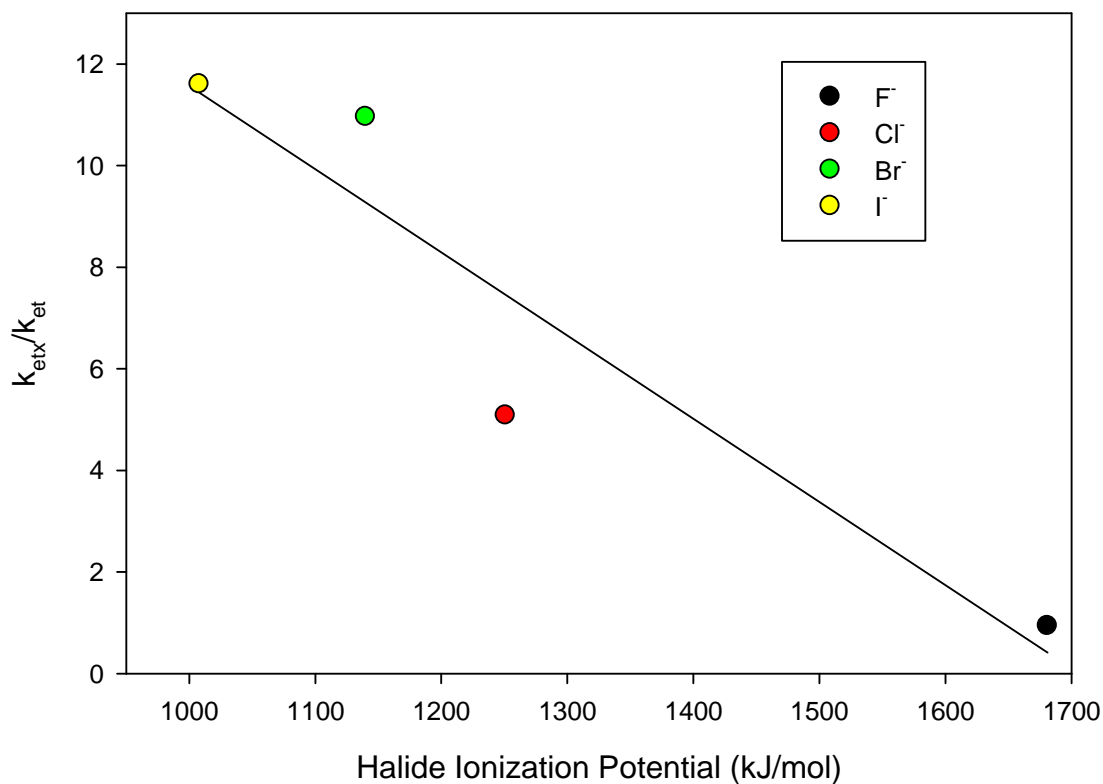
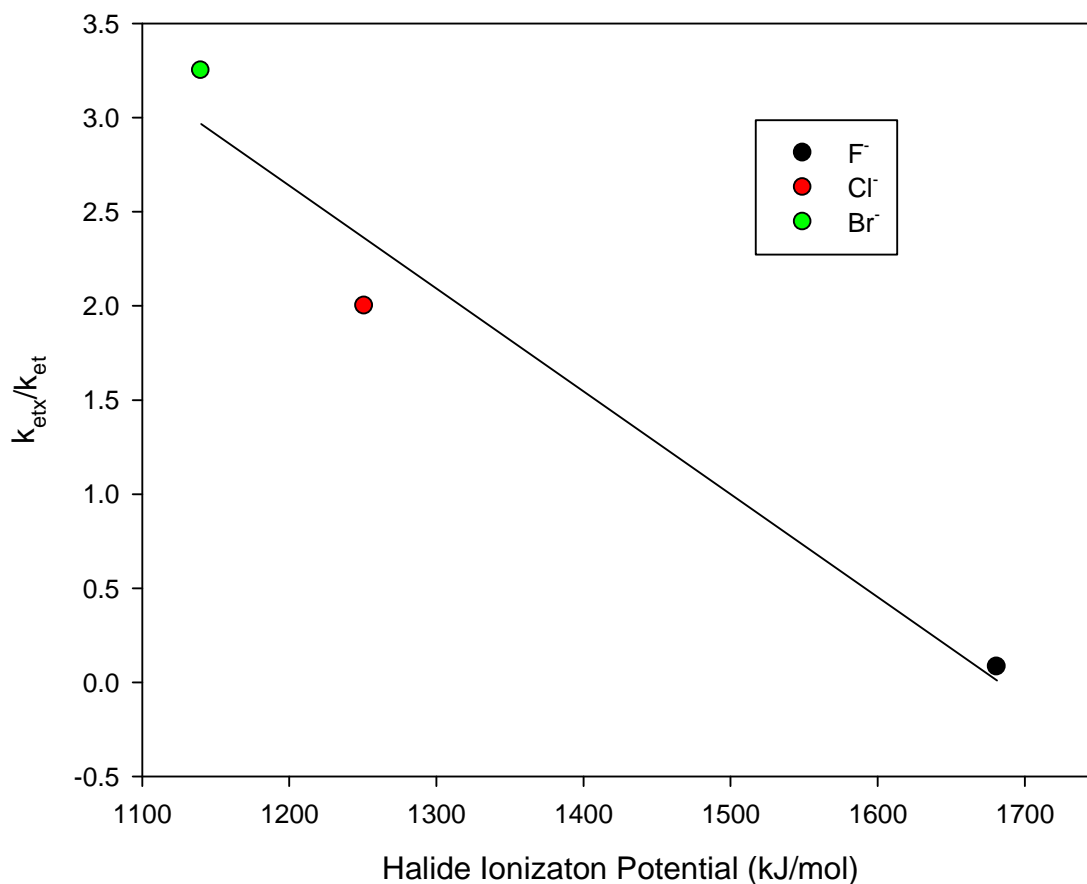


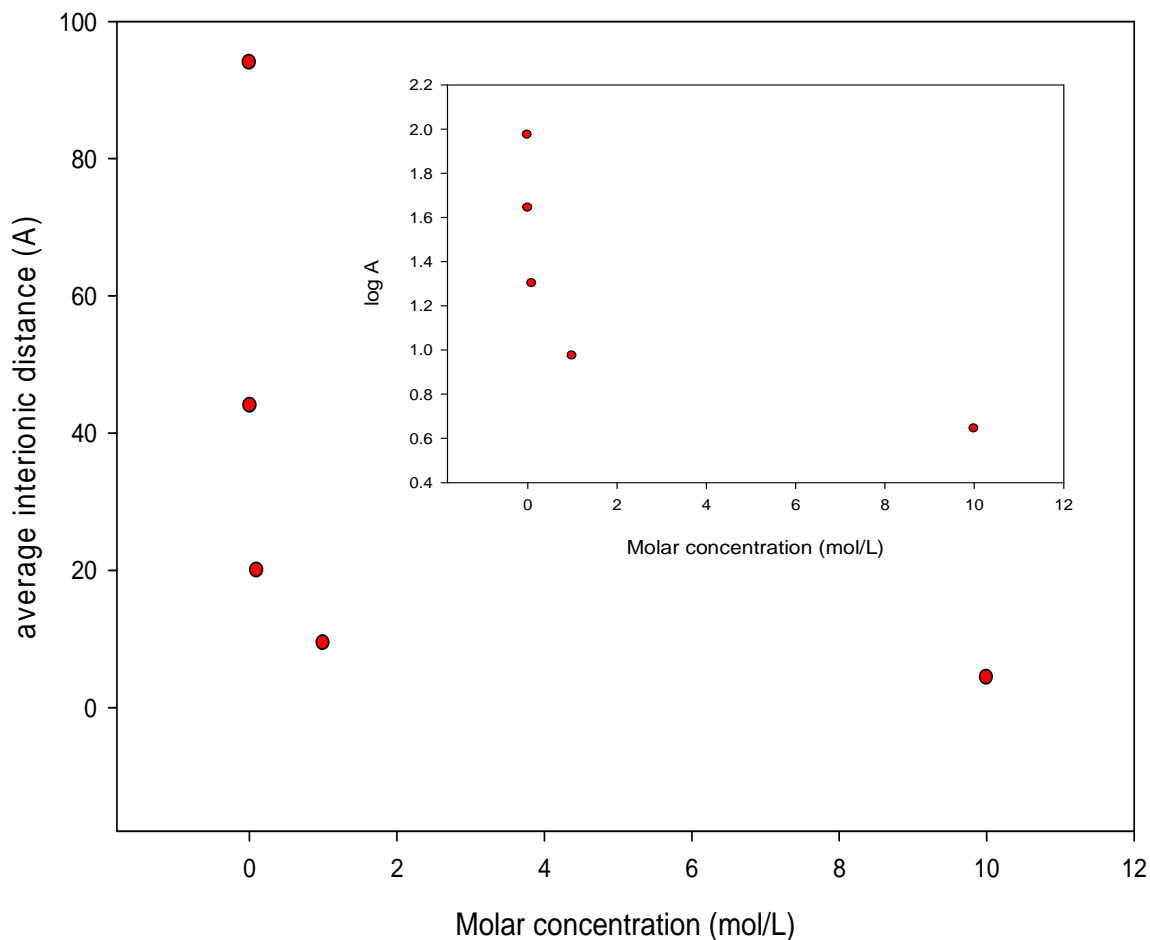
Figure 3-27. $k_{\text{etx}}/k_{\text{et}}$ values from Table 3-13 plotted against ionization potential⁴⁶



Here we see a qualitatively similar relationship in that as the ionization potential of the halides decreases, the $k_{\text{etx}}/k_{\text{et}}$ catalysis ratio increases. The simplest interpretation would be that as the halides are more easily ionized (or more precisely, oxidized in our case), it should be easier for a virtual hole to form on the halide ion (with concerted electron transfer to Ru^{III} and hole transfers to Ru^{II}, so as to allow the “hole-transfer” superexchange process to happen. The magnitude of each of the halide effects as measured by NMR is puzzlingly low as compared to the one

observed by stopped-flow.⁷ See Figure 3-8 for example, and note how shallow our NMR-based F^- slope is (~0.92) compared to the predicted Debye-Huckel slope of 6.1; in Sista's stopped-flow work, experiment and theory match almost exactly. This may have to do with poor matching between the assumptions of the Debye-Huckel treatment which underlie Equation 3-9 and the conditions of our NMR experiments. The stopped-flow work was done at $[Ru^{III}] = [Ru^{II}] = 1.0 \times 10^{-4} \text{ M}$, whereas our NMR kinetics were measure at $[Ru^{III}] = [Ru^{II}] = 5.0 \text{ mM}$. Figure 3-28 shows a graph of average interionic distance (\AA) vs. molar concentration.⁴⁷

Figure 3-28. Average interionic distance (\AA) vs. molar concentration in a solution of 1:1 electrolyte

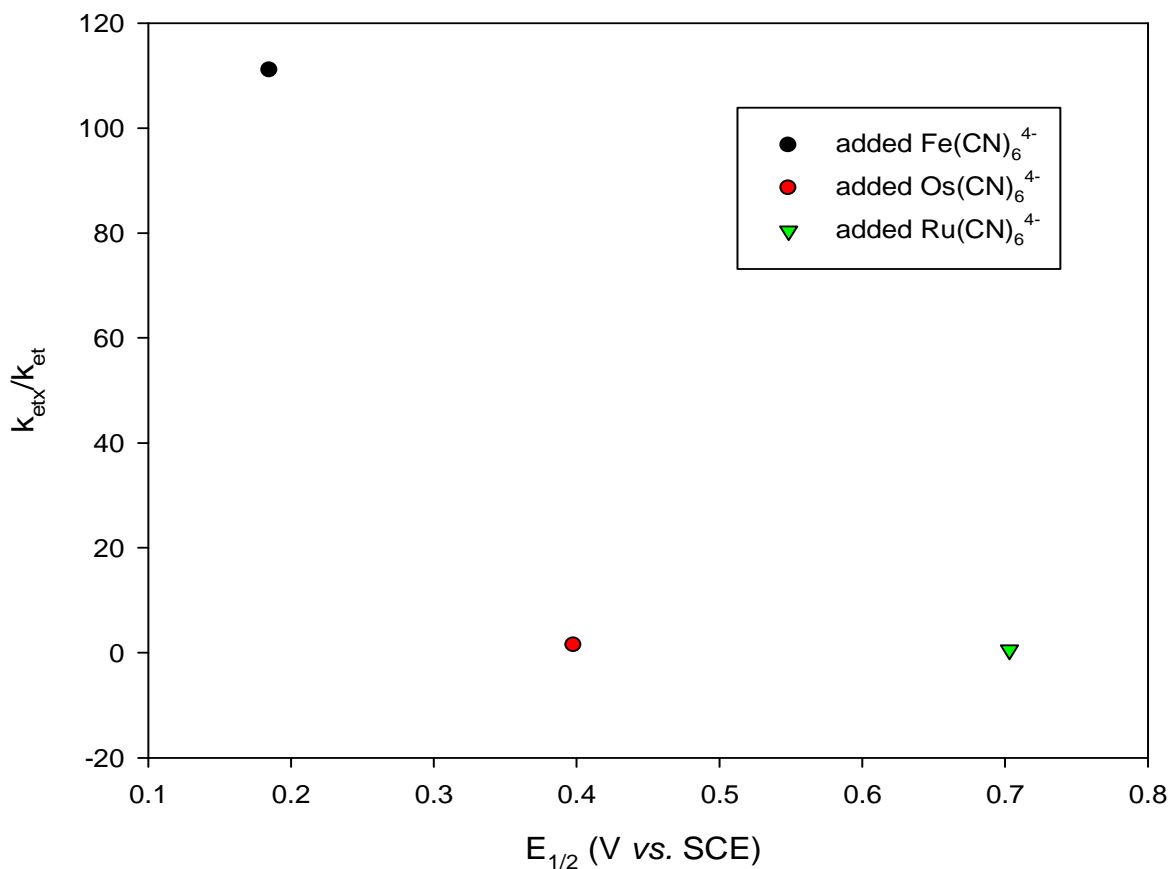


From the graph, we can estimate that the average oxidant-reductant interionic distance at $1.0 \times 10^{-4} \text{ M}$ is $\sim 200 \text{ \AA}$, while that at 5.0 mM is $\sim 69 \text{ \AA}$. The sharp divergence between our stopped-flow and NMR-derived kinetic salt effects would implicate this seemingly modest increment in average diffusional encounter distance as somehow taking the system(s) across some crucial threshold in defining the

operational limits for quantitative application of the Debye-Huckel model (at least for this particular ET reaction between these relatively small and highly-charged ionic reactants). By this same reasoning we might expect that our NMR-measured ET catalysis by $M(CN)_6^{4-}$ is actually much smaller than what would be observed by stopped-flow. Previous attempts to do this measurement by stopped-flow have been frustrated by an inability to control the $M(CN)_6^{4-}$ concentration well enough to keep the resulting kinetic decay within the time-resolution of the stopped-flow instrument.

In the case of the hexacyanides, we are able to graph the data using the (probably) more-relevant redox potentials of the aqueous $M(CN)_6^{4-}$ species along the horizontal axis as shown in Figure 3-29.

Figure 3-29. $k_{\text{etx}}/k_{\text{et}}$ ratio from best-fit simulations of the $\text{M}(\text{CN})_6^{4-}$ kinetic data plotted here against redox potentials (vs. SCE) of the aqueous $\text{M}(\text{CN})_6^{4-}$ species



Since the ionic radii of the $\text{M}(\text{CN})_6^{4-}$ species are nearly the same³⁴ and since our K_{IP} measurements indicate that they behave nearly the same in at least the simple ion-pairing equilibrium (see Table 3-22), Figure 3-29 probably gives us the most definitive evidence yet that hole-transfer superexchange (see Figure 3-3) is at the root of the observed ET catalysis by added anions. The idea here is simply that as the ionization potential of X^- , or the redox potential of $\text{M}(\text{CN})_6^{4-}$, in some presumed ternary association complex, $[\text{A}_5\text{Ru}^{\text{II}}\text{L}, \text{X}^-, \text{A}_5\text{Ru}^{\text{III}}\text{L}]^{4+}$ or $[\text{A}_5\text{Ru}^{\text{II}}\text{L}, \text{M}^{\text{II}}(\text{CN})_6^{4-}, \text{A}_5\text{Ru}^{\text{III}}\text{L}]^+$,

decreases, it is easier to create a “hole” in the HOMO of the associated $M^{II}(\text{CN})_6^{4-}$ anion (via a “virtual” anion $\rightarrow \text{Ru}^{III}$ IPCT state) such that superexchange coupling is progressively “turned on” over the series $M = \text{Ru} \rightarrow \text{Os} \rightarrow \text{Fe}$. As has been discussed elsewhere,^{4,7,20} the energy gap necessary to populate the relevant virtual state affects superexchange coupling and hence the tunneling frequency in the transition state, in a non-linear way,

$$v_{\text{tunneling}} = \frac{2\pi H_{DA}^2}{\hbar} \sqrt{\frac{1}{4\pi\lambda RT}} \quad 3-31^{48}$$

and this is especially clear in the vertical axis range shown in Figure 3-29.

Activation Parameters and Mechanistic Interpretation

To further characterize the mechanism of the ET catalysis quantum-superexchange effect, temperature dependent kinetic studies were conducted and then analyzed using the Eyring formalism (see Chapter Two) to obtain the activation parameters for the $A_5\text{Ru}^{II/III}(\text{3-tfmpy})^{2+/3+}$ self-exchange reaction in the presence of $K_4M(\text{CN})_6$ complex salts. Tables 3-23 through 3-25 list the resulting data, and Figure 3-30 shows the Eyring plots of all the data for $K_4\text{Fe}(\text{CN})_6$, $K_4\text{Os}(\text{CN})_6$ and $K_4\text{Ru}(\text{CN})_6$, as well as for a blank sample of exchanging $(\text{3-tfmpy})A_5\text{Ru}^{II/III}$ without any added salt (see Table 2-11). The activation parameters derived from Figure 3-30 are listed in Table 3-26 (see Chapter Two for details on how to obtain activation parameters from an Eyring plot).

Table 3-23. Eyring plot data for the $[(\text{NH}_3)_5\text{Ru}^{\text{II/III}}(\text{3-tfmpy})]^{2+/3+}$ self-exchange in the presence of added $\text{K}_4\text{Fe}(\text{CN})_6$ (all k_{ex} values calculated from fast exchange Equation 1-36)^{a,b}

| T(K) | k_{ex} | 1/T | $\ln(k_{\text{ex}}/T)$ |
|------|--------------------|----------|------------------------|
| 277 | 2.53×10^6 | 0.00361 | 9.12 |
| 280 | 3.57×10^6 | 0.003571 | 9.45 |
| 283 | 5.06×10^6 | 0.003529 | 9.79 |
| 288 | 7.66×10^6 | 0.003475 | 10.19 |
| 293 | 1.36×10^7 | 0.003410 | 10.75 |
| 299 | 2.05×10^7 | 0.003347 | 11.13 |
| 304 | 3.39×10^7 | 0.003287 | 11.62 |
| 310 | 4.88×10^7 | 0.003228 | 11.97 |
| 315 | 7.04×10^7 | 0.003172 | 12.32 |
| 321 | 9.86×10^7 | 0.003118 | 12.64 |

a) $[(\text{NH}_3)_5\text{Ru}^{\text{II}}(\text{3-tfmpy})]^{2+} = [(\text{NH}_3)_5\text{Ru}^{\text{III}}(\text{3-tfmpy})]^{3+} = 5.0 \text{ mM}$; $\mu_{\text{rcts}} = 0.0450$;

$$\text{GP}_{\text{rcts}} = 0.175$$

b) $[\text{K}_4\text{Fe}(\text{CN})_6]_{\text{added}} = 3.92 \times 10^{-4} \text{ M}$ (0.0784 equivalents); $\mu_{\text{total}} = 0.0480$; $\text{GP}_{\text{total}} = 0.180$

Table 3-24. Eyring plot data for the $[(\text{NH}_3)_5\text{Ru}^{\text{II/III}}(\text{3-tfmpy})]^{2+/3+}$ self-exchange in the presence of added $\text{K}_4\text{Os}(\text{CN})_6$ (For $T = 310\text{K}$, k_{ex} was calculated from intermediate exchange rate Equation 1-35; For $T = 315, 326\text{K}$, k_{ex} was obtained from fast exchange rate Equation 1-36.)^{a,b}

| T(K) | k_{ex} | 1/T | $\ln(k_{\text{ex}}/T)$ |
|------|--------------------|----------|------------------------|
| 277 | 6.65×10^4 | 0.003614 | 5.48 |
| 280 | 7.82×10^4 | 0.003571 | 5.63 |
| 283 | 1.02×10^5 | 0.003529 | 5.88 |
| 288 | 1.14×10^5 | 0.003475 | 5.98 |
| 293 | 2.07×10^5 | 0.003410 | 6.56 |
| 299 | 2.50×10^5 | 0.003347 | 6.73 |
| 304 | 5.08×10^5 | 0.003287 | 7.42 |
| 310 | 5.81×10^5 | 0.003228 | 7.54 |
| 315 | 1.52×10^6 | 0.003172 | 8.48 |
| 326 | 1.49×10^6 | 0.003065 | 8.43 |

a) $[(\text{NH}_3)_5\text{Ru}^{\text{II}}(\text{3-tfmpy})]^{2+} = [(\text{NH}_3)_5\text{Ru}^{\text{III}}(\text{3-tfmpy})]^{3+} = 5.0 \text{ mM}$; $\mu_{\text{rcts}} = 0.0450$;

$$\text{GP}_{\text{rcts}} = 0.175$$

b) $[\text{K}_4\text{Os}(\text{CN})_6]_{\text{added}} = 3.92 \times 10^{-4} \text{ M}$ (0.0784 equivalents); $\mu_{\text{total}} = 0.0480$;

$$\text{GP}_{\text{total}} = 0.180$$

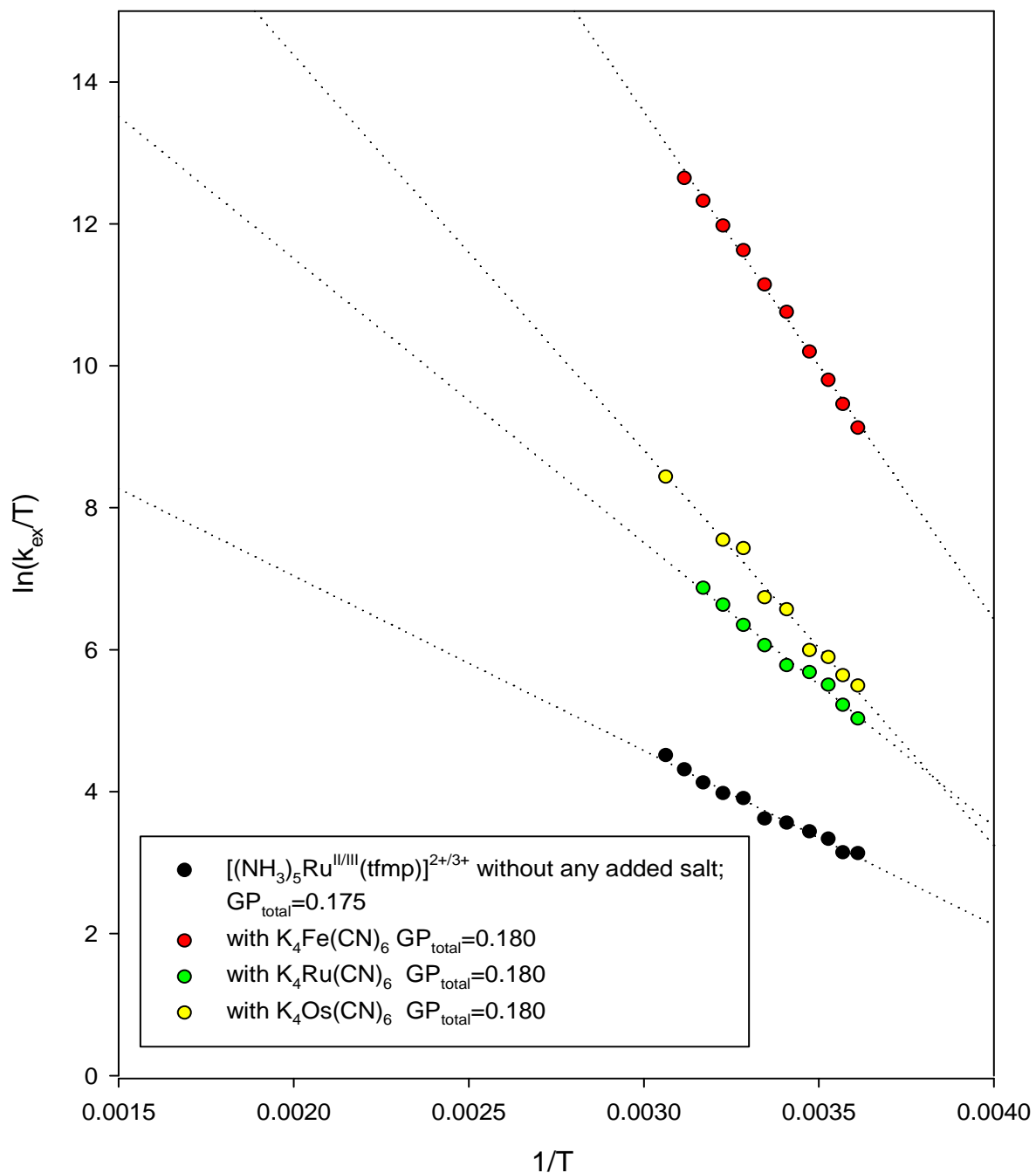
Table 3-25. Eyring plots data data for the $[(\text{NH}_3)_5\text{Ru}^{\text{II/III}}(\text{3-tfmpy})]^{2+/3+}$ self-exchange in the presence of added $\text{K}_4\text{Ru}(\text{CN})_6$ ^{a,b}

| T(K) | k_{ex} | 1/T | $\ln(k_{\text{ex}}/T)$ |
|------|--------------------|----------|------------------------|
| 277 | 4.18×10^4 | 0.003614 | 5.02 |
| 280 | 5.14×10^4 | 0.003571 | 5.21 |
| 283 | 6.90×10^4 | 0.003529 | 5.50 |
| 288 | 8.38×10^4 | 0.003475 | 5.67 |
| 293 | 9.39×10^4 | 0.003410 | 5.77 |
| 299 | 1.27×10^5 | 0.003347 | 6.05 |
| 304 | 1.72×10^5 | 0.003287 | 6.34 |
| 310 | 2.33×10^5 | 0.003228 | 6.62 |
| 315 | 3.01×10^5 | 0.003172 | 6.86 |

a) $[(\text{NH}_3)_5\text{Ru}^{\text{II}}(\text{3-tfmpy})]^{2+} = [(\text{NH}_3)_5\text{Ru}^{\text{III}}(\text{3-tfmpy})]^{3+} = 5.0 \text{ mM}$; $\mu_{\text{rcts}} = 0.0450$; $\text{GP}_{\text{rcts}} = 0.175$

b) $[\text{K}_4\text{Os}(\text{CN})_6]_{\text{added}} = 3.92 \times 10^{-4} \text{ M}$ (0.0784 equivalents); $\mu_{\text{total}} = 0.0480$; $\text{GP}_{\text{total}} = 0.180$

Figure 3-30. Eyring plots for the $[(\text{NH}_3)_5\text{Ru}^{\text{II/III}}(3\text{-tfmpy})]^{2+/3+}$ self-exchange reaction in the presence of $\text{K}_4\text{M}(\text{CN})_6$ (M=Fe, Os, Ru) and by itself. ^{a,b}



a) $[(\text{NH}_3)_5\text{Ru}^{\text{II}}(3\text{-tfmpy})]^{2+} = [(\text{NH}_3)_5\text{Ru}^{\text{III}}(3\text{-tfmpy})]^{3+} = 5.0 \text{ mM}$; $\mu_{\text{rcts}} = 0.0450$; $\text{GP}_{\text{rcts}} = 0.175$
 b) $[\text{K}_4\text{M}(\text{CN})_6]_{\text{added}} = 3.92 \times 10^{-4} \text{ M}$ (0.0784 equivalents); $\mu_{\text{total}} = 0.0480$; $\text{GP}_{\text{total}} = 0.180$

Table 3-26. ET self-exchange activation parameters for reaction 3-2 derived from Figure 3-30

| | slope | intercept | ΔH^\ddagger (kJ/mol) | ΔS^\ddagger (J/mol·K) | ΔG^\ddagger_{298} (kJ/mol) | E_{IPCT} (kJ/mol) | E_{IPCT} eV |
|--|-------|-----------|---------------------------------|----------------------------------|---------------------------------------|------------------------|------------------|
| (3-tfmpy) $A_5Ru^{II/III}$ without salt | -2500 | 12.07 | 20.8 ± 0.8 | -97.2 ± 2.8 | 49.8 ± 1.7 | - | - |
| With $K_4Ru(CN)_6$ | -4000 | 19.51 | 33.3 ± 1.3 | -35.3 ± 4.5 | 43.8 ± 1.5 | 2.90E-22 | 1.81 |
| With $K_4Os(CN)_6$ | -5570 | 25.52 | 46.3 ± 1.9 | 14.6 ± 6.4 | 41.9 ± 1.5 | 2.83E-22 | 1.77 |
| With $K_4Fe(CN)_6$ | -7150 | 35.04 | 59.5 ± 1.1 | 93.8 ± 3.8 | 31.5 ± 1.1 | 1.71E-22 | 1.07 |

The $K_4Fe(CN)_6$ salt shows the highest enthalpy of activation at 59.5 ± 1.1 kJ/mol and also the least negative entropy of activation at 93.8 ± 3.8 J/mol·K. The $K_4Os(CN)_6$ shows an enthalpy of activation at 46.3 ± 1.9 kJ/mol and an entropy of activation of 14.6 ± 6.4 J/mol. The $K_4Ru(CN)_6$ salt has the least enthalpy of activation for the $M(CN)_6^{4-}$ catalyzed reactions at 33.3 ± 1.3 KJ/mol and most negative entropy of activation at -35.3 ± 4.5 J/mol·K.

The enthalpy of activation for a reaction essentially measures the work which must be done against bonding and other force interactions in order to bring the reactants to the transition state. The entropy of activation reflects the change in the overall degree of order required of the system so that it can “find” the transition state. Also, in the case of an ET reaction, the degree of adiabaticity of the electron transfer step itself, once the transition-state geometry has been attained, shows up in the value of ΔS^\ddagger .^{49,50} According to Equations 1-22 and 2-7, the following equation can be obtained⁴

$$\Delta S^\ddagger \cong \ln[(k_b / h)(4\pi N r^3 / 3000)] + \ln \kappa_{el} \quad 3-32$$

and it shows the changes in κ_{el} (due to the degree of superexchange coupling) will show up in the value of ΔS^\ddagger obtained from an Eyring plot (ΔS^\ddagger arises with the increase of κ_{el}). The huge variations in ΔS^\ddagger can be used to extract underlying variation in κ_{el} in the improbable limit of this being the sole causal basis. If we set $\kappa_{el} \equiv 1$ for the M = Fe case, we then arrive at $\kappa_{el} = 0.83, 0.88$ and 0.92 for the “none”, Ru and Os cases. These values seem reasonable since the rate enhancement from Ru→Os→Fe is more obvious due to more superexchange coupling. Also, it agrees with the fact that these outer-sphere ET reactions are generally thought of as being at or near the adiabatic limit.⁵¹

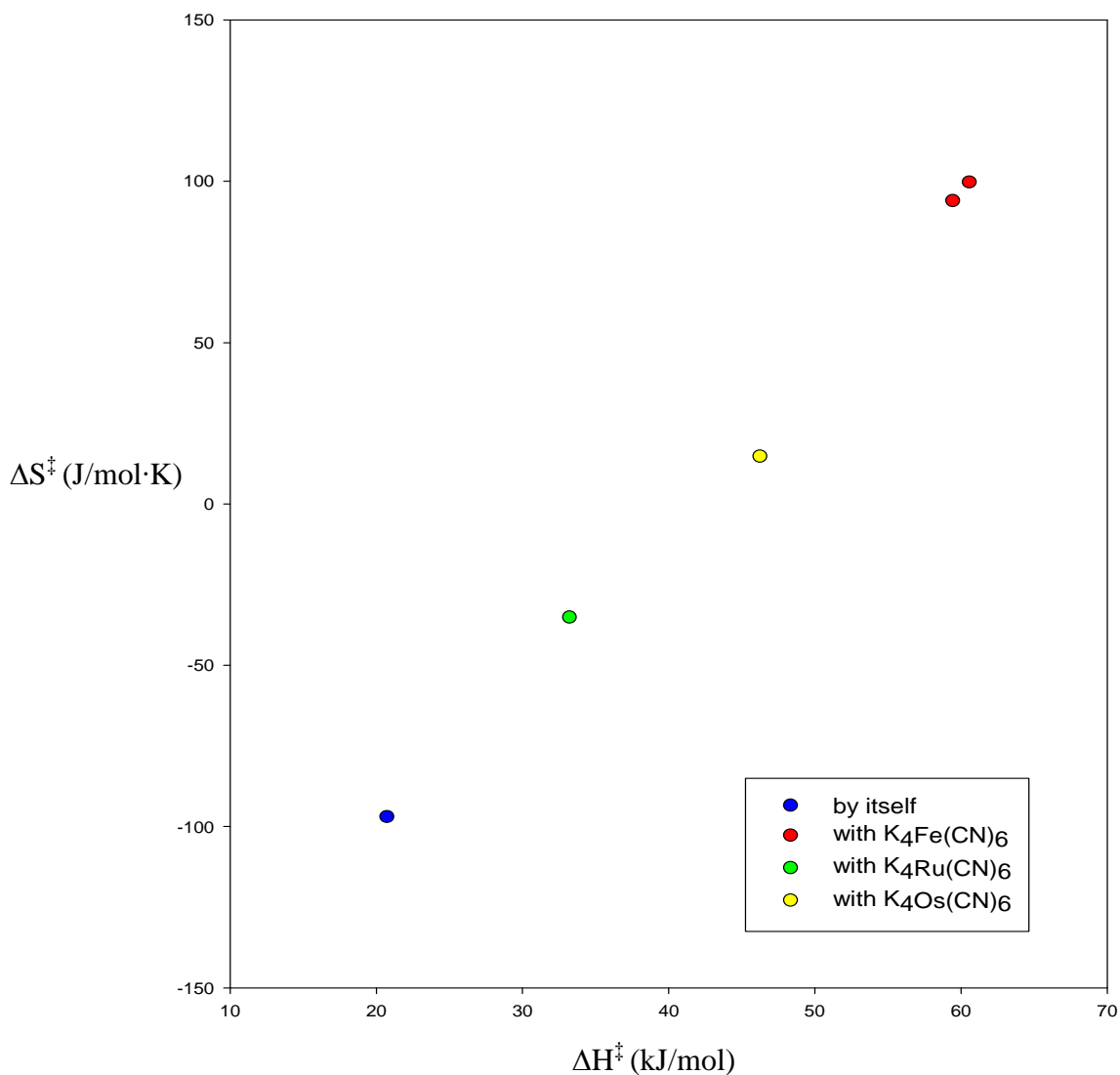
In the case of the added simple salts, rate enhancements (with the increased GP value) were very small compared to those observed with added $K_4M(CN)_6$. Therefore, we can eliminate the possibility of the acceleration being due to added GP, since the amount of added ionic strength of $K_4M(CN)_6$ salt was trivial and the $GP_{rcts} = 0.175$ barely differs from $GP_{total} = 0.180$ (note Figure 3-30).

If we compare Tables 3-21 and 3-26, we note that with the greatly increased value of k_{etx}/k_{et} , ΔS^\ddagger changed from a negative to a positive value. A positive entropy of activation for an associative reaction where things have to collide/associate to react is very unusual. One possible explanation would be that stronger ion-pair formation (upon going from Ru to Os to Fe) might cause a lesser degree of electrostriction of the solvent molecules around the reactant ions because solvent molecules are released after an ion pair forms between the highly oppositely charged $(NH_3)_5Ru^{III}(3\text{-tfmpy})^{3+}$ and $M(CN)_6^{4-}$ ions.^{34,50,52} However, our studies of the ion pair

association constants for the series of mixed-valence ion pairs indicates little, if any, difference in ion pairing behavior.

The values in Table 3-26 show that there is a strong inverse correlation between the enthalpic and entropic barriers. Since ΔH^\ddagger progressively increases while ΔS^\ddagger goes from negative to positive as $M = Ru \rightarrow Os \rightarrow Fe$. The overall increase in ET rate means that the entropic term clearly dominates. If ΔS^\ddagger is plotted vs ΔH^\ddagger , we obtain Figure 3-31. It shows an essentially perfect compensation effect⁵³ between the activation entropy and enthalpy barriers; as ΔH^\ddagger becomes more positive, ΔS^\ddagger goes up as well as the magnitudes are such that there is a progressively smaller net free energy barrier and hence a faster rate as we go from no added $M(CN)_6^{4-}$ to $M = Ru \rightarrow Os \rightarrow Fe$. Since the ΔH^\ddagger and ΔS^\ddagger terms have opposite algebraic signs in the Gibbs free energy equation (Equation 2-8), they can compensate for each other in a related series of reactions (as has been discussed in detail by Guo⁵⁴).

Figure 3-31. Activational entropy-enthalpy compensation effect between measured ΔS^\ddagger vs ΔH^\ddagger for the ET self-exchange reaction of $[(\text{NH}_3)_5\text{Ru}^{\text{II/III}}(\text{3-tfmpy})]^{2+/3+}$ both by itself and in the presence of added $\text{K}_4\text{M}^{\text{II}}(\text{CN})_6$ ^{a,b} as $\text{M} = \text{Ru} \rightarrow \text{Os} \rightarrow \text{Fe}$



a) $[(\text{NH}_3)_5\text{Ru}^{\text{II}}(\text{3-tfmpy})]^{2+} = [(\text{NH}_3)_5\text{Ru}^{\text{III}}(\text{3-tfmpy})]^{3+} = 5.0 \text{ mM}$; $\mu_{\text{rcts}} = 0.0450$;

$$\text{GP}_{\text{rcts}} = 0.175$$

b) $[\text{K}_4\text{M}(\text{CN})_6]_{\text{added}} = 3.92 \times 10^{-4} \text{ M}$ (0.078 eq.); $\mu_{\text{total}} = 0.0469$; $\text{GP}_{\text{total}} = 0.178$

It is surprising to us that the no-added salt point lines up so well with the $M = Ru \rightarrow Os \rightarrow Fe$ series since the presumed mechanism and transition state configuration are so different. The mechanistic difference arises since the known K_{IP} values in Table 3-22 allow us to calculate that the ratio of the ternary association complex $[A_5Ru^{II}L, M(CN)_6, Ru^{III}A_5L]^+$ to binary complex $[A_5Ru^{II}L, Ru^{III}A_5L]^{5+}$ is on the order of IPCT energy under the conditions relevant to Figure 3-31. The progression in ΔH^\ddagger of $+33.3 \text{ kJ/mol} \rightarrow +46.3 \rightarrow 59.5$ as $M = Ru \rightarrow Os \rightarrow Fe$ is also surprising since, in the traditional interpretation, ΔH^\ddagger mostly reflects work done against inter- and intramolecular forces in order to attain the transition state. The very similar natures of the $M(CN)_6^{4-}$ species, similar solvation energies, and similar $w(r, \mu)$ terms (see Equation 3-12) for pairing with $A_5Ru^{III}L^{3+}$ offer no obvious explanation for the observed ΔH^\ddagger progression. Work in progress now seeks to explore whether the observed variation in ΔH^\ddagger , ΔS^\ddagger and ΔG^\ddagger for the $M(CN)_6^{4-}$ series are compatible with the idea of a progressively “turned on” hole-transfer superexchange mechanism. However, the data in Table 3-26 present us with a puzzle of why ΔH^\ddagger changes so much with $M(CN)_6^{4-}$ and why the enthalpic barrier should be highest in the case of the most easily-oxidized $M(CN)_6^{4-}$ anion catalyst when $M = Fe$ (with the smallest E_{IPCT}).

One interpretation of the data at this point would be that the participation of the hole transfer state requires additional enthalpic activation in order to become effective and catalyze ET. It is well-known that the entropy change associated with the outer-sphere ET reaction $(NH_3)_5Ru^{III}py^{3+} + Fe^{II}(CN)_6^{4-} \rightarrow (NH_3)_5Ru^{II}py^{2+} + Fe^{III}(CN)_6^{3-}$ is favorable by $\sim 40 \text{ e.u.}$ ⁵⁵ due to the large degree of solvent release which occurs upon charge neutralization around the metal centers when $Ru(III)$, $M(II)$

→ Ru(II), M(III) = (3⁺, 4⁻) → (2⁺, 3⁻). Some substantial fraction of this quantity would be expected to still apply inside our ternary association complexes, and there would not be a strong dependence on the identity of M. Note that the vibrational spectra of Fe(CN)₆⁴⁻, Os(CN)₆⁴⁻ and Ru(CN)₆⁴⁻ are not very different and therefore entropy changes should be dominated by solvation effects. The strong decrease in the entropic barrier as M goes from none → Ru → Os → Fe could be due to increasing reaction adiabaticity (note κ_{el} in Equation 1-22) since the prefactor in the equation gets swept into ΔS^\ddagger in the Eyring formalism. The strongly increasing enthalpic barrier along the series would then be associated with extra work being done against forces so that the reactants can achieve the very specific transition state geometries that provide maximum supercharge coupling across the ternary ionic assembly.

References

1. Tobe, M.L; Burgess, J. *Inorganic Reaction Mechanisms*, Addison Wesley Longman Inc., New York, **1999**, Chapter 8.
2. Plane, R.A. *J. Phys. Chem.* **1952**, 56(1), 33-38.
3. Burgess, J.; Sanchez, F.; Morillo, E. et al. *Transition Metal Chemistry*, **1986**, 11(5), 166-169.
4. Chun, S. J. Master's Thesis, University of San Francisco, **2001**.
5. Inagaki, M. Master's Thesis, University of San Francisco, **2006**.
6. Luo, X. Master's Thesis, University of San Francisco, **1997**.
7. Sista, P. Master's Thesis, University of San Francisco, **2009**.
8. Tanaka, M. Master's Thesis, University of San Francisco, **2004**.
9. Bertini, I. Luchinat, C. *NMR of Paramagnetic Molecules in Biological Systems*, Benjamin/Cummings Publishing Company, Inc. **1986**, p 12.
10. Mao, W. Qian, Z. Yen, H. Curtis, J.C. *J.Am.Chem.Soc.* **1996**, 118, 3274.
11. (a) Moore, J.W.; Pearson, R.G. *Kinetics and Mechanism: A study of homogeneous chemical reactions*, 3rd Edition, John Wiley & Sons Inc. **1981**, p 272.

(b) Bulter, J.N. *Ionic Equilibrium: Solubility and pH Calculations*, John Wiley & Sons Inc, **1998**, 46.
12. Bronsted, J. N. *Z. Phys. Chem.*, **1925**, 115, 337.
13. Debye, P. Huckel E. *Physikalische Zeitschrift*. **1923**, 24, 185.
14. Rieger, P.H. *Electrochemistry*, 2nd Edition. Springer. **1993**, 90.
15. Harris, D.C. *Quantitative Chemical Analysis*, 6th Edition, W.H. Freeman and Company, **2003**.

16. Bjerrum, N. *Z. Phys. Chem.*, **1925**, 118, 251.
17. Mortimer, R.G. *Physical Chemistry*, 2nd Edition, Academic Press, 1993, p 233
18. Brown, G.M.; Sutin, N. *J. Am. Chem. Soc.* **1979**, 101, 883.
19. Guggenheim, E.A.; Turgen, J.C. *Trans Faraday Soc.* **1955**, 15, 747 .
20. Curtis J.C., Inagaki M., Chun S.J., Eskandari V., Luo X., Pan Z. N.,
Sankararaman U., Pengra G. E., Zhou J., Hailey P., Laurent J., Utalan D.,
Chem. Phys. **2006**, 326, 43.
21. Kramers, H. A. *Physica* **1934**, 1, 182.
22. McConnell H. M. *J. of Chem. Phys.* **1961**, 35, 508.
23. Wolf, E. *Progress in Optics*, Volume XXXVII, North Holland, **1997**, 355.
24. Levi, A.F.J. *Applied Quantum Mechanics*, 2nd Edition, Cambridge University
Press, **2006**, p 145.
25. Weiss, U. *Quantum Dissipative Systems*. World Scientific Publishing
Company, **2008**, p 300.
26. Ratner, M.A. *Quantum Mechanics in Chemistry*. Dover Publications. 2002, p
255.
27. Paulson, B.P.; Miller, J.R.; Gan, W; Closs, G. *J. Am. Chem. Soc.* **2005**, 127,
4860.
28. Todd, M.D.; Nitzan, A and Ratner, M.A. *J. Phys. Chem.* **1993**, 97, 29.
29. Fuoss, R.M. *J. Am. Chem. Soc.* **1958**, 80 (19), 5059.
30. Eigen, M. *J. Phys. Chem.* **1954**, 1, 176.
31. Claudio Chiorboli, Maria Teresa Indelli, Maria Anita Rampi Scandola, and
Franco Scandola *J. Phys. Chem.* **1988**, 92, 156-163.
32. Howe, J. L. *J. Am. Chem. Soc.* **1896**, 18, 981.

33. Walker, J.M.; Wilson, K. Principles and Techniques of Biochemistry and Molecular Biology, 6th Edition. Cambridge University Press, **2005**, p 7.
34. Curtis, J.C.; Meyer, T. J. *Inorg. Chem.* **1982**, 21, 1562.
35. Rudd, D.P., Taube, H. *Inorg Chem.* **1971**, 10, 1543.
36. Olson, A.R.; Simonson, T.R. *J. Chem. Phys.* **1949**, 17, 1167.
37. De Cola, L. *Molecular Wires: From Design to Properties*. (Topics in Current Chemistry). Springer, **2005**, p 68.
38. Connors, K.A. *Chemical Kinetics: The Study of Reaction Rates in Solution*. Vch Pub, **1990**.
39. Marcus, R.A. *J. Phys. Chem. B.* **1998**, 102, 10071.
40. Chang, J.P., Fung, E.Y., Curtis, J.C. *Inorg. Chem.* **1986**, 25, 4233.
41. Frisch, M. J.; Trucks, G. W.; Schlegel, H. B.; Scuseria, G. E.; Robb, M. A.; Cheeseman, J. R.; Scalmani, G.; Barone, V.; Mennucci, B.; Petersson, G. A.; Nakatsuji, H.; Caricato, M.; Li, X.; Hratchian, H. P.; Izmaylov, A. F.; Bloino, J.; Zheng, G.; Sonnenberg, J. L.; Hada, M.; Ehara, M.; Toyota, K.; Fukuda, R.; Hasegawa, J.; Ishida, M.; Nakajima, T.; Honda, Y.; Kitao, O.; Nakai, H.; Vreven, T.; Montgomery, Jr., J. A.; Peralta, J. E.; Ogliaro, F.; Bearpark, M.; Heyd, J. J.; Brothers, E.; Kudin, K. N.; Staroverov, V. N.; Kobayashi, R.; Normand, J.; Raghavachari, K.; Rendell, A.; Burant, J. C.; Iyengar, S. S.; Tomasi, J.; Cossi, M.; Rega, N.; Millam, N. J.; Klene, M.; Knox, J. E.; Cross, J. B.; Bakken, V.; Adamo, C.; Jaramillo, J.; Gomperts, R.; Stratmann, R. E.; Yazyev, O.; Austin, A. J.; Cammi, R.; Pomelli, C.; Ochterski, J. W.; Martin, R. L.; Morokuma, K.; Zakrzewski, V. G.; Voth, G. A.; Salvador, P.; Dannenberg, J. J.; Dapprich, S.; Daniels, A. D.; Farkas, Ö.; Foresman, J. B.; Ortiz, J. V.;

- Cioslowski, J.; Fox, D. J. Gaussian 09, Revision A.1, Gaussian, Inc., Wallingford CT, **2009**.
42. Waysbort,D; Evenor,M; Navon, G *Inorg. Chem.* **1975**, 14 (3), 514.
43. Sexton,D.A.; Curtis, J.C.; Cohen, H.; Ford, P.C. *Inorg. Chem.* **1984**, 23 (1), 49.
44. Han, Z. Master Thesis in progress, University of San Francisco.
45. Curtis, J.C. PH.D. Thesis, University of North Carolina, Chapel Hill, **1982**.
46. Wulfsberg, G. *Principles of Descriptive Inorganic Chemistry*. University Science Books, **1992**, p 210.
47. Robinson, R.A.; Stokes, R.H. *Electrolyte Solutions*, 2nd Revised Edition. Dover Publications, **2002**, p15.
48. Alstrum-Acevedo, J.H; Brennaman, M.K.; Meyer, T. J. *Inorg. Chem.*, **2005**, 44 (20), 6802–6827.
49. Gallicchio, E; Kubo, M.M.;Levy, R.M. *J. Am. Chem. Soc.* **1998**, 150, 4526
50. Rakitzis, E.T. *Biochem. J.* **1990**, 269, 835.
51. Newton, M.D. *J. Phys. Chem.* **1988**, 92, 3049-3056.
52. El-Hammamy, N. H.; El-Kholy, M.M.; Ibrahim, G. A.; Kawana, A.I. *Advances in Applied Science Research*, **2010**, 1 (3): 168-173.
53. Anslyn, E.V.; Dougherty, D.A. *Modern Physical Organic Chemistry*, University Science Books, **2006**, p 469.
54. Liu, L.; Guo, Q.X. *Chem. Rev.*, **2001**, 101 (3), 673–696.
55. Miralles, A.J. Armstrong, R.E. Haim, A. *J. Am. Chem. Soc.* 1977, 99(5), 1416.